

Understanding the Physical Processes Driving Galaxy Evolution in Clusters: A Case Study of Two $z \sim 0.5$ Galaxy Clusters

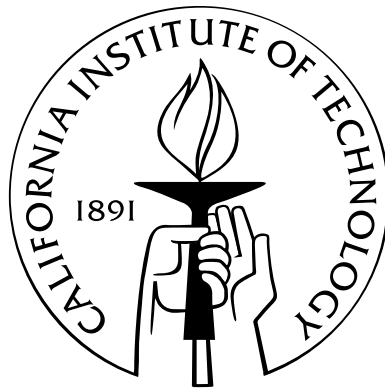
Thesis by

Sean M. Moran

In Partial Fulfillment of the Requirements

for the Degree of

Doctor of Philosophy



California Institute of Technology

Pasadena, California

2008

(Defended August 1st, 2007)

© 2008

Sean M. Moran

All Rights Reserved

To waking up at 4 a.m. on Rangiroa for a glimpse of the LMC...

Acknowledgements

Wanting to begin with a witty remark, I Googled for “Welsh jokes.” They were all terrible. So I turned my search to “famous Welshmen,” and, aha!, I found just what I was looking for. I can now emphatically say that I owe a great debt of gratitude to two famous Welshmen, without whom I would never have completed this thesis: Richard Ellis (famous advisor of students) and Samuel Adams (famous brewer of fine Boston lager).

In all seriousness, I thank Richard especially for his expertise in keeping me focused on the big picture and plan of my thesis, and in navigating the political pitfalls of Caltech and colleagues alike. And all those galaxy morphologies! Also, I would like to thank Tommaso Treu for his invaluable mentoring and help with all things galaxy evolution. And I thank them both for reading lots of drafts of lots of papers, providing great advice with never a complaint! And for many a lunch at Cafe Pesto.

I would like to thank Graham Smith for his work on MS 0451 and for advice about photometric redshifts and all sorts of other issues. And to the rest of the revolving crew of postdocs who have enlisted for tours of duty in the Ellis empire, thanks for both the valuable and the off-the-wall discussions, particularly: Chris Conselice who first cornered me getting coffee first year with an “I hear you might be interested in galaxy evolution,” James Taylor for good discussions on cluster velocity dispersions and for always seeming to pop up randomly in whatever city you happen to be in, and Richard Massey, Lauren MacArthur, Johan Richard, and Daisuke Nagai for scientific insight and good company on observing runs or at conferences. Thanks also to past and present advisees of Richard Ellis, for soldiering on with me: Kevin Bundy, Dave Sand, Mike Santos, and Dan Stark.

I acknowledge all the hard work of other collaborators whom I have not mentioned, whose contributions to the published papers making up this thesis were essential. I thank also the members of my thesis committee for taking the time to read my work and serve on the panel: Geoff Blake, Andrew Blain, George Djorgovski, and Marc Kamionkowski.

And it would be criminal to forget to thank Judy McClain for her amazing mastery of booking travel, handling page charges, and somehow always keeping track of “Where in the world is Richard Ellis?” Thanks also go to the Robinson computer support folks, Patrick, Cheryl, and Anu, for keeping *bera* healthy and for their mad skills in disk cross-mounting every which way.

I acknowledge all the amazing folk at Keck, particularly Greg Wirth, Grant Hill, and Jim Lyke for their expert help with DEIMOS. Their enthusiasm makes me want to move to Hawaii. That, and the beaches. And that Kalua Pork...Oh, man, that stuff’s good.

Thanks to my classmates and fellow grad students for their companionship, commiseration, and humor, particularly all of my various officemates and roommates. Thanks for putting up with me. I also pause to recognize my brothers who were cut down all too early: Luke, Rob, Irvin, Chao, Mike, Eli, and yes, Billy. *Sometimes you eat the bar, and sometimes, well, he eats you.*

Organizing the annual graduate-student ski trip was great fun, and I would like to thank the P. J. Young fund for making that possible every year.

I must also acknowledge all of the support I have received over the years from family and friends back home, here in California, and everywhere, especially Bryan, Mark, Peter, Andrew, Ian, and my brothers James and Matt. Thanks for the laughs, you chowderheads. Mr. Dave Wilbur and Mr. Jim Sullivan, my high school physics and math teachers, deserve some long overdue thanks for instilling in me the basics I need, through the wonders of mousetrap-powered cars and polynomial plotting as a computer game.

Thanks to my Uncle Jim for giving me a taste of backyard astronomy way back when. And thanks to Aunt Mary’s lawyerly eye for false claims, *this* thesis does not

begin with the phrase “It is commonly known that...” (“Commonly known? *I* don’t commonly know that!”) Nan and G. P., thanks for all of your love, your good advice, and for always being lots of fun! I may get my scientist’s mind from G. P., but I think I get my mischievous streak from Nan. (Nana, where did you get that “No Parking” sign?)

I cannot give enough thanks to my parents for all their love and support through the years, even though—and I may be mistaken here—I believe my mom would rather I had not moved so far from home. So thanks, Mom, for always telling me “Don’t work too hard!”, and Dad, for providing the counterpoint, “Keep plowing ahead; don’t lose your momentum.”

Finally, thanks to my wonderful wife Laura, my astronomer girl and best friend. I came to Caltech for a degree, but I am leaving with a much bigger prize than that! And I took you to Tahiti!

And even if he’s a lazy man—and the Dude was most certainly that. Quite possibly the laziest in all of Los Angeles County, which would place him high in the runnin’ for laziest worldwide. Sometimes there’s a man, sometimes, there’s a man. Well, I lost my train of thought here. But... aw, hell. I’ve done introduced it enough.

—*The Big Lebowski*

Abstract

Clusters of galaxies represent the largest laboratories in the universe for testing the incredibly chaotic physics governing the collapse of baryons into the stars, galaxies, groups, and diffuse clouds that we see today. Within the cluster environment, there are a wide variety of physical processes that may be acting to transform galaxies.

In this thesis, we combine extensive Keck spectroscopy with wide-field *HST* imaging to perform a detailed case study of two intermediate redshift galaxy clusters, Cl 0024+1654 ($z = 0.395$) and MS 0451-03 ($z = 0.540$). Leveraging a comprehensive multiwavelength data set that spans the X-ray to infrared, and with spectral-line measurements serving as the key to revealing both the recent star-formation histories and kinematics of infalling galaxies, we aim to shed light on the environmental processes that could be acting to transform galaxies in clusters.

We adopt a strategy to make maximal use of our *HST*-based morphologies by splitting our sample of cluster galaxies according to morphological type, characterizing signs of recent evolution in spirals and early types separately. This approach proves to be powerful in identifying galaxies that are currently being altered by an environmental interaction: early-type galaxies that have either been newly transformed or prodded back into an active phase, and spiral galaxies where star formation is being suppressed or enhanced all stand out in our sample.

We begin by using variations in the early-type galaxy population as indicators of recent activity. Because ellipticals and S0s form such a homogeneous class in the local universe, we are sensitive to even very subtle signatures of recent and current environmental interactions. This study has yielded two key results: By constructing the Fundamental Plane (FP) of Cl 0024, we observe that elliptical and S0 galaxies

exhibit a high scatter in their FP residuals, which occurs only among galaxies in the cluster core, suggesting a turbulent assembly history for Cl 0024 early types. Near the Virial radius of Cl 0024, we observe a number of compact, intermediate-mass ellipticals undergoing a burst of star formation or weak AGN activity, indicated by strong [O II] emission; their locations may mark the minimum radius at which merging is effective in each cluster.

While E+S0 galaxies do prove to be sensitive indicators of environmental interaction, it is the spiral galaxies that, of course, host the bulk of star formation within and around these clusters. We therefore probe for kinematic disturbances in spiral disks by measuring resolved rotation curves from optical emission lines, and constructing the Tully-Fisher relation for spirals across Cl 0024 and MS 0451. We find that the cluster Tully-Fisher relation exhibits significantly higher scatter than the field relation. In probing for the origin of this difference, we find that the central mass densities of star-forming spirals exhibit a sharp break near the cluster Virial radius, with spirals in the cluster outskirts exhibiting significantly lower densities. We argue that these results considered together demonstrate that cluster spirals are kinematically disturbed by their environment, likely due to galaxy–galaxy interactions (harassment).

We then discuss our most powerful method of tracking galaxy evolution across Cl 0024 and MS 0451: identifying and studying “transition galaxies”—galaxies whose stellar populations or dynamical states indicate a recent or ongoing change in morphology or star formation rate. Such galaxies are often revealed by star formation histories that seem to be at odds with the galaxy morphologies: for example, spiral galaxies with no signs of star formation, or elliptical galaxies that *do* show signs of star formation.

We identify and study one such class of objects, the “passive spirals” in Cl 0024. These objects exhibit no emission lines in their spectra, suggesting a lack of star formation, yet are surprisingly detected in the UV, revealing the presence of young stars. By modeling the different temporal sensitivities of UV and spectroscopic data to recent activity, we show that star formation in Cl 0024 passive spirals has decayed on timescales of less than 1 Gyr, consistent with the action of “gas starvation”.

We then build on and link together our previous indications of galaxy evolution at work, aiming to piece together a more comprehensive picture of how cluster galaxies are affected by their environment at intermediate redshift. To accomplish this, we document what we believe to be the first direct evidence for the transformation of spirals into S0s: through an analysis of their stellar populations and recent star formation rates, we link the passive spiral galaxies in both clusters to their eventual end states as newly generated cluster S0 galaxies. Differences between the two clusters in both the timescales and spatial location of this conversion process allow us to evaluate the relative importance of several proposed physical mechanisms that could be responsible for the transformation. Combined with other diagnostics that are sensitive to either ICM-driven galaxy evolution or galaxy–galaxy interactions, we describe a self-consistent picture of galaxy evolution in clusters.

We find that spiral galaxies within infalling groups have already begun a slow process of conversion into S0s primarily via gentle galaxy–galaxy interactions that act to quench star formation. The fates of spirals upon reaching the core of the cluster depend heavily on the cluster ICM, with rapid conversion of all remaining spirals into S0s via ram-pressure stripping in clusters where the ICM is dense. In the presence of a less-dense ICM, the conversion continues at a slower pace, with galaxy–galaxy interactions continuing to play a role along with “starvation” by the ICM. We conclude that the buildup of the local S0 population through the transformation of spiral galaxies is a heterogeneous process that nevertheless proceeds robustly across a variety of different environments from cluster outskirts to cores.

Contents

Acknowledgements	iv
Abstract	vii
List of Figures	xiv
List of Tables	xvi
1 Introduction	1
1.1 Nature vs. Nurture in the Evolution of Galaxy Morphologies and Star- Formation Rates	1
1.2 Understanding “Nurture”: A Wide Field Survey of Two $z \sim 0.5$ Clusters	4
1.2.1 Physical Processes	6
1.2.1.1 Cluster Gas Interactions	6
1.2.1.2 Galaxy–Galaxy Interactions	8
1.2.1.3 Tidal Processes	9
1.2.2 Disentangling the Effects of the Various Processes	9
1.3 Plan of the Thesis	12
1.3.1 Overall Strategy	13
1.3.2 Using E+S0s as Sensitive Indicators of Interaction	14
1.3.3 Kinematic Disturbances in Spiral Disks	15
1.3.4 When Stellar Population and Morphology Tell Conflicting Stories	15

2	A Wide-Field Survey of Two Intermediate Redshift Galaxy Clusters: Characteristics of the Survey	18
2.1	Imaging	18
2.1.1	Source Extraction and Photometry	22
2.1.2	Morphological Classification	25
2.2	Spectroscopy	28
2.2.1	Data Reduction and Redshift Determination	30
2.2.2	Completeness	35
3	Signatures of Environmental Interaction in Cl 0024 Early-Type Galaxies	38
3.1	Introduction	39
3.2	Observations	41
3.3	Analysis	42
3.3.1	Local Density Measurements	44
3.3.2	Stellar Velocity Dispersions	46
3.3.3	Surface Photometry	47
3.3.4	Line-Strength Measures	51
3.4	Results	55
3.4.1	Cluster: Empirical Scaling Laws	55
3.4.1.1	The Fundamental Plane	55
3.4.1.2	$[\text{MgFe}]'-\sigma$ and Balmer- σ Relations	59
3.4.2	Radial Trends	63
3.4.2.1	Fundamental Plane	63
3.4.2.2	Line Strengths	68
3.4.2.3	Residual Correlations	75
3.4.3	Luminosity Trends	77
3.5	Discussion	78
3.5.1	Radial Trends and Star-Formation Timescales	79
3.5.2	A Simple Infall Model	80

3.5.3	Physical Mechanisms	86
3.6	Summary	91
4	Dynamical Evidence for Environmental Evolution of Intermediate Redshift Spiral Galaxies	102
4.1	Introduction	103
4.2	Observations	104
4.3	Rotation Curve Analysis	105
4.3.1	Extraction of Rotation Curves	106
4.3.2	Surface Photometry	108
4.3.3	Model Fitting	113
4.3.4	Quality Control	114
4.4	The Tully-Fisher Relation	116
4.4.1	A Comparison to Independent Measurements	120
4.5	Trends in Spiral Masses, Densities, and M/L	122
4.5.1	Tully-Fisher Residuals and M/L	122
4.5.2	Densities and Masses	124
4.6	Discussion	128
4.7	Conclusions	130
5	<i>GALEX</i> Observations of “Passive Spirals” in Cl 0024: Clues to the Formation of S0 Galaxies	136
5.1	Introduction	137
5.2	Observations and Sample Selection	139
5.2.1	Data	139
5.2.2	Sample Selection	140
5.3	UV Emission in Passive Cluster Spirals	141
5.4	Model Star Formation Histories	141
5.5	Discussion	145

6	Identifying the Physical Processes Responsible for the Observed Transformation of Spirals into S0s	147
6.1	Introduction	148
6.2	A Comparative Survey of Two $z \sim 0.5$ Clusters	150
6.2.1	Kinematic Structure of the Two Clusters	151
6.2.2	Previous Work	155
6.3	Data and Analysis	158
6.3.1	Spectral Line Measurement and Velocity Dispersion	159
6.4	Passive Spirals	161
6.5	Star Formation Histories of E+S0 Galaxies	170
6.6	The Local Environments of Passive Spirals and Young S0s	175
6.7	Physical Processes Driving the Transformation	180
6.7.1	The Cluster Outskirts	180
6.7.2	The Cluster Cores	184
6.7.2.1	Compact Emission-Line Ellipticals	185
6.7.2.2	Fundamental Plane	186
6.8	Discussion and Conclusions	191
7	Conclusions and Future Work	195
7.1	Summary	195
7.2	Reconciling Nature and Nurture	197
7.3	Future Work	199
	Bibliography	203

List of Figures

1.1	Evolution in $f(\text{E+S0})$ as a function of local density	2
1.2	The expected regimes of influence for various physical processes	11
2.1	Mosaic of 39 WFPC2 images of Cl 0024	20
2.2	Mosaic of 41 ACS images of MS0451	21
2.3	Cl 0024 K_S -band mosaic	23
2.4	MS 0451 K_S -band mosaic	24
2.5	Montage of MS 0451 cluster members from ACS imaging	27
2.6	Example spectrum with velocity dispersion fit	30
2.7	Montage of reduced 2D spectra from DEIMOS	31
2.8	Redshift distributions for Cl 0024 and MS 0451	33
2.9	Redshift completeness for the Cl 0024 and MS 0451 spectroscopic samples	37
3.1	Example surface photometry fits for Cl 0024 E+S0s	50
3.2	Fundamental Plane of Cl 0024	56
3.3	Measured $[\text{MgFe}]'$ and $(\text{H}\gamma+\text{H}\delta)$ vs. σ	61
3.4	FP residuals $\Delta \log(M/L_V)$ vs. R and Σ , for Cl 0024 E+S0s	65
3.5	EWs of $\text{H}\delta_A+\text{H}\gamma_A$ and $[\text{O II}]$ vs. R and Σ	69
3.6	Postage stamps of narrow emission line E+S0s	71
3.7	Coadded spectra, by radial zone and spectral type	73
3.8	Fractions of Balmer-strong and $[\text{O II}]$ -emitting E+S0s vs. R	74
3.9	Residuals from the $[\text{MgFe}]'-\sigma$ and $(\text{H}\delta+\text{H}\gamma)-\sigma$ relations	76
3.10	Radial trends in the residuals of dynamical relations	82

3.11	Spatial distribution of [O II] emitters and galaxies with excess Balmer absorption	85
4.1	Demonstration of rotation curve measurement	107
4.2	Images and rotation curves of cluster spirals	109
4.3	Images and rotation curves of field spirals	111
4.4	Tully-Fisher relations	117
4.5	Tully-Fisher residuals vs. color	123
4.6	Tully-Fisher residuals vs. R	124
4.7	Central densities of cluster spirals	126
4.8	Dynamical mass of cluster spirals vs. R	127
5.1	Coadded spectra of Cl 0024 E+S0s, passive spirals, and star-forming spirals	138
5.2	Histogram of $(FUV - V)_{AB}$ colors for subsets of Cl 0024 galaxies . . .	140
5.3	$(FUV - V)_{AB}$ vs. $H\delta_A$ for passive and active spirals	143
6.1	Dressler-Shectman plots for both clusters	154
6.2	Distributions of $FUV - V$ colors for both clusters	163
6.3	Color montage of active and passive spirals in Cl 0024	164
6.4	$FUV - V$ colors vs. $D_n(4000)$ for spirals in both clusters	167
6.5	$D_n(4000)$ vs. [O II] for cluster E+S0s	171
6.6	Coadded spectra of passive spirals and young S0s in both clusters . . .	173
6.7	Spatial distributions of key galaxy types in the fields of both clusters .	177
6.8	Strength of ram pressure as a function of radius in Cl 0024 and MS 0451	179
6.9	The Fundamental Planes of Cl 0024 and MS 0451	187
6.10	$\Delta \log(M/L_V)$ versus dynamical mass, M, for both clusters	190
7.1	Kinematic discrimination of Es and S0s	201

List of Tables

1.1	Basic properties of the clusters	10
2.1	Cl 0024+17 redshift catalog	34
2.2	MS 0451–03 redshift catalog	35
3.1	$\langle \Delta \log (M/L_V) \rangle$ for several subsets of our data	58
3.2	Listing of observed E+S0 cluster members	94
3.3	All measurements of E+S0 members of Cl 0024	97
4.1	Summary of Tully-Fisher sample selection	115
4.2	Inverse fits to Tully-Fisher relation	119
4.3	Information and rotation measurements of Cl 0024, MS 0451, and field spirals	132
6.1	Photometric and spectroscopic measurements for all cluster galaxies . .	160
6.2	Passive spirals and UV emission	162

Chapter 1

Introduction

1.1 Nature vs. Nurture in the Evolution of Galaxy Morphologies and Star-Formation Rates

In the local universe, the dense central regions of rich galaxy clusters are overwhelmingly populated by early-type (elliptical and S0) galaxies (>90%), with virtually no ongoing star formation. The fraction of star-forming, spiral galaxies increases as one looks further from the cluster center, eventually matching the field value ($\sim 55\%$), where early types and spiral galaxies are both common (Dressler et al. 1997). This trend was first quantified by Dressler (1980), and has come to be known as the *morphology–density relation*.

More recently, a variety of studies (e.g., Dressler et al. 1997; Smith et al. 2005a; Postman et al. 2005; Desai et al. 2007; Treu et al. 2003, hereafter T03) have traced the evolution of the morphology–density relation since $z \sim 1$. They find that the early-type fractions at high and intermediate densities, corresponding to cluster cores and groups of galaxies, respectively, have increased with time, as can be seen in Figure 1.1. The increase of the early-type fraction, f_{E+S0} , in the cores of clusters from 0.7 ± 0.1 at $z = 1$ to 0.9 ± 0.1 today stands in contrast to the lack of evolution among field galaxies, and demonstrates that galaxy morphologies evolve in a manner that depends on the environment in which the galaxies reside.

At the same time, evidence suggests that there has been a parallel decline in the integrated star-formation rate of cluster galaxies since at least $z \sim 1$ (Butcher

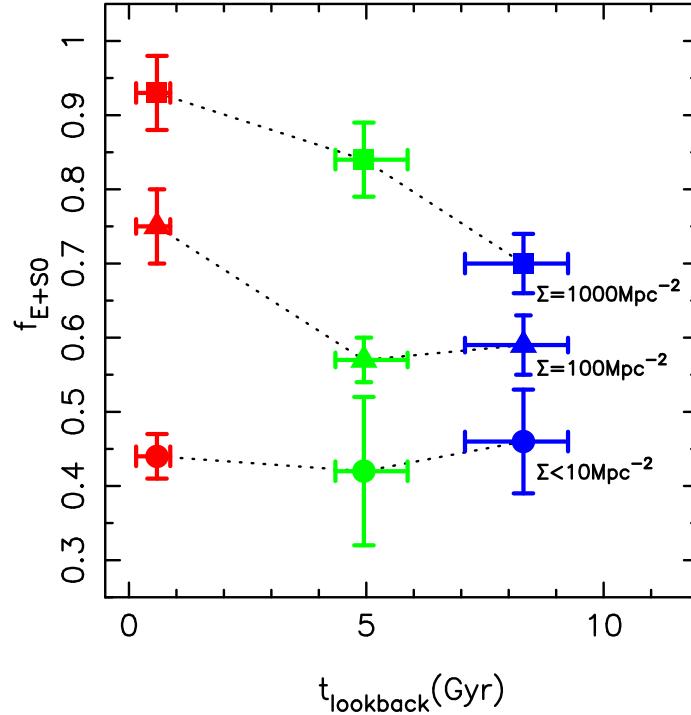


Figure 1.1 The time evolution in the fraction of E+S0 galaxies in three different bins of local density, from Smith et al. (2005a). Density, in Mpc^{-2} , is defined in terms of the projected area enclosed by a galaxy's ten nearest bright neighbors (absolute magnitude $M_V < -20$). Note that in the highest-density regions, corresponding to the cores of clusters, the E+S0 fraction rises monotonically from $z = 1$ to today, while the early-type fraction in moderately dense regions (corresponding to groups or the infall regions of clusters) has increased dramatically only in the last 5 Gyrs ($z \sim 0.5$).

& Oemler 1978; Margoniner et al. 2001; Poggianti et al. 2006). Little evolution is observed in the early types at the cores of clusters (Ellis et al. 1997; Tran et al. 2007), but wide field studies of clusters have traced an increasing star-formation rate with increasing cluster-centric radius (Poggianti et al. 1999; Balogh et al. 1999; Kodama et al. 2001, 2004; Kauffmann et al. 2004).

Given these observations, understanding *why* a galaxy's environment is so strongly correlated with its current appearance and star-formation history becomes a key question in developing a unified picture of how galaxies form and evolve. This long-standing question can be posed in a simple, somewhat philosophical way: nature or nurture? That is, do massive, red early-type galaxies predominate in the cores of clusters because they represent the descendants of the first objects to form in

the universe, with characteristics today that are the inevitable result of their longer evolutionary history (*nature*)? Or are these galaxies stripped of their star formation and spiral morphologies because of the harsh environment in which they live, an environment that inevitably shapes the properties of galaxies to be red and early type (*nurture*)?

In fact, as is almost always the case when such a stark choice is presented, the answer likely lies somewhere in the middle. Indeed, even the precise definitions of nature and nurture are muddled. The earliest galaxies to grow and turn red through the successive mergers of hierarchical formation—galaxies that we consider to have reached their current state by nature—have of course resided in a special environment right from their beginnings in the largest overdensities in the early universe. Nevertheless, if we restrict our definition of nurture to include only those interactions with gas, galaxies, and gravity that occur as a galaxy migrates through a range of environments, there remains abundant observational evidence in support of *both* scenarios, nature and nurture.

For example, in order to explain the fact that the most massive galaxies in the universe are red, a host of recent studies have proposed the action of “feedback” via winds from AGN or starbursts, an *intrinsic* mechanism that serves to halt star formation within a galaxy once a particular mass threshold is passed (e.g., Granato et al. 2004; Cattaneo et al. 2006). Without feedback, simulations of the hierarchical evolution of galaxies would incorrectly predict that the most massive galaxies at any epoch are blue, because these are the systems that have most recently merged out of smaller objects (many of which are star-forming) (Croton et al. 2006; de Lucia et al. 2006). Under the feedback scenario, galaxies by *nature* will turn red as their hierarchical assembly progresses.

At the same time, other observations point to a role for environmental interactions. The large fraction of spiral galaxies observed near the centers of intermediate redshift clusters ($\sim 30\%$) is remarkably similar to the fraction of non-star-forming disk galaxies (S0s) that appear to have been created since that time (e.g., Tran et al. 2005; Dressler et al. 1997). Arguments have been made for (Kodama & Smail 2001) and against

(Burstein et al. 2005) the idea that these spirals will directly transform into S0s by being *nurtured* through interactions specific to their local environment. Nevertheless, spirals near the centers of clusters must disappear via some sort of transformation by $z = 0$, at a rate that is much faster than is observed in spirals of similar mass in lower density environments (Smith et al. 2005a). The large populations of “poststarburst” galaxies seen in some clusters ($>5\%$, Dressler et al. 1999; Poggianti et al. 1999; Tanaka et al. 2007) only reinforces the notion that galaxies are having their star formation halted in the cluster environment, sometimes quite suddenly.

One might imagine a simple picture where giant ellipticals form through mergers accompanied by feedback to halt star formation, and S0s form from spirals that experience interactions with their local environment. Whether or not this simple picture holds up to greater scrutiny, at least some of the observed trends in galaxy morphology and star-formation rate should be due to physical processes that act only in the dense cluster environment. Gaining a better understanding of the precise physical processes that drive this environmental evolution will be the focus of this thesis.

1.2 Understanding “Nurture”:

A Wide Field Survey of Two $z \sim 0.5$ Clusters

Clusters of galaxies represent the largest laboratories in the universe for testing the incredibly chaotic physics governing the collapse of baryons into the stars, galaxies, groups, and diffuse clouds that we see today. Within the cluster environment, there are a wide variety of physical processes that may be responsible for the evolutionary trends detailed above—including galaxy mergers, harassment, interactions with the intracluster medium, or tidal processes (Moore et al. 1999; Fujita 1998; Bekki et al. 2002; Gunn & Gott 1972), which will each be described in §1.2.1 below.

While the action of different physical mechanisms will leave distinct spectral and dynamical signatures in the affected galaxies, many physical processes occur simulta-

neously in the central 0.5–1 Mpc of a cluster. In addition, clusters themselves exhibit a range of assembly states and intracluster gas densities (e.g., Smith et al. 2005b). As a result of the overlapping regimes of influence and the intrinsic variation among clusters, it has, so far, been impossible to disentangle the effects of the various processes (see Figure 1.2). Further complicating the picture, the relation between the overall decline in star formation rate and any morphological transformation is unclear, and may occur over different timescales (Poggianti et al. 1999; Kodama et al. 2004). But gaining an understanding of the complex interplay between the cluster gas, the internal properties of assembling galaxies, and the overall cluster dynamical state is crucial if we are to have a complete picture of the growth and evolution of galaxies in a hierarchical universe.

Much recent work on environmentally driven galaxy evolution has focused on intermediate redshift clusters, with redshifts in the range $0.3 < z < 0.8$ (e.g., Tran et al. 2007; Tanaka et al. 2007; Poggianti et al. 2006; Tran et al. 2005; Kodama et al. 2004; Lubin et al. 2002; Kodama et al. 2001; Balogh et al. 1999; Poggianti et al. 1999). Clusters in this redshift range are excellent targets for tracing the effect of environmental processes on galaxies, as they represent the period in time when the mix of galaxy morphologies and star-formation rates was evolving most rapidly. Particularly in the moderately dense regions outside the cores of such clusters, the morphologies of galaxies are transforming rapidly with redshift (Smith et al. 2005a), and so spectroscopic surveys are likely to catch galaxies in a transitional state, as they first encounter the cluster environment.

However, few such studies so far have combined spectroscopy that reaches to the outskirts of the cluster (e.g., Balogh et al. 1999) with detailed morphological information that can only be provided by *HST* imaging at these redshifts. In order to make progress in disentangling the effects of the various processes, it is essential to combine spectral diagnostics with morphologies that span the full range of cluster environments from the outskirts to the core, allowing simultaneous study of morphological evolution and the decline in star-formation rate.

In this thesis, we aim to take this fundamental next step, combining extensive

Keck spectroscopy with wide-field *HST* imaging to perform a detailed case study of two intermediate redshift galaxy clusters, Cl 0024+1654 ($z = 0.395$) and MS 0451–03 ($z = 0.540$). Leveraging a comprehensive multiwavelength data set that spans the X-ray to infrared, and with spectral line measurements serving as the key to revealing both the recent star-formation histories and kinematics of infalling galaxies, we aim to shed light on the environmental processes that could be acting to transform galaxies in clusters.

By undertaking an in-depth, wide-field comparative study of two prominent clusters, we hope to provide a complement to other observational (e.g., Cooper et al. 2007; Poggianti et al. 2006) and theoretical investigations (e.g., de Lucia et al. 2006) which trace with a broad brush the evolution in star-formation rate and the buildup of structure in the universe. As these two clusters have now been observed in more detail than perhaps any others at these redshifts, we have also endeavored to make as much of our data as practical available to other investigators through our web site.

1.2.1 Physical Processes

Before presenting a plan for the thesis that outlines our strategy for identifying the most important processes acting on infalling galaxies, we give a brief overview of the variety of physical mechanisms that have been proposed to be important in the transformation of star-formation rates and/or morphologies of galaxies as they assemble onto clusters.

1.2.1.1 Cluster Gas Interactions

Over 90% of the baryonic mass in galaxy clusters is not found within galaxies, but rather takes the form of a hot diffuse plasma—the intracluster medium (ICM) (White et al. 1993). Due to temperatures of up to 10 keV (10^8 K), thermal free–free emission from the gas is well traced by X-ray observations, and in the unperturbed case the ICM is in virial equilibrium with the deep potential well of the cluster. Due to its dominant mass and high thermal energy, the cluster ICM can have a dramatic effect

on a galaxy newly infalling into the cluster.

In the simplest scenario, a galaxy that is freely infalling at speeds of up to $\sim 1000 \text{ km s}^{-1}$ experiences a head wind, or “ram pressure”, due to the ICM, with pressure equal to $P = \rho v^2$, where ρ is the mass density of the ICM and v is the relative velocity of the galaxy with respect to the ICM (Gunn & Gott 1972). In general, this pressure is inversely proportional to radius, r , as both the ICM density and free-fall velocity increase as a galaxy approaches the cluster center.

If the ram pressure is high enough to overcome the gravitational binding energy ($\sim 2\pi G \Sigma_{gas} \Sigma_{star}$), gas that was once bound to the infalling galaxy can be stripped away, likely leading to a cessation of star formation. While the ICM even in the most massive clusters is not dense enough to disrupt cold molecular clouds (Boselli & Gavazzi 2006), both analytical arguments (Fujita 2001) and simulations (Quilis et al. 2000) show that stripping of the HI disk of a galaxy should be possible, and likely occurs at least in the cores of most massive galaxy clusters across a range of redshifts. A mild starburst due to gas compression may or may not precede the stripping (Fujita 1998).

However, other, more subtle interactions between a galaxy and the ICM may also be acting, and could serve to halt star formation in a galaxy even before ram pressure becomes important. Two such processes are thermal evaporation of galactic gas by contact with the hot ICM (Cowie & Songaila 1977), and stripping of gas due to turbulence in the ICM (Nulsen 1982). Recent calculations show that the effects of each of these mechanisms are less important than ram pressure in the restricted case where we consider typical large spirals ($>0.1 L_*$) assembling onto a massive cluster with velocity dispersion, $\sigma \gtrsim 500 \text{ km s}^{-1}$ (Boselli & Gavazzi 2006).

A final potentially important interaction with the ICM is “starvation” (Larson et al. 1980; Bekki et al. 2002). Starvation is a process by which the ICM strips away only the loosely bound halo gas surrounding a disk galaxy. In a normal galaxy, this loosely bound gas—only recently observed for the first time (Oosterloo et al. 2007, and references therein)—is thought to slowly accrete onto the galactic disk, acting as a reservoir of gas to fuel star formation. As proposed by Larson et al. (1980) and

modeled by Bekki et al. (2002), when this gas is stripped away via starvation, no new gas accretion occurs, and so star formation decays over the course of ~ 1 Gyr. Intriguingly, the simulations of Bekki et al. (2002) also predict a slow conversion of spiral galaxies to S0 after star formation stops.

1.2.1.2 Galaxy–Galaxy Interactions

Before an infalling galaxy ever reaches the core of a cluster where ICM interactions become important, it may well be altered or transformed by the ever increasing frequency of interactions with other galaxies. The observation that mass and light trace each other on large to small scales around clusters (Kneib et al. 2003) suggests that groups of roughly constant mass to light ratio—rather than individual galaxies—are the fundamental building blocks that coalesce to build up the cluster.

Galaxies within these infalling groups may well undergo “preprocessing” during initial infall, and being located in a group presents a rich opportunity for a galaxy to experience mergers or other close interactions with neighbors. It has been shown that a merger between spirals of unequal mass may result in the creation of an S0 galaxy (Bekki 1998), while major mergers are commonly presumed to result in a giant elliptical galaxy (e.g., Naab & Burkert 2003). Mergers therefore represent a viable mechanism for the decline in abundance of spiral galaxies and the corresponding increase in E+S0s.

In the inner regions of galaxy clusters, mergers are suppressed due to the high relative speeds of galaxies, which prevent the creation of a gravitationally bound pair during close encounters. Instead, an infalling cluster galaxy is likely to experience repeated close encounters at high speed due to the high density of galaxies in the cluster. This process, called galaxy–galaxy harassment, can lead to dramatic changes in a galaxy (Mastropietro et al. 2005; Moore et al. 1996, 1999). Moore et al. (1999) have shown through simulations that the fate of a harassed galaxy depends on its original mass and central density. Strongly concentrated Sa/Sb-type galaxies were seen to puff up their disks during infall, and so harassment may represent one way in which spirals transform into S0s in clusters. On the other hand, lower density Sc/Sd

spirals are more strongly affected by harassment; Moore et al. (1999) found that they were either completely disrupted, or else transformed into an object resembling a dwarf galaxy.

1.2.1.3 Tidal Processes

At the very cores of clusters, tidal interactions between galaxies and between a galaxy and the cluster potential can be intense. Several authors have suggested that these tidal interactions can dramatically affect the distribution of any remaining gas in a galaxy (Fujita 1998), as well as the kinematic structure itself (Natarajan et al. 1998), particularly in the case of spirals, which are less centrally concentrated than the giant ellipticals that reside stably in cluster cores. Due to the wide variety of processes hostile to galactic gas that operate much further from the cluster core, it may be that the primary role of tidal interactions in the cluster core would be to alter the morphology of a galaxy whose star formation has already been suppressed.

1.2.2 Disentangling the Effects of the Various Processes

Each of the processes discussed above provides a viable explanation for the observed decline in star formation and increase in early-type morphology that has been well traced from $z \sim 1$ to today. As introduced above, we aim in this thesis to use detailed case studies of Cl 0024 and MS 0451 to help reveal the most important processes contributing to environmental evolution in clusters and to identify the regimes within clusters where the most active transformations are taking place. To accomplish this, we have chosen two clusters for study whose global characteristics are similar, but which exhibit key differences in properties that serve to either highlight or suppress the action of one or more physical mechanisms.

Specifically, Cl 0024 and MS 0451 are similar in having comparable total masses, Abell richness class (Abell et al. 1989), and strong lensing features, yet they exhibit X-ray properties that are quite distinct (see Table 1.1). While MS 0451 is one of the most X-ray luminous clusters known (Donahue et al. 2003), Cl 0024 is somewhat

Table 1.1. Basic properties of the clusters

Name	RA ($^{\circ}$)	DEC ($^{\circ}$)	R_{VIR} (Mpc)	M_{200} (M_{\odot})	z	L_X (L_{\odot})	T_X (keV)
Cl 0024	6.65125	17.162778	1.7 ⁽¹⁾	8.7×10^{14} ⁽²⁾	0.395	7.6×10^{10} ⁽³⁾	3.5 ⁽³⁾
MS 0451	73.545417	-3.018611	2.6	1.4×10^{15} ⁽⁴⁾	0.540	5.3×10^{11} ⁽⁴⁾	10.0 ⁽⁴⁾

Note. — ⁽¹⁾ Treu et al. (2003), ⁽²⁾ Kneib et al. (2003), ⁽³⁾ Zhang et al. (2005), ⁽⁴⁾ Donahue et al. (2003).

underluminous in the X-ray, with a mass inferred from *XMM/Newton* observations that significantly underestimates the mass derived from other methods (Zhang et al. 2005). MS 0451 has X-ray luminosity seven times larger than Cl 0024, with a corresponding gas temperature nearly three times as high. This implies a large difference in the density and radial extent of the intracluster medium (ICM) between the two clusters. As a result, ICM-related physical processes are naively expected to be more important in the evolution of currently infalling MS 0451 galaxies than in Cl 0024.

In addition, as we will discuss in more detail in Chapter 6, there are marked differences in the levels of substructure between the two clusters, including evidence that Cl 0024 has recently experienced a merger with a smaller subcluster along the line of sight (Czoske et al. 2002). These differences in overall assembly state may be important in the evolution of the galaxy populations.

In the schematic diagram shown in Figure 1.2, we apply simple scaling relations to estimate the regimes of influence for several key physical processes which could be acting on infalling galaxies. Following the procedure described in T03 for Cl 0024, we construct a simple mass model for each cluster, assuming $\rho \propto r^{-2}$ with total mass derived from X-ray measurements (Table 1.1), and allow a galaxy to freely fall from the outskirts on a radial orbit. Under this model, we estimate the radius at which ram pressure becomes strong enough to strip a Milky Way-like spiral, the radius at which tidal truncation of a galaxy is important, and the radii at which harassment and

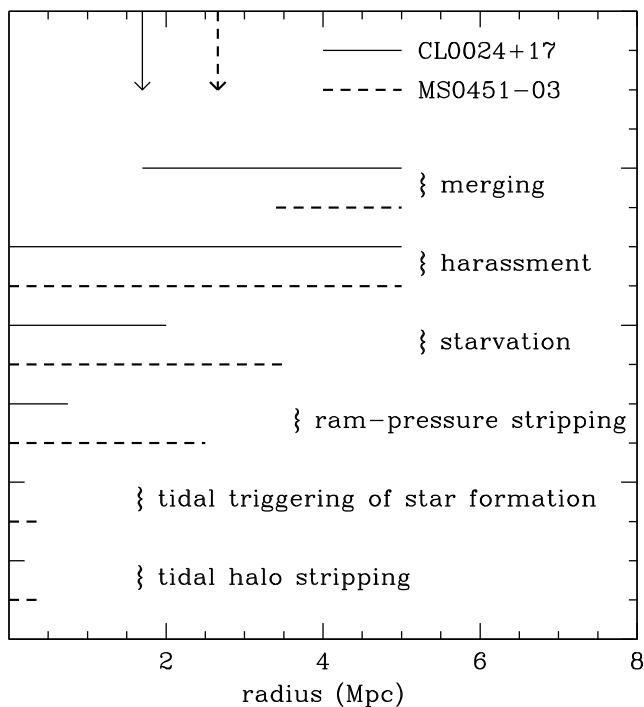


Figure 1.2 Schematic diagram indicating the cluster-centric radius over which each of several listed physical mechanisms may be effective at fully halting star formation or transforming the visual morphology of a radially infalling galaxy. Each physical mechanism listed can act effectively over the radial range indicated by the solid (Cl 0024) or dashed line (MS 0451). Each regime of influence was calculated according to the simple models described in T03 for Cl 0024, using the global cluster properties given in Table 1.1. The virial radius of each cluster is marked with an arrow at the top.

galaxy mergers are possible (see T03). Variation in the physical conditions and orbital characteristics of galaxies will, of course, matter a great deal, but this simplistic case yields conservative estimates of the maximal radial range over which each process could operate within each cluster.

From Figure 1.2, we see that ICM-related processes, such as gas starvation (Larson et al. 1980; Bekki et al. 2002) and ram-pressure stripping (Gunn & Gott 1972) begin to affect galaxies at much larger radius in MS 0451. An important caveat, however, is that the role of difficult-to-observe shocks in the ICM are unknown, and are not accounted for in Figure 1.2 (but see Chapters 3 and 6). Similarly, the two clusters' differing masses set the radial regions where galaxy merging will be effective; because of the $\sim 50\%$ higher mass of MS 0451, typical galaxy relative velocities become too

fast for mergers to occur at a higher radius than in Cl 0024.

The differing regimes of influence for the physical mechanisms illustrated in Figure 1.2 provide the key template for our attempt to disentangle the relative importance of the various processes. By surveying the galaxies of both clusters for signs of recent transformation or disturbance, across the entire radial range to ~ 5 Mpc, we hope to associate the sites and characteristics of galaxies in transition with the likely causes from Figure 1.2.

An important limitation of Figure 1.2, however, is that it does not take into account the variations in overall assembly state and level of substructure between each cluster. The effects of tidal processes and galaxy–galaxy harassment, for example, should occur in much the same regions across both clusters, according to Figure 1.2, yet in reality they may very well differ greatly between clusters depending on how well each is virialized. Therefore, Figure 1.2 can only be used as a guide, and we must carefully consider throughout this thesis the effects that large-scale cluster assembly and irregularities may have on galaxies as well.

1.3 Plan of the Thesis

In this section, we outline our plan for leveraging our wide-field surveys of Cl 0024 and MS 0451 into a better understanding of the physics behind galaxy transformations in clusters. Before delving into analysis of the various galaxy populations in each cluster, we first introduce, in Chapter 2, the characteristics of the data set and sample selection, as well as key reduction and analysis techniques that are common to the investigations presented in later chapters. We discuss the optical *HST* mosaics along with the complementary ground- and space-based imaging from the X-ray to mid-IR. We also describe our extensive ground-based optical spectroscopy, primarily obtained with DEIMOS on Keck II. Observations in all bands cover an area extending from the cluster core to the turn-around radius in the cluster outskirts, >5 Mpc physical radius. Together, Cl 0024 and MS 0451 have been observed in more depth and in more wavelength ranges than perhaps any other systems at intermediate redshift.

1.3.1 Overall Strategy

The core of this thesis, contained in Chapters 3 through 6, has been divided into parts following a strategy to make maximal use of our *HST*-based morphologies: we split our sample of cluster galaxies according to morphological type, characterizing signs of recent evolution in spirals and early types separately. This approach is similar to using the color–magnitude relation to divide our sample into “red sequence” and “blue cloud” galaxies (as a proxy for star-formation rate, e.g., Cooper et al. 2007), but it provides additional leverage to identify galaxies undergoing evolution. Early-type galaxies that have either been newly transformed or prodded back into an active phase, or spiral galaxies where star formation is being suppressed or enhanced, will all stand out in our sample. At the same time, their morphologies reveal important information about their formation histories prior to their current transition state, information that colors alone do not provide. Our strategy also has the benefit of allowing us to directly investigate the hypothesis that many cluster spirals transform into S0s between $z \sim 0.5$ and today (Poggianti et al. 2001) (see Chapter 6).

A detailed understanding of how the cluster environment affects infalling galaxies requires the use of a control sample, composed of galaxies that are either unperturbed by the environment or else represent an end state of evolution. Attempting to directly compare cluster galaxies at $z \sim 0.5$ to their presumed descendants in nearby clusters presents a challenge due to redshift-dependent biases and selection effects. The difficulties arise both from the different rest wavelengths we are probing (e.g., morphological identification through redshifted bandpasses, the substitution of [O II] for $H\alpha$ as a star-formation indicator), as well as the uncertainty involved in associating local galaxies with their likely progenitors ~ 5 Gyrs in the past (so-called progenitor bias, van Dokkum & Franx 2001), compounded by the vastly differing spatial resolutions of local vs. $z \sim 0.5$ observations. Such difficulties largely limit us to qualitative comparisons to local galaxy samples.

As an alternative, throughout this work we quantitatively measure the effects of environment at $z \sim 0.5$ through a comparison to galaxies in the *field* at this same

redshift. As our field sample is assembled from foreground or background galaxies identified in the course of our observations of Cl 0024 and MS 0451, they have been observed in an identical fashion, thus minimizing any biases. By comparing cluster galaxies to their counterparts in the field, we can pinpoint the locations and strengths of cluster-related processes by identifying peculiarities in star formation or galaxy dynamics that occur only in the cluster population and not in the field. Then, armed with a better understanding of the physics that drives galaxy transformations at this particular redshift, we can make informed predictions for the processes affecting galaxies at other redshifts, even though the precise conditions within clusters vary and evolve with time.

1.3.2 Using E+S0s as Sensitive Indicators of Interaction

In Chapter 3, we consider spectral diagnostics of galaxy evolution restricted to E+S0 members of Cl 0024. In the local universe, cluster early-type galaxies are an extremely homogeneous population in terms of their stellar populations and structural properties (e.g., Dressler et al. 1987; Djorgovski & Davis 1987; Bower et al. 1992; Bender, Burstein, & Faber 1992). By studying these galaxies at intermediate redshift and contrasting their spectral properties with those of their counterparts in the field and local universe, we are sensitive to even very subtle signatures of recent and current environmental interactions. In this sense, we explore early-type galaxies as “test particles” of recent activity. This study has yielded two key results:

By constructing the Fundamental Plane (FP) of Cl 0024, we observe that elliptical and S0 galaxies exhibit a high scatter in their FP residuals, equivalent to a spread of 40% in mass to light ratio (M/L_V). The high scatter occurs only among galaxies in the cluster core, suggesting a turbulent assembly history for cluster early types, perhaps related to the recent cluster–subcluster merger (Czoske et al. 2002).

Around the virial radius of Cl 0024, we observe a number of compact, intermediate-mass ellipticals undergoing a burst of star formation or weak AGN activity, indicated by strong [O II] emission. Due to their locations within a narrow range in radius, we

raise the possibility that the observed activity is caused by a rapidly acting physical process: two candidates are galaxy harassment and shocks in the ICM, though we return to these objects in Chapter 6 to consider the possibility that mergers are responsible.

1.3.3 Kinematic Disturbances in Spiral Disks

While E+S0 galaxies do prove to be sensitive indicators of environmental interaction, it is the spiral galaxies that of course host the bulk of star formation within and around these clusters. In Chapter 4, we probe for kinematic disturbances in spiral disks by measuring resolved rotation curves from optical emission lines, and constructing the Tully-Fisher relation (Tully & Fisher 1977) for spirals across Cl 0024 and MS 0451.

We find that the cluster Tully-Fisher relation exhibits significantly higher scatter than the field relation, in both V and K_S bands. In probing for the origin of this difference, we find that the central mass densities of star-forming spirals exhibit a sharp break near the cluster virial radius, with spirals in the cluster outskirts exhibiting significantly lower densities. We argue that the lower-density spirals in the cluster outskirts, combined with the high scatter in both K_S - and V -band TF relations, demonstrate that cluster spirals are kinematically disturbed by their environment, even as far from the cluster center as twice the virial radius. We propose that such disturbances may be due to a combination of galaxy merging and harassment.

1.3.4 When Stellar Population and Morphology Tell Conflicting Stories

Analysis of just the early types or just the spiral populations of these two clusters provide valuable clues to the environmental processes that may be acting. However, the most powerful method of tracking galaxy evolution across Cl 0024 and MS 0451 involves the identification and study of “transition galaxies”—galaxies whose stellar populations or dynamical states indicate a recent or ongoing change in morphology or star-formation rate. Such galaxies are often revealed by star-formation histories that

seem to be at odds with the galaxy morphologies: for example, spiral galaxies with no signs of star formation, or elliptical galaxies that *do* show signs of star formation.

In Chapter 5, we identify and study one such class of objects, the “passive spirals” in Cl 0024. These objects exhibit no emission lines in their spectra, suggesting a lack of star formation, yet are surprisingly detected in the UV, revealing the presence of young stars. By modeling the different temporal sensitivities of UV and spectroscopic data to recent activity, we show that star formation in Cl 0024 passive spirals has decayed on timescales of less than 1 Gyr, consistent with the action of “gas starvation” (Bekki et al. 2002). Intriguingly, the fraction of spirals currently observed in the passive phase is consistent with the longer period expected for the morphological transformation and the subsequent buildup of cluster S0s observed since $z \simeq 0.4$.

In Chapter 6, we build on and link together our previous indications of galaxy evolution at work, aiming to piece together a more comprehensive picture of how cluster galaxies are affected by their environment at intermediate redshift. To accomplish this, we document what we believe to be the first direct evidence for the transformation of spirals into S0s: through an analysis of their stellar populations and recent star-formation rates, we link the passive spiral galaxies in both clusters to their eventual end states as newly generated cluster S0 galaxies.

Differences between the two clusters in both the timescales and spatial location of this conversion process allow us to evaluate the relative importance of several proposed physical mechanisms that could be responsible for the transformation. Combined with other diagnostics that are sensitive to either ICM-driven galaxy evolution or galaxy–galaxy interactions—including the residuals from the Fundamental Plane and the properties of “signpost” compact emission line galaxies—we describe a self-consistent picture of galaxy evolution in clusters. We find that spiral galaxies within infalling groups have already begun a slow process of conversion into S0s primarily via gentle galaxy–galaxy interactions that act to quench star formation. The fates of spirals upon reaching the core of the cluster depend heavily on the cluster ICM, with rapid conversion of all remaining spirals into S0s via ram-pressure stripping in clusters where the ICM is dense. In the presence of a less-dense ICM, the conversion continues at

a slower pace, with galaxy–galaxy interactions continuing to play a role along with “starvation” by the ICM.

Using our successful model for the sites and strengths of the various important physical processes, in Chapter 7 we assess future opportunities for testing our conclusions in several different manners at a variety of redshifts. We also discuss how our simple picture of evolution in clusters fits in with the popular picture that is emerging on the role of AGN- or star-formation fueled feedback as a mechanism for halting star formation and building up the red sequence of galaxies.

Chapter 2

A Wide-Field Survey of Two Intermediate Redshift Galaxy Clusters: Characteristics of the Survey

We describe our comprehensive wide-field survey of two intermediate redshift galaxy clusters, Cl 0024+17 ($z = 0.395$) and MS 0451-03 ($z = 0.540$), which forms the basis of the investigations presented in later chapters. For both clusters, optical *HST* mosaics are complemented by ground- and space-based imaging from the X-ray to mid-IR, as well as extensive ground-based optical spectroscopy, primarily obtained with DEIMOS on Keck II. Observations in all bands cover an area extending from the cluster core to the turn-around radius in the cluster outskirts, >5 Mpc physical radius. Together, Cl 0024 and MS 0451 have been observed in more depth and in more wavelength ranges than perhaps any other systems at intermediate redshift. We describe here the characteristics of the data set and sample selection, as well as key reduction and analysis techniques that are common to the investigations presented in later chapters. We also present our full spectroscopic catalogs, which we make available to the community.

2.1 Imaging

The key *HST* imaging of Cl 0024 and MS 0451 have been introduced and described in T03 and G. P. Smith et al. (2007, in preparation), respectively. Details of the image reduction are presented in those works, but we present here the key characteristics

of each data set. In Cl 0024, *HST* coverage consists of a sparsely sampled mosaic of 39 WFPC2 images taken in the F814W filter ($\sim I$ band), providing coverage to a projected radius of >5 Mpc at exposure times of 4–4.4 ks. MS 0451 observations were taken with the ACS, also in F814W, and provide contiguous coverage within a 10 Mpc \times 10 Mpc box centered on the cluster, with single orbit (2 ks) depth over the field. Both sets of observations are complete to $F814W > 25.0$. Astrometry for each frame of each mosaic has been calibrated to match that of the wide-field ground-based images detailed below. In Figures 2.1 and 2.2, we display each entire *HST* mosaic with the locations of confirmed cluster members marked with blue circles.

Cl 0024 and MS 0451 were respectively observed for 15 ks and 80 ks with *The Galaxy Evolution Explorer (GALEX)* (Martin et al. 2005) in 2004 October (GO-22; Cycle 1; PI Treu), in both near (NUV) and far ultraviolet (FUV) filters (Martin et al. 2005; Morrissey et al. 2005). As *GALEX*'s field of view is $\sim 1.2^\circ$, the images readily cover the full *HST* mosaics. The two exposures reach comparable depths in rest frame FUV, which is a close match to observed NUV at the redshifts of the clusters. Images were reduced and sky-subtracted using the standard automated *GALEX* reduction pipeline.

We also use panoramic ground-based K_s -band imaging of both clusters, and J -band imaging of Cl 0024, with the WIRC camera (Wilson et al. 2003) on the Hale 200" Telescope. These data comprise a 3×3 mosaic of pointings, spanning a contiguous area of $26' \times 26'$ centered on each cluster. Observations were made in 2004 November for MS 0451 and 2002 October for Cl 0024. The details of the observations and data reduction are described by Smith et al. (2005a) and Kneib et al. (2003) for Cl 0024, and for MS 0451 data were reduced the same way: we used standard IRAF tasks to dark subtract, linearize, flat field using a local sky median, integer pixel align, and coadd the individual frames to remove defects and cosmic rays. The total integration time per pointing was 1.1 ks for Cl 0024 and 2.4–2.7 ks in MS 0451. Point sources in the final reduced mosaics have a full width half maximum (FWHM) of $0.9''$ and $1.0''$ in Cl 0024 and MS 0451 respectively, and the 3σ point source detection thresholds are $J = 21.6$ and $K_s = 19.7$ for Cl 0024 and $K_s = 20.2$ for MS 0451. The full mosaics

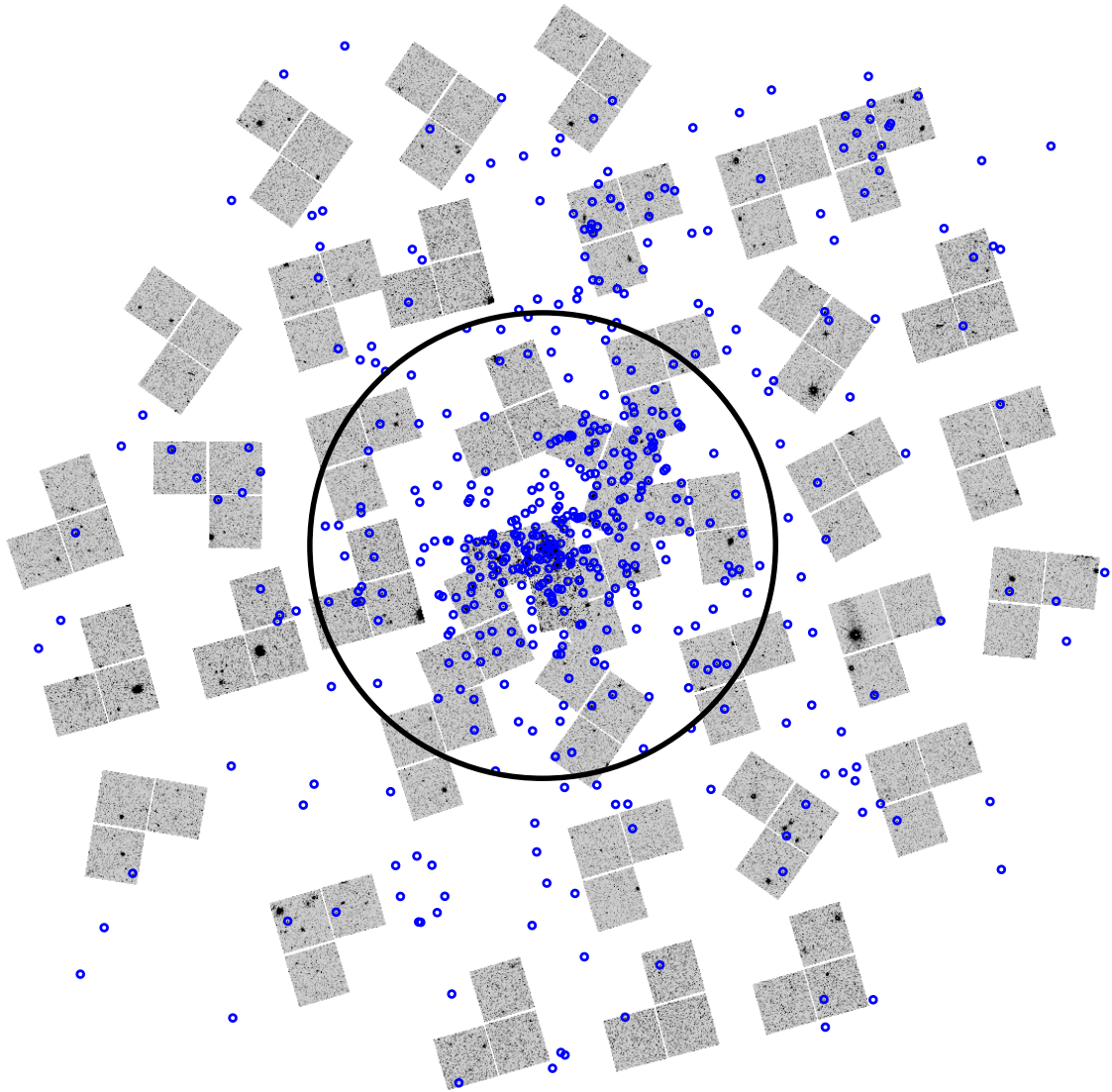


Figure 2.1 Mosaic of 39 WFPC2 images of Cl 0024, arranged as they are distributed on the sky. The locations of all spectroscopically confirmed cluster members are marked as blue circles. The large black circle indicates the virial radius of the cluster, 1.7 Mpc, corresponding to $5.4'$ on the sky. Cluster members located outside of the *HST* coverage are covered by ground-based imaging, but do not have morphological typing available.

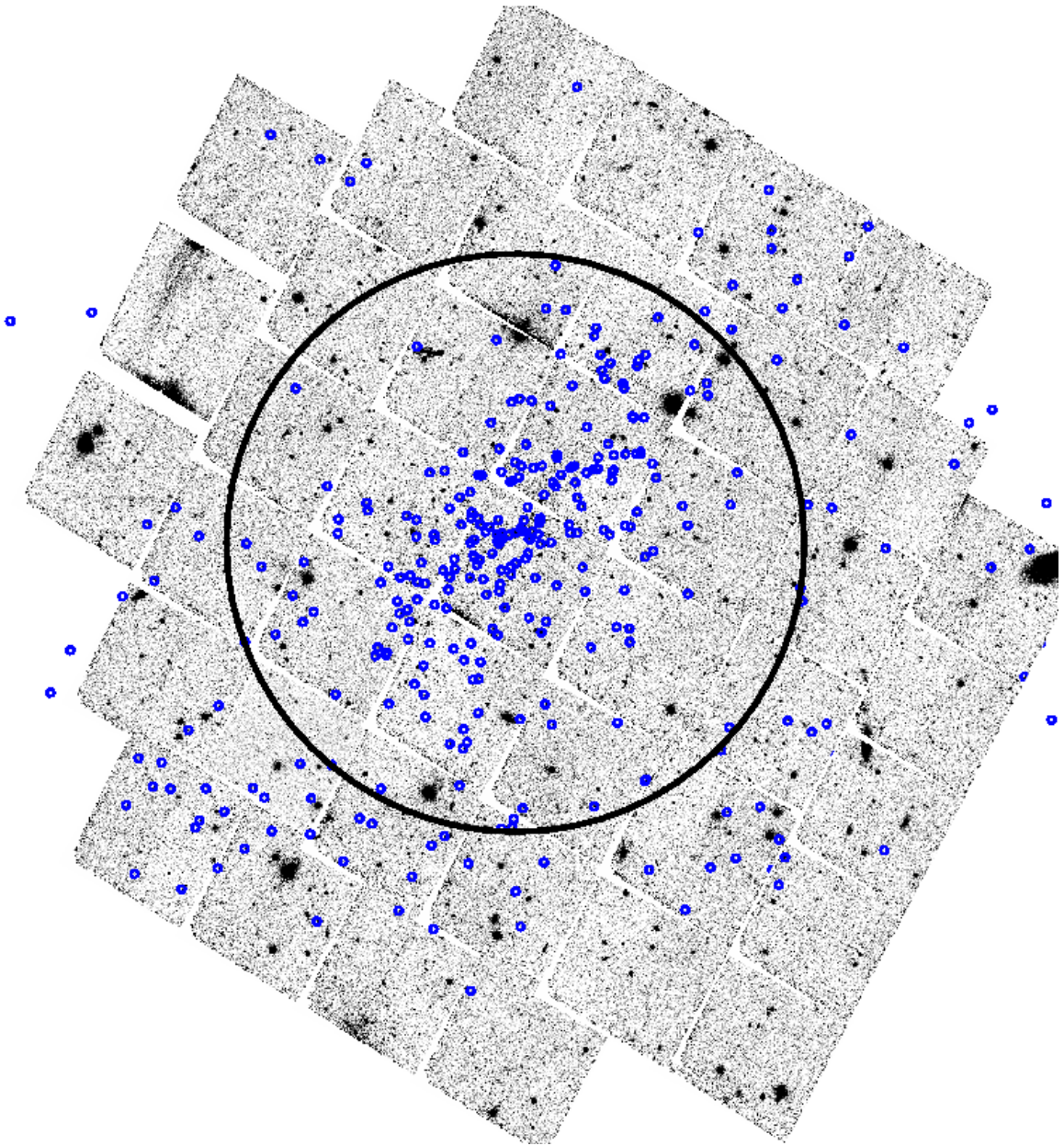


Figure 2.2 Mosaic of 41 ACS images of MS0451, arranged contiguously on the sky. The locations of all spectroscopically confirmed cluster members are marked as blue circles. The large black circle indicates the virial radius of the cluster, 2.66 Mpc, corresponding to $7.0'$ on the sky. Cluster members located outside of the *HST* coverage are covered by ground-based imaging, but do not have morphological typing available.

for Cl 0024 and MS 0451 are displayed in Figures 2.3 and 2.4, respectively.

The *HST* and near-infrared data are supplemented with wide-field ground-based optical imaging. We make use of *BVRI*-band imaging of Cl 0024 with the 3.6 m Canada-France-Hawaii Telescope (CFHT) using the CFH12k camera (Cuillandre et al. 2000), full details of which are available in Czoske et al. (2002) and T03. MS 0451 was observed by Kodama et al. (2005) for the PISCES survey through the *BVRI*-band filters using Suprime-Cam on the Subaru 8 m Telescope. Full details of these data are published by Kodama et al. (2005). The CFH12k data reach 3σ depths of $B = 27.8$, $V = 26.9$, $R = 26.6$ and $I = 25.9$ in $\sim 0.9''$ seeing, and the Suprime-Cam data reach 3σ depths of $B = 28.1$, $V = 27.0$, $R = 27.3$, $I = 25.8$ in seeing ranging from $0.6''$ to $1''$. All near-IR, UV, and *HST* imaging has astrometry matched to these ground-based optical image sets. The fields of view of all imaging sets are well matched to the ground-based data.

X-ray observations of Cl 0024 with *XMM/Newton* (Zhang et al. 2005) and *Chandra* (Ota et al. 2004), and MS 0451 with *Chandra* (Donahue et al. 2003) reveal markedly different X-ray luminosities and temperatures for these two clusters, as discussed in Chapter 1. The clusters' X-ray properties shed light on the physical processes that may be working to transform galaxies, and will be discussed further in Chapter 6. However, we do not directly make use of the X-ray images themselves in this work.

2.1.1 Source Extraction and Photometry

Photometry was measured using SExtractor version 2.2.2 (Bertin & Arnouts 1996). For ground-based imaging, we use SExtractor in two-image mode with source detection performed on the ground-based *I*-band images. Source detection on the *HST* images was performed independently, and then matched to the ground-based catalog. For all imaging, we adopt magnitudes from the MAG_AUTO measurement of SExtractor.

For *GALEX* data, galaxy fluxes were measured within $6''$ circular apertures, centered on the optical position of each galaxy of interest. The aperture size is chosen

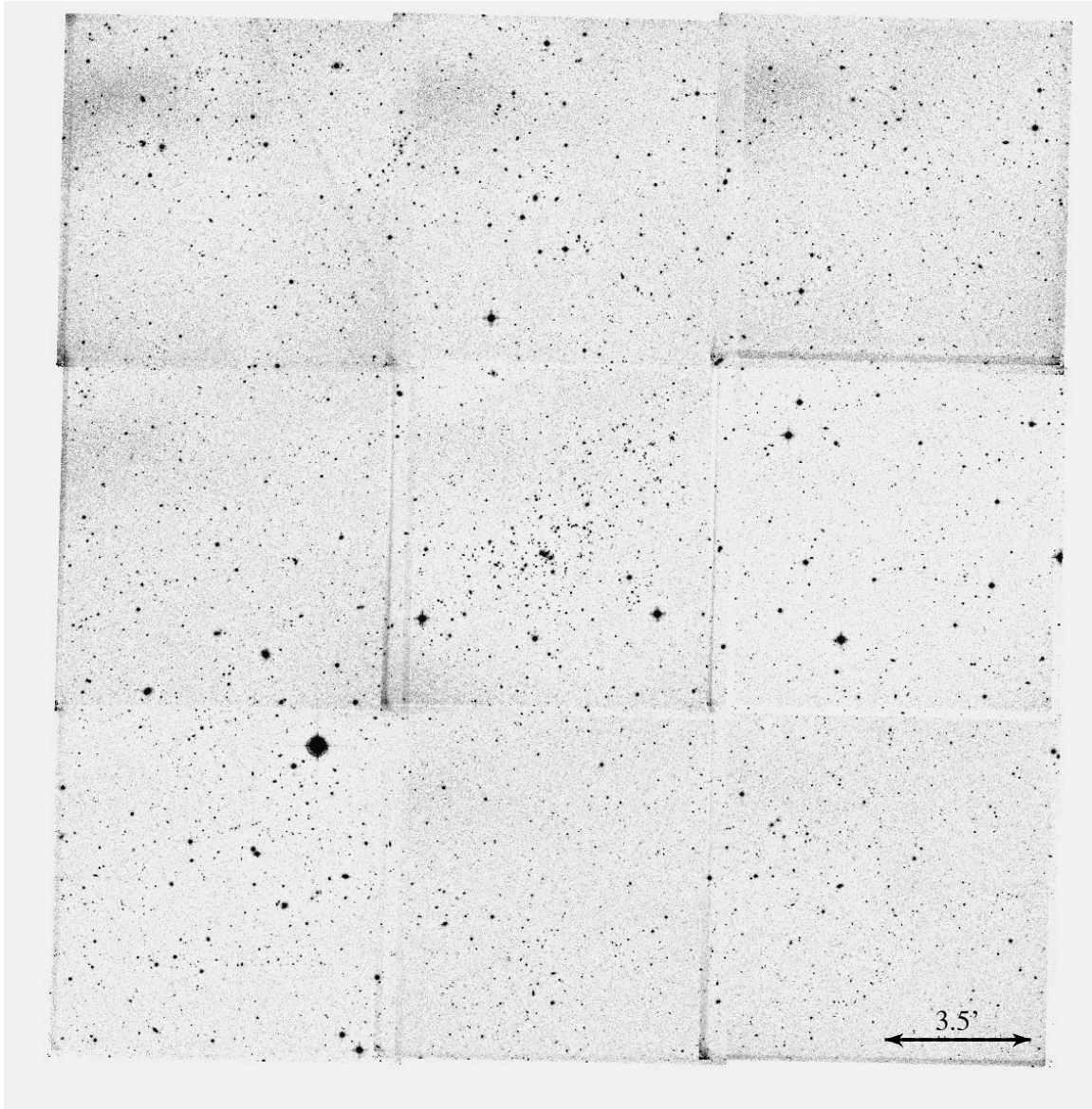


Figure 2.3 Cl 0024 K_S -band mosaic obtained with WIRC on the Palomar 200" telescope. The cluster core is visible as the overdensity of objects in the central pointing.

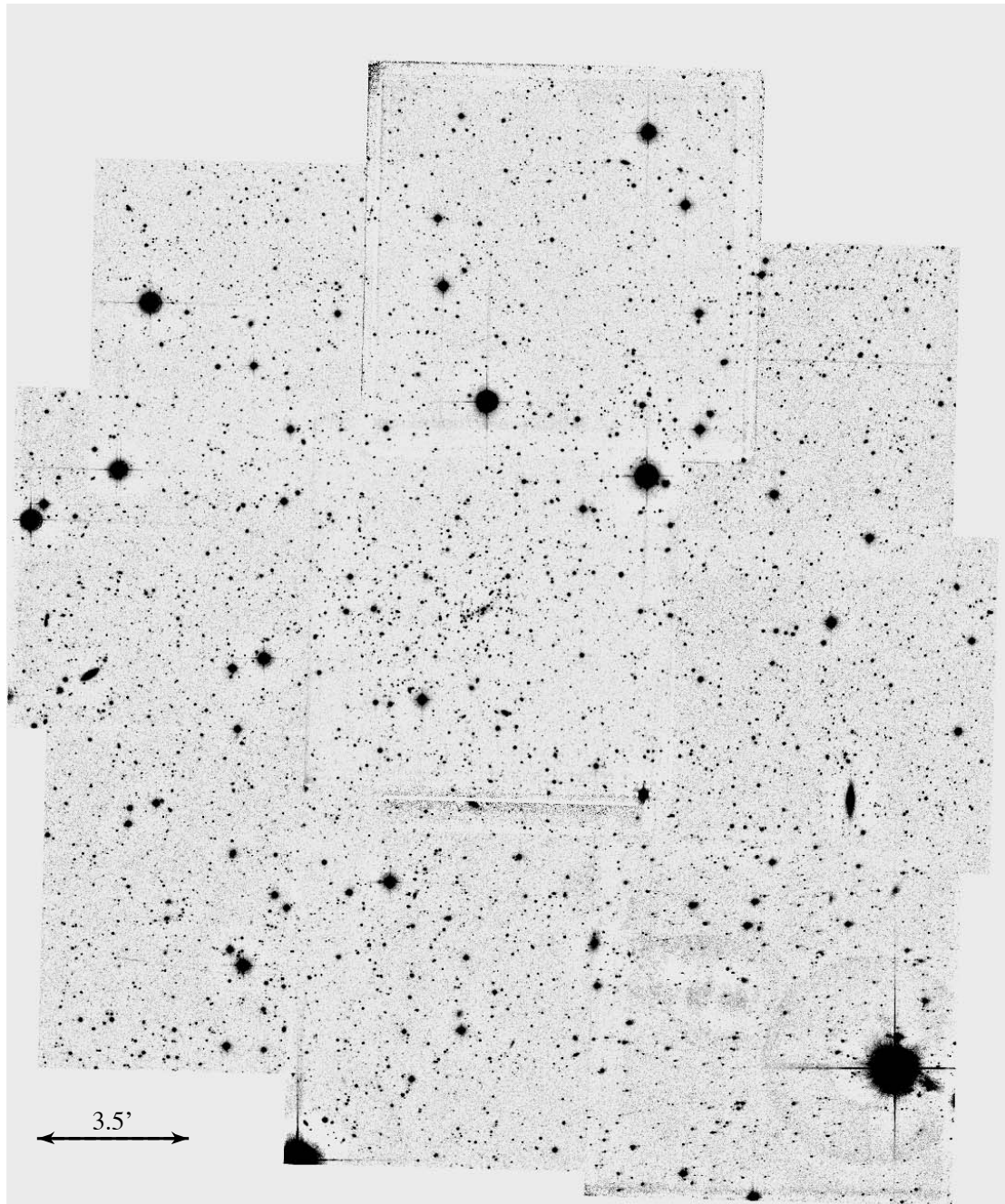


Figure 2.4 MS 0451 K_S -band mosaic obtained with WIRC on the Palomar 200" telescope. More sources are visible in this mosaic compared to Cl 0024 due to the increased depth, as more than twice the observing time was required to reach similar rest-frame luminosity limits in the more distant MS 0451.

to be comparable to the measured NUV FWHM (5.5"). We apply an aperture correction to bring the fluxes into agreement with SExtractor-derived total magnitudes (MAG_AUTO), and for comparison to MAG_AUTO magnitudes in F814W (Bertin & Arnouts 1996).

For most of our analysis, we convert observed magnitudes into rest-frame absolute magnitudes using k -corrections. We use the `kcorrect` software v.4.1.2 (Blanton et al. 2003) to estimate the necessary k -corrections; we make use of imaging in all available bands from NUV to K_s , modeling each galaxy's spectral energy distribution and deriving the best-fit correction on a galaxy by galaxy basis. However, we find that the derived k -correction is mostly insensitive to the omission of one or several bands. As the observed and rest-frame bands match well, the required k -corrections are typically small, and the rms scatter in k -corrections for all spiral or all early-type galaxies is typically only ~ 0.1 magnitudes. We assume a Galactic extinction of $E(B-V)=0.056$ for Cl 0024 and 0.033 for MS 0451 (Schlegel et al. 1998), and all absolute magnitudes in this work will be expressed on the AB system. Observed optical magnitudes are quoted on the Vega system, but *GALEX* photometry is AB.

2.1.2 Morphological Classification

For both clusters, reliable morphological classification is possible to rest frame absolute V -band magnitude $M_V = -19.6$, corresponding to $I = 22.1$ in MS 0451 and $I = 21.1$ in Cl 0024. Broader classification as early or late type is possible to a fainter limit, $M_V = -18.0$. All galaxies that have spectroscopically confirmed redshifts and are brighter than this limit are classified visually following the procedure described in T03 for Cl 0024. In MS 0451, galaxies were classed by R. S. E., and we expect that the typing is accurate to the quoted limits based on previous experience with ACS imaging of similar depth (e.g., Treu et al. 2005b). Morphologies were assigned according to the Medium Deep Survey scheme introduced by Abraham et al. (1996b): T=-2=star, -1=compact, 0=E, 1=E/S0, 2=S0, 3=Sa+b, 4=S, 5=Sc+d, 6=Irr, 7=Unclass, 8=Merger, 9=Fault. In the following, all galaxies assigned types

T=0, 1, 2 are together labeled as “early types” or E+S0s, and all galaxies with T=3, 4, 5 are labeled as spirals. An M_V^* galaxy corresponds to $I \sim 19.5$ in Cl 0024 (Smail et al. 1997), where M_V^* indicates the absolute magnitude equivalent to the characteristic luminosity, L_* , of the cluster luminosity function. Our sample with fine morphological distinction reaches to $M_V^* + 1.6$, and our deeper sample with only broad classification extends to $M_V^* + 3.0$.

In Figure 2.5, we display a montage of example MS 0451 cluster members from our ACS imaging. The chosen galaxies span all morphological types considered in this thesis, at each of three luminosities, roughly corresponding to L_* galaxies ($M_V = -21.2$), galaxies near the limit for fine morphological typing ($M_V = -19.6$), and fainter galaxies where only distinction between early and late types is reliable ($M_V = -18.2$). Similar examples of morphological typing are available for Cl 0024 in T03.

Crucial to our strategy of studying galaxy evolution by analyzing early- and late-type galaxies separately is understanding our accuracy at distinguishing elliptical from S0 galaxies on the one hand, and spirals from S0s on the other. Either type of misclassification could bias our results, especially in comparison to samples at higher or lower redshift, due to the effects of band shifting and surface brightness dimming on our ability to class galaxies (Smail et al. 1997; Fabricant et al. 2000).

In the following chapters, we take several steps to mitigate any confusion between classes. These include using the *GALFIT* software (Peng et al. 2002) to subtract smooth, fitted galaxy profiles from each galaxy image. We inspect these residuals for signs of low-contrast spiral arms, in the case of galaxies classed S0, or else unnoticed disk components in the case of galaxies classed E. More details on these procedures are detailed in Chapters 3 and 6, but we note that few signs of misclassified galaxies have been found. We also avoid uncertainties due to misclassification by comparing our cluster samples, where possible, to similar field samples constructed from the same data set, but in the background of each cluster field.

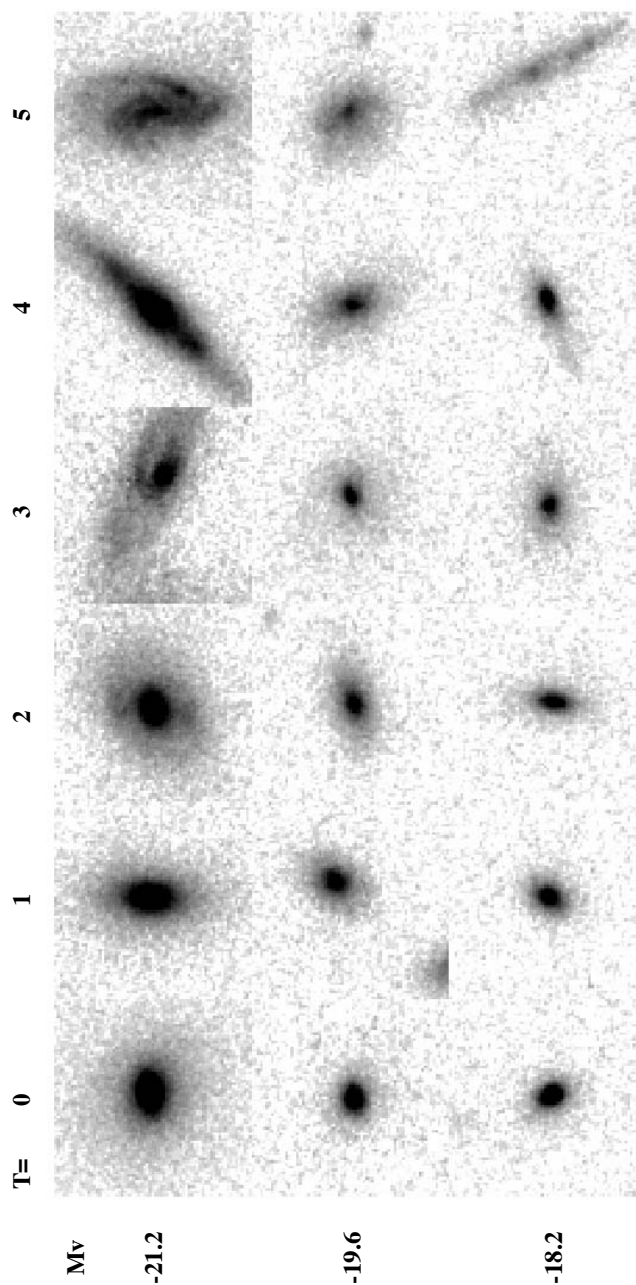


Figure 2.5 Montage of MS 0451 cluster members from ACS imaging. Galaxies span all morphological types from $T = 0$ (elliptical) to $T = 5$ (Sc/d), at each of three luminosities, as indicated on the figure. Luminosities roughly correspond to L_* galaxies ($M_V = -21.2$), galaxies near the limit for fine morphological typing ($M_V = -19.6$), and galaxies where only distinction between early and late types is reliable ($M_V = -18.2$). We note that, in some cases, limitations in the dynamic range of the figure obscure morphological characteristics that are important in assigning types.

2.2 Spectroscopy

We have used the DEIMOS spectrograph on Keck II to obtain deep spectra of ~ 1500 galaxies/cluster in the fields of Cl 0024 and MS 0451. In both clusters, we observe with $1''$ wide slits with lengths much larger than the galaxy size (typically $8'' - 12''$). For each cluster, spectral setups were chosen to span rest-frame wavelengths from $\sim 3500 \text{ \AA}$ to $\sim 6700 \text{ \AA}$, covering optical emission lines [O II], [O III], $H\beta$, and, more rarely, $H\alpha$.

Designed to both identify cluster members and acquire high signal to noise spectra of galaxies in Cl 0024, we began our spectroscopic campaign in 2001 October with LRIS on Keck I. While some observations were completed that year (see T03), the bulk of our spectroscopic campaign has been completed in four observing seasons from 2002 October through 2005 December, all using the DEIMOS spectrograph on Keck II (Faber et al. 2003).

Cl 0024 targets were selected from the CFHT I -band mosaic, with priority given to known cluster members with *HST* morphologies, followed by galaxies in the *HST* survey without a known redshift, to $I < 22.5$. Galaxies without *HST* images filled the remainder of each slit mask, with priority given to known members. All targeted galaxies were brighter than $I = 22.5$. Masks were designed so as to provide good coverage across the Cl 0024 field, while also maximizing the number of known-member spiral galaxies that could be observed with tilted slits (for extracting rotation curves from extended line emission; see Chapter 4).

We observed Cl 0024 with a total of 12 DEIMOS slit masks in 2002 and 2003, covering the entire field of the *HST* mosaic. We employed the 900 line/mm grating, with a central wavelength of 6200 \AA . This setup provides spectral coverage from 4500 to 8000 \AA , with a pixel scale of approximately $0.12'' \times 0.44 \text{ \AA}$, and yielding a spectral resolution of $\sigma \sim 50 \text{ km s}^{-1}$. For most masks, the exposure time was 2.5 hr ($5 \times 1800\text{s}$), though four masks were only observed for 2 hr ($4 \times 1800\text{s}$). In December 2004, we observed a single additional mask for 3 hr, 10 m, ($5 \times 1200 \text{ s}$ plus $3 \times 1800 \text{ s}$) with the 600 line/mm grating, providing resolution of $\sim 70 \text{ km s}^{-1}$. The central

wavelength was again 6200Å, providing similar spectral coverage. In 2002, conditions were fairly poor, with thin clouds frequently interrupting observations. Seeing was approximately 0.7". In 2003, seeing was good (0.5"–0.6"), though conditions were not photometric. And in 2004, conditions were generally good, with seeing varying between 0.7" and 1.1" across three nights.

We undertook an initial redshift survey of MS 0451 during 2003 October, observing 14 slit masks for one hour each, with the 600 l/mm grating set to central wavelength 7500Å. This allowed redshift identification for 1300 objects, including 250 cluster members. Targets were selected from the *I*-band Subaru image discussed above, as the ACS mosaic was not yet available. We first selected objects randomly from the set with $I < 21.5$, and then filled in slit mask gaps with fainter objects ($I < 23.0$).

In 2004, most targeted objects in MS 0451 were selected for deeper follow-up after already being identified as cluster members in our previous year's redshift survey. However we excluded bright cluster members that had already yielded spectra of sufficient signal to noise in the 1hr integrations of 2003. We observed 3 masks for 4 hr each, with gaps between high-priority targets filled as before with random objects to $I < 23.0$. Observations used a 600 l mm⁻¹ grating set to a central wavelength of 6800Å.

In 2005 October, objects in both clusters were observed with the same spectral setup and integration times as in 2004, with six masks observed per cluster. However, in 2005 our goal was to follow up on sources detected in both *GALEX* imaging and *Spitzer* MIPS imaging (Geach et al. 2006), and so we filled masks with these sources preferentially. Targets in these latest observations were not constrained to the same magnitude limits as previous observations, so some fainter objects were observed, to $I < 24.0$ in MS 0451 and $I < 23.0$ in Cl 0024.

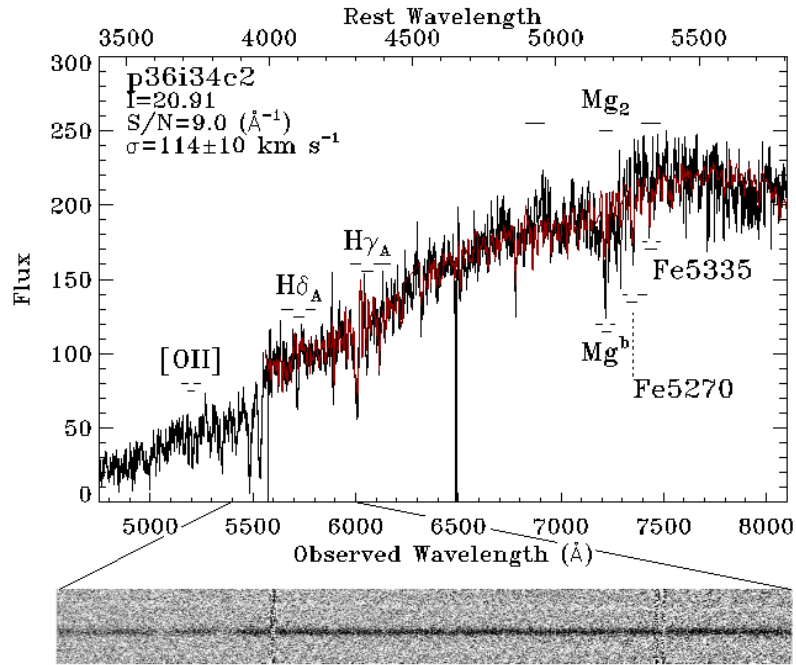


Figure 2.6 A typical spectrum for a galaxy with luminosity near the median of our sample. The entire 1D spectrum is plotted at top, with a segment of the 2D spectrum displayed below it. We have measured equivalent widths for the spectral lines indicated (see Chapter 3). Overplotted in red is the best-fit template spectrum used in measuring the stellar velocity dispersion, discussed further in Chapter 3.

2.2.1 Data Reduction and Redshift Determination

Spectra were reduced using the DEEP2 DEIMOS data pipeline¹ (Davis et al. 2003). The pipeline performs bias removal, flat fielding, and cosmic-ray rejection. It then separates slitlets and performs wavelength calibration and sky subtraction. For wavelength calibration, the pipeline uses an optical model of the DEIMOS mask to generate an initial wavelength solution. Arc-lamp frames, consisting of 1 s exposures with Ne, Ar, Kr, and Xe lamps, are then used to refine the calibration.

From the reduced two-dimensional (2D) spectra, the pipeline extracts one-dimensional (1D) spectra using either a variance-weighted boxcar function, or a variant of the optimal extraction method described by Horne (1986). We perform our analysis on spectra extracted via the boxcar method, though the difference using the optimal

¹Software available at <http://astron.berkeley.edu/~cooper/deep/spec2d>

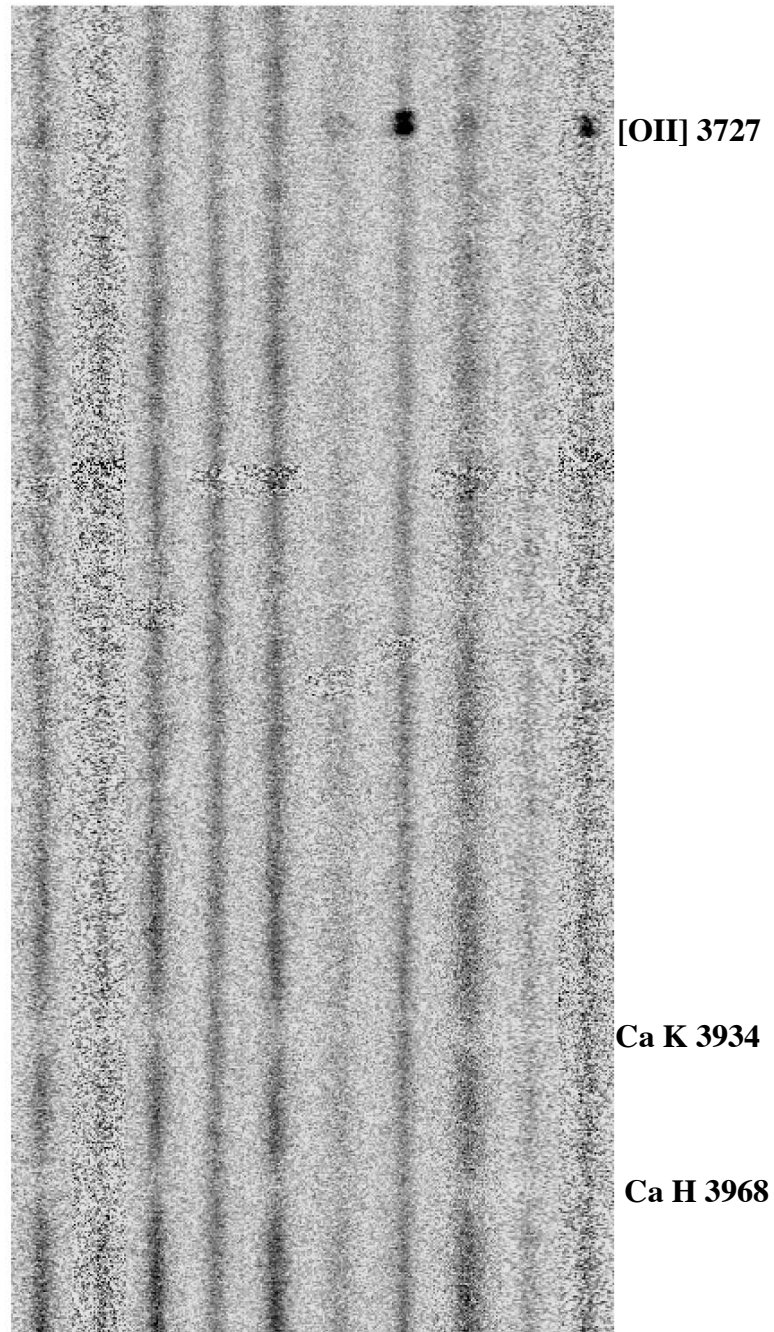


Figure 2.7 Montage of reduced 2D spectra from DEIMOS, for ten MS 0451 cluster members. Galaxy spectra are aligned side by side, shifted to a common rest-frame spectral axis running vertically from $\sim 3700\text{\AA}$ to $\sim 4000\text{\AA}$. Readily apparent spectral features are marked to the side. The full spectral range of each DEIMOS observation is over ten times longer than the portion shown here.

extraction is minimal. We further correct each spectrum for the instrumental response function before measuring line strengths, but we do not perform flux calibration. Figure 2.6 presents a 1D reduced spectrum of a Cl 0024 member galaxy that is near the median luminosity targeted, along with a portion of the reduced 2D spectrum for the same object. Figure 2.7 displays a selection of reduced 2D spectra of MS 0451 cluster members, spanning a range of magnitudes to $M_V < -19.6$.

For LRIS data, individual slitlets were separated and reduced in a standard manner (see, e.g., Treu et al. 1999, 2001b).

For each reduced spectrum, redshifts were determined by examining the spectra to identify key absorption and emission lines. We obtained initial redshift guesses via automated fitting of template stellar spectra to each object spectrum. Each spectrum was then judged by eye to determine the correct redshift.

Following Czoske et al. (2002), we define a Cl 0024 cluster member to be a galaxy that lies in either of the two prominent redshift peaks in the cluster distribution, as illustrated in Figure 2.8. This encompasses a redshift range from $z = 0.374$ to $z = 0.402$. In MS 0451, we define cluster membership to include all galaxies in the range $0.52 < z < 0.56$; as can be seen in Figure 2.8, the galaxy counts fall to a minimum at approximately these two limits. In total, we have obtained spectra of over 300 member galaxies per cluster, to $M_V = -18.0$ ($I = 22.7$ in Cl 0024 and $I = 23.6$ in MS 0451), boosting the total known cluster members to 504 in Cl 0024 and 319 in MS 0451. We have also obtained spectra for over 2500 field objects, with 700 having redshifts similar to the clusters ($0.3 < z < 0.65$), suitable for use as a comparison sample to the cluster members (see Chapter 4).

As in T03, we combine our new spectroscopy with data from previous surveys (Czoske et al. 2001; Dressler et al. 1999) to compile a comprehensive redshift catalog for objects in the fields of Cl 0024 and MS 0451. In Tables 2.1 and 2.2, we present a sample of our full redshift catalogs for Cl 0024 and MS 0451, respectively. The two catalogs contain redshifts for 1632 (Cl 0024) and 1562 (MS 0451) objects. The full catalogs are made available in electronic form on our web site,² including positions

²<http://www.astro.caltech.edu/~smm/clusters/>

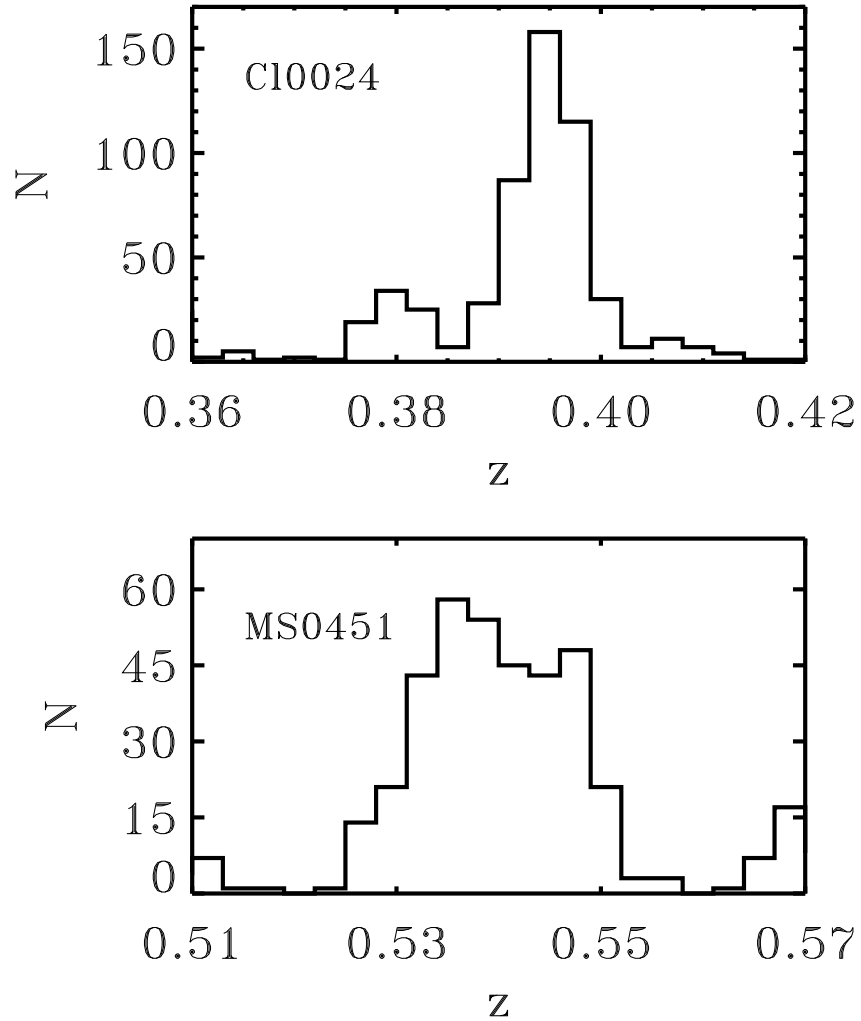


Figure 2.8 Distribution of redshifts for both Cl 0024 (top) and MS0451 (bottom), including all galaxies with spectroscopically confirmed redshifts from our observations as well as previously published redshifts. In Cl 0024, we identify 508 cluster members, defined to lie in the range $0.373 < z < 0.402$. In MS 0451, we count 319 cluster members in the range $0.52 < z < 0.56$.

Table 2.1. Cl 0024+17 redshift catalog

α ($^{\circ}$)	δ ($^{\circ}$)	z_{best}	Quality ^a	Source ^b	$\langle z \rangle$	δz	N_z
6.845741	17.133789	0.3940	0	2	0.3940	0.0000	1
6.837580	16.997200	0.3966	1	1	0.3964	0.0004	2
6.827622	17.378466	0.3792	0	2	0.3792	0.0000	1
6.821529	17.200779	0.3758	0	2	0.3758	0.0000	1
6.812725	17.213043	0.3813	0	2	0.3813	0.0000	1
6.801040	17.199699	0.3955	1	5	0.3955	0.0001	2
6.765210	17.191099	0.3955	1	5	0.3956	0.0002	3
6.759056	17.073933	0.3790	0	2	0.3790	0.0000	1
6.744001	17.070641	0.3940	0	2	0.3940	0.0000	1
6.737525	17.066620	0.1870	2	3	0.1870	0.0000	1
...							

^aQuality codes: 0 = Quality unspecified by source, 1 = Secure, 2 = Probable, 3 = Uncertain

^bSource codes: 1 = Czoske et al. (2001), 2 = Frazier Owen (private communication), 3 = Hale/COSMIC, 4 = Keck/LRIS, 5 = Keck/DEIMOS

Note. — The complete version of this table is available at <http://www.astro.caltech.edu/~smm/clusters/> or via Moran et al. (2005). Explanation of columns: z_{best} , Quality, and Source refer to the most reliable redshift for each object. If a redshift is available from more than one source, then $\langle z \rangle$ gives the mean redshift from all sources, δz is the rms difference between them, and N_z is the number of redshifts included in the mean.

Table 2.2. MS 0451–03 redshift catalog

α ($^{\circ}$)	δ ($^{\circ}$)	z	Source ^a
73.321434	−3.022260	0.6670	1
73.328568	−3.033381	0.3704	1
73.325325	−3.024078	0.3000	1
73.334717	−3.043395	0.1281	1
73.331795	−3.002323	0.5391	1
73.344551	−3.028507	0.7254	1
73.346550	−3.024269	0.3707	1
73.339874	−3.009066	1.1598	1
73.337769	−3.004604	0.3882	1
73.343781	−3.007794	0.9951	1
...			

^aSource codes: 1 = Keck/DEIMOS, 2 = Ellingson et al. (1998)

Note. — The complete version of this table is available at <http://www.astro.caltech.edu/~smm/clusters/>

matched with photometric measurements, *HST* morphologies, and redshifts.

2.2.2 Completeness

We define the redshift completeness of each catalog, as a function of magnitude or cluster radius, as the number of objects with identified redshifts divided by the total number of objects in the imaging catalog (see T03). As the Cl 0024 *HST* mosaic does not provide full coverage across the field of that cluster, we can define two completeness measures: redshift completeness for galaxies that fall within the *HST* coverage (and hence have morphologies available), and completeness across the entire field delineated by the ground-based coverage.

In Figure 2.9, we plot both completeness measures for Cl 0024, as well as com-

pleteness for MS 0451, as a function of absolute magnitude at the cluster redshift, M_V . The corresponding observed F814W magnitudes are given in the axis at the top and bottom of the plot. Overall completeness in both clusters is $\sim 25\%$ to a limiting magnitude $M_V = -19.6$, roughly 1.5 magnitudes below M_* , and the approximate point where completeness begins to fall rapidly. Brighter than this limit, our samples are representative of the clusters as a whole: if we divide the completeness histogram into early- and late-type galaxies, the two subsamples do not differ substantially. However, in the range $-19.6 < M_V < -18.0$, we are biased toward detection of emission line cluster galaxies over absorption line galaxies, and completeness is lower in MS 0451 than Cl 0024. In the following chapters, we will focus our analysis on cluster members with $M_V < -19.6$, except where specified otherwise.

Within the *HST* coverage of Cl 0024, completeness is much higher to this same $M_V = -19.6$ limit, $\sim 75\%$. Likewise, if we confine ourselves to within 3 Mpc radius of each cluster center, completeness also jumps, to 40% and 60% for MS 0451 and Cl 0024, respectively. Both of these figures indicate that we have identified a substantial fraction of the total population of bright cluster galaxies within the virialized regions of these clusters. Hence, our analysis in later chapters should yield a reliable and representative picture of the spectral properties and dynamical states of cluster galaxies.

In this thesis, our goals are to combine our *HST* imaging, used for morphological classification and photometry, with high signal/noise Keck spectroscopy to probe star-formation rates, star-formation histories, and galaxy kinematics through the various methods described in later chapters. Supplementary imaging in various bands is used to characterize galaxy spectral energy distributions for k -correction of photometry, and to provide further valuable constraints on the recent star-formation histories of cluster galaxies. Together, *HST* imaging and Keck spectroscopy will prove to be a powerful combination for uncovering galaxy evolution at work.

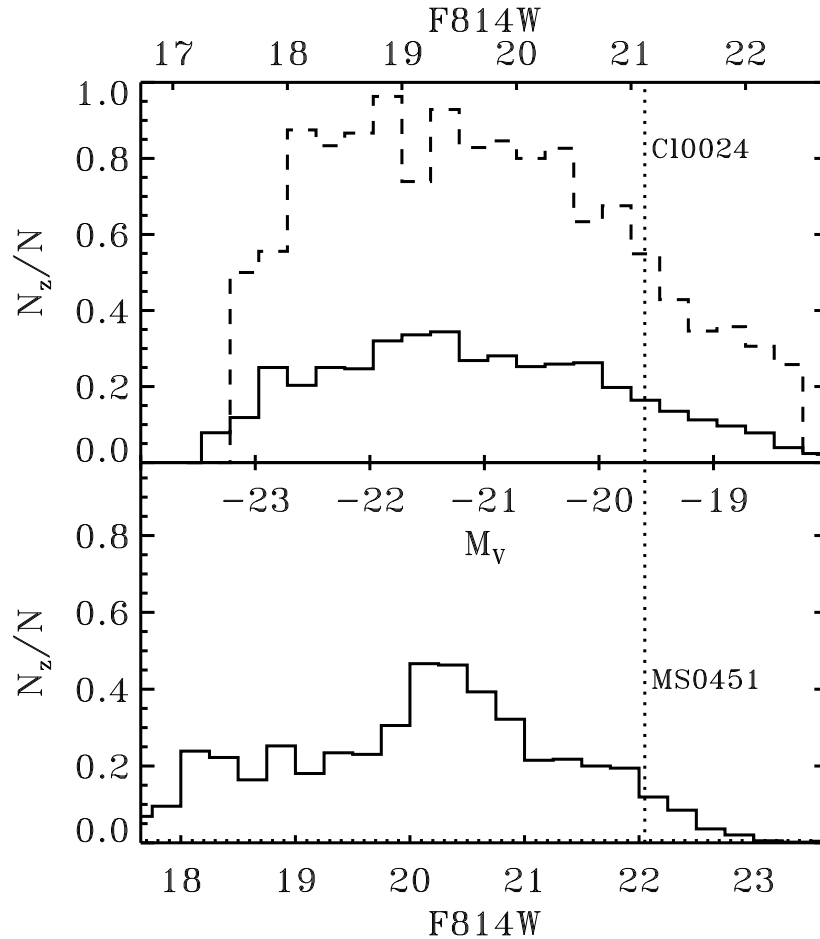


Figure 2.9 Redshift completeness of the Cl 0024 and MS 0451 spectroscopic samples, as a function of absolute magnitude M_V (middle axis), with the corresponding observed F814W for each cluster indicated on the top and bottom axes. Completeness is defined as the number of objects with a spectroscopically confirmed redshift in a magnitude bin (N_z), divided by the total number of objects at that magnitude (N). In the top panel, the dashed line indicates the completeness for just those areas covered by the sparsely sampled *HST* mosaic of Cl 0024, while the solid line indicates completeness for the full area covered by the ground-based imaging. In MS 0451, the *HST* mosaic has full spatial coverage, so the overall completeness is shown. Dotted vertical line indicates $M_V = -19.6$; below this limit, completeness falls off, and we are biased towards emission line galaxies. In Cl 0024, the brightest cluster galaxy (BCG) has magnitude $M_V = -23.5$, and in MS 0451 the BCG is at $M_V = -23.8$.

Chapter 3

Signatures of Environmental Interaction in Cl 0024 Early-Type Galaxies¹

In this work, we analyze the properties of early-type (E+S0) members of Cl 0024 as a function of environment, using them as sensitive tracers of the various physical processes that may be responsible for galaxy evolution. By constructing the Fundamental Plane of Cl 0024, we infer an evolution in the mean mass to light ratio of early types with respect to $z = 0$ of $\Delta \langle \log(M/L_V) \rangle = -0.14 \pm 0.02$. In the cluster center, we detect a significantly increased scatter in the relationship compared to that seen in local clusters. Moreover, we observe a clear radial trend in the mass to light ratios of individual early types, with the oldest galaxies located in the cluster core. Galaxies are apparently younger at larger radius, with E+S0s in the periphery having M/L_V ratios that nearly match values seen in the field at a similar redshift. The strong radial trend is seen even when the sample is restricted to a narrow range in galaxy mass. Independent spectral indicators used in combination reveal an abrupt interaction with the cluster environment which occurs near the virial radius of Cl 0024, revealed by small bursts of star formation in a population of dim early types, as well as by enhanced Balmer absorption for a set of larger E+S0s closer to the cluster core. We construct a simple infall model used to compare the timescales and strengths of the observed interactions in this cluster. We examine the possibility that bursts of star formation are triggered when galaxies suffer shocks as they encounter the intracluster medium, or by the onset of galaxy harassment.

¹Much of this chapter has been previously published as Moran et al. (2005).

3.1 Introduction

Environmental processes have clearly played a significant role in shaping the morphological evolution of galaxies. Butcher & Oemler (1978) first noted the increased fraction of actively star-forming galaxies in cluster cores at redshifts of $z \simeq 0.4$, and subsequent studies clarified direct evolution in the relationship between morphological fractions and local density (Dressler et al. 1997). Recent work has extended these measures to galaxy samples in lower density environments and at higher redshifts (Treu et al. 2003; Smith et al. 2005a; Postman et al. 2005), delineating a picture where the fraction of early-type (hereafter elliptical and S0, E+S0) galaxies to some rest-frame luminosity limit grows with time, and at a rate that seems to depend sensitively on the local density.

What processes govern this apparent transformation of star-forming disk and irregular galaxies into the abundant elliptical and S0 population seen in present-day clusters? As discussed in Chapter 1, galaxy clusters provide excellent laboratories to study these environmental effects, particularly at intermediate redshifts (where the relevant processes were perhaps most active) and over the full range of cluster radii, from the well-mixed cluster core to the outermost regions where field galaxies are falling into the cluster for the first time.

Much of course has been learned from detailed spectroscopy of galaxies in intermediate redshift clusters (e.g., Dressler & Gunn 1983; Couch & Sharples 1987; Poggianti et al. 1999, and references therein). However, previous studies of this type have either focused on the cluster core, where morphologies are available or relied on spectral types or colors to trace the effects of environment out to the cluster periphery (Abraham et al. 1996b; Kodama et al. 2001). With a larger sample of morphologies and high-quality spectra over the full range of local densities in Cl 0024, we aim to provide a more complete picture of the environmental processes involved and their range of application.

Spectroscopy of cluster members at various stages of infall can provide a key to the dominant environmental processes. As discussed in Chapter 1, different physical

mechanisms will produce recognizable spectral and dynamical signatures in the affected galaxies. While several independent processes can operate simultaneously in the central 0.5–1 Mpc, these can be separated by contrasting differences over a wider dynamic range in radius and local density.

In this chapter, we consider spectral diagnostics of galaxy evolution in Cl 0024 cluster members classified as early type (E+S0) in our morphological catalog (Chapter 2; T03). In the local universe, cluster early-type galaxies are an extremely homogeneous population in terms of their stellar populations and structural properties (e.g., Dressler et al. 1987; Djorgovski & Davis 1987; Bower et al. 1992; Bender, Burstein, & Faber 1992). Nevertheless, the evolution of the morphology density relation indicates that a substantial fraction was accreted or transformed at intermediate redshift. Indeed, several of the proposed environmental mechanisms are thought to have transformed spirals into S0s (Dressler et al. 1997; Fasano et al. 2000; Smith et al. 2005a; Postman et al. 2005).

By studying these galaxies at intermediate redshifts and contrasting their spectral properties with those of their counterparts in the field and local universe, we expect to be sensitive to signatures of past and current environmental activity. In this sense, we will explore early-type galaxies as “test particles” of recent activity. Building on the conclusions herein, later chapters will address the properties of spiral galaxies in Cl 0024 and MS 0451 and discuss the galaxy population as a whole, taking into account morphological evolution (see, e.g., the discussion of *progenitor bias* in van Dokkum & Franx 2001).

The signal/noise of our early-type spectra was designed to be adequate to measure reliable stellar velocity dispersions for each galaxy, enabling us to construct the Fundamental Plane and, in particular, its possible variation with location. This emerges as a powerful probe of variations in the M/L_V ratios and hence the luminosity-weighted ages of the stellar populations. Precise measures of various line diagnostics permit us to independently probe the star-formation histories over well-understood timescales. In combination, both methods allow us to examine the relative importance of the environment and to constrain the physical mechanisms responsible.

A key issue is the relationship between trends found in Cl 0024 at various radii and those found in the field at approximately the same cosmic epoch. To facilitate such a comparison we make use of the recent comprehensive study of 163 field E+S0s undertaken by Treu et al. (2005a,b) in the northern GOODS field.

A plan of the chapter follows. We briefly recap the key observational data for this work in §3.2. In §3.3 we discuss our measurements of the stellar velocity dispersions, the fits to the surface photometry, the various spectral line indices, as well as an improved estimate of the local environmental densities. In §3.4 we present our results focusing first on the Fundamental Plane and the implications of the scatter and various trends seen as a function of luminosity and location, and correlations between the Balmer absorption and metal line strengths with the velocity dispersion. We also analyze both radial trends and those seen in the residuals from our global cluster and field relations. In §3.5, we develop an integrated picture which combines these independent methods and discuss this in light the results of other studies. For consistency with T03, in this chapter we have adopted the cosmology used in T03 ($H_0 = 65.0 \text{ km s}^{-1}$, $\Omega_m = 0.3$, $\Omega_\Lambda = 0.7$).

3.2 Observations

We base our current investigation on the comprehensive spectroscopic and imaging survey of Cl 0024 described in Chapter 2. In this work, we analyze data for 104 E+S0 galaxies identified as members of Cl 0024, of which 71 have particularly high-quality spectra (generally defined in this work to be those for which reliable stellar velocity dispersions were measured). Twelve of these E+S0s (6 high quality) come from the LRIS observations discussed in Chapter 2 and T03, with the remainder from DEIMOS. Broken down by specific morphological type, our sample includes 34 galaxies classified as E, 50 as S0, and 20 as E/S0. Of the galaxies with high-quality spectra available, 27 are E, 38 S0, and 10 E/S0.

The high-resolution *HST* imaging of Cl 0024 described in Chapter 2 is a crucial complement to the spectroscopic study, both for the purpose of selecting a sample

of E+S0 galaxies, and to allow us to analyze the surface photometry of the selected galaxies. To summarize, the *HST* survey consists of a sparsely-sampled mosaic of 39 WFPC2 images taken in the F814W filter ($\sim I$ band), providing good coverage of the cluster field out to radius of >5 Mpc ($\sim 14'$). T03 reported morphological classifications down to $I = 22.5$. Classifications to a limiting magnitude of $I = 21.1$ ($M_V = -19.5$) were found to be very reliable, in that several authors, working independently, agreed upon the morphology for most objects. This included differentiation between the subtypes E, E/S0, and S0. While ellipticals and S0s were grouped together in T03, it is useful in this work to detect any differences between the populations of Es and S0s: if spirals are actively transforming into S0s at $z \sim 0.4$, we might expect to detect differences in the stellar populations of the two groups.

Although face-on S0s are notoriously hard to distinguish from ellipticals, especially at high redshift where S0 disks may be too dim to detect (Smail et al. 1997; Fabricant et al. 2000), we can partially avoid this difficulty by focusing on the brightest early-type galaxies where all but the faintest disks should be detectable. In this chapter, therefore, we will report distinctions between E, E/S0, and S0 galaxies for a brighter subset of this sample, to $I = 21.1$. We additionally employ a technique to further distinguish between E and S0 by examining the residual signals found after subtraction of an axisymmetric de Vaucouleurs profile (§3.3 and §3.4).

3.3 Analysis

The powerful combination of *HST* imaging and high-quality DEIMOS spectroscopy enables us to combine measures of the kinematic and photometric structure of cluster early types with detailed spectral information that reveals the underlying stellar population. Locally, early-type galaxies show several tight correlations between kinematic, photometric, and spectral properties, such as the Fundamental Plane (FP) (Djorgovski & Davis 1987), the Mg- σ relation (Bender, Burstein, & Faber 1993), and the Balmer- σ relation (Kuntschner 2000; Kelson et al. 2001). Examining these relations at $z \sim 0.4$ not only gives insight into the redshift evolution of cluster early types,

but, by examining the residuals from these relations as a function of cluster environment, we can uncover subtle trends in the mass to light ratios (M/L_V), metallicities, and star-formation histories of these galaxies.

Of course, it is important first to clearly define meaningful measures of the cluster environment of a galaxy. Following T03, we measure radius as the distance from the center of the cluster’s X-ray emission. Our results would be negligibly affected if we instead adopted the center of mass of the system determined by Kneib et al. (2003), as the two positions are separated by less than $5''$ (<30 kpc). In order to more reliably study variations in galaxy properties as a function of local density, we recalculate the local densities presented in T03, now making use of our extensive spectroscopic catalog, supplemented by the photometric redshift catalog of Smith et al. (2005a).

Stellar velocity dispersions serve as a tracer of galaxy mass, and allow us to quantify how stellar populations vary with a galaxy’s size (and, by extension, the formation history of the galaxy.) The redshift evolution of early-type galaxies can be constrained by comparing the tight σ correlations observed locally to what is observed at higher redshift. We can also use velocity dispersions to determine if trends in stellar populations are more tightly correlated with environment or with galaxy mass.

With the addition of surface photometry from the *HST* images, we can derive the parameters of the fundamental plane (FP) in Cl 0024: effective radius R_e , mean surface brightness $\langle\mu_V\rangle$, and central velocity dispersion σ_0 (Djorgovski & Davis 1987; Dressler et al. 1987). The residuals from the FP reveal variations in the mass to light ratios of galaxies; from this, we can trace how the luminosity-weighted ages of early types vary across the cluster environment. We can also measure the evolution of M/L_V with redshift, and examine whether the amount of this evolution depends on galaxy mass and/or cluster environment.

We also wish to directly examine environmental trends in spectral line strengths, as these can reveal trends in current star formation (via [O II], [O III], or $H\beta$ emission), recently completed star formation (via $H\gamma$ and $H\delta$ absorption line strengths), or metallicity (via Mg_2 , Mg^b or the composite index $[MgFe]'$).

Below, we discuss the methods we follow to accurately measure each of the quanti-

ties necessary for our analysis: local density, velocity dispersion, surface photometry, and spectral line indices.

3.3.1 Local Density Measurements

Local density measurements in T03 relied on a statistical field subtraction, following the methods of previous work (e.g., Whitmore et al. 1993; Dressler et al. 1997). While adequate, we can improve on these measurements by making use of our large spectroscopic catalog (§2.2), supplemented by the extensive catalog of photometric redshifts from Smith et al. (2005a). These catalogs allow us to eliminate most foreground and background galaxies, and calculate local densities based only on the positions of confirmed or possible cluster members. A standard method of measuring local density, first introduced by Dressler (1980), involves calculating the area enclosed by the ten nearest neighbors of a galaxy (to $M_V \sim -20$, following Dressler et al. (1997)). In order to obtain local density measurements for our entire sample of 104 galaxies ($I \leq 22.5$), we modify the method to include all fainter galaxies to $I = 22.5$ ($M_V \sim -18$) in the tally of nearest neighbors. Our method is as follows:

Each object with $I < 22.5$ is given a weight between zero and one, according to the procedure outlined below. Then, for each object, we calculate the total area enclosed by a set of neighboring galaxies whose cumulative weight equals about 10. (Fractional weights are common, so the total weight rarely equals exactly 10.) The local density is then calculated by dividing the total weight by the area in Mpc^2 . Compared to the method used in T03, this should give a value of Σ_{10} that is a better reflection of the true density of galaxies in the cluster, minimizing errors due to chance superpositions of background galaxies or groups.

As we wish to include only cluster members in the calculations of local density, we assign weights to galaxies based on how confident we are that it is a cluster member. If a spectroscopic redshift is available from the combined catalog, then the object's weight equals one if it is a cluster member ($0.374 < z < 0.402$), and zero otherwise.

For objects with no spectroscopic redshift, we check for a photometric redshift in

the catalog of Smith et al. (2005a). While the cluster is clearly evident in the redshift distribution of galaxies in the Smith et al. (2005a) catalog, the limited accuracy of photometric redshifts means that the cluster galaxies are smeared across the redshift range $z_{phot} = 0.39 \pm 0.09$. We give all galaxies within this range a weight of 1, even though some non-cluster members will be mistakenly included. From an analysis of galaxies with both spectroscopic and photometric redshifts available, we find that approximately 85% of cluster members have photometric redshifts in the adopted range, and about one-third of all galaxies with photometric redshifts in this range will actually lie outside of the cluster. This will lead us to slightly overestimate the total number of cluster members, and, by extension, local densities. But the effect is minimal given the large fraction of spectroscopic redshifts. We also explored a more elaborate weighting scheme based on the joint probability that a given galaxy will be a member according to its photometric redshift and projected radius. The rms variation in Σ_{10} between the this and our simple scheme is about 12%—less than other sources of uncertainty and therefore not worthy of adopting.

The photometric redshift catalog is J -limited at $J \leq 21.5$, so there are some objects with $I < 22.5$ that have neither a spectroscopic nor photometric redshift available. For these, we assign weights according to the radial dependence of the probability that a random galaxy will be a cluster member. For example, based on the combined spectroscopic redshift catalog, the probability is 81% that an unknown galaxy within 0.75 Mpc of the cluster core is a cluster member; such a galaxy is assigned a weight of 0.81. We calculate and assign similar probabilities for galaxies in several different radial bins out to 5 Mpc. Since we only consider galaxies within the magnitude range $17.75 \leq I < 22.5$, the probabilities we have adopted do not vary strongly with magnitude, and so we do not further subdivide our probability estimates into different bins for different ranges of galaxy magnitude.

In order to properly compare densities calculated with our method to those used in T03, we also calculate Σ_{10} using objects brighter than $I = 21.1$. A tight correlation is seen between the two estimates which agree to within 20%; we also reproduce the overdensities at ~ 1 Mpc and ~ 3 Mpc given in T03. Similarly, we can compare the

density of background objects predicted by our method to the field number counts of, e.g., Abraham et al. (1996a) and Postman et al. (1998). We calculate background count densities of $\log(N)/deg^2 = 4.45 \pm 0.05$ (to $I = 22.5$) and 3.90 ± 0.07 (to $I = 21.1$). Our predicted counts agree with both Abraham et al. (1996a) and Postman et al. (1998), within the uncertainties, for both magnitude limits. As an additional check on the uncertainty in Σ_{10} measured to our deeper limit ($I = 22.5$), we calculated a density (Σ_5) for a total weight of 5. The rms variation between Σ_5 and Σ_{10} is about 25%. Conservatively, we adopt this as the uncertainty in Σ_{10} . Σ_{10} for each object, along with other basic properties, are listed in Table 3.2.

3.3.2 Stellar Velocity Dispersions

We are able to measure velocity dispersions only for our brighter sample of early-type members ($I < 21.1$), as our spectra of fainter galaxies do not have sufficiently high signal to noise. In order to determine velocity dispersions, we fit to a grid of stellar templates degraded to the instrumental resolution and smoothed to various velocity dispersions (van der Marel 1994). A high-quality spectrum for an object near our magnitude limit is displayed in Chapter 2 as Figure 2.6, with the best-fitting template spectrum overplotted.

To determine the signal/noise limit at which our velocity dispersion measures become unreliable, we performed a series of Montecarlo simulations. We construct fake galaxy spectra from stellar templates smoothed to the resolution and pixel scale of DEIMOS (for the 900 line/mm grating), truncated to an identical length of $\sim 2600 \text{ \AA}$, convolved with a Gaussian of various widths to simulate different velocity dispersions, and degraded to a variety of signal to noise ratios. We then attempt to recover the velocity dispersion of the fake galaxy by running the same code as above.

We find that the approximate mean S/N where systematic errors in σ reach $\sim 10\%$ corresponds to $S/N = 7 - 8$ (\AA^{-1} , observer's frame). Below this level, velocity dispersion measures rapidly become inaccurate. In our high-quality sample, we include galaxies with S/N near this limit, though most have $S/N > 10$. However, we place

a somewhat stricter limit ($S/N > 8$) on the spectra observed with LRIS and the DEIMOS 600 lines/mm grating which have slightly worse spectral resolution. Only 10 high-quality spectra have $S/N < 10$, so our results are fairly insensitive to these choices. Table 3.3 lists all galaxies with high-quality spectra, along with their velocity dispersions, formal errors, and the mean signal/noise of the spectrum.

The typical uncertainty in our velocity dispersion measurements is $\pm 10\%$. These errors are dominated by differences in σ that depend on the template spectrum used, though systematic errors rise to become equally important as we approach the signal to noise limit. Of the early types where we measured velocity dispersions, there were three galaxies in common with an earlier study of Cl 0024 by van Dokkum & Franx (1996); the velocity dispersions quoted in van Dokkum & Franx (1996) match ours in all three cases, with $\langle \delta\sigma/\sigma \rangle = -0.02 \pm 0.13$. Treu et al. (2005b) derived stellar velocity dispersions from DEIMOS spectra using a similar method to our own. They pursued several tests to determine the accuracy of their dispersions, and found an rms uncertainty of $\sim 12\%$, in agreement with our own uncertainty estimates. For more discussion of such accuracy tests, see Treu et al. (2005b).

For each galaxy, we apply a correction to match the central velocity dispersion measured through a $3''.4$ aperture at the distance of Coma, following the prescription of Jørgensen, Franx, & Kjørgaard (1995a). This choice of aperture size for the correction is somewhat arbitrary, but is a common choice for studies of early-type galaxies at low to intermediate redshift (e.g., Kelson et al. 2000b; Wuyts et al. 2004) because it facilitates comparison to local measurements of the Fundamental Plane (e.g., Jørgensen, Franx, & Kjørgaard 1996). The magnitude of this correction depends on the physical scale over which the 1D spectrum was extracted, which varies from object to object. The average correction applied is $6.6\% \pm 0.4\%$. Corrected velocity dispersions are denoted by σ_0 , and are listed in Table 3.3.

3.3.3 Surface Photometry

GALFIT (Peng et al. 2002) was used to derive effective radii and surface bright-

nesses for all galaxies with measured velocity dispersions. For each galaxy, we extract postage stamps approximately 200 pixels on a side ($\sim 10''$). We then use *GALFIT* to fit against a model de Vaucouleurs ($r^{1/4}$) profile. Following other authors, e.g., Jørgensen, Franx, & Kjærgaard (1995b), we fit all E+S0s to the same profile shape, even though some may be better described by a lower Sérsic index, or a de Vaucouleurs plus exponential function. (See Peng et al. (2002) for a definition of the Sérsic function, a more general form of the de Vaucouleurs function.)

GALFIT minimizes the χ^2 residuals between the galaxy image and a 2D galaxy model that it constructs. The free parameters in this model profile include R_e , total magnitude, axis ratio, galaxy position angle, the position of the galaxy center, and the sky level. Sky levels were set according to the header of each WFPC2 image, but were allowed to vary within a small range to ensure that *GALFIT* converges to the correct fit.

Model galaxies are convolved with a PSF before fitting; we use a star observed on the same WFPC2 chip, with approximately the same exposure time. We tested with a number of different stars, and found that the specific choice of PSF star did not significantly affect the derived photometric parameters.

When fitting a galaxy to a de Vaucouleurs profile, the best-fit parameters are particularly sensitive to extra flux far from the galaxy’s center (Peng et al. 2002), since the function declines relatively slowly beyond R_e . Neighboring or overlapping galaxies thus contribute light that must be either masked or removed by fitting multiple galaxy profiles. To best remove this extra light, we simultaneously fit a Sérsic profile to each bright neighbor within the postage-stamp image. The Sérsic function is the best choice for such a fit because its form is general enough to successfully model a wide range of galaxy types; according to Peng et al. (2002) this ensures that the galaxy’s flux is subtracted uniformly.

The magnitude of the best-fit model galaxy returned by *GALFIT* is measured in the observed F814W filter. At $z \sim 0.4$, this is a close match to rest-frame V, but we must still apply a small *k-color correction* to derive the mean surface brightness in rest frame V. $\langle \mu_V \rangle$ is defined as:

$$\begin{aligned}
\langle \mu_V \rangle &= I_{814W} + 2.5 \log(2\pi R_e^2) + \Delta m_{VI} - A_I - 10 \log(1+z) \\
&= I_{814W} + 5 \log(R_e) + 1.29 \pm 0.04
\end{aligned}$$

where $A_I = 1.95E(B - V)$ (Schlegel et al. 1998) corrects for galactic extinction, the redshift term accounts for cosmological dimming, and Δm_{VI} is the *k-color correction*. In the second line of the above equation, we insert our adopted values: $\Delta m_{VI} = 0.85 \pm 0.03$, adopted from calculations by Treu et al. (2001a), $A_I = 0.11 \pm 0.01$ from Schlegel et al. (1998), and $z \sim 0.395$. Note that this value of Δm_{VI} is in agreement with our own *k*-correction estimates from the multi-band photometry described in Chapter 2.

Since we only measure surface photometry for our brighter sample of galaxies ($I < 21.1$), formal statistical errors in the measured parameters are very small: less than $0''.05$ in R_e , and 0.05 in magnitude. We estimate that systematic errors are double these values, and adopt $0''.1$ and 0.1 mag as typical errors in R_e and magnitude, respectively. There may be additional uncertainty in R_e and μ_V related to the choice of a de Vaucouleurs profile over other structural forms, but previous work (Fritz et al. 2005; Kelson et al. 2000a; Saglia et al. 1993) has shown that the combination of R_e and μ_V that enters into the Fundamental Plane (see §3.4) is largely insensitive to the galaxy profile adopted. Figure 3.1 shows three example fits, for galaxies classified as E, E/S0, and S0. For each galaxy, we display the original galaxy image, the best-fit model image, and the residuals. As might be expected, the residuals are smaller for the fit to the elliptical galaxy; the residuals for the S0 galaxy clearly show a disk component that is not well fit by a de Vaucouleurs profile.

We observed two clear edge-on S0s which had to be removed from our sample of high-quality spectra, due to the uncertainty in trying to fit a de Vaucouleurs profile to such an edge-on disk. We also removed two galaxies with bad fits, defined as where the SExtractor magnitude from the *HST* image and *GALFIT* model magnitude differ

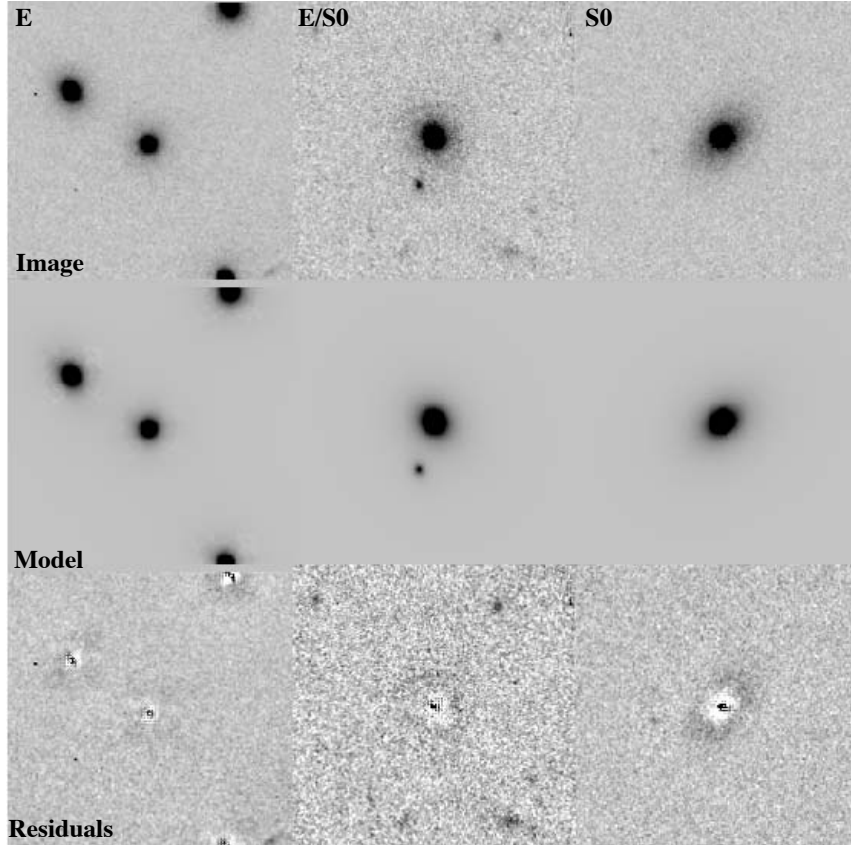


Figure 3.1 Example surface photometry fits, for galaxies classified as E, E/S0, and S0. Top row is the galaxy image. Middle row shows the GALFIT model image. Bottom row shows the residuals of the image fit to model.

by more than 0.75—the two magnitudes for most galaxies in our sample match to much better than 0.75 magnitudes. None of these four galaxies are included in the previously defined sample of 71 high-quality early types, though they are included in the larger sample of 104 galaxies. The photometric parameters for the high-quality galaxies are listed in Table 3.3.

As a check on our measurements, we compared our R_e and $\langle\mu_V\rangle$ for three galaxies that also were studied in the work by van Dokkum & Franx (1996). (This is not the same set of three we used to compare velocity dispersions in §3.3.2: for one galaxy where each group has measured surface photometry, we have not measured σ . And for one galaxy where we have both measured σ , we do not have an *HST* image for surface photometry.) In each case, our surface photometry matches theirs, within the

adopted errors on our measurements. We exclude one additional galaxy that we have in common with van Dokkum & Franx (1996), as it exhibits a disturbed morphology (the triple nucleus galaxy discussed in their paper).

3.3.4 Line-Strength Measures

We measure the strengths of several diagnostic spectral lines for the entire sample of early-type galaxies (to $I < 22.5$). In order to best probe the stellar population of each galaxy, we select a set of indices that are sensitive to a range of star-formation histories and metallicities. Emission lines, such as [O II], [O III], and sometimes $H\beta$ indicate ongoing star formation (or possibly nuclear activity). Balmer absorption lines, such as $H\gamma$ and $H\delta$ are sensitive to recently completed star formation; these lines are strongest in A-stars, which contribute prominently to a galaxy’s integrated starlight within the first Gyr after a burst of star formation. We also measure several metallicity indicators, such as Mg_2 , Mg^b , Fe5270, Fe5335, and the composite index $[MgFe]'$, which is defined as:

$$[MgFe]' \equiv \sqrt{Mg^b (0.72 * Fe5270 + 0.28 * Fe5335)}$$

In the local universe, $[MgFe]'$ seems to be insensitive to variations in α -element abundance (Thomas et al. 2003), making it a valuable tracer of total metallicity.

Where possible, we adopt the Lick index definitions to measure the strength of each spectral line (Worthey et al. 1994). In the Lick system, the equivalent width of a line is measured by defining a wavelength range to either side of a main index bandpass. The mean level of each sideband is determined, and a straight line is fit, defining the “pseudocontinuum” across the index bandpass. The equivalent width of the line within the index bandpass is then measured with respect to the pseudocontinuum level. The Lick system does not include an index for [O II], so we adopt the one defined by Fisher et al. (1998). In Figure 2.6 (Chapter 2), we have plotted an example spectrum with the wavelength ranges of several indices and their sidebands marked.

For clarity, the results in §3.4 will concentrate primarily on three representative sets of measurements: [O II], ($H\gamma_A + H\delta_A$), and [MgFe]’.

Table 3.3 lists the strengths of several key spectral lines for all 104 galaxies in our sample. These raw indices are suitable for examining environmental trends within our own data set, but in order to make a proper comparison to other published data or theoretical models, we must carefully correct for any systematic differences between each set of measurements. In particular, index strengths are known to vary with the spectral resolution of the data. While we attempt to compare our data only to measurements made at high spectral resolution, to take full advantage of the high resolution available with DEIMOS, in some cases we are forced to degrade the resolution of our spectra to match that of the comparison data or model.

In §3.4 and §3.5, we will compare some of our results to the stellar population models of Bruzual & Charlot (2003), which include full synthetic spectra at a resolution of 3\AA ; this is the closest match available to the intrinsic resolution of our DEIMOS spectra ($\sim 1\text{\AA}$). We will also examine the Balmer- σ relation in comparison to data measured at 10\AA resolution (Kelson et al. 2001), the approximate resolution of the original Lick system (Worthey et al. 1994). Therefore, we convolved our DEIMOS spectra with Gaussians to produce degraded spectra at both 3\AA and 10\AA resolutions. We then remeasured the relevant spectral line indices. While not included in Table 3.3, spectral index measurements from our degraded DEIMOS spectra are available from the authors by request.

To compare our Balmer- σ relation to previous work by Kelson et al. (2001) on the redshift evolution of this correlation, we apply an aperture correction to our $H\delta_A$ and $H\gamma_A$ line strengths; we adopt their estimate that the quantity ($H\delta_A + H\gamma_A$) varies with aperture as:

$$\Delta(H\delta_A + H\gamma_A) = 1.78 \pm 0.16 \Delta \log(D_{ap})$$

and correct to an aperture of $1''.23$ at $z = 0.33$. This is a very small correction to our

data, which was measured through a similar aperture size at slightly higher redshift.

For any fixed-width absorption line index, Doppler broadening of lines will cause measured equivalent widths to be underestimated: as velocity dispersion increases, more of the line’s flux falls outside of the index bandpass. We can correct for this effect by modeling how each index varies with σ , with the help of the Bruzual & Charlot (2003) population synthesis models. We select several of their theoretical spectra at 3\AA resolution and zero velocity dispersion, and broaden them to a series of different velocity dispersions. At each σ , we measure the line indices we wish to correct: $[\text{MgFe}]'$, $\text{H}\delta_A$, and $\text{H}\gamma_A$. We then fit a quadratic function in σ to the resulting set of measurements. We find that the σ correction depends on the initial resolution of the spectrum, so we also degrade the Bruzual & Charlot (2003) spectra to 10\AA resolution, and repeat the procedure to determine the proper correction for our low-resolution measures of $\text{H}\delta_A$ and $\text{H}\gamma_A$.

Since we are not able to measure velocity dispersions for our full sample of 104 galaxies, corrected indices only appear in plots that are limited to the 71 bright galaxies where we have accurate measurements of σ . All plots that demonstrate trends in the full sample of 104 E+S0s are shown with uncorrected indices only. However, not applying a σ correction in these cases produces only a small error: less than $\pm 0.8\text{\AA}$ in $(\text{H}\delta_A + \text{H}\gamma_A)$. Emission lines like $[\text{O II}]$ do not vary regularly with σ , as the source of emission is generally not spread evenly across a galaxy.

In order to compare observed spectral line strengths to the predictions of Bruzual & Charlot models with various star-formation histories, we need to calibrate our observed $[\text{O II}]$ equivalent widths to specific star-formation rates ($M_\odot/M_{gal} \text{ yr}^{-1}$). We make such a calibration using the deep $\text{H}\alpha$ imaging of Cl 0024 by Kodama et al. (2004, and private communication). First, equivalent widths from the two catalogs are cross-correlated: our $[\text{O II}]$ widths closely track those in $\text{H}\alpha$, approximately reproducing the locally observed trend (Kennicutt 1992). For each $\text{H}\alpha$ detection, Kodama also provide an estimated star-formation rate, which we convert to a specific star-formation rate by dividing by an estimated mass for each member. For galaxies with velocity dispersions available, we calculate a galaxy’s dynamical mass according to

$M = 5\sigma^2 R_E / G$. To estimate a stellar mass for a galaxy with no available velocity dispersion, we first determine the typical M/L_B for a local galaxy of this luminosity from Gerhard et al. (2001), and correct M/L_B to M/L_V by subtracting a factor equal to $\log(M/L_V) - \log(M/L_B) = -0.06$, estimated from the typical colors of nearby early-type galaxies. We then correct for redshift evolution in M/L_V (based on our Fundamental Plane results below), and multiply by the observed luminosity of the galaxy:

$$\log(M) \simeq \log(M/L_V) + \langle \Delta \log(M/L_V) \rangle + \log(L_V)$$

For galaxies with velocity dispersions, masses estimated in this way are consistent with the calculated dynamical masses ($\Delta \log(M/M_\odot) = \pm 0.3$). We then fit a straight line to measured [O II] versus specific star-formation rate ($M_\odot/M_{gal} \text{ yr}^{-1}$), to yield a conversion relationship between the two.

In order to visualize overall trends in the spectral properties of cluster early types, we also produce a series of coadded spectra for each radial zone. Each spectrum is normalized, shifted to the rest frame, and then coadded. Bad pixels and sky lines are given zero weight in the addition. This method provides a snapshot of what the average spectrum of each ensemble of galaxies looks like. While weighting by luminosity would better represent the integrated stellar population of each ensemble, in practice, the coadded spectrum is dominated by the brightest galaxy in each group. We must be careful, however, in interpreting differences between the coadded normalized spectra for each radial zone: each coadded spectrum will reflect an ensemble of galaxies with a different average size and magnitude. Therefore, it is difficult to separate radial trends in the spectra from trends with magnitude or size. These coadded spectra will be discussed below in conjunction with the environmental trends in the spectral indices of individual galaxies.

3.4 Results

3.4.1 Cluster: Empirical Scaling Laws

Before we examine environmental trends in galaxy properties, we present the overall Fundamental Plane, $[\text{MgFe}]'$ - σ relation and the Balmer- σ relation for the cluster sample with high-quality spectra, and discuss how each has evolved between $z \sim 0.4$ and the present epoch.

3.4.1.1 The Fundamental Plane

Previous studies have traced a mild shift in the intercept of the cluster FP with redshift (Fritz et al. 2005; Wuyts et al. 2004; Kelson et al. 2000b). This seems to be consistent with passive luminosity evolution of stellar populations with a high redshift of formation (Wuyts et al. 2004), though biases due to morphological evolution are difficult to quantify. However, most earlier studies have concentrated on measuring the evolution of the FP from data taken in intermediate or high redshift cluster cores. With our broader spatial coverage, we can uncover any significant difference in the mean M/L_V of early types as a function of radius. Our sample also extends to fainter magnitudes than previous studies at $z \sim 0.4$, allowing us to probe M/L_V for smaller early types that perhaps formed later than the most massive cluster ellipticals.

Figure 3.2 presents the FP of Cl 0024 compared to that of the Coma cluster, adopting the parameters determined locally by Lucey et al. (1991): $\alpha = 1.23$, $\beta = 0.328$, and $\gamma = -8.71$, where the fundamental plane is defined as

$$\log(R_e) = \alpha \log(\sigma_o) + \beta \langle \mu_V \rangle + \gamma$$

If we assume for the moment that α and β remain fixed with redshift—i.e., that E+S0s evolve passively—then we can relate the offset in the intercept γ between Cl 0024 and Coma to the change in the mean mass to light ratio of cluster early types since $z = 0.4$:

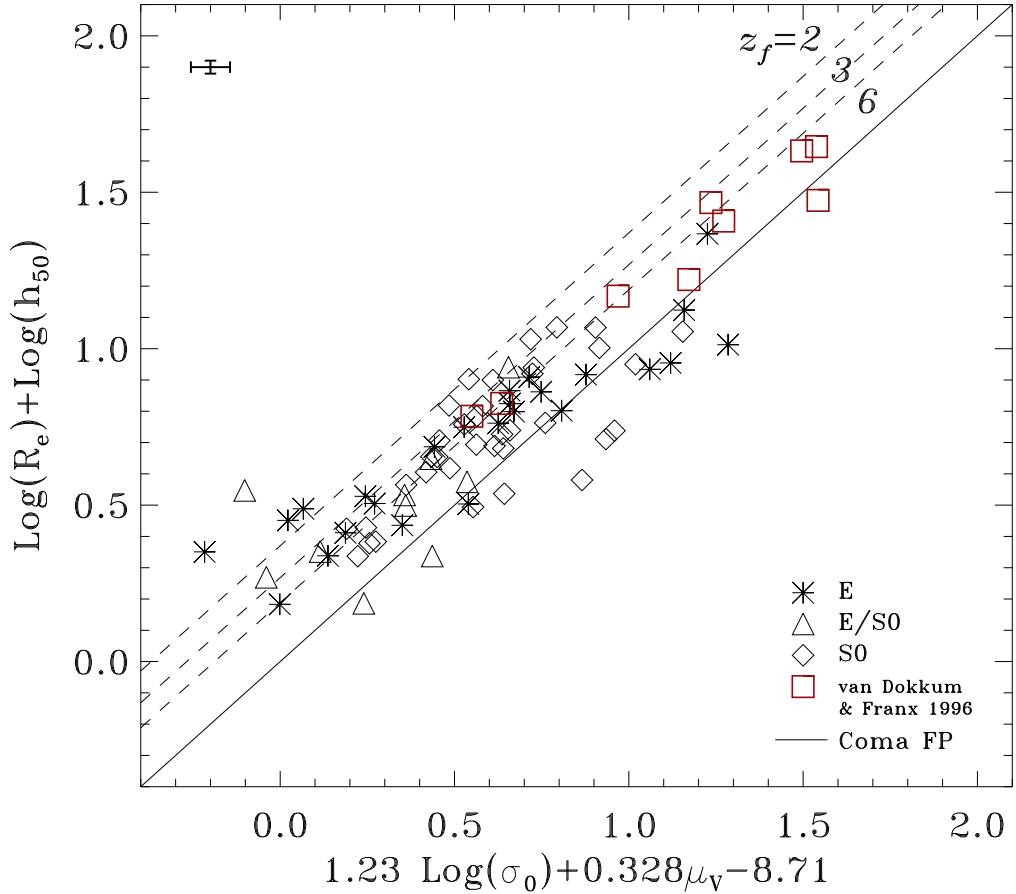


Figure 3.2 FP of Cl 0024, compared to Coma cluster (solid line). Symbols represent different morphologies, as indicated. Dotted lines correspond to the expected shift in FP zero point from Coma to $z \sim 0.4$, for SSP models with $z_f = 2.0, 3.0, 6.0$.

$$\langle \Delta \log (M/L_V) \rangle = \langle \Delta \gamma \rangle / (2.5\beta)$$

We find that the average offset from the Coma FP implies a change in the M/L_V ratio between $z = 0.4$ and $z = 0.02$ of $\langle \Delta \log (M/L_V) \rangle = -0.14 \pm 0.02$, excluding galaxies with velocity dispersions below 100 km s^{-1} . (Including those galaxies, the zero point shift rises to $\langle \Delta \log (M/L_V) \rangle = -0.18 \pm 0.03$) This is a smaller evolution than found in the field at $z \sim 0.3 - 0.5$ by Treu et al. (2005b), $\langle \Delta \log (M/L_V) \rangle = -0.23 \pm 0.05$, though it is in agreement with the offset determined by Kelson et al. (2000b) for

a cluster at $z = 0.33$ ($\langle \Delta \log (M/L_V) \rangle = -0.17 \pm 0.03$). Overplotted in Figure 3.2 are dotted lines representing the expected evolution of the FP zero point from the Coma cluster back to $z = 0.4$. These are based on the passive evolution of Single Stellar Population (SSP) galaxy models, with a redshift of formation, z_f , of 2, 3, or 6 (Bruzual & Charlot 2003). The observed FP in Cl 0024 is consistent with $z_f > 3$ for most cluster early types.

Open squares in Figure 3.2 indicate points from van Dokkum & Franx (1996), who also measured the FP in Cl 0024. The two sets of data fall on the same plane, and our inferred $\langle \Delta \log (M/L_V) \rangle$ is consistent with their work: they calculated $\langle \Delta \log (M/L_V) \rangle = -0.12 \pm 0.03$. Our much-larger sample should allow for greater precision in calculation of the FP zero point, yet the two measurements yield similar uncertainties in $\langle \Delta \log (M/L_V) \rangle$. This is due to the surprisingly high scatter that we uncover in the Cl 0024 FP, which was not apparent in the earlier sample of 9 galaxies in van Dokkum & Franx (1996).

Importantly, we find the intrinsic scatter in the FP of Cl 0024 is 40% in M/L_V , significantly higher than the $\sim 20\%$ found locally (e.g., Jørgensen, Franx, & Kjaergaard 1996), and also higher than the $\sim 13\%$ scatter in the FP of Cl 1358+62 at $z = 0.33$ (Kelson et al. 2000b). While we probe the FP for a larger range of galaxy masses than Kelson et al. (2000b), we see a higher scatter even in the more massive galaxies that are comparable to those in their study. Interestingly, this increased scatter is due almost entirely to an enhanced scatter in M/L_V for galaxies within the inner 1 Mpc of the cluster, a region that has been well studied in other clusters in this redshift range (Bender et al. 1998; Kelson et al. 2000b; Ziegler et al. 2001). To verify this increased scatter is a true physical effect, we examined the possibility that errors in our surface photometry are higher in the more crowded cluster core, but found that galaxies with nearby neighbors cannot account for the high scatter. We also checked for errors in our velocity dispersion measurements: when removing five early-type spectra ($\sigma > 100 \text{ km s}^{-1}$) with $S/N < 10$ from our high-quality sample, we find no significant change in our FP zero point or scatter.

A similarly large scatter was found by Wuyts et al. (2004) for the cluster MS

Table 3.1. $\langle \Delta \log (M/L_V) \rangle$ for several subsets of our data

	E	E/S0	S0	All	All+vDF
All σ:					
N:	24	10	35	69	77
$\langle \Delta \log (M/L_V) \rangle$:	-0.18 ± 0.05	-0.23 ± 0.08	-0.14 ± 0.03	-0.18 ± 0.03	-0.18 ± 0.02
$\pm 1\sigma$:	0.23	0.26	0.20	0.20	0.19
$\sigma > 100 \text{kms}^{-1}$:					
N:	21	8	33	62	70
$\langle \Delta \log (M/L_V) \rangle$:	-0.14 ± 0.03	-0.14 ± 0.06	-0.14 ± 0.03	-0.14 ± 0.02	-0.14 ± 0.02
$\pm 1\sigma$:	0.15	0.17	0.18	0.16	0.16
$R < 1 \text{Mpc}$, $\sigma > 100 \text{kms}^{-1}$:					
N:	10	6	15	31	39
$\langle \Delta \log (M/L_V) \rangle$:	-0.09 ± 0.06	-0.10 ± 0.06	-0.06 ± 0.06	-0.07 ± 0.03	-0.09 ± 0.03
$\pm 1\sigma$:	0.18	0.16	0.22	0.20	0.19

Note. — The first three columns present the mean evolution in M/L_V broken down by morphological type, both with and without galaxies of $\sigma < 100 \text{ km s}^{-1}$, and for the whole cluster sample or just galaxies with projected radius $R < 1 \text{ Mpc}$. Column four includes all our E+S0s, but excludes two disturbed-morphology galaxies with outlying values of $\Delta \log (M/L_V)$. In the fifth column, we add our data to the eight galaxies from van Dokkum & Franx (1996) that do not overlap with our own. Values for $\pm 1\sigma$ are logarithmic, representing the scatter in $\Delta \log (M/L_V)$.

2053–04 at $z = 0.58$ ($\sim 42\%$), so this may be an effect seen only in some fraction of intermediate redshift clusters. At even higher redshift, Holden et al. (2005) finds a large scatter in M/L_B for massive early types at $\langle z \rangle = 1.25$. We will defer further discussion of this effect to §3.4.2, where we discuss radial trends.

Recent results indicate that the parameters of the FP at intermediate redshift may differ from the local values (e.g., Treu et al. 2005a,b, Wuyts et al. 2004; van der Wel et al. 2005). We investigated using the method of Jørgensen, Franx, & Kjaergaard (1996) to derive an independent fit for the parameters of the FP from our sample, including Montecarlo simulations to account for bias in our magnitude-limited sample, but found no conclusive evidence for a change in FP parameters from the local values.

Nevertheless, the group of galaxies with $\sigma < 100 \text{ km s}^{-1}$ in Figure 3.2, located at the lower left of the plot, seem to deviate significantly from the FP. As most calculations of the FP parameters specifically exclude galaxies with $\sigma < 100 \text{ km s}^{-1}$

(e.g., Jørgensen, Franx, & Kjaergaard 1996; Lucey et al. 1991), including our own, it is not surprising that such galaxies in our sample deviate from the FP. Yet there is also evidence that, in the local universe, these small ellipticals and dwarf ellipticals may behave differently as a population than larger E+S0s (e.g., Burstein et al. 1984). Our data suggest that this population split may have existed already at $z \sim 0.4$.

When dividing our sample into three subclasses (E, S0, and E/S0), we find no evidence of significant variation between the populations, either in scatter or intercept. Table 3.1 lists values of $\langle \Delta \log (M/L_V) \rangle$ and the scatter about the mean for several different subsamples of our data. For galaxies with $\sigma > 100 \text{ km s}^{-1}$ in particular, there appears to be no variation at all between E, E/S0, and S0 morphological types. This lack of variation is in disagreement with recent results by Fritz et al. (2005), who marginally detect a difference between ellipticals and S0s in two clusters at $z \sim 0.2$, equivalent to a difference in $\delta \langle \log (M/L_V) \rangle$ of approximately -0.16 ± 0.11 (with S0s being the younger/more luminous population). On the other hand, Kelson et al. (2001) find no such distinction between ellipticals and S0s at $z = 0.33$. Our sample is larger than either of these other studies, and so we place stronger constraints on the possible M/L_V variations between Es and S0s at $z \sim 0.4$. As discussed in Chapter 2, we attempted to improve our E:S0 classification by examining residuals from our surface photometry fits as a means of locating faint disks or bars (see Figure 3.1). Two coauthors (R. S. E. and T. T.) independently examined the residuals and, although the revised classes agreed fairly closely, no significant FP differences between ellipticals and S0s were found.

3.4.1.2 [MgFe]'- σ and Balmer- σ Relations

While the FP helps to connect the dynamic and photometric structure of an early-type galaxy to the overall mass to light ratio of its stellar population, we can seek an improved picture of a galaxy's stellar population by also examining correlations between spectral line strengths and σ . Local early-type galaxies exhibit a tight correlation between the Mg_2 line index and σ , for example (e.g., Kuntschner et al. 2001). The narrower Mg^b index is centered over the same spectral feature, and, at least lo-

cally, behaves in the same way as Mg_2 (Burstein et al. 1984). Similarly, correlations are observed between σ and the strengths of several Balmer lines: $H\beta$, $H\gamma$, and $H\delta$ (Kelson et al. 2001; Kuntschner et al. 2001).

Our current set of high-quality spectra of early types in Cl 0024 provides a large sample of galaxies at $z \sim 0.4$ where diagnostic spectral lines can be measured with some accuracy for the first time. We measure Mg^b , Mg_2 and the composite index $[MgFe]'$ to make a broad comparison between the metallicity features of early types at intermediate redshift and those seen locally.

We also measure Balmer line strengths, which are commonly used to judge the age of early-type galaxies (Worthey & Ottaviani 1997). However, low levels of recent star formation can make an early-type galaxy's stellar population appear much younger than the true average age of its stars. For the first 1 Gyr after a starburst, the strong Balmer absorption present in the spectra of A stars can be prominent in the integrated galaxy spectrum. The $H\beta$ index is a particularly age-sensitive indicator, but is affected by contamination from emission. While $H\alpha$ can be used to correct $H\beta$ for small amounts of emission, this line falls outside of the range of our spectra, so we choose to study the $H\delta$ and $H\gamma$ lines instead, which are relatively unaffected by emission. Measuring $H\delta$ and $H\gamma$ in Cl 0024 can thus allow us to probe both galaxy age and episodes of recent star formation, if the two effects can be separated.

Early attempts to trace the evolution of these relations with redshift have produced a variety of results. Kelson et al. (2001) reported a correlation between $(H\delta+H\gamma)$ and σ for several clusters between redshifts of 0.08 and 0.83. The slope they measure for Cl 1358+62 at $z = 0.33$ is consistent with their data at all other redshifts, though they are unable to measure slope for each cluster individually. They plot the zero point evolution of this relation, and find that the change in mean Balmer absorption strength from $z = 0.83$ to the present epoch is consistent with passive evolution models of early types, and constrain $z_f > 2.4$. Likewise, Barr et al. (2005) study a poor cluster at $z = 0.28$ and find that the zero point evolution of the $(H\delta+H\gamma)-\sigma$ relation, when compared to Kelson et al. (2001), is only marginally inconsistent with passive evolution.

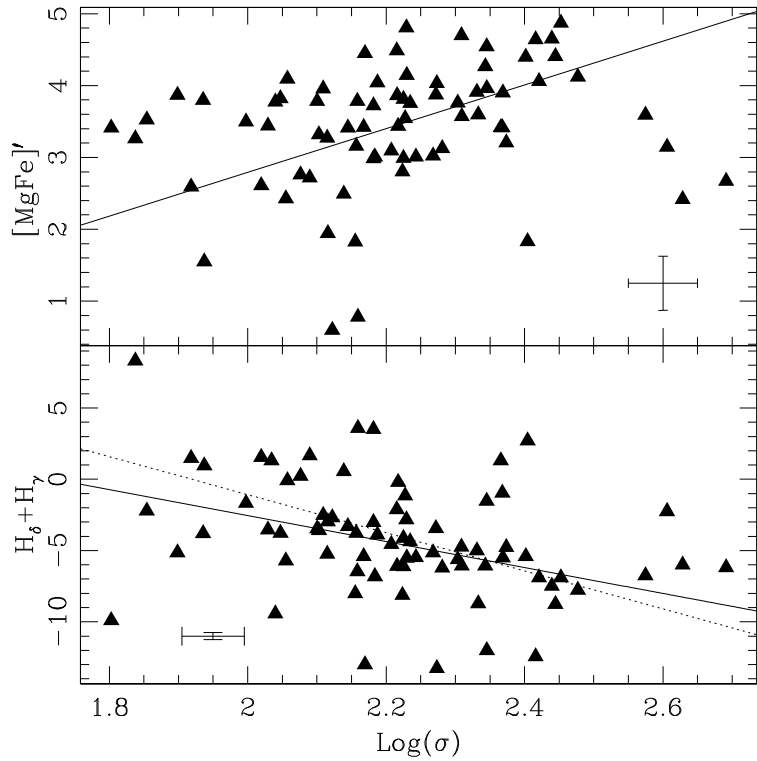


Figure 3.3 Top: $[\text{MgFe}]'-\sigma$ at resolution of 3\AA . The solid line is the best least-squares fit to our data, excluding the outlier points at $\sigma \geq 300 \text{ km s}^{-1}$. Bottom: $(\text{H}\gamma+\text{H}\delta)-\sigma$ at resolution of $\sim 10\text{\AA}$, compared to Kelson et al. (2001), at same spectral resolution. Indices are corrected to match the aperture used by Kelson et al. The solid line represents the best-fit relation from Kelson et al. (2001). The dashed line is the line of best fit to our data. The scatter is large, so our best-fit relation is highly uncertain. In both panels, velocity dispersions are aperture corrected to a $3''.4$ diameter aperture at the distance of the Coma cluster.

Conversely, the evolution of the metallicity correlations has proven more complicated. The question of using spectral line strengths to uniquely determine ages, metallicities, and α -element enhancement ratios for elliptical galaxies is not yet solved even for local galaxies, as made clear by the excellent study of the problem by Tantalo & Chiosi (2004). Further, our data likely fall short of the S/N needed to determine these galaxy properties reliably (Trager et al. 1998). It is therefore beyond the scope of this thesis to examine how the various $\text{Mg}-\sigma$, $[\text{MgFe}]'-\sigma$ and Balmer- σ relations evolve with redshift.

However, we note that correlations with velocity dispersion do exist as far back

as $z \sim 0.4$, regardless of the origin of such a relation. Secondly, large deviations from these relations may indicate a recent episode of star formation in that galaxy. It will be useful then to look later at the residuals from the $[\text{MgFe}]'$ and Balmer– σ relations, as a function of cluster environment.

We can minimize uncertainties due to variations in abundance ratio by focusing on the $[\text{MgFe}]'$ index, which should provide a reliable estimate of the total metallicity of a galaxy (Thomas et al. 2003). Figure 3.3 presents the correlation between $[\text{MgFe}]'$ and σ . The bulk of galaxies measured fall along the solid best-fit line plotted, though the scatter is high. The high scatter could be due to the large error bars on each measurement. However, there are a significant number of outliers with anomalously low $[\text{MgFe}]'$ that seem not to be due to measurement errors. These outliers correlate with other properties of the each galaxy’s stellar population, and will be discussed further in §3.5.

Figure 3.3 presents $(\text{H}\delta+\text{H}\gamma)$ vs. σ for Cl 0024. The two quantities correlate in the sense that the largest, highest σ galaxies exhibit the weakest Balmer absorption. This is as expected if the stellar populations are oldest in the largest elliptical galaxies. Overplotted in Figure 3.3 is the best-fit relation from Kelson et al. (2001), where we adopt their slope and interpolate between their points at $z = 0.33$ and $z = 0.58$ to determine the zero point at $z = 0.39$. Our data are consistent with their findings, though again our scatter is quite large. We also overplot our best fit relation as a dotted line, though the high scatter makes this relation highly uncertain.

In fact, just as we saw with the FP of Cl 0024, we see a scatter that is much larger than that observed in Cl 1358+62 at similar redshift. Both the FP and $(\text{H}\delta+\text{H}\gamma)$ – σ relation are reported to be much tighter for Cl 1358+62 than for Cl 0024 (Kelson et al. 2001, 2000b). On the other hand, Barr et al. (2005) also find an increased scatter in the $(\text{H}\delta+\text{H}\gamma)$ – σ relation at $z = 0.28$, though they do not measure the FP. As with the FP and metallicity– σ relation in Cl 0024, some of the enhanced scatter we observe in Balmer line strengths is a direct signature of environmental evolution, and will be discussed below.

3.4.2 Radial Trends

We now turn to discuss environmental trends present in the early-type population of Cl 0024. For the brighter sample of galaxies with high-quality spectra, we can analyze the residuals from the empirical scaling laws presented in §3.4.1, and look for variations with local density, cluster radius, or galaxy luminosity. For the full sample of galaxies to $I = 22.5$ we additionally examine the environmental variations in several key spectral lines.

In the analysis of Cl 0024 *HST* imaging by T03, it was noted that local density was the primary measure of environment outside of the cluster core, suggesting that infalling groups are the logical unit out of which clusters are built. Looking at the detailed spectral properties of early types now, it would be useful to determine whether spectral properties depend more closely on local density, as the morphological mix seems to, or on radius. Because we are only tracing a much smaller population of 104 galaxies of a single morphological class, we are unable to make such a distinction reliably. We will, however, present plots of spectral features as a function of both R and Σ_{10} . Because projected radius R is more easily measured than Σ_{10} , we will focus our discussion on radial trends. Anticipating the results, we note that the observed trends with R and Σ_{10} are qualitatively similar.

3.4.2.1 Fundamental Plane

The high scatter about the FP of Cl 0024, discussed in §3.4.1 above, leads us to examine $\Delta \log (M/L_V)$ on a galaxy by galaxy basis. For an individual early type (labeled by subscript i), the evolution in M/L_V with respect to the prediction of the local FP is related to its offset from the local intercept γ according to:

$$\Delta \gamma^i = \log R_e^i - \alpha \log \sigma^i - \beta \mu_V^i - \gamma$$

and

$$\Delta \log \left(\frac{M}{L_V} \right)^i = -\frac{\Delta \gamma^i}{2.5\beta}$$

In Figure 3.4, we plot $\Delta \log(M/L_V)$ as a function of projected radius and local density. Both plots show a trend toward increased scatter near the cluster core, at small radius and high densities.

In the radial plot, the open triangles overplotted represent the mean $\Delta \log(M/L_V)$ for galaxies within each of the three radial zones delimited by dotted lines: cluster core ($R < 1$ Mpc), transition region ($1 \leq R < 2.4$ Mpc), and periphery ($R \geq 2.4$ Mpc). These three zones were introduced in T03, and represent regimes where different physical mechanisms may be effective in transforming galaxies. We see a clear trend of increasingly negative $\Delta \log(M/L_V)$ as we move outward, indicating that galaxies are more luminous for their mass, and hence appear younger, at larger distances from the cluster center.

Galaxies marked with a filled triangle in Figure 3.4 have $\sigma < 100$ km s⁻¹. These, along with two disturbed-morphology galaxies marked with filled circles, are not included in the calculation of the means for each radial zone. The low- σ galaxies are likely biased toward low M/L_V , due to the selection effect where only the brightest of the small, compact cluster members are within our limiting magnitude.

The solid diamond plotted within 1 Mpc on Figure 3.4 is the mean $\Delta \log(M/L_V)$ found by van Dokkum & Franx (1996); it is clear now why our mean value of $\Delta \log(M/L_V)$ is slightly larger than theirs: the additional contribution from lower M/L_V galaxies in the transition region and periphery boost the mean luminosity evolution we calculate. It is interesting also to note that our new wide-field data bridge the gap between the mass to light ratios typical of cluster cores and those found in the field at this redshift. The other solid diamond plotted in Figure 3.4, labeled “Field”, is from Treu et al. (2005b), who measured the FP of field galaxies at intermediate redshift. Similar values for the field are reported by Treu et al. (2001a) and van der Wel et al. (2005). While some studies of the field FP at intermediate redshift have reported a slower redshift evolution (e.g., Ziegler et al. 2005; van Dokkum & Franx 2001; Rusin et al. 2003), van der Wel et al. (2005) have shown that most of the discrepancy between studies of field early types can be attributed to differences

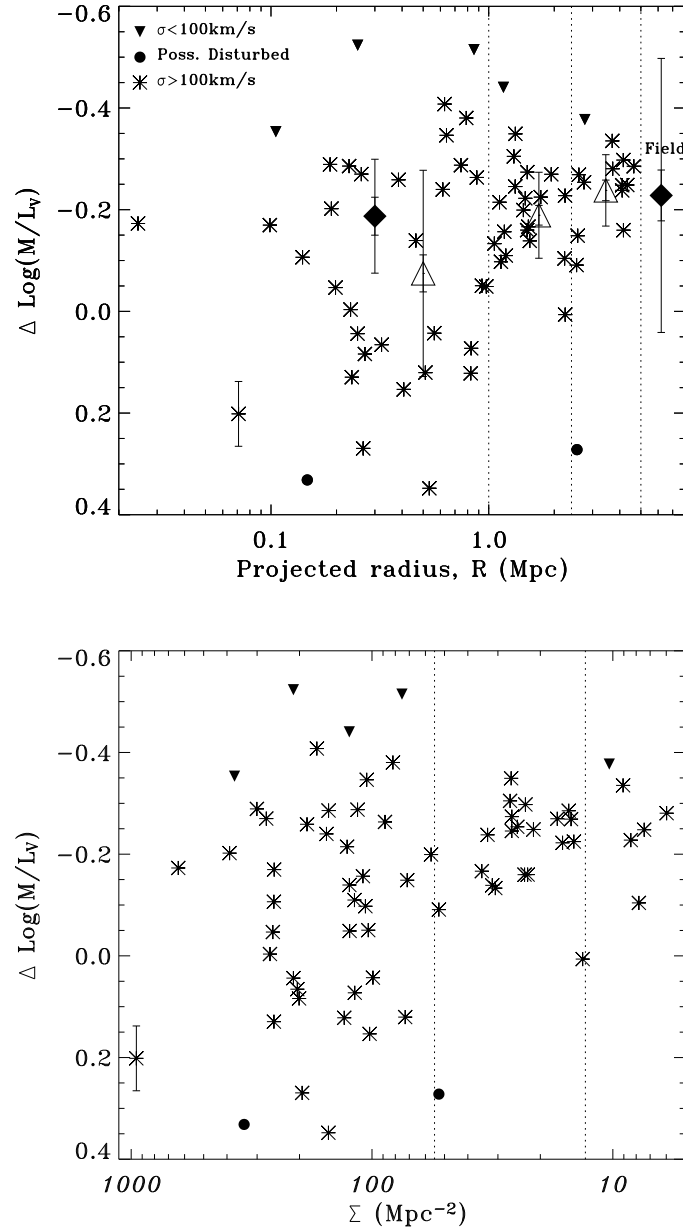


Figure 3.4 Change in M/L_V ratio for galaxies in Cl 0024, with respect to $\langle M/L_V \rangle$ for Coma. Plotted with respect to radius, top, and local density, bottom. Asterisks represent individual galaxies, with a typical error bar shown on a point near the lower left of each plot. For the upper plot, open triangles represent averages for the three radial zones indicated. Large error bars reflect the rms scatter, and small bars are the error on the mean. Filled diamonds are points from van Dokkum & Franx (1996) and Treu et al. (2005b) for cluster core and field, respectively. Dotted lines at 1 Mpc and 2.4 Mpc delimit the three radial zones discussed in the text; corresponding dotted lines in the local density plot represent the mean values of Σ_{10} at 1 Mpc and 2.4 Mpc, respectively.

in analysis methods and selection criteria. Since the reported variations are small on the scale of Figure 3.4 (less than ± 0.1 in $\log(M/L_V)$), we can be confident that $\langle M/L_V \rangle$ does actually vary with environment at intermediate redshift. This gradient in $\langle M/L_V \rangle$ across the cluster appears to directly reflect the difference in formation history between galaxies in high and low density environments.

Within the cluster core, the scatter in $\Delta \log(M/L_V)$ is highest, as noted above in §3.4.1. We caution that projection effects could contribute to the apparent scatter near the cluster center, especially if there is a strong gradient in M/L_V with 3D radius, r . However, for any sensible distribution, we would expect that the number of true core members is higher than those at large radii projected onto the core. As we see approximately equal numbers of galaxies both above and below the mean $\Delta \log(M/L_V)$ in the core, we conclude that projection effects cannot account for the increased scatter. This is confirmed by Kolmogorov–Smirnov tests that compare various simulated distributions of galaxies to our observed distribution.

Similarly, we find no evidence that the high- or low- M/L_V early types in the core are part of an infalling group; $\Delta \log(M/L_V)$ appears uncorrelated with the velocities or spatial distribution. It has been hypothesized that Cl 0024 is currently undergoing a face-on merger with a large group, as indicated by the double-peaked redshift distribution first reported by Czoske et al. (2002), and replicated in the redshift distribution of Figure 2.8. However, none of the galaxies on our FP lie in the secondary “Peak B”. While the high scatter may still be related to the subcluster merger, whatever mechanism affects the mass to light ratios of early types in the cluster core is not apparent in any other measurements.

Although the observed scatter seems at variance with the notion that massive cluster ellipticals are uniformly old and quiescent, if we use the Bruzual & Charlot (2003) SSP models to predict the passive evolution of these galaxies to $z = 0$, the resulting scatter will match that observed locally. Furthermore, the scatter in the field FP reported by Treu et al. (2005b) in this redshift range is larger than in the core of Cl 0024, as expected if the range in ages and star-formation histories is greater in the field than in the cluster environment.

There may be two separate populations of E+S0s in the core, then: older galaxies that formed earliest and which have M/L_V already similar to that of local E+S0s, and galaxies with a lower M/L_V which have more recently fallen into the cluster core. While there is no obvious separation between these two groups in Figure 3.4, we do notice a residual correlation between $\Delta \log(M/L_V)$ and σ , in the sense that the most massive, highest- σ cluster galaxies also have the highest mass to light ratios, indicating the oldest stellar populations. This is not a surprising correlation, but it does confirm that the high M/L_V galaxies are typically the oldest and largest found in the cluster. It is also in agreement with a more general trend identified by Treu et al. (2005a), who found that less massive galaxies exhibit a younger luminosity-weighted age than do the most massive ones.

It is important to note, however, that the radial trend observed in $\Delta \log(M/L_V)$ is not due solely to this “downsizing” relation between galaxy mass and M/L_V . There is still a radial gradient in M/L_V , even when we further restrict our sample to a narrow range of galaxy masses.² For example, if we limit our sample to the mass range $10.9 < \log(M/M_\odot) \leq 11.4$, we observe a significant difference in M/L_V between the cluster periphery and core: $\delta \langle \log(M/L_V) \rangle = 0.13 \pm 0.07$. Using field galaxies from the Treu et al. (2005b) sample within this same mass range (and in the redshift range $0.3 < z < 0.5$), we find an offset between the Cl 0024 cluster core and the field equal to $\delta \langle \log(M/L_V) \rangle = 0.09 \pm 0.06$. The lower mass limit was chosen because galaxies above $\log(M/M_\odot) = 10.9$ are negligibly biased due to the luminosity limit of both surveys. The upper mass limit is chosen so that we include only galaxies that are well represented across the entire cluster, excluding the high-mass galaxies found only in the core.

It makes sense to search for morphological differences between the old and young E+S0s in the cluster core. The existence of the morphology–density relation in Cl 0024 (T03) leads us to consider whether the younger, low M/L_V galaxies are preferentially S0s that have recently been created or transformed from spirals. How-

²We calculate a galaxy’s dynamical mass, in solar units, according to $M = 5\sigma^2 R_e / G$, which is equal to $M = 1162\sigma_0^2 R_e$, with R_e in pc and σ_0 in km s^{-1} .

ever, when we divide our sample into groups that lie above and below the mean M/L_V in the cluster core, we see no evidence for morphological segregation. (But see Chapter 6 for further investigation of this issue.)

In their gravitational lensing analysis of Cl 0024, Kneib et al. (2003) estimated the global mass to light ratio of the cluster as a function of radius, by combining a mass map based on their weak lensing analysis with K_S -band observations which trace the stellar mass. They concluded that the overall M/L of the cluster is remarkably flat, at least within 2 Mpc of the cluster core. (Their result was the same whether they measured total light via K or rest-frame V observations.) At first glance, the radial gradient in M/L_V seen in Figure 3.4 may appear to contradict the results of Kneib et al. (2003). However, the *cluster* M/L ratio measured in their work is much more strongly dominated by dark matter than the *early-type galaxy* M/L_V discussed here, and so variations in mass to light ratios of individual galaxies can be consistent with an overall cluster M/L_V that is constant.

3.4.2.2 Line Strengths

In the next two subsections, we will consider environmental trends in several different indicators of star formation and metallicity, in both our high-quality sample of galaxies and the full sample to $I = 22.5$. It is important to gauge the effect of any recent star formation on the overall M/L_V of these galaxies, to ensure that we can correctly attribute differences in M/L_V to differences in mean galaxy age, rather than the effects of relatively recent and small star-forming events. We also wish to trace the star formation itself, as any significant star formation in early-type galaxies can act as a signpost to the different physical mechanisms that could be at work.

We focus on two key indicators of star formation, the [O II] emission line, and the combination ($H\delta+H\gamma$), which respectively measure ongoing star formation, and recently completed star formation, as discussed in §3.3. Figure 3.5 plots the equivalent widths of these two diagnostic indices as a function of radius and local density. Solid symbols indicate galaxies with $I \leq 21.1$; we note that some of these brighter galaxies do not have measured velocity dispersions, and so were not included in the high-

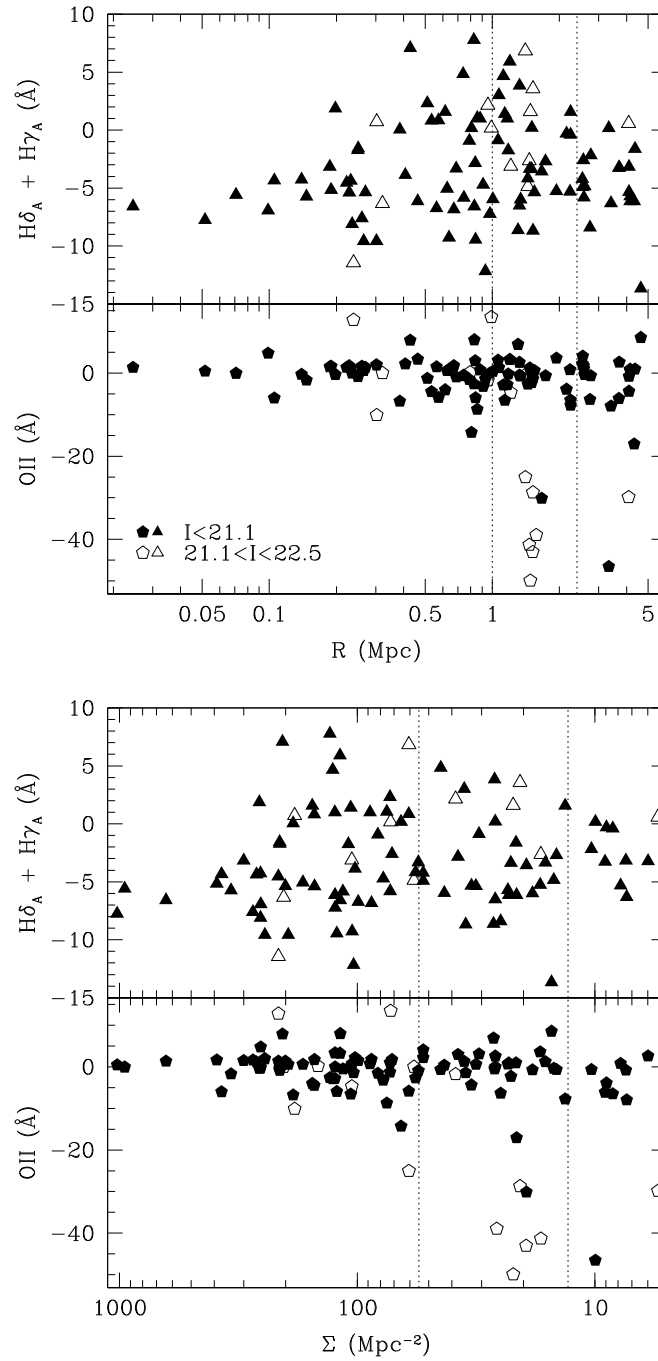


Figure 3.5 $H\delta_A + H\gamma_A$ and [O II] EWs for all E+S0 members as function of radius (top) and local density (bottom). Negative values represent emission in [O II], but can be considered weak absorption for the Balmer lines, due to an effect where the continuum flux in the index sidebands falls completely below the flux in the index bandpass. In the upper plot, dotted lines delineate the core, transition region, and periphery. Dotted lines in the lower plot mark the mean values of the local density at these same radii. Open symbols: $21.1 < I < 22.5$. Filled symbols: $I < 21.1$.

quality sample discussed in previous sections. Open symbols are galaxies in the magnitude range $21.1 < I \leq 22.5$. As we saw with the FP, we note that the strengths of these indices vary in a similar way with both local density and projected radius.

Examining individual measurements of $EW([O\ II])$, we find a population of galaxies with strong emission, which are concentrated in a narrow range in radius, close to the virial radius at 1.7 Mpc. The spectra of these galaxies are dominated by emission lines, including $[O\ III]$ and several Balmer lines (see Figure 3.7). These emission line galaxies are preferentially dim; as denoted by the unfilled pentagons in Figure 3.5, most are in the magnitude range $21.1 < I \leq 22.5$. Most previous studies have not been sensitive to early-type cluster galaxies at these luminosities and in this radius range, though a recent survey of a cluster at $z = 0.83$ by Homeier et al. (2005) has uncovered a similar population of dim emission-line E+S0s, discussed in more detail in §3.5.

What could be the nature of these emission line galaxies clustered in radius? While we leave most of the discussion of this question to §3.5, we can quickly address some of the possibilities. Figure 3.6 shows postage-stamp images of each of these active galaxies. The top row contains the three emission line galaxies with $I < 21.1$; one of these may be interacting with a neighbor, though the redshift of the neighboring galaxy is not known. None of the others seem to be undergoing major mergers, so merger-induced star formation is an unlikely cause of the emission (but see Chapter 6). One other bright $[O\ II]$ -emitter could possibly be a misclassified spiral. We looked at the residuals from surface photometry fits for the rest of these galaxies, but found no other indication of spiral arms. Seven of these ten galaxies are also detected by the $H\alpha$ imaging survey of Kodama et al. (2004), and two of the three nondetections have redshifts that would likely place the $H\alpha$ line outside the bandwidth of the narrow-band filter employed by Kodama et al.

Line ratio tests meant to distinguish between star formation and AGN activity are inconclusive for these galaxies. *XMM-Newton* observations are available which cover a field including most of these emission line early types: none are associated with an X-ray point source (Zhang et al. 2005), even though the *XMM-Newton* observations

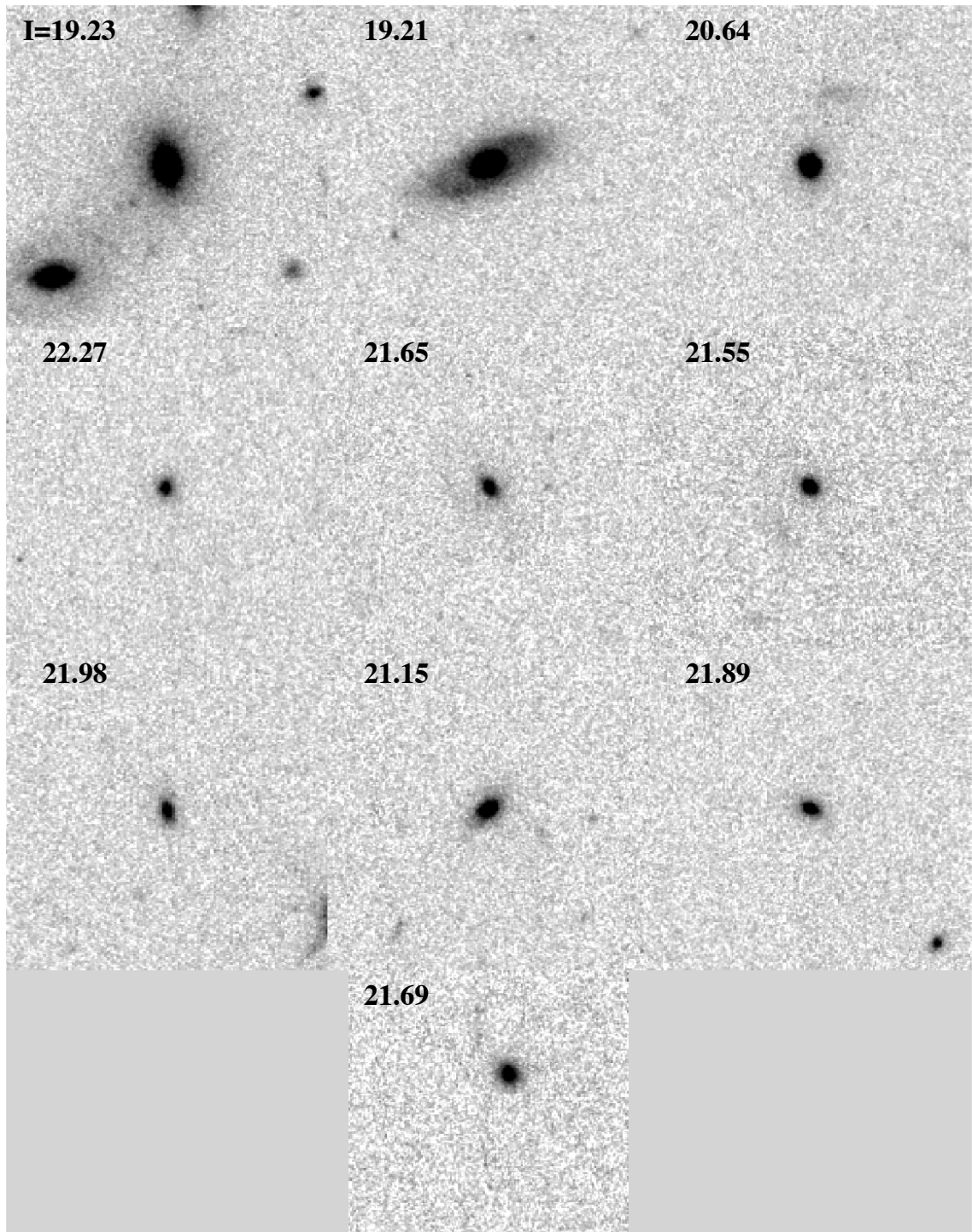


Figure 3.6 Postage stamp images of all galaxies with $\text{EW}(\text{O II}) < -15\text{\AA}$. The top row shows galaxies with $I \leq 21.1$, and the lower rows contain galaxies in the range $21.1 < I \leq 22.5$. Stamps are $10''$ on a side.

are deep enough to detect any clear-cut AGN with $L_X > 10^{42}$ erg s $^{-1}$. Therefore, while we cannot rule out AGN activity for these galaxies, none are definitively AGN. An interesting hypothesis that we will explore in §3.5 is that these galaxies have suffered harassment or disturbances from their interaction with the intracluster medium (ICM).

In addition to the emission line galaxies, we see a higher mean EW([O II]) at larger radius. Figure 3.7 shows the coadded normalized spectra of all early types binned by radial zone; top to bottom, they trace the mean early-type spectrum from the periphery to the core. All galaxies with $\text{EW}(\text{O II}) < -15\text{\AA}$ were coadded separately; see Figure 3.7, right. Coadded spectra of “normal” E+S0 members in Figure 3.7 show an increase in an average galaxy’s [O II] emission outside of the cluster core. This trend is qualitatively similar to radial gradients in emission line strength seen for samples of cluster galaxies that include all morphologies, both at intermediate (e.g., Gerken et al. 2004) and low redshift (e.g., Gómez et al. 2003; Lewis et al. 2002).

In Figure 3.8, we plot the fraction of all E+S0 galaxies with $\text{EW}([\text{O II}]) < -5\text{\AA}$, averaged across each of the radial zones indicated. At all luminosities, it is clear that the fraction of [O II] emitting early types is highest in the cluster periphery and field. Though the fraction of emission line galaxies may be elevated due to selection effects (§3.3), especially at fainter magnitudes, there still exists radial variation within any single magnitude bin. This radial variation holds (in the two brighter magnitude bins) even if we exclude the cluster core, where the fraction of [O II] emitters may be affected by the process causing the strong [O II] emission at the virial radius.

We see then that both the fraction of galaxies with measurable [O II] emission, and the average strength of that emission rises slightly with radius. This suggests an encounter with the cluster environment which serves to gradually suppress the already low levels of early-type star formation during infall. Another possibility is a simple gradient in galaxy formation age: older early types near the cluster core may simply contain less residual gas available for star formation. However, this scenario is more difficult to reconcile with other studies that have found strong gradients in the overall star-formation rates within clusters (e.g., Kodama et al. 2004; Poggianti

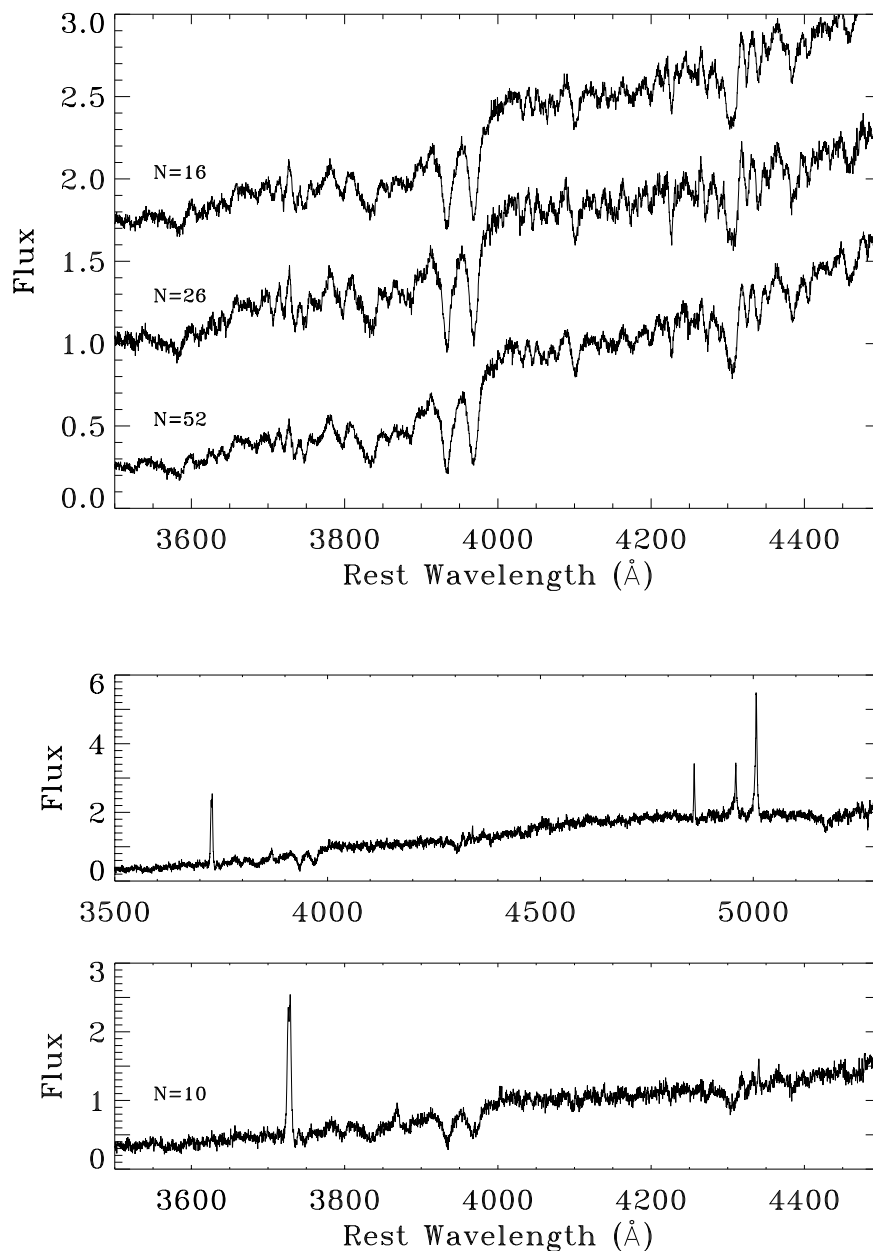


Figure 3.7 Normalized, coadded spectra. The bottom panel shows coadded spectrum of E+S0 members with $\text{EW}(\text{O II}) < -15\text{\AA}$. The full spectrum is in the upper half-panel, with an excerpt below it which shows $[\text{O II}]$ emission, Ca H & K, and Balmer absorption lines in more detail. The top panel shows coadded spectra for all other E+S0 members, divided by distance from cluster core. From top to bottom: periphery, transition region, and cluster core. Wavelengths in rest frame.

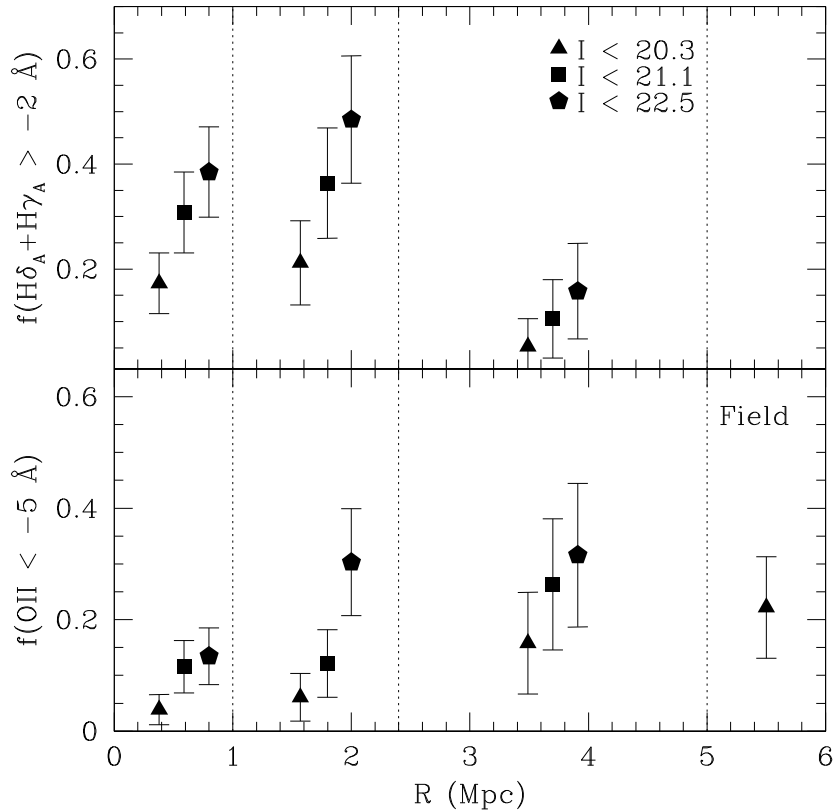


Figure 3.8 Fraction of E+S0 galaxies with $\text{EW}(\text{H}\delta_A + \text{H}\gamma_A) > -2\text{\AA}$, top, and $\text{EW}([\text{O II}]) < -5\text{\AA}$, bottom, as a function of radial zone. Triangles represent fraction for galaxies with $I < 20.3$. The field value is from Treu et al. (2002). Squares and pentagons are the same measure, but to $I = 21.1$ and $I = 22.5$, respectively.

et al. 1999; Balogh et al. 2000).

Turning now to the Balmer absorption strengths, we see a mix of galaxies in Figure 3.5 with low to moderate Balmer absorption in the periphery and transition region. These are consistent with the low levels of ongoing star formation indicated by $[\text{O II}]$ emission. Almost coincident with the set of strong $[\text{O II}]$ emitters discussed above, we begin to see galaxies with much higher values of $(\text{H}\delta + \text{H}\gamma)$, which appears to decay toward the center of the cluster. If the $[\text{O II}]$ emission seen at the virial radius is, in fact, due to star formation, these galaxies with enhanced Balmer absorption may have undergone a similar burst of star formation in the recent past. The excess absorption then seems to decay away as galaxies migrate further toward the center of the cluster.

Figure 3.8 confirms that the fraction of early types with strong Balmer absorption rises dramatically for galaxies in the transition region, and stays high even in the cluster core. Since so few early types in the periphery show similarly high Balmer absorption, there is likely an interaction with the cluster environment that triggers both the enhanced [O II] emission and the longer-lived Balmer absorption that we observe. We will discuss the possible link between these two populations of E+S0s in more detail in §3.5. Another possibility, that spiral galaxies are being transformed into new E or S0 galaxies within the virial radius, is addressed in Chapter 6.

We additionally searched for environmental trends in the metal line indices Mg_2 , Mg^b , and $[MgFe]'$, but detect no significant trends. In contrast with the correlation between, e.g., $[MgFe]'$ and σ , it seems that the overall metallicity of early-type galaxies is not dependent on environment, but mainly on the galaxy's formation history, as traced by σ . While the highest values of $[MgFe]'$ that we measure tend to be seen in galaxies within the virial radius, this is simply a reflection of the fact that most of the massive cluster galaxies with highest velocity dispersion are also located in the cluster core.

3.4.2.3 Residual Correlations

In addition to the environmental trends in spectral line strengths discussed above, we can probe environmental effects on the early-type population even more sensitively by examining the residuals from the $[MgFe]'$ - σ and Balmer- σ relations presented in §3.4.1. In Figure 3.9, we plot $\Delta[MgFe]'$ and $\Delta(H\delta+H\gamma)$ versus projected radius. Similar to what we saw in Figure 3.5, we see a population of galaxies with enhanced Balmer absorption within the virial radius at 1.7 Mpc. In this plot, though, we are able to remove the effects of galaxy mass by looking, in effect, at galaxies that have excess Balmer absorption *compared to other galaxies at the same velocity dispersion*. This is clear evidence, then, that the observed Balmer excess is an environmental effect, and not simply due to a dual correlation between line strength-mass and mass-cluster radius.

In the top panel of Figure 3.9, where we plot $\Delta[MgFe]'$, galaxies that also exhibit

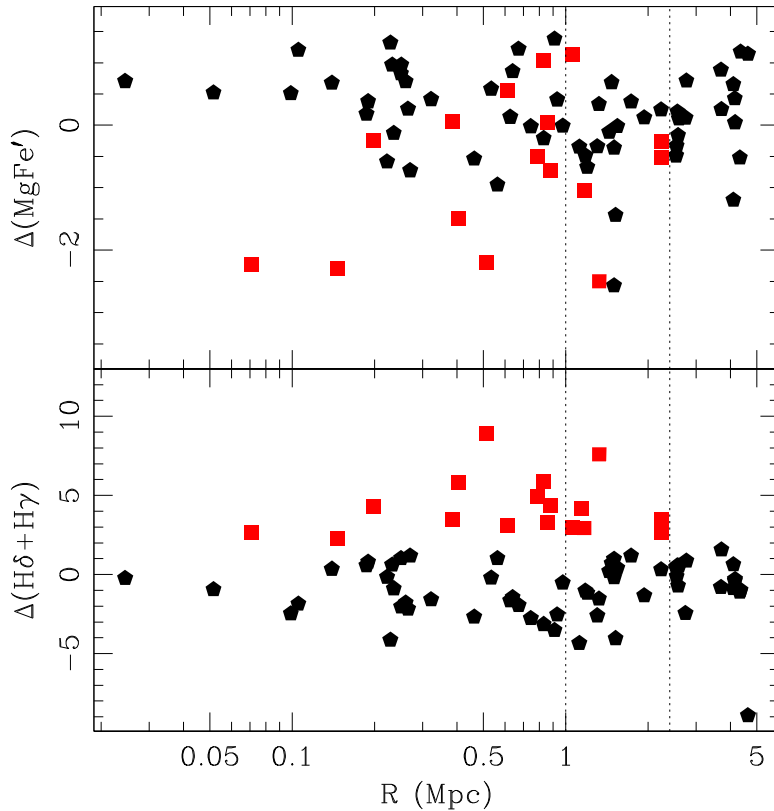


Figure 3.9 Residuals from the $[\text{MgFe}]' - \sigma$ and $(\text{H}\delta + \text{H}\gamma) - \sigma$ relations. The interaction with the environment has spurred increased star formation within the virial radius. Galaxies that lie above ~ 2 in the bottom panel have Balmer absorption that is unexpectedly strong for their velocity dispersion. Similarly, galaxies with $\Delta[\text{MgFe}]'$ below -1 are showing unexpectedly weak metal lines. In both panels, galaxies with $\Delta(\text{H}\delta + \text{H}\gamma) > 2.0$ are marked with red squares.

$\Delta(\text{H}\delta + \text{H}\gamma) > 2\text{\AA}$ are marked with red squares. Virtually all of the galaxies with anomalously low $[\text{MgFe}]'$, which we made note of in Figure 3.3, belong to this population of Balmer-strong galaxies. For the first 1 Gyr after a burst of star formation, we would in fact expect that the A-stars causing the enhanced Balmer absorption would also tend to fill the metal absorption lines with emission, as these lines are much weaker in A-stars than they are in the older stars making up the bulk of the stellar population. In fact, Tantaló & Chiosi (2004) suggests that a young stellar population has just this effect: $[\text{MgFe}]'$ is very low for mean ages less than 2 Gyrs, while $\text{H}\beta$, and presumably the other Balmer indices are enhanced.

We find no evidence that any of Mg_2 , Mg^b , $[\text{O II}]$, or any Balmer lines are correlated with the residuals from the FP, $\Delta \log(M/L_V)$. Nor is there evidence that the residuals from any of the $\text{Mg}-\sigma$, or Balmer- σ relations are correlated with $\Delta \log(M/L_V)$. This indicates that recent perturbations to the stellar population of an early type are somewhat decoupled from its overall mass to light ratio. While the FP, $[\text{MgFe}]'-\sigma$, and Balmer- σ relations establish a clear link between the formation histories of E+S0s and their current appearance, the lack of correlation between residuals indicates that environmental effects play a relatively minor role in determining M/L_V . The initial time of formation and mass-assembly history seem to be the dominant factors.

3.4.3 Luminosity Trends

Figure 3.8 reveals that there is a luminosity trend in the fraction of E+S0 galaxies with $\text{EW}([\text{O II}]) < -5$, as well as the fraction with enhanced Balmer absorption. For the brightest galaxies, $I < 20.3$, the fraction of $[\text{O II}]$ -emitters decreases monotonically, from the field measurement of Treu et al. (2002) to the cluster core. However, when we include slightly dimmer galaxies, to $I = 21.1$, we see an enhanced fraction of emitters in the cluster periphery, though $[\text{O II}]$ emission is still rare within 2.4 Mpc. Now including our full sample to $I = 22.5$, the fraction of star-forming galaxies in both the transition region and periphery are higher than expected. In the transition region, the jump represents the addition of the dim but strongly emitting galaxies discussed above (which have a mean magnitude of $I = 21.1$). The overall trend suggests that the star formation observed in the outskirts of this cluster is suppressed earliest in the largest and brightest E+S0s.

A similar trend is seen in the fraction of early types with $(\text{H}\delta + \text{H}\gamma) > -2\text{\AA}$. As discussed above, we see a jump at all luminosities in the fraction of Balmer-strong galaxies within the virial radius, possibly due to the same mechanism that causes the enhanced $[\text{O II}]$ emission. But within each radial zone, the fraction of galaxies with prominent Balmer absorption increases with increasing magnitude; the mean magnitude of all such Balmer-strong early types is $I = 20.3$. However, unlike

[O II], which probes current star formation only, the Balmer lines are also sensitive to the stellar population age. This gradient in Balmer strength with luminosity could simply reflect an earlier formation time for the brightest galaxies, regardless of local environment.

The brightest galaxies in our sample ($I < 20.3$) follow the FP and show few signs of star formation. Similarly, galaxies to $I = 21.1$ lie on the FP (albeit with a high scatter) and exhibit star formation mainly in the periphery. Perhaps star formation is quenched early during infall of these galaxies, with mostly passive luminosity evolution from that point. Because the dimmest galaxies seem to undergo the most prominent bursts of star formation (though AGN activity has yet to be ruled out), it seems that the physical mechanism responsible affects smaller galaxies more dramatically than larger galaxies. Of course, the elevated fraction of galaxies with strong Balmer absorption demonstrates that early types of all luminosities are affected to some degree. When evaluating the physical mechanisms that lead to the observed environmental evolution, we must also consider this dependence on luminosity.

3.5 Discussion

Having presented our results in the previous section, we now proceed to a more comprehensive discussion of our findings trying to put together the various pieces of information and reconstruct the evolutionary process, its timescales and the physical mechanisms driving it. First, in §3.5.1, we will combine the radial trends obtained so far and discuss them jointly. Then, in §3.5.2 we will present a simple infall model which indicates that a common physical mechanism may cause several of the radial trends seen in various subpopulations of E+S0s. In §3.5.3 we discuss the physical mechanisms at work and conclude that our study of early-type galaxies has revealed the action of at least two different environmental processes: starvation and/or galaxy harassment is quenching low-level star formation over a long timescale in early types beyond the cluster core, while harassment and/or interactions with shocks in the outer parts of the ICM are producing the sudden bursts of star formation observed

in small E+S0s around the virial radius.

3.5.1 Radial Trends and Star-Formation Timescales

In the residuals from the Fundamental Plane, we have observed a gradient in the mean mass to light ratios of E+S0s, allowing us to observe the transition from the oldest, highest M/L_V galaxies in the cluster core, to the galaxies in the cluster periphery with younger luminosity-weighted ages, nearly matching the values of M/L_B seen in field E+S0s (Treu et al. 2001a, 2005b; van der Wel et al. 2005). The scatter in the FP residuals is unexpectedly high within the inner 1 Mpc of the cluster, but the FP appears tighter outside of this radius. Direct measurements of spectral line strengths (Figure 3.5) and the fraction of [O II]-emitting early types (Figure 3.8) both reveal a mildly declining star-formation rate within early types, from the field toward the cluster core. This is interrupted by an interaction at the virial radius that causes enhanced [O II] emission in a population of small, dim early types, along with enhanced Balmer absorption and depressed [MgFe]' absorption strength for a population of larger, typical cluster E+S0s.

In Figure 3.10, we combine the previously shown radial trends in $\Delta \log(M/L_V)$, $\Delta(MgFe')$, $\Delta(H\gamma+H\delta)$, and $EW([O II])$ into a single plot. As in Figure 3.9, in the top three panels we indicate every galaxy exhibiting high Balmer absorption with a red mark. Likewise, all galaxies with significant [O II] emission in the bottom panel are plotted with open symbols in each panel. While the galaxies with unexpectedly low [MgFe]' correlate with the Balmer-strong galaxies, as mentioned in §3.4 above, there is no similar correlation with $\Delta \log(M/L_V)$. We see some Balmer-strong galaxies at both low and high M/L_V , which indicates that the star formation causing the enhanced Balmer line strengths does not drive the variations in M/L_V that we observe; the bursts of star formation are perhaps too minor to affect the overall M/L_V of the galaxy, at least to levels detectable in our data.

Briefly, we recap the characteristic timescales for changes in each of the quantities plotted. [O II] emission traces the instantaneous rate of star formation, so that the

observed strong [O II] emitters mark the location of a “hot spot” of current star formation at 1.7 Mpc radius (though we emphasize that these objects are not spatially clustered). Enhanced Balmer absorption will persist for about 1 Gyr after a burst of star formation, and so there is a time lag of <1 Gyr between the termination of star formation in these galaxies and the time when we observe them. Changes in M/L_V should persist for a similar amount of time after a recent burst of star formation (until the luminous A-stars begin to disappear), though we expect that M/L_V is less sensitive to low-level star formation because it depends more closely on the integrated stellar light of the galaxy, which changes by a smaller amount than the strong spectral lines.

3.5.2 A Simple Infall Model

We have so far presented evidence for a seemingly abrupt encounter with the environment that triggers star formation in early types at or near the virial radius, along with a moderate decline in star formation from the periphery to the core, and a trend in M/L_V that suggests that the stellar populations of early types at larger radius are younger. In this section we present a simple infall model as a tool to compare the timescales and strengths of several of the observed features in the early-type population. Specifically, we wish to examine the possibility that both the galaxies with strong [O II] emission and those with excess Balmer absorption could be caused by a common physical process. And while we have shown in §3.5.1 that the FP residuals, $\Delta \log(M/L_V)$, do not correlate with the Balmer-strong galaxies, we will also use this simple infall model to constrain the level of variation in M/L_V that could be induced by the environment.

In this idealized model, we follow an early-type galaxy as it proceeds toward the cluster center evolving passively, until it reaches the virial radius where it undergoes a short burst of star formation (adding 1% to the total stellar mass, 200 Myrs of duration). After the burst, the galaxy continues its infall evolving passively. For this model we use the prescription of T03 to convert from infall time to cluster projected

radius: assuming that the galaxy is on its first infall toward the cluster, it begins with a small velocity at $R = 5$ Mpc and accelerates freely toward the cluster potential.

The observable properties of this model are then computed using stellar population synthesis models by Bruzual & Charlot (2003) to compare with observations. Although this is clearly a simplified model—for example it neglects “backsplash” (Gill et al. 2005; Ellingson 2004), i.e., the fact that especially in the cluster center, and even out to two virial radii, some galaxies might not be on their first approach toward the cluster (see discussion in T03), and it is a closed boxed model, i.e., there is no provision for galaxies being transformed into E+S0s during the infall (but see Chapter 6)—we will show that this model reproduces the strengths and timescales of many of the observed features and provides useful guidance to interpret the observations.

The predictions of the model are shown as a dashed line in Figure 3.10. Specifically, we plot the difference in $\Delta \log(M/L_V)$, $\Delta(MgFe')$, $\Delta(H\gamma+H\delta)$, and star-formation rate (SFR) between the infalling model galaxy and an identical model without the starburst. Since we are interested only in the predicted change in line strengths due to a recent star-formation event, the proper quantity to plot is this difference between the index strengths predicted by the passive model and the one with a small starburst overlaid. We emphasize that the model track for $\Delta \log(M/L_V)$ is meant to replicate only the change in M/L_V caused by a small starburst, and does not account for the radial gradient in $\Delta \langle \log(M/L_V) \rangle$ seen in the data.

To calibrate the star-formation rates predicted by the models to the [O II] equivalent widths observed, we used SFRs derived by Kodama et al. (2004, and private communication) from their deep H α images, according to the procedure outlined in §3.3.4.

The choice of a 1% starburst produces a SFR and [O II] equivalent width equal to that observed in the largest/brightest of our low-luminosity [O II] emitting galaxies, which we estimate to have a stellar mass up to around $5 \times 10^{10} M_\odot$ (see § 3.3.4). The 200 Myr timescale approximately matches the spread in cluster radius over which we see these [O II] emitters. The stellar mass associated with the starburst could vary with galaxy size and need not add up to 1% of the galaxy mass. For our [O II]

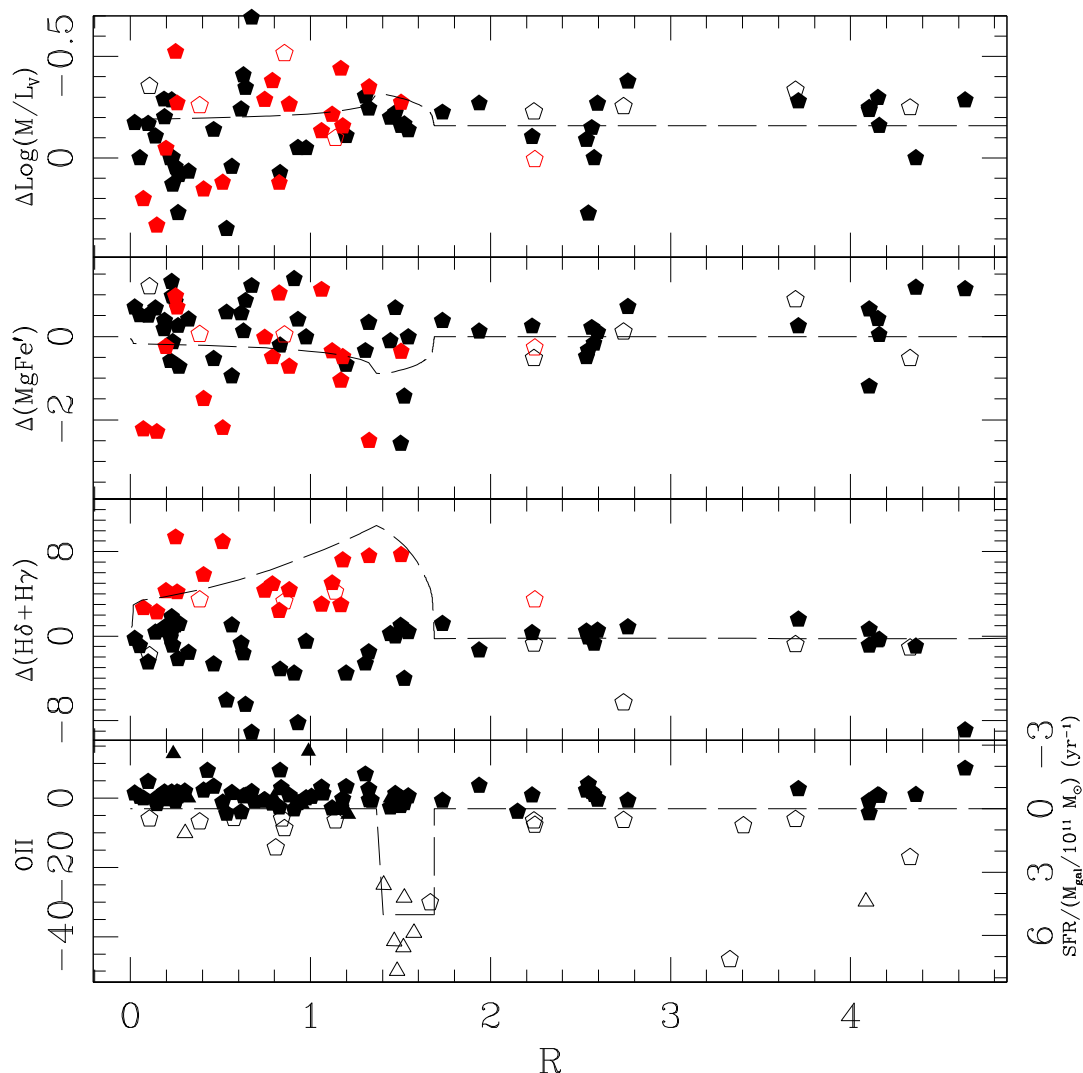


Figure 3.10 Radial trends in the residuals of dynamical relations. From top to bottom, $\Delta \log (M/L_V)$, $\Delta ([\text{MgFe}]')$, $\Delta (H\delta + H\gamma)$, and $[\text{O II}]$ vs. R for reference. Galaxies brighter than $I = 21.1$ are marked with pentagons, and triangles represent galaxies in the range $21.1 < I \leq 22.5$. In the top three panels, we indicate every galaxy exhibiting high Balmer absorption ($\Delta (H\delta + H\gamma) > 2\text{\AA}$) with a red mark. Likewise, all galaxies with $[\text{O II}] < -5\text{\AA}$ in the bottom panel are plotted with open symbols in each panel. Overplotted on each plot is the track of a simple early-type galaxy model, as the galaxy falls freely from the outskirts of the cluster, and has an encounter at the virial radius which triggers a starburst of duration 200 Myr, totaling 1% of the galaxy's mass.

emitters, the luminosities and equivalent widths imply that up to a 5% burst could be involved, depending on its duration. However, 1% represents a good upper limit for the larger galaxies with enhanced Balmer absorption, as we would otherwise expect to observe “poststarburst” k+a spectra; the excess Balmer absorption is not strong enough to place any in this category.

Examining the track of the model in Figure 3.10, it is remarkable how well the expected change in Balmer line strength matches the observations in both maximum strength and in the time it takes this enhanced absorption to decay away. This lends strength to our contention that the enhanced Balmer absorption and the high [O II] emission are reflections of the same physical process.

We also observe a dip in the strength of [MgFe]’ just where we would expect it, though the magnitude of this dip does not seem great enough to account for the observed [MgFe]’ decrement. This may simply be a deficiency in the Bruzual & Charlot (2003) models, as the observed values of [MgFe]’ span a larger range than could be predicted by the models at any SSP age or metallicity. In contrast, the models easily account for the full range of observed Balmer line strengths. Therefore, changes in [MgFe]’ due to a small starburst could be under predicted by the Bruzual & Charlot (2003) models.

We note that the population of [O II] emitters observed cannot evolve directly into the population of galaxies with strong Balmer lines, though they could still be indicators of the same physical mechanism. The Balmer-strong E+S0s are brighter and larger in effective radius, and any fading of the [O II] emitters would only increase the difference between these populations. Since they are near our spectroscopic magnitude limit, we would not expect to observe faded remnants of the [O II] emitting galaxies. On the other hand, the lack of bright early types with strong [O II] emission might arise because the timescale for the Balmer lines to decay (1 Gyr) exceeds the starburst timescale (200 Myr), so that we would not expect to observe more than one of the emission line progenitors of these Balmer-strong galaxies. This is partly due to the overall smaller number of bright E+S0s observed within the transition region (1–2.4 Mpc), in comparison to the ~ 50 observed in the cluster core.

To further examine our hypothesis that the [O II]-emitting and Balmer-strong galaxies are caused by the same environmental interaction during infall, we can examine the 2D spatial distribution of these galaxies. In Figure 3.11, we plot [O II] emitters in blue and early types with strong Balmer absorption in red, on top of the overall distribution of cluster members from the combined spectroscopic and photometric redshift catalogs. The [O II]emitters and Balmer absorbers follow the overall distribution of cluster members closely, lying mostly along the major axis of the cluster (stretching from the overdensity NW of the cluster core through to the SE side of the core). Though the [O II]-strong galaxies perhaps extend in a larger arc at ~ 1.7 Mpc, their small number makes it difficult to determine their azimuthal distribution. The distribution supports the idea that they have been perturbed during infall, as this is most likely occurring predominantly along the NW to SE path.

Turning to the top panel in Figure 3.10, it seems that the small starbursts at the virial radius cannot alter the overall M/L_V of early types by a large enough amount to account for the large scatter that we see in the cluster core. It seems that there must simply exist a mix of older, high M/L_V galaxies and more recently arrived low M/L_V galaxies in this region. On the other hand, the triggered star formation may help prolong the length of time that an infalling E+S0 remains at low M/L_V after reaching the cluster core. This could possibly explain why the scatter in M/L_V seen in this cluster is so much higher than that observed in Cl 1358+62 at $z = 0.33$ (Kelson et al. 2000b); the mechanism causing this star formation in Cl 0024 might not be active or significant in all clusters at this redshift. An alternative explanation, that these newly arrived E+S0 galaxies were once star-forming spirals before conversion, will be investigated in Chapter 6.

While the simple model presented here does not attempt to account for the observed radial gradient in M/L_V , we note that the difference in $\log(M/L_V)$ between a galaxy at 5 Mpc radius, of age 2.7 Gyr, and that same galaxy 5 Gyr later (corresponding to the total free-fall time to the cluster center), is equal to -0.35 . This is nearly identical to the observed difference in $\log(M/L_V)$ between the mean value in the periphery, and the M/L_V of the oldest galaxies in the core. While the galaxies

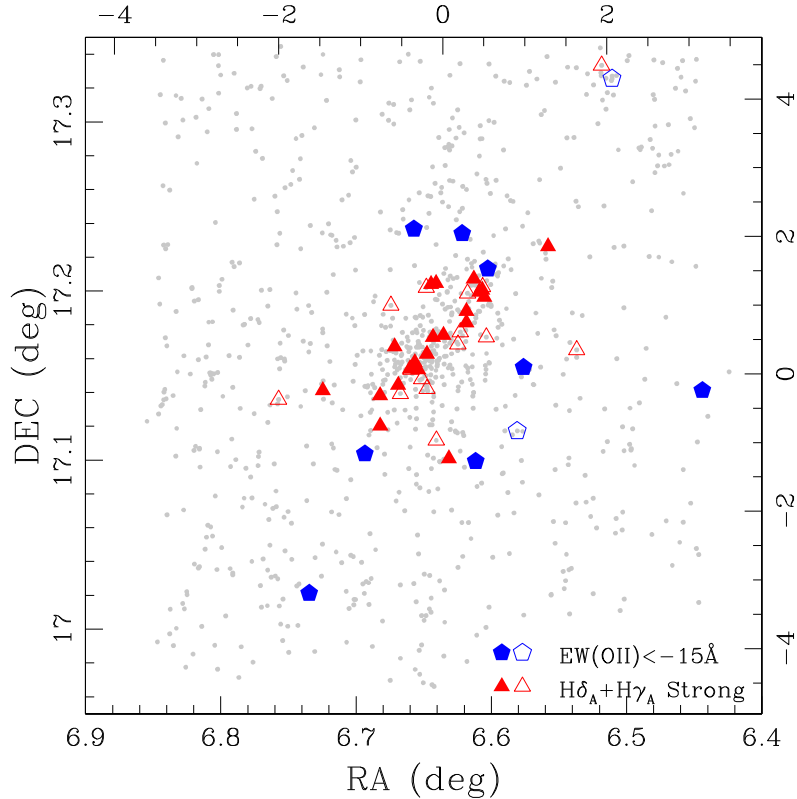


Figure 3.11 Spatial distribution of [O II] emitters and galaxies with excess Balmer absorption, in comparison to the overall distribution of cluster members in the combined spectroscopic and photometric (Smith et al. 2005b) redshift catalog (gray dots). Blue pentagons are strong [O II] emitters, with two open symbols marking the merger system and possible spiral interloper seen in Figure 3.6. Filled red triangles mark galaxies where the Balmer- σ residuals are $\Delta(H\delta + H\gamma) > 2\text{\AA}$, and unfilled triangles represent galaxies without measured velocity dispersions, with $EW(H\delta_A + H\gamma_A) > -2\text{\AA}$. Top and right axes show projected radius from the cluster center, in Mpc.

in the periphery are almost certainly not this young, the observed gradient in M/L_V seems consistent with a difference in formation age (or in time since the last major burst, cf. Bower et al. 1998 and Treu et al. 2005b) of a few Gyr between cluster periphery and core. A gradient in formation age, then, is a viable explanation for the M/L_V gradient we observe, though the gradual decline in star formation that we observe could also be important in generating the M/L_V gradient.

Having suggested that the observed spectral features of our early-type sample are due to a small starburst, it is natural to ask if such a burst is realistic; in other words, do E+S0s at redshift of ~ 0.4 contain enough residual gas to undergo such episodes

of star formation? According to Bettoni et al. (2003), the fraction of molecular gas detected in local “normal” early-type galaxies (i.e. showing no signs of current or recent interaction or dwarf cannibalism, but otherwise selected across all local environments), can approach 1% of the total stellar mass (with typical values ranging from 0.05 to 0.5%). At intermediate redshifts, some field E+S0s have peculiar color gradients that may indicate recent star formation (e.g., Menanteau et al. 2004). Allowing for the possibility of faint, undetected interaction features in our much more distant sample, as well as the expected decrease in the remnant molecular gas in ellipticals since $z = 0.4$, we expect that a small burst of star formation of up to 1% is entirely plausible for early-type galaxies in Cl 0024. Additional evidence comes from the observation (e.g., Treu et al. 2005b; Bressan et al. 1996) that the combinations of spectral line strengths observed in early-type galaxies are best explained if most early types have undergone secondary episodes of star formation at some point in their past; the Balmer-strong galaxies observed here could possibly have undergone such secondary bursts in the last 1 Gyr.

3.5.3 Physical Mechanisms

The early-type galaxies in Cl 0024 have proven to be effective signposts for identifying two possible forms of environmental evolution in this cluster, but can we identify the physical processes responsible? We observe a slow decline in remnant star formation from the field/periphery to the core which may indicate a physical mechanism at work which slowly quenches star formation. Seemingly overlaid on top of this mild trend is a nearly instantaneous interaction that triggers a small burst of star formation in many of these early-type galaxies at the virial radius.

First, we address physical mechanisms that could be responsible for the gradual decline in star-formation rate toward the cluster core, best illustrated in Figure 3.8. In analyzing the cause of the observed decline, we must also consider the morphology–density (T– Σ) relation observed in Cl 0024. In T03, it was argued that the existence of the T– Σ relation across several orders of magnitude in projected local density

indicates that whatever process causes the morphological segregation of galaxies by environment, it acts slowly. The slow “starvation” (Chapter 1) of galaxies during infall is consistent with the existence of the T– Σ relation, as is the action of galaxy harassment (Moore et al. 1996, 1999; Moore, Lake & Katz 1998).

Starvation encompasses several physical mechanisms that serve to slowly deprive a galaxy of cold gas available for star formation. For example, thermal evaporation of the galaxy interstellar medium (ISM) by interaction with the hot cluster ICM (Cowie & Songaila 1977), or turbulent and viscous stripping of the ISM (Nulsen 1982; Toniazzo & Schindler 2001) are two possible causes of starvation. The version of starvation proposed by Larson et al. (1980) and modeled by Bekki et al. (2002), which involves stripping of the halo reservoir of gas, is especially attractive because it also predicts a slow conversion of spiral galaxies to S0 after star formation stops. Any process in this family could be acting in Cl 0024, and would be consistent with both the observed gradient in star-formation rate and the existence of the T– Σ relation.

Kodama et al. (2004), however, argue that the truncation of star formation in cluster galaxies must be rapid, based on their observation that the H α luminosity function does not vary with environment. Both our work and theirs find a similar decline in the *fraction* of star-forming galaxies, but they do not observe a decline in the mean strength of emission. The discrepancy may be due to the different levels of star formation probed: the low levels of remnant star formation in the early-type population discussed here may be quenched slowly, while a separate physical process (such as harassment) could rapidly decrease the moderate star formation observed by Kodama et al. (2004), which occurs mostly in the spiral population. Combined with a longer timescale for morphological transformation, this could lead to the “passive spirals” they discuss. (See also Chapters 5 and 6.)

T03 also argued that the existence of the T– Σ relation means that the morphological mix is set by the precluster environment: the overall formation history within assembling groups is the dominant factor in determining the morphological mix seen in the cluster. This view is consistent with the trend we observe in the M/L_V ratios of cluster early types. We find that the differences in M/L_V must arise partially out

of variations in the mass-assembly history of early-type galaxies, though the radial trend in $\langle \log(M/L_V) \rangle$ may also reflect the quenching of remnant star formation during infall.

Interrupting the slow decline in star formation are the small bursts of star formation we observe. Rapidly acting mechanisms that could trigger such a burst include galaxy harassment or some encounter with the ICM. As noted in §3.4, major mergers are unlikely because the galaxies seem to be in low density regions, and all but one of the galaxies involved show no visual evidence for such a disturbance. However, the merger hypothesis will be reconsidered in Chapter 6 in light of the results presented there.

Galaxy harassment becomes important near the virial radius as both galaxy crowding and the typical velocity of an interaction become high enough. (See Chapter 1, T03.) Further, it is a rapid interaction, and the galaxy that triggers one of our observed starbursts can quickly move away from the vicinity of the starburst galaxy. Moore et al. (1999) present simulations of the harassment of small Sc/Sd spiral galaxies as they fall into the cluster. Such galaxies can be quickly transformed into objects that appear to have an early-type morphology. These harassment remnants are small objects ($R_e = 1 - 3$ kpc), similar to our observed [O II] emitters, and could represent the origin of the large population of dwarf spheroidals observed in clusters today. In addition, Moore et al. (1999) predict that harassment would drive the gas within a spiral toward the galaxy's center, thus providing a natural mechanism for fueling the starbursts (or AGN) we observe.

If these are the remnants of harassed spirals, they may not be on their first infall into the cluster; the timescale for passage from the cluster core back out to the virial radius may be short enough (< 1 Gyr) that star formation induced by interactions with large ellipticals in the cluster center could still be visible. A possible explanation, then, for finding them preferentially at the virial radius could be that this is near the apse of their orbit within the cluster.

Under the harassment scenario, we speculate that the population of Balmer-strong galaxies could represent the large cluster ellipticals which cause the harassment, per-

haps cannibalizing young stars from smaller harassed galaxies. Alternatively, they could be undergoing harassment themselves, albeit with a much smaller gas reservoir and a correspondingly smaller episode of star formation.

Ram-pressure stripping or triggering of star formation has been thought to be effective only much closer to the cluster core, and should not be significant near the virial radius where the environmental interaction is taking place. However, recent work on large-scale shocks and particularly the virial shock—the shock boundary between the hot, dense ICM and the colder, diffuse infalling gas from outside the cluster—suggests that a galaxy passing through this shock boundary could be given enough of an impulse to trigger stripping of HI gas and the collapse of any molecular clouds (Evrard 1991; Quilis et al. 2000; Ryu et al. 2003; Furlanetto & Loeb 2004). Particularly relevant to Cl 0024 is the work by Roettiger et al. (1996). They showed that a merger between two clusters or subcluster clumps can cause powerful shocks to propagate through the ICM. As the redshift distribution of galaxies in Cl 0024 is double peaked (Czoske et al. 2002), indicating a large infalling group or subcluster, such strong shocks could be responsible for the triggered starbursts we observe. If this is the case, we would not expect to see such bursts in other clusters with more regular structure.

Our sample of 104 E+S0s contains only four galaxies from the smaller Peak B of the redshift distribution in Cl 0024 (Figure 2.8), so we are unable to more carefully explore possible differences between early-type galaxies in these two peaks. But in the local universe, Poggianti et al. (2004) finds a population of star-forming dwarf galaxies that lie along contours in the X-ray substructure of the Coma cluster. It is possible that the [O II] emitters in Cl 0024 lie along similar boundaries in the cluster substructure, but the nearly face-on orientation of the merger between Peak A and Peak B makes testing this hypothesis difficult. In this scenario, the existence of Balmer-strong galaxies interior to the virial radius would imply that some sort of boundary shock between Peak A and Peak B has persisted for at least ~ 1 Gyr, the timescale for the excess Balmer absorption to decay away.

Our small population of strong [O II] emitters is a signpost to an important phys-

ical interaction, and is not a peculiarity unique to this cluster. A similar population of dim, compact, E+S0s with [O II] emission has also been reported by Homeier et al. (2005), for a galaxy cluster at $z = 0.84$. While the cluster they study is not virialized, the [O II] emitters they observe seem to reside in a region outside of the contours of the cluster X-ray emission. And work by Ruderman & Ebeling (2005) examining the radial distribution of X-ray point sources in the MACS sample of clusters has uncovered a prominent spike in the number of cluster AGN detected in the area around the virial radius (~ 2.5 Mpc in the clusters studied). These AGN may be stimulated by the cluster environment via the same physical mechanism causing the [O II]-strong early types. Therefore, even though they only represent a small fraction of the total mass and star formation in clusters, these galaxies warrant further study of their role as indicators of environmental interaction (see Chapter 6).

While the exact physical mechanisms responsible for the environmental evolution are still not known, further work on this cluster, as well as the complementary cluster MS 0451–03 ($z = 0.54$) may allow us to determine which processes are dominant. Analyzing the star-formation rates and rotation curves of spirals (Chapter 4) may help us trace the gradual decline in star-formation rate hinted at here, as star formation in spirals is in general much more vigorous than in the early types studied so far. Other authors have found similar declines in the star-formation rate in spiral populations of clusters at intermediate redshift (Abraham et al. 1996b; Balogh et al. 1999, 2000). Rotation curves have also been used to study variations in the kinematics and mass to light ratios of spirals, in distant clusters by, e.g., Bamford et al. (2005); Ziegler et al. (2003); Milvang-Jensen et al. (2003), and in Cl 0024 by Metevier & Koo (2004).

Likewise, the X-ray luminosity of MS 0451 is much higher than that of Cl 0024. If shocks in the ICM really do cause the bursts of star formation observed in early types near the virial radius, then we should see a similar or even stronger effect in MS 0451, but at a higher radius. If the strength of the ICM shocks in Cl 0024 is enhanced by the subcluster merger, however, we might expect to see no starbursting early types at all in MS 0451. The importance of galaxy harassment should be nearly the same between the two clusters, so we would expect to see similarly strong starbursts in

MS 0451 if the Cl 0024 bursts are due to harassment (Chapter 6).

3.6 Summary

In this chapter we have presented the results of an extensive spectroscopic survey of the cluster Cl 0024+1654, undertaken primarily with DEIMOS on Keck II. We examine the detailed spectral and photometric properties of cluster early types across an area 10 Mpc in diameter. The principal goal of this wide area survey is to examine variations in galaxy properties with local environment, in order to identify the physical processes that may affect the star-formation properties or morphological characteristics of infalling galaxies. In this chapter, we have used the early-type galaxy population as sensitive indicators of interaction with the cluster environment. Our main observational results are:

(1) By constructing the Fundamental Plane of Cl 0024, we observe that E+S0s at $z \sim 0.4$ still have old stellar populations; from a comparison with the FP of the Coma cluster ($z \sim 0.02$), we infer an evolution in mass to light ratio of $\Delta(\log(M/L_V)) = -0.14 \pm 0.02$. While the mean change in M/L_V is in line with that expected by passive evolution of an old stellar population, the high scatter of 40% in M/L_V suggests a more complex assembly history for this cluster. The high scatter may be an effect of the cluster merger currently underway (Czoske et al. 2002), though at least one other intermediate redshift cluster (Wuyts et al. 2004) exhibits a similarly high scatter.

(2) We observe radial trends in the mass to light ratios of individual early types, with the oldest galaxies located in the cluster core ($\langle \Delta \log(M/L_V) \rangle_{R < 1 Mpc} = -0.13 \pm 0.04$). Galaxies seem to be younger at higher radius, with E+S0s in the cluster periphery ($\langle \Delta \log(M/L_V) \rangle_{R > 2.4 Mpc} = -0.24 \pm 0.02$) nearly matching the values of M/L_V seen in the field at this redshift (Treu et al. 2005b). We therefore have bridged the gap between the observed properties of cluster and field early types at intermediate redshift. Similar trends are seen as a function of local density. Some fraction of this radial gradient could be caused by the “downsizing” effect described

by, e.g., Treu et al. (2005b); Holden et al. (2005); van der Wel et al. (2005). But even when we select a subsample of galaxies within a narrow range of galaxy mass ($10.9 < \log(M/M_\odot) \leq 11.4$), we observe a significant difference in age (or time since the latest burst) between galaxies in the cluster periphery and core, equivalent to $\delta < \log(M/L_V) \geq 0.13 \pm 0.07$. Physically, this trend could be explained by some combination of a gradient in formation age and variations in recent star formation, perhaps modulated by “starvation”.

(3) Around the virial radius, we observe a number of small galaxies undergoing a burst of star formation, indicated by strong [O II] emission. Further, we observe enhanced Balmer absorption for many galaxies interior to this radius. This is consistent with an infall scenario where, after a starburst, Balmer absorption from young stars decays away over the course of ~ 1 Gyr, as the galaxy continues toward the cluster core. The radial distribution of enhanced-Balmer E+S0s is consistent with the expected infall timescale of such galaxies. Galaxy mergers are not expected to be the source of this enhanced activity; the [O II] emitters reside in relatively low density regions, and do not appear to reside in groups. The small starbursts are likely caused by a rapidly acting physical process: possibilities include galaxy harassment and shocks in the ICM, perhaps generated by the subcluster merger in Cl 0024.

(4) While the overall early type population is older in the cluster core than in the outskirts, we see trends with luminosity that indicate that smaller early types have more active star formation than larger ones. This seems to confirm evidence for downsizing seen by Treu et al. (2005a), and indicates that galaxy mass is a primary indicator of star-formation activity, even as environmental effects work on top of this to produce radial variations in star formation. Both of these ultimately serve to decrease star formation toward the highest density regions, though the precise link to morphological transformation is still unclear because of the different timescales involved.

We have uncovered environmental processes working on cluster early types, but we have also seen variations in galaxy properties across the cluster that indicate that

both galaxy mass and environment of initial formation are important in determining the overall assembly history of early-type galaxies.

By obtaining high-quality spectra of cluster members across a large area around Cl 0024, and combining with a panoramic *HST* mosaic, we have been able to uncover physical mechanisms at work that never would have been seen if we only looked at the cluster core. This underscores the importance of looking wide as well as far when attempting to understand how galaxies evolve within the large scale structure of the universe.

Acknowledgements We thank Michael Cooper and Jeffery Newman for help with the DEIMOS data reduction pipeline, F. Owen, A. Metevier, and D. Koo for sharing redshifts, T. Kodama for allowing us access to $H\alpha$ equivalent widths and star-formation rates from their survey, and J. Richard for assisting with DEIMOS observations in 2003. We thank M. Balogh, E. Ellingson, B. Holden, B. Poggianti, A. Babul and A. van der Wel for valuable discussions.

Table 3.2: Listing of observed E+S0 cluster members

Object	α ($^{\circ}$)	δ ($^{\circ}$)	z	F814W (mag)	R (Mpc)	Σ_{10} (Mpc^{-2})	Morph
p0i102c3	6.65796	17.16050	0.3897	19.42	0.14	255	S0
p0i139c3	6.66004	17.16630	0.3974	20.15	0.19	300	E/S0
p0i15c3	6.64000	17.15560	0.3984	19.84	0.27	195	S0
p0i170c3	6.64412	17.17120	0.3931	19.24	0.22	214	E
p0i1c3	6.65400	17.15350	0.3940	20.23	0.20	257	E/S0
p0i1c4	6.66014	17.15402	0.3967	20.54	0.25	212	E
p0i206c3	6.64763	17.16280	0.3972	18.51	0.07	951	E
p0i209c3	6.64012	17.16750	0.3893	21.76	0.24	214	S0
p0i217c3	6.65629	17.16270	0.3912	20.18	0.10	254	E/S0
p0i24c2	6.65271	17.14714	0.3954	21.11	0.32	204	E/S0
p0i38c4	6.66325	17.15350	0.3860	20.36	0.30	244	S0
p0i39c3	6.64025	17.15860	0.3919	19.62	0.23	265	S0
p0i3c3	6.65633	17.15240	0.3915	19.64	0.24	255	S0
p0i42c3	6.65792	17.15610	0.3994	18.85	0.19	390	E
p0i45c2	6.65133	17.14800	0.3951	21.46	0.30	183	S0
p0i49c2	6.64896	17.14980	0.3946	19.26	0.27	200	S0
p0i4c4	6.65950	17.15350	0.3910	20.95	0.25	212	E
p0i53c4	6.67150	17.16720	0.3976	18.88	0.41	102	E
p0i55c2	6.64754	17.14220	0.3960	19.91	0.43	206	S0
p0i66c3	6.65321	17.15800	0.3843	20.01	0.11	372	S0
p0i72c3	6.64875	17.16200	0.3920	18.11	0.05	1024	E
p0i79c3	6.65000	17.16280	0.3883	17.75	0.02	637	E
p0i85c3	6.65663	17.15780	0.3943	19.02	0.15	339	E
p0i91c3	6.64575	17.17260	0.3887	19.57	0.23	151	E
p0i95c3	6.64313	17.17280	0.3876	18.77	0.26	274	E
p10i1c2	6.78233	17.18040	0.3967	18.66	2.59	14	S0
p11i147c4	6.72475	17.17760	0.3955	20.36	1.47	16	S0
p12i160c2	6.67425	17.19140	0.3951	20.40	0.74	44	E
p12i160c3	6.64088	17.20460	0.3955	19.79	0.88	88	E/S0
p12i168c4	6.65725	17.23670	0.3800	21.55	1.52	20	E/S0
p12i73c4	6.66853	17.23410	0.3962	20.14	1.50	22	S0
p13i130c3	6.62154	17.23410	0.3934	21.98	1.57	25	E/S0
p13i133c4	6.59632	17.20980	0.3967	21.42	1.45	57	E
p13i135c4	6.59546	17.20870	0.3965	18.61	1.44	56	S0
p13i1c4	6.60596	17.22300	0.3975	19.88	1.52	34	E
p13i25c2	6.58954	17.23660	0.3962	19.59	1.94	17	S0
p13i78c4	6.61300	17.20720	0.3973	18.93	1.18	109	E
p13i86c4	6.60258	17.21320	0.3929	22.27	1.41	60	E/S0
p14i2c2	6.55800	17.22640	0.3933	20.61	2.25	13	E

Table 3.2 – Continued

Object	α ($^{\circ}$)	δ ($^{\circ}$)	z	F814W (mag)	R (Mpc)	Σ_{10} (Mpc $^{-2}$)	Morph
p15i144c4	6.47717	17.27400	0.3967	19.99	4.10	7	S0
p17i2c4	6.75733	17.13590	0.3941	20.92	2.15	8	S0
p18i43c2	6.72658	17.14080	0.3925	19.01	1.54	31	E
p18i51c2	6.72458	17.14120	0.3933	19.87	1.50	26	E
p18i66c3	6.71600	17.14440	0.3934	19.98	1.32	26	E
p19i1c3	6.58353	17.17150	0.3939	20.48	1.34	18	E/S0
p19i75c4	6.60362	17.17270	0.3941	21.41	0.96	38	E/S0
p19i92c2	6.57613	17.15490	0.3811	21.15	1.48	22	E/S0
p20i35c4	6.53687	17.16520	0.3971	19.42	2.24	8	S0
p20i48c3	6.54025	17.18710	0.3921	20.12	2.23	7	E
p24i115c3	6.61158	17.09930	0.4082	21.65	1.52	19	S0
p24i1c3	6.63138	17.10100	0.3981	18.87	1.33	26	E/S0
p24i42c4	6.63029	17.11800	0.4018	20.64	1.01	42	E
p24i79c4	6.64067	17.11160	0.3927	20.64	1.07	35	E
p24i87c3	6.62296	17.10520	0.3972	19.32	1.30	26	S0
p25i29c3	6.57688	17.11700	0.3924	20.32	1.73	14	E
p25i93c3	6.58088	17.11730	0.3970	19.21	1.66	19	S0
p27i174c3	6.46279	17.14510	0.3978	19.06	3.71	5	S0
p27i9c2	6.44396	17.14130	0.3792	21.89	4.09	5	E/S0
p28i87c2	6.73458	17.02130	0.3950	20.64	3.33	9	E
p35i112c2	6.51850	17.33350	0.3833	20.12	4.36	21	S0
p35i143c2	6.49954	17.33630	0.3951	19.94	4.64	15	S0
p35i43c3	6.52433	17.32190	0.3927	19.13	4.10	33	E
p35i6c3	6.51429	17.31730	0.3946	18.85	4.15	23	E
p35i78c2	6.51071	17.32570	0.3931	19.23	4.33	21	S0
p35i82c3	6.52896	17.32850	0.3956	19.28	4.16	23	S0
p36i106c3	6.61754	17.19870	0.3970	22.05	0.99	72	S0
p36i146c3	6.60642	17.20250	0.3987	19.72	1.20	118	S0
p36i182c2	6.62129	17.17350	0.3959	19.28	0.63	169	S0
p36i182c3	6.60512	17.19650	0.3930	20.65	1.14	106	S0
p36i184c2	6.61846	17.18120	0.3955	19.19	0.75	114	S0
p36i187c3	6.60879	17.19940	0.3965	20.17	1.12	126	E/S0
p36i1c4	6.63014	17.20229	0.3907	19.45	0.91	77	E/S0
p36i2c2	6.63088	17.18210	0.3958	18.01	0.56	99	E
p36i2c3	6.61833	17.18800	0.3922	19.92	0.83	130	S0
p36i31c4	6.63221	17.20670	0.3905	18.73	0.97	123	E
p36i32c4	6.63254	17.19910	0.3916	20.14	0.83	117	S0
p36i34c2	6.63088	17.17420	0.3950	20.91	0.46	124	S0
p36i36c4	6.63254	17.19970	0.3949	20.96	0.84	121	E
p36i3c2	6.62933	17.18590	0.3931	20.22	0.64	105	E

Table 3.2 – Continued							
Object	α ($^{\circ}$)	δ ($^{\circ}$)	z	F814W (mag)	R (Mpc)	Σ_{10} (Mpc $^{-2}$)	Morph
p36i48c3	6.61658	17.19380	0.3934	19.74	0.93	103	S0
p36i5c2	6.63542	17.17390	0.3969	19.18	0.39	186	S0
p36i67c4	6.64803	17.20200	0.3951	20.87	0.81	65	E/S0
p36i70c4	6.64450	17.20400	0.3975	20.38	0.86	75	E
p36i71c3	6.60769	17.20461	0.3996	21.25	1.21	105	E/S0
p36i76c2	6.62469	17.16852	0.3959	20.29	0.53	151	S0
p36i76c3	6.60667	17.20060	0.3932	19.95	1.17	124	S0
p36i89c2	6.62292	17.17570	0.3977	19.97	0.62	154	S0
p37i110c2	6.68208	17.12020	0.3954	20.86	1.06	30	S0
p37i122c2	6.69346	17.10380	0.3918	21.69	1.47	16	E/S0
p37i16c4	6.68229	17.13830	0.3975	18.02	0.79	81	S0
p37i206c4	6.68004	17.14495	0.3965	20.44	0.67	87	E
p37i207c4	6.68607	17.14283	0.3953	21.47	0.80	146	S0
p37i64c4	6.66879	17.14430	0.3977	20.18	0.51	72	E/S0
p37i9c4	6.66721	17.13930	0.3999	20.81	0.57	60	S0
p38i1c4	6.62454	17.14090	0.4003	20.39	0.69	55	E
p38i76c4	6.62533	17.13030	0.3976	20.88	0.84	37	S0
p3i72c2	6.63067	17.32760	0.4007	20.67	3.40	7	S0
p5i9c3	6.74192	17.26600	0.3904	20.69	2.76	10	E/S0
p7i128c3	6.63150	17.28690	0.3934	19.85	2.57	72	S0
p7i133c3	6.63194	17.28540	0.3967	20.82	2.54	52	S0
p7i136c3	6.63197	17.28490	0.3960	19.93	2.53	52	S0
p7i1c2	6.60829	17.28990	0.3981	18.64	2.74	24	E
p7i67c3	6.62904	17.28590	0.3961	20.60	2.56	71	S0
p9i20c3	6.83968	17.16743	0.3953	19.01	3.69	9	S0

Object names are coded to indicate WFPC2 pointing, WFPC2 chip, and ID number for each object. For example, p0i102c3 refers to object number 102 on WFPC2 chip 3, from pointing 0. Right ascension (α) and declination (δ) are for epoch J2000. F814W magnitudes are corrected for galactic extinction, adopting $E(B - V) = 0.057$ (Schlegel et al. 1998). R and Σ_{10} denote, respectively, the projected radius and local density of each galaxy, calculated according to the method described in the text. Typical uncertainty in Σ_{10} is 25%, equal to the rms variation in the local density across different measurement methods. Errors in F814W magnitudes are less than 0.05 mag rms.

Table 3.3: All measurements of E+S0 members of Cl 0024

Object	[O II] (Å)	H δ_A (Å)	H γ_A (Å)	Mg ^b (Å)	Fe5270 (Å)	Fe5335 (Å)	σ_0 (km s ⁻¹)	$\langle\mu_V\rangle$ (mag '' ⁻²)	R_e ('')	S/N Å ⁻¹ Obs.
p0i102c3	-0.3	-0.1	-4.1	4.7	2.2	2.4	154 ± 10	21.13	1.3	23.4
p0i139c3	0.0	-0.4	-2.8	4.0	2.8	2.8	140. ± 7	18.85	0.3	16.7
p0i15c3	0.0	-3.2	-6.3	4.7	2.2	1.3	278 ± 26	20.30	0.7	12.3
p0i170c3	0.0	-1.3	-3.2	4.8	1.5	1.9	185 ± 13	—	—	26.6
p0i1c3	-0.3	3.3	-1.4	4.0	2.0	3.3	105 ± 19	20.61	0.5	6.9
p0i1c4	-0.5	0.5	-2.0	—	2.6	2.5	69 ± 10	19.72	0.4	11.9
p0i206c3	-0.1	0.0	-5.6	1.2	0.7	1.2	491 ± 22	19.87	1.2	19.9
p0i209c3	0.0	-5.0	-6.5	2.7	2.8	0.9	—	—	—	1.6
p0i217c3	0.0	-1.3	-5.6	4.2	2.3	1.9	144 ± 11	19.55	0.4	14.0
p0i24c2	0.0	0.0	-6.3	2.2	3.2	2.7	165 ± 24	18.97	0.2	8.2
p0i38c4	0.0	-0.6	-9.0	3.9	3.6	0.1	—	—	—	6.5
p0i39c3	0.0	0.3	-4.7	6.7	2.4	2.6	204 ± 22	20.20	0.8	16.3
p0i3c3	0.0	-2.5	-5.6	4.2	1.8	1.8	300. ± 31	19.22	0.5	24.4
p0i42c3	0.0	-0.4	-4.7	4.3	2.9	2.3	252 ± 18	19.55	0.9	40.9
p0i45c2	-10.1	6.4	-5.6	0.1	3.4	3.3	—	—	—	6.6
p0i49c2	0.0	-1.6	-3.8	2.8	1.4	2.3	236 ± 16	20.75	1.2	22.5
p0i4c4	-0.8	-0.6	-1.1	3.8	3.0	2.3	128 ± 13	20.28	0.4	9.5
p0i53c4	0.0	-1.8	-2.0	3.2	1.1	0.9	403 ± 32	20.00	1.2	17.2
p0i55c2	0.0	5.9	1.1	—	2.9	0.8	—	—	—	5.8
p0i66c3	-6.0	-0.3	-4.0	3.2	3.6	2.4	86 ± 7	21.15	1.1	15.3
p0i72c3	0.0	-1.9	-5.8	4.6	2.4	2.3	275 ± 23	—	—	42.2
p0i79c3	0.0	-1.2	-5.4	5.4	2.1	2.5	283 ± 23	21.08	3.1	28.5
p0i85c3	-1.7	-0.4	-5.4	2.4	0.5	0.1	425 ± 49	20.61	1.4	20.8
p0i91c3	0.0	-2.2	-3.1	5.6	2.9	2.5	169 ± 15	19.01	0.4	24.8

Table 3.3 — Continued

Object	[O II] (Å)	H δ_A (Å)	H γ_A (Å)	Mg ^b (Å)	Fe5270 (Å)	Fe5335 (Å)	σ_0 (km s ⁻¹)	$\langle\mu_V\rangle$ (mag '' ⁻²)	R_e ('')	S/N Observed
p0i95c3	0.0	-1.3	-6.3	4.9	2.7	1.9	221 ± 24	19.36	0.8	36.9
p10i1c2	-0.4	-0.2	-4.6	2.3	2.5	2.8	214 ± 13	19.52	0.8	38.4
p11i147c4	0.0	-1.0	-2.3	7.6	3.3	3.1	126 ± 7	19.42	0.4	18.9
p12i160c2	-0.7	6.0	-1.1	6.4	2.9	3.5	—	—	—	6.0
p12i160c3	0.0	0.4	0.6	6.5	3.4	3.0	138 ± 19	19.84	0.6	8.7
p12i168c4	-28.7	1.4	2.2	2.3	2.3	4.0	—	—	—	4.8
p12i73c4	-2.3	-0.2	-3.2	—	—	—	132 ± 12	20.07	0.6	12.3
p13i130c3	-38.9	1.1	—	—	-0.3	7.2	—	—	—	2.1
p13i133c4	0.0	-0.3	-4.5	—	—	—	—	—	—	4.0
p13i135c4	-2.7	-0.6	-3.6	3.4	1.8	2.2	143 ± 11	21.21	1.6	17.1
p13i1c4	-1.4	-3.0	-5.7	8.4	—	—	143 ± 22	20.37	0.8	8.4
p13i25c2	0.0	-0.3	-5.0	1.1	2.6	2.8	147 ± 8	19.74	0.6	23.4
p13i78c4	-0.2	-0.1	-1.6	—	2.5	2.0	232 ± 21	19.72	0.8	19.6
p13i86c4	-25.1	7.5	-0.7	—	—	—	—	—	—	2.5
p14i2c2	-7.7	2.0	-0.4	6.1	1.4	1.5	119 ± 13	21.22	0.8	12.5
p15i144c4	-0.8	1.9	-5.0	—	0.7	2.9	130. ± 11	19.71	0.5	12.4
p17i2c4	-3.9	-0.9	0.6	2.7	3.4	5.2	—	—	—	6.4
p18i43c2	0.0	-0.9	-4.4	4.3	1.8	2.4	234 ± 21	19.94	1.0	32.6
p18i51c2	0.0	-0.1	0.4	—	2.1	1.5	152 ± 10	18.93	0.3	18.9
p18i66c3	0.0	-1.6	-4.9	4.2	2.3	2.0	168 ± 14	18.62	0.3	20.8
p19i1c3	-0.7	0.0	-6.0	—	—	—	—	—	—	7.0
p19i75c4	-1.8	2.7	-0.5	5.4	0.0	1.6	—	—	—	5.0
p19i92c2	-49.9	3.4	-1.8	2.2	-0.6	0.4	—	—	—	6.8
p20i35c4	-6.5	0.3	-0.7	1.6	1.8	2.0	175 ± 11	19.41	0.5	25.1
p20i48c3	0.0	-1.3	-4.0	3.9	2.5	0.5	172 ± 11	19.23	0.4	10.0

Table 3.3 — Continued

Object	[O II] (Å)	H δ_A (Å)	H γ_A (Å)	Mg ^b (Å)	Fe5270 (Å)	Fe5335 (Å)	σ_0 (km s ⁻¹)	$\langle\mu_V\rangle$ (mag '' ⁻²)	R_e ('')	S/N Observed
p24i115c3	-43.1	3.8	—	9.0	1.2	-0.2	—	—	—	4.5
p24i1c3	-0.5	2.8	1.1	1.9	-0.7	0.9	144 ± 16	20.44	1.2	12.4
p24i42c4	0.0	-4.9	-1.1	1.7	2.6	-1.2	—	—	—	5.6
p24i79c4	0.0	-0.8	3.9	2.6	1.0	1.1	—	—	—	4.8
p24i87c3	0.0	-2.4	-6.3	3.8	1.8	0.7	153 ± 8	19.75	0.7	11.0
p25i29c3	-0.7	-0.2	-2.5	3.2	2.8	2.9	152 ± 16	18.36	0.2	13.4
p25i93c3	-30.1	-1.2	-2.3	2.8	3.0	2.2	—	—	—	5.5
p27i174c3	0.0	0.2	-3.4	5.0	2.7	1.9	187 ± 17	19.64	0.8	24.8
p27i9c2	-29.8	-3.2	3.8	2.7	—	-1.7	—	—	—	3.9
p28i87c2	-46.5	2.4	-2.2	1.8	0.5	1.2	—	—	—	7.4
p35i112c2	0.0	-1.4	-0.3	3.9	2.5	1.7	71 ± 8	—	—	9.6
p35i143c2	0.0	-4.0	-9.6	5.4	2.8	2.7	148 ± 9	18.99	0.4	19.8
p35i43c3	-4.4	-0.9	-4.4	3.6	3.0	2.5	170. ± 12	20.36	1.1	18.2
p35i6c3	0.0	-1.1	-5.0	4.2	2.5	2.9	220 ± 12	19.11	0.7	27.0
p35i78c2	-17.0	-1.6	-4.5	3.5	1.4	2.2	191 ± 13	19.36	0.6	36.1
p35i82c3	0.0	-0.7	-5.1	4.9	2.3	2.4	201 ± 16	19.62	0.7	36.4
p36i106c3	0.0	3.1	-3.0	—	—	—	—	—	—	3.0
p36i146c3	0.0	-1.2	7.1	3.4	2.2	3.0	167 ± 12	20.15	0.7	12.5
p36i182c2	0.0	-0.6	-4.4	2.6	2.2	2.4	130. ± 6	20.09	0.9	26.6
p36i182c3	-6.6	2.4	-1.0	—	7.6	1.5	108 ± 24	20.93	0.7	6.8
p36i184c2	-0.5	-2.5	-3.4	4.9	1.6	2.7	165 ± 10	20.00	0.9	27.2
p36i187c3	-2.9	-0.2	4.9	4.4	1.3	3.1	123 ± 10	19.80	0.5	8.8
p36i1c4	-3.3	-0.6	-4.2	4.1	2.9	2.5	79 ± 10	19.12	0.5	22.2
p36i2c2	0.0	-1.7	-5.1	2.0	2.1	1.6	376 ± 24	20.42	1.8	22.6
p36i2c3	-2.6	1.3	6.5	6.8	3.0	2.5	164 ± 10	21.76	1.5	16.2

Table 3.3 — Continued

Object	[O II] (Å)	H δ_A (Å)	H γ_A (Å)	Mg ^b (Å)	Fe5270 (Å)	Fe5335 (Å)	σ_0 (km s ⁻¹)	$\langle\mu_V\rangle$ (mag '' ⁻²)	R_e ('')	S/N Observed
p36i31c4	0.0	-3.1	-4.1	4.4	2.0	1.6	264 ± 28	20.14	1.1	32.6
p36i32c4	0.0	-3.1	-3.4	4.5	2.9	3.1	215 ± 19	19.48	0.4	7.6
p36i34c2	0.0	-1.1	-5.0	—	1.7	2.6	114 ± 10	19.52	0.3	10.4
p36i36c4	-5.9	0.0	-9.5	4.7	1.3	0.8	—	—	—	5.8
p36i3c2	0.0	-0.4	-8.9	2.3	2.6	2.2	110. ± 9	19.64	0.5	15.3
p36i48c3	-1.4	-4.1	-8.1	7.1	1.9	2.1	188 ± 15	19.97	0.6	12.8
p36i5c2	-6.8	2.1	-2.1	0.3	2.5	1.7	169 ± 15	20.41	1.2	12.5
p36i67c4	-14.3	1.0	-0.8	4.4	—	—	—	—	—	7.0
p36i70c4	-8.7	2.0	-0.9	2.3	2.6	1.6	83 ± 8	19.55	0.4	18.5
p36i71c3	-4.7	1.1	-4.2	4.3	1.3	1.4	—	—	—	7.3
p36i76c2	-4.5	0.1	0.7	4.3	2.8	2.7	261 ± 13	20.12	0.5	13.2
p36i76c3	-2.8	3.0	-2.0	5.7	0.3	0.9	87 ± 14	20.93	1.1	9.8
p36i89c2	-4.0	1.2	0.4	—	2.1	2.2	107 ± 10	21.14	1.1	14.9
p37i110c2	0.0	2.7	-3.5	7.3	3.2	3.2	114 ± 8	19.67	0.3	10.5
p37i122c2	-41.3	0.8	-3.4	2.0	1.7	1.4	—	—	—	4.0
p37i16c4	-1.6	1.5	-2.5	3.7	2.2	1.9	233 ± 11	19.86	1.4	55.1
p37i206c4	0.0	0.5	-7.3	—	2.7	2.7	64 ± 6	19.12	0.3	14.5
p37i207c4	0.0	-0.8	12.5	7.8	2.2	1.8	—	—	—	1.8
p37i64c4	-1.3	1.1	1.2	4.6	1.7	-2.3	254 ± 45	18.86	0.3	7.1
p37i9c4	-5.9	2.1	-1.3	0.4	3.1	1.2	—	—	—	10.1
p38i1c4	-0.9	-2.9	-0.4	—	-0.8	2.1	—	—	—	5.5
p38i76c4	0.0	5.6	-8.5	—	0.5	1.6	—	—	—	6.7
p3i72c2	-7.9	0.5	-6.8	0.8	6.9	5.9	—	—	—	2.8
p5i9c3	-0.7	-0.3	-1.9	4.2	2.0	2.3	100. ± 10.	18.93	0.2	14.3
p7i128c3	0.0	-0.8	-5.0	3.4	2.3	2.5	204 ± 14	—	—	27.2

Table 3.3 — Continued

Object	[O II] (\AA)	H δ_A (\AA)	H γ_A (\AA)	Mg ^b (\AA)	Fe5270 (\AA)	Fe5335 (\AA)	σ_0 (km s ⁻¹)	$\langle \mu_V \rangle$ (mag '' ⁻²)	R_e ('')	S/N Observed
p7i133c3	0.0	-1.3	-3.6	—	3.4	-0.6	161 ± 21	21.12	0.7	7.7
p7i136c3	0.0	0.2	-4.4	2.3	3.4	1.9	168 ± 10	20.08	0.7	18.4
p7i1c2	-6.4	-1.5	-6.9	3.6	2.2	2.5	222 ± 14	19.75	1.0	46.8
p7i67c3	0.0	1.0	-3.6	9.9	2.6	3.2	127 ± 8	19.44	0.3	16.5
p9i20c3	-6.1	0.3	-3.6	3.3	3.2	2.1	112 ± 10	21.29	1.6	22.3

Line strengths are given in \AA of equivalent width, with negative values denoting emission, and positive values indicating absorption. No aperture corrections have been applied to the indices. σ_0 lists velocity dispersions, when measured, and the values are aperture-corrected to a 3''.4 diameter aperture at the distance to the Coma cluster. $\langle \mu_V \rangle$ indicates the mean surface brightness within the effective radius, R_e , in rest frame V -band, and is corrected for cosmological dimming. Typical errors on line indices are less than $\pm 0.2 \text{\AA}$ on H δ_A and H γ_A , and $\pm 0.1 \text{\AA}$ on [O II], Mg^b, Fe5270, and Fe5335. Errors on μ_V and R_e are 0.1 mag and 0''.1, respectively.

Chapter 4

Dynamical Evidence for Environmental Evolution of Intermediate Redshift Spiral Galaxies ¹

In this chapter, we study the dynamical properties of spiral galaxies as a function of position across Cl 0024 and MS 0451, and we compare the cluster population to field galaxies in the same redshift range. By modeling the observed rotation curves, we derive maximal rotation velocities for 40 cluster spirals and 37 field spirals, yielding one of the largest matched samples of cluster and field spirals at intermediate redshift. We construct the Tully-Fisher relation in both V and K_S bands, and find that the cluster Tully-Fisher relation exhibits significantly higher scatter than the field relation, in both V and K_S bands. Under the assumption that this increased scatter is due to an interaction with the cluster environment, we examine several dynamical quantities (dynamical mass, mass to light ratio, and central mass density) as a function of cluster environment. We find that the central mass densities of star-forming spirals exhibit a sharp break near the cluster Virial radius, with spirals in the cluster outskirts exhibiting significantly lower densities. We argue that the lower-density spirals in the cluster outskirts, combined with the high scatter in both K_S - and V -band TF relations, demonstrate that cluster spirals are kinematically disturbed by their environment, even as far as $2R_{VIR}$ from the cluster center. We propose that such disturbances may be due to a combination of galaxy merging and harassment.

¹Much of this chapter has been previously published as Moran et al. (2007a).

4.1 Introduction

The observed tight correlation between the rotation velocities of spiral galaxies and their total luminosities, first noted by Tully & Fisher (1977), has proven invaluable in helping to pin down the extragalactic distance scale in the local universe (e.g., Tully & Pierce 2000). Since then, many authors have attempted to leverage the so-called Tully-Fisher relation to study the evolution of spiral galaxies as a function of redshift, generally interpreting any deviation from the local Tully-Fisher (TF) relation as an evolution in luminosity.

These studies have yielded mixed results, however, with conflicting estimates of the rate of B -band evolution as a function of redshift (Bamford et al. 2006; Böhm et al. 2004; Milvang-Jensen et al. 2003; Vogt et al. 1996). Recently, several authors have documented many of the systematic errors that make comparisons between studies very difficult (Metevier et al. 2006; Nakamura et al. 2006). Indeed, Nakamura et al. (2006) argue that the most certain method of using the TF as a measure of evolution is to construct a large matched sample of galaxies, consisting of nearly equal numbers of cluster and field galaxies all measured in the same way.

In a similar manner, large matched samples such as those presented by Nakamura et al. (2006) and Bamford et al. (2005) can also be effectively used to measure a different sort of spiral galaxy evolution: that caused by infall into a galaxy cluster. By carefully selecting galaxies across a wide range of environments, in and out of clusters, we can gain a better understanding of the changes in star formation and kinematics that a spiral may undergo as it falls into a cluster potential.

In this chapter, we attempt to construct such a sample out of our large survey of Cl 0024 ($z = 0.39$) and MS 0451 ($z = 0.54$). We make use of high-quality spiral rotation curves determined from Keck spectroscopy to measure the Tully-Fisher relation. The sample is large enough to allow a first investigation of the scatter of the relation as a function of cluster-centric radius. We also study a control sample of field galaxies in a range of redshifts centered about the cluster redshifts, in order to assess differences between field and cluster spirals. Our sample of 40 cluster galaxies is the largest yet

reported with an associated field sample (37 galaxies), and provides a powerful means to examine the effect of the cluster environment on infalling star-forming spirals.

In order to disentangle environmental processes affecting the dynamics of infalling spirals and those affecting their stellar populations, we contrast the trends in the TF relation with those observed for integrated $V - K_S$ colors and disk mass density. The latter quantity is constructed from rotation curves and *HST* scale lengths, and is predicted to be sensitive to the strength of the “harassment” process (Moore et al. 1999).

A plan of the chapter follows. In §4.2, we give a summary of the data from our cluster survey that we use here, and discuss the sample selection. We then detail our procedure for deriving maximal rotation velocities in §4.3. In §4.4, we present our results on the cluster and field Tully-Fisher relation, with an examination of other dynamical quantities in §4.5. The Tully-Fisher relation in Cl 0024 has also been studied by Metevier et al. (2006), and in §4.4 we also directly compare rotation measurements for several galaxies in common between studies. In §4.6 we discuss these results in light of proposed physical mechanisms acting in the cluster environment. In this chapter, we adopt a cosmology with $\Omega_m = 0.3$, $\Omega_\Lambda = 0.7$, and $H_0 = 70 \text{ km s}^{-1} \text{ Mpc}^{-1}$.

4.2 Observations

In this study, we leverage our large imaging and spectroscopic survey Cl 0024 and MS 0451. From the survey, we select a sample of high-quality resolved spectra of both field and cluster spirals, suitable for extracting rotation curves. While the parameters of this survey are more fully described in Chapter 2, in the following we briefly describe the photometric and spectroscopic observations used here, and discuss the sample selection for this work.

Our current sample is drawn from the set of surveyed galaxies with both *HST* imaging and available spectra. From the *HST* imaging, we select candidate galaxies that are morphologically classified as spirals (T-types 3, 4, or 5). For ease of comparing cluster spirals to field, we construct a matched sample of field spirals, all with

HST imaging from the Cl 0024 or MS 0451 mosaics, and selected to lie in a redshift range that brackets the two clusters, $0.3 \leq z < 0.65$.

We calculate absolute V -band magnitudes (M_V) for our objects, using F814W photometry from our *HST* imaging and applying k -corrections as described in Chapter 2. We also use panoramic ground-based K_s -band imaging of both cluster with the WIRC camera (Wilson et al. 2003) on the Hale 200" Telescope. These data comprise a 3×3 mosaic of pointings, spanning a contiguous area of $26' \times 26'$ centered on each cluster, and allow measurement of rest-frame K_s -band magnitudes (M_K). Cl 0024 K_s images are not deep enough to detect all cluster spirals of interest; we therefore report K_s magnitudes only for objects detected with $> 3\sigma$ significance. All absolute magnitudes in this chapter are expressed on the AB magnitude system.

In our spectroscopic survey, targets were selected randomly from an F814W-limited sample, to $F814W = 22.5$ in the field of Cl 0024, and to $F814W = 23.0$ in MS 0451. Here, we focus on a subset of these galaxies that have been observed with slits aligned along the galaxy major axis, in order to secure resolved spectra of spirals with extended emission lines. The Cl 0024 campaign primarily targeted known cluster spirals for spectroscopy along the major axis, but serendipitous alignments with the major axes of field galaxies allowed us to include some of these in our sample. In MS 0451, we observed most galaxies with aligned slits, and, as a result, our field sample of spirals is weighted toward galaxies in the field around MS 0451.

As our field sample is composed of objects in the same redshift range as the clusters, biases introduced by the magnitude-limited survey should affect both samples equally, except at the faint end of the luminosity function. This effect will be discussed further in §4.4.

4.3 Rotation Curve Analysis

In order to construct the Tully-Fisher relations, and to study other kinematic properties of spirals (such as mass, density, or M/L), we seek to determine the maximum velocity of the rotation curve for each disk. Our process involves extracting the ob-

served rotation curve from the spectrum and then creating artificial rotation curves for each galaxy, determining the best-fit maximum velocity by χ^2 fitting against the extracted rotation curve. In order to do this it is important to determine various parameters about the galaxy from photometric data including the position angle of the slit with respect to the position angle of the major axis of the galaxy, the scale length of the galaxy, and the seeing when the galaxy was observed. Along each step, we filter out the galaxies with weak spectral lines or those which, for reasons of inclination, etc., would not be possible to fit using our model. We further divide the remaining fits into two subsamples, those with secure rotation velocities ($Q = 1$), and those where the velocity is less certain but probably correct ($Q = 2$). We largely follow the procedure of Böhm et al. (2004), though several other authors have followed similar procedures (e.g., Metevier et al. 2006; Nakamura et al. 2006; Bamford et al. 2005; Vogt et al. 1996). We have made several modifications to the procedure, detailed below.

4.3.1 Extraction of Rotation Curves

From each complete 2D spectrum, we extract postage stamps about the position of every emission line present, using the known redshift of each object to identify lines. In the left-hand panel of Figure 4.1, we display an example postage stamp centered on $H\alpha$ for the galaxy N57426, a $z = 0.39$ field galaxy in the vicinity of MS 0451. As the observed center of $H\alpha$ emission clearly varies across the spatial dimension of the spectrum, the rotation in this galaxy is already apparent. In order to determine the observed rotation curve, we fit a Gaussian function or double Gaussian (in the case of [O II]) to each row along the spectral direction, as demonstrated in the right-hand panel of Figure 4.1. For the double Gaussian, we assumed a fixed separation and that the FWHM of each Gaussian component was the same, but allowed the amplitudes to differ independently.

We bin spectral rows together in the spatial dimension, as necessary, to meet a signal to noise (S/N) requirement of $\sim 5(\text{\AA}^{-1})$ per bin. This rebinning allows us to

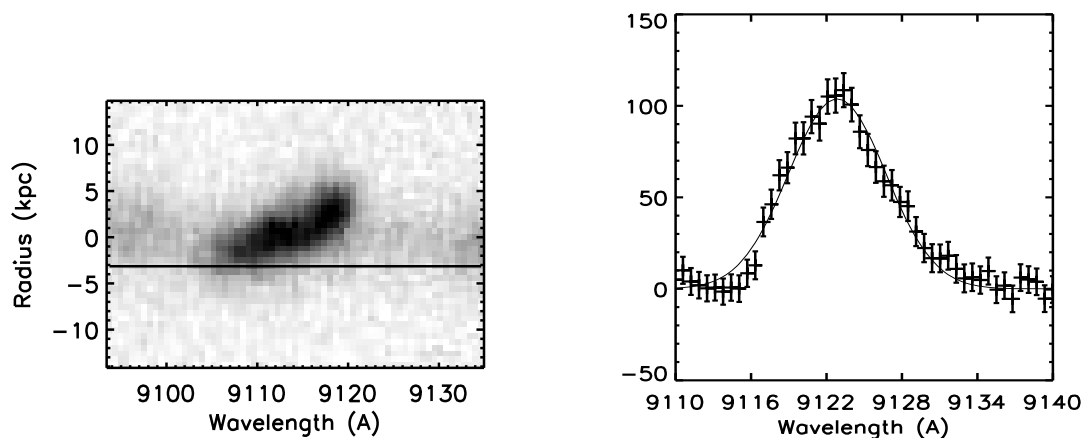


Figure 4.1 Left: Cutout from a 2D spectrum, centered on the observed wavelength of $H\alpha$ for the galaxy N57426, in the field of MS 0451. The solid line across the image indicates the spectral row that is plotted in the right-hand panel. Right: One spectral row from the 2D spectrum. The solid curve indicates the Gaussian fit to this row. The stellar continuum emission has been subtracted according to the method described in the text.

sum up regions of the emission line that are too faint to fit individually, essentially trading spatial resolution, which is less important near the outer flat regions of a rotation curve, for a more reliable velocity measurement. When rows are binned, the x position (i.e., radius) of the resulting velocity point is calculated by taking a S/N weighted mean of the x positions of all the constituent spectral rows. Each of these binned fits were checked by hand to ensure that they were meaningful. All extracted rotation curves for our complete sample are displayed in Figures 4.2 and 4.3.

We found that the fit worked best when we subtracted off the continuum to all the rows before fitting. We measured the continuum on the spectrum for each spectral line separately by summing together about 50 spectral columns on either side of the emission line's center. By extracting and continuum subtracting over small postage stamps, we avoid any issues that might be caused by spatial distortion in the spectrum.

4.3.2 Surface Photometry

From our *HST* imaging, we extract a $9'' \times 9''$ postage stamp image of each galaxy in our sample, with the galaxy centered (see Figures 4.2 and 4.3). We then use the GALFIT software (Peng et al. 2002) to fit the galaxy photometry to a Sérsic profile. This fit yields estimates of the galaxy position angle on the sky, axis ratio, and scale length. These parameters are necessary to determine the maximum velocity of the galaxy in the following step. While we experimented with fitting to an exponential disk plus bulge component, we find that the scale length as derived from the Sérsic profile fit yields the best estimate of the rotation curve’s turnover scale length, as described below.

In local Tully-Fisher studies, internal extinction of spiral galaxies has been found to depend on the galaxy’s inclination to the line of sight (Tully & Fouque 1985; Tully et al. 1998; Verheijen 2001). Galaxies viewed close to edge on have a larger fraction of their luminosity extinguished by dust than the same galaxy would have if viewed face on. We correct for this effect by adopting the particularly simple form of the correction introduced by Tully et al. (1998):

$$A_\lambda = -\gamma_\lambda \log\left(\frac{a}{b}\right) \quad (4.1)$$

where a/b is the axis ratio of the galaxy. This formula corrects toward the face-on case, but does not correct for additional extinction in a face on galaxy. We choose not to apply any additional correction for the internal extinction of a face-on galaxy.

Following Tully et al. (1998), we determine γ in each band by minimizing the scatter in the rest-frame color magnitude relations $B - K_S$ vs. M_K and $V - K_S$ vs. M_K , using the entire cluster plus field sample together. Since the luminosity function of cluster spirals may not be uniform across all studied environments, we ignore any luminosity dependence of the γ correction, in order to avoid “fitting away” real deviations that may be due to the cluster environment. We find $\gamma_B = 1.37$, $\gamma_V = 1.12$, and $\gamma_K \equiv (0.15\gamma_B) = 0.206$. These values are consistent with the range specified in, e.g., Tully et al. (1998) and Verheijen (2001).

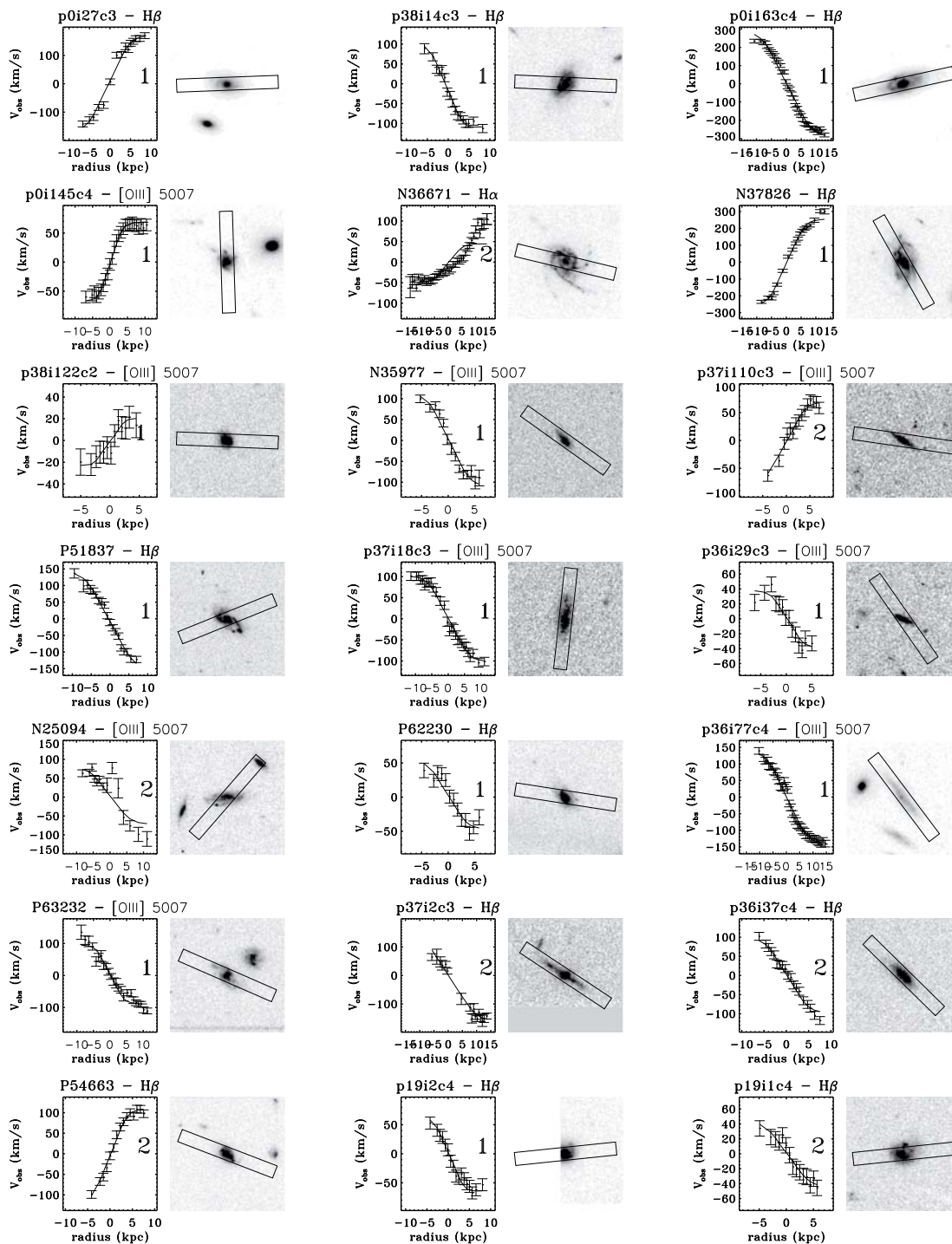


Figure 4.2 Images and rotation curves for cluster spirals, in order of ascending radius, R , normalized by R_{VIR} . Images are $9'' \times 9''$. Observed rotation curves are plotted as error-barred points, solid lines represent the best-fit rotation curve model, and the quality code is displayed. On the postage stamp images, the $1'' \times 8''$ slit is indicated by the solid black box. The spectroscopic seeing $0.8''$ is equivalent to ~ 4.5 kpc physical.

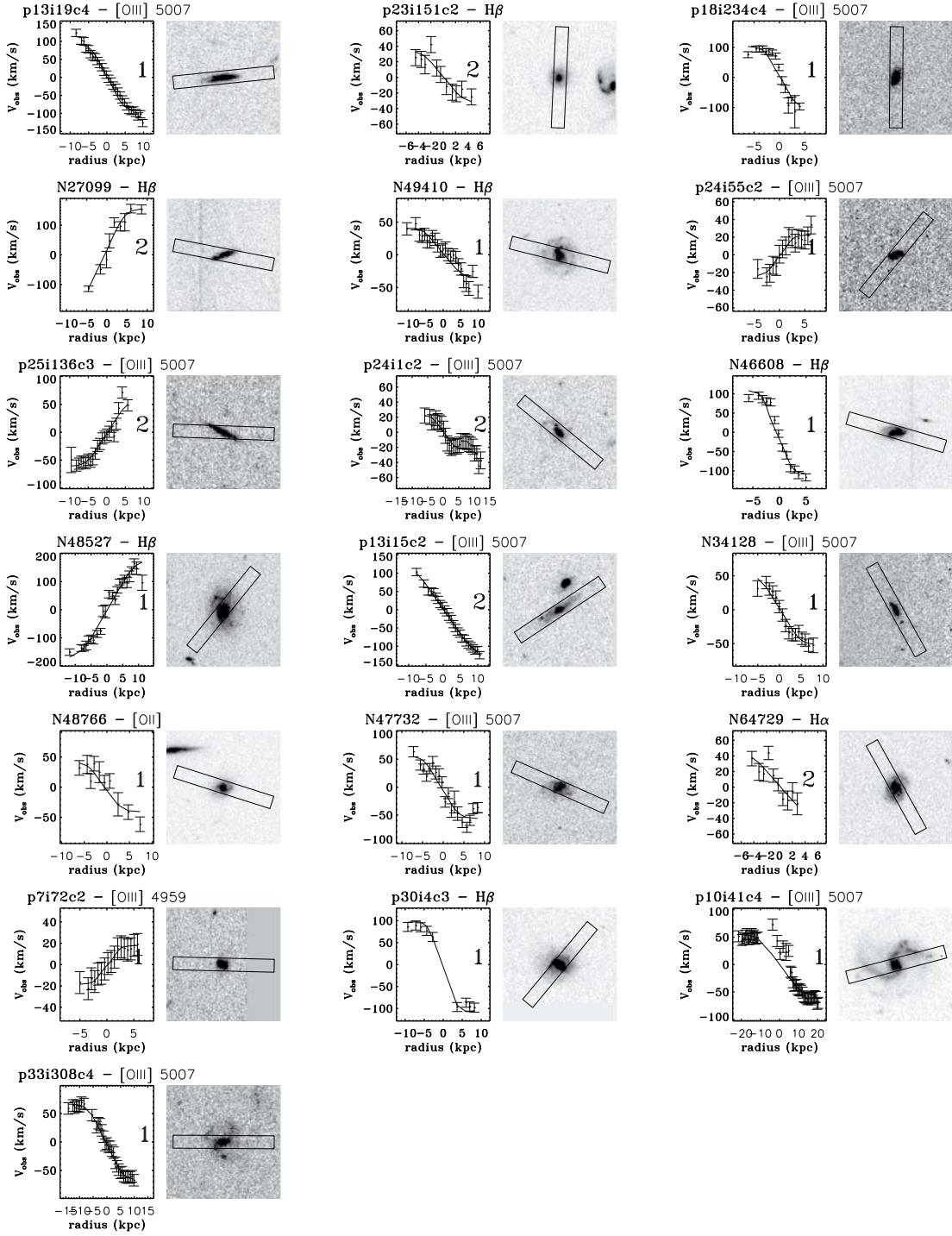


Fig. 4.2. — Continued.

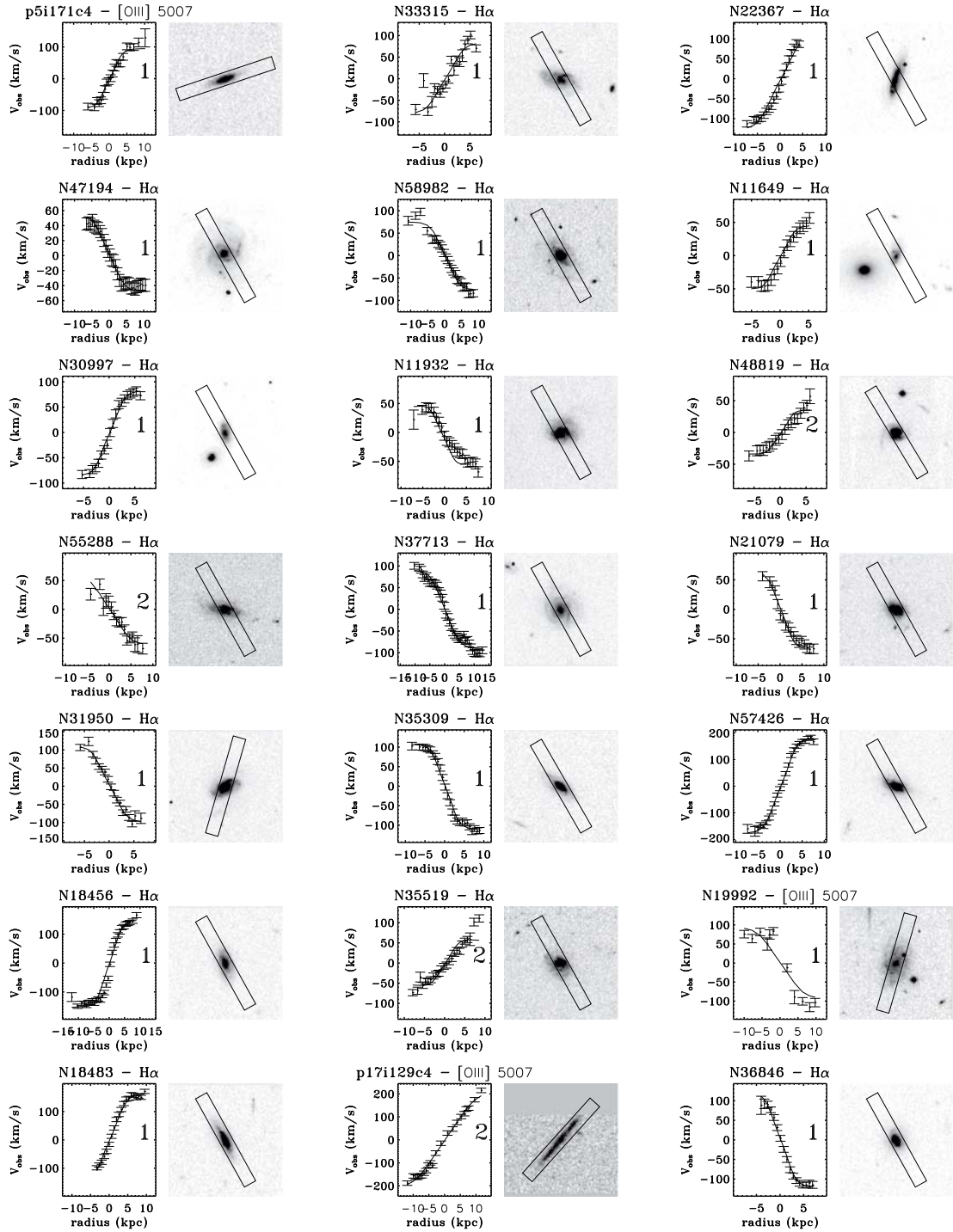


Figure 4.3 Postage stamp images and rotation curves for all field spirals, arranged in ascending redshift order.

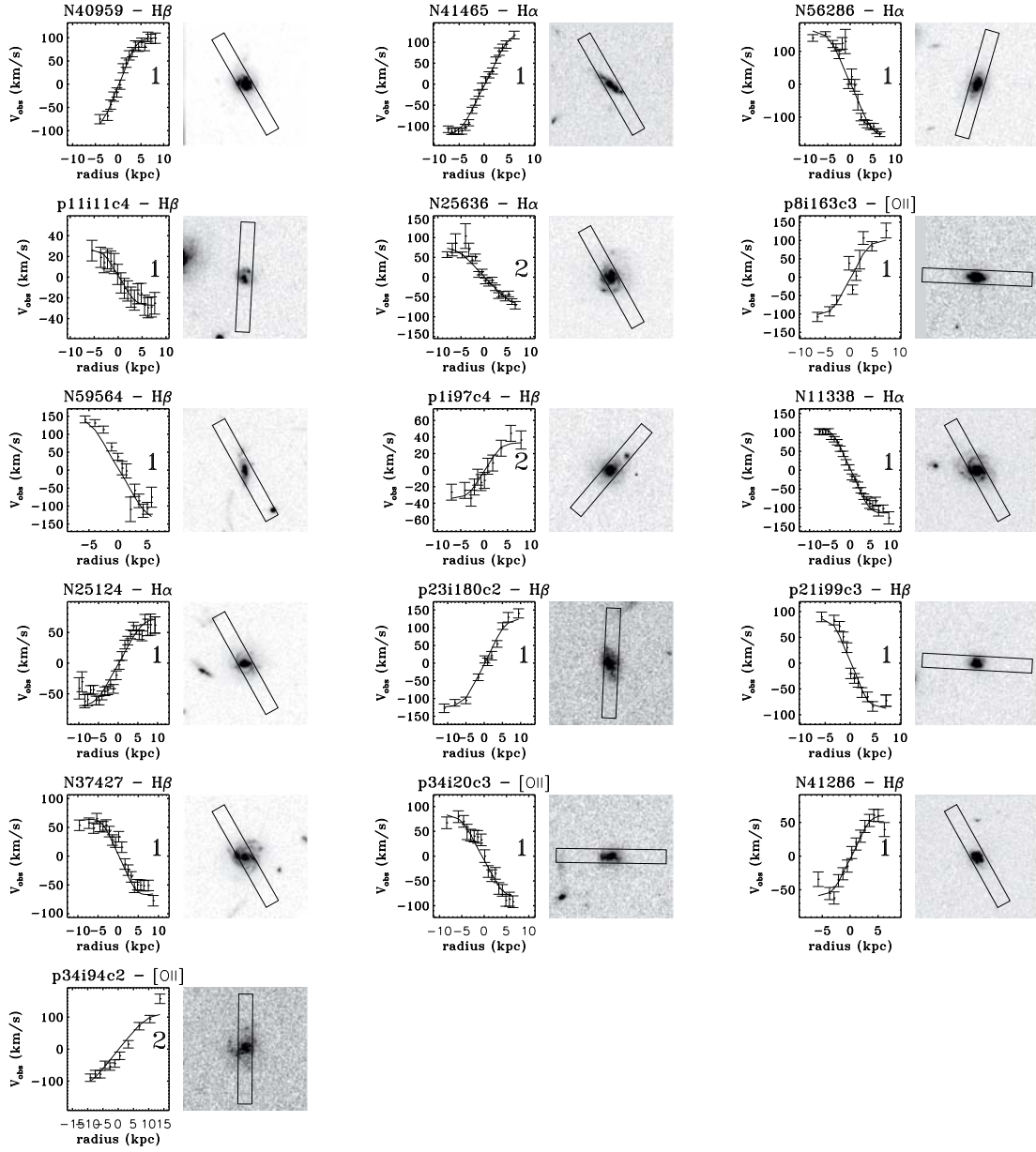


Fig. 4.3. — Continued.

4.3.3 Model Fitting

In order to determine the peak rotation velocity of a galaxy, we used the parameters obtained from GALFIT to construct an estimated velocity field for some maximum velocity. We adopt a standard rotation curve function of the form

$$V(r) = \frac{V_{MAX}r}{(r^a + r_s^a)^{1/a}} \quad (4.2)$$

where r_s is the Sérsic profile scale length as determined by GALFIT and $a = 5$, following Böhm et al. (2004). For two galaxies in our sample, p1i97c4 and N46608, r_s from GALFIT appeared to be an overestimate of the rotation curve scale length, and so we manually adjusted it to achieve a better fit. From the intrinsic rotation curve specified above, we construct a 2D velocity field by populating a grid of line-of-sight velocities, under the following formula:

$$V_{\text{obs}} = V(r) \cdot \cos(\phi) \cdot \sin(i) \quad (4.3)$$

where ϕ is the azimuth in the plane of the disk and i is the inclination, with $i = 90^\circ$ defined to be edge on to the line of sight.

We then convolve this velocity field with a point spread function (PSF) with FWHM equal to the seeing. For our data, we used a fixed seeing of $0.8''$, equal to the median seeing of our observations. We adopt this fixed seeing correction because of the relative insensitivity of the results to small variations in seeing; we find that our uncertainty in the seeing correction affects the final V_{MAX} by $<1\%$, which is insignificant compared to errors due to inclination or position angle.

Then, comparing the slit PA of our observation to the GALFIT estimate of the galaxy major axis angle, we place a mock $1''$ -wide slit across the model velocity field, at an angle reflecting the alignment between the real slit and the galaxy major axis. Finally, at each position along the length of the slit, we averaged the pixels across the slit width to determine an observed velocity. We use a χ^2 minimization technique to vary the maximum velocity in the model to match our observed rotation curves.

For each observed spectrum, we estimate the position of the galaxy’s spatial center by fitting a Gaussian function to the spatial profile of the 2D absorption spectrum, integrated along the spectral dimension in two bands bracketing the emission line of interest. An initial estimate of the velocity center is calculated from the previously determined redshift of each galaxy. Both the spatial center and velocity center are left to be free parameters in the χ^2 minimization. However, in no case does the best-fit spatial center of a $Q = 1$ rotation curve differ by more than two pixels (~ 1.5 kpc physical) from the calculated position, with typical offsets of much less than one pixel.

We first fit the rotation curve using fixed values for the PA and inclination, i . In order to determine the error values on our fits, we factor in the error from the fit as well as computing a PA error and inclination error for the model by running it at $\pm 10^\circ$ for each parameter. Especially for galaxies that present a somewhat face-on profile, it is important to account for this uncertainty due to PA and inclination errors, as it can be large in some cases, and in fact causes us to discard several emission line galaxies from our sample. We choose to vary over $\pm 10^\circ$ because the formal errors in the photometric fit are small in comparison to the systematic uncertainty in measuring the PA and inclination from the inherently asymmetric light profile of a spiral galaxy.

4.3.4 Quality Control

We began with a sample of 257 candidate spiral galaxies, each with visible, spatially resolved emission lines. Out of this sample, we removed 142 galaxies because the rotation curve lacked enough spatial extent to detect a reliable turnover, or else no significant velocity gradient was measured, in most cases because the galaxy is oriented nearly face on. Additionally, we removed 33 galaxies because the spectroscopic slit was too misaligned, or because the galaxy appeared too face on to estimate the direction of its major axis.

After fitting models to the rotation curves of our candidate spirals, and culling bad fits from our sample as described above, we remove five additional objects with highly uncertain velocities, $\Delta \log(2V_{MAX}) > 0.2$. Our final sample then consists of 37 field

Table 4.1. Summary of Tully-Fisher sample selection

	CI 0024 $0.37 < z < 0.41$	MS 0451 $0.52 < z < 0.56$	Field $0.3 < z < 0.65$	Total
a. Spirals in this redshift range with <i>HST</i> imaging and spectra	103	130	194	427
b. Those with extended emission lines and aligned slits	92	103	62	257
c. Significant spatial extent, with a measured velocity gradient	42	26	47	115
d. After removing very face-on galaxies and other misaligned slits	28	16	38	82
e. Velocity uncertainty small enough	24	16	37	77
f. $Q=1$ rotation curve	17	11	30	58

spirals and 40 cluster spirals (24 from Cl 0024). The observed rotation curves, model fits, and images of these galaxies are presented in postage stamp form in Figures 4.2 (cluster galaxies) and 4.3 (field galaxies).

We further divide this sample into two quality classes: $Q = 1$ rotation curves have turnovers detected on both sides of the curve, with a model fit that accurately matches the turnover at each end. $Q = 2$ curves, about 25% of the total, only show a turnover at one end, or show other signs of an uncertain fit to the model. We do not simply throw out all galaxies with signs of disturbed kinematics, but rather keep them in the $Q = 2$ sample, as they are of considerable interest for our study of possible interactions with the cluster environment. However, the requirement that we identify a reasonably secure value of V_{MAX} must necessarily exclude some number of spirals with highly disturbed rotation curves.

We summarize the sample selection process for both clusters and the field in Table 4.1. We note that we remove roughly equal fractions of galaxies from the cluster and field samples, at each step of the process. The two notable exceptions have ready explanations: In step b., a larger fraction of field galaxies than cluster galaxies are removed due to misaligned slits, because we did not consistently observe field galaxies with aligned slits. Similarly, in step c., a low fraction of MS 0451 cluster galaxies exhibited large enough spatial extent in their rotation curves, due to an observed suppression or lack of star formation across this massive cluster (Chapter 6). Basic data, as well as extinction-corrected magnitudes and velocities for all 77 objects of our main sample, are listed in Table 4.3.

4.4 The Tully-Fisher Relation

In Figure 4.4, we plot the Tully-Fisher relation for both cluster and field galaxies, in both rest frame K_S and V bands (expressed as absolute magnitudes M_K and M_V , respectively). Shaded regions indicate the $\pm 1\sigma$ scatter of the local TF from Verheijen (2001). Solid lines indicate the best fit TF zero point for each of our subsamples, with the slope fixed to the local values from Verheijen (2001), adopting their RC/FD

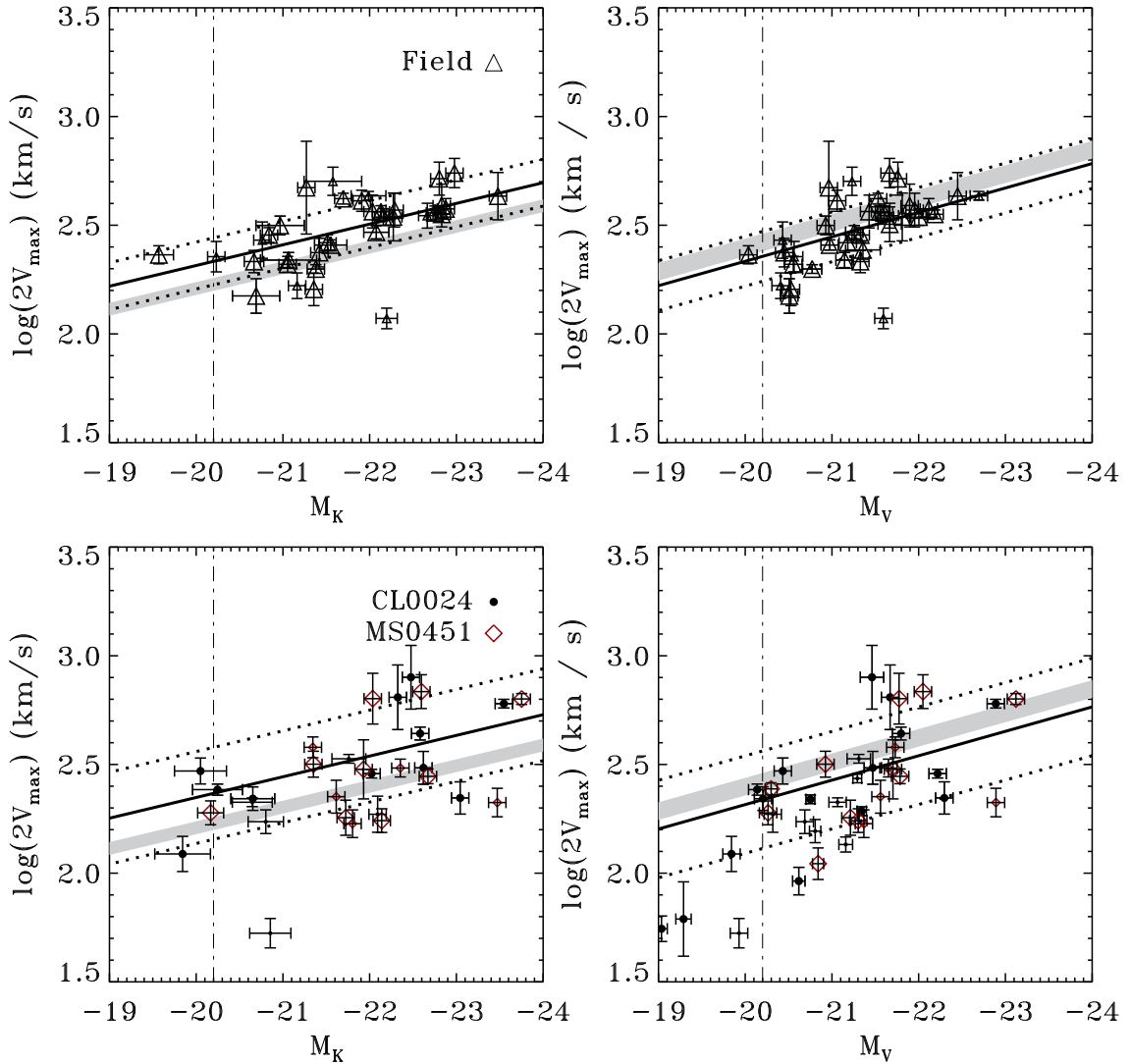


Figure 4.4 V -band (right) and K -band (left) Tully-Fisher relations for cluster and field spirals. The field relation is plotted in the top two panels, and cluster galaxies are plotted on the bottom. Cl 0024 members are marked as black circles, while MS 0451 members are indicated by red diamonds. Shaded regions indicate the 1σ scatter of the local Tully-Fisher relation, from Verheijen (2001). We adopt their R -band relation to compare to our V -band relation, neglecting any small correction to account for the different filters. In each panel, the thick solid line represents the inverse-fitted TF relation for those points (but fixing the slope to the local value), and the dotted lines represent the 1σ scatter about the mean. Dash-dotted line indicates where we apply a cut in magnitude for this calculation. Symbols are as indicated by the legend; small symbols indicate $Q = 2$ rotation curves, and large symbols are $Q = 1$.

sample, which includes only galaxies where a turnover in the rotation curve is seen. Dotted lines indicate the 1σ RMS scatter of the relation about the mean. Zero points are calculated by finding the biweight mean of the residuals about the local TF. To minimize bias, zero point and scatter are calculated only from $Q = 1$ rotation curves. We further impose an absolute magnitude cut of $M_V \leq -20.2$ and $M_K \leq -20.2$, to eliminate bias due to the differing magnitude distributions between the cluster and field samples.

For purposes of determining the intrinsic scatter in the TF relation for each of our samples, we also perform a least-squares fit to find the best-fit parameters of the TF relation, weighting each point by the measurement uncertainties in both $\log(2V_{MAX})$ and absolute magnitude. We follow other authors (e.g., Bamford et al. 2006; Metevier et al. 2006; Nakamura et al. 2006) and adopt $\log(2V_{MAX})$ as the dependent variable in the fit, such that

$$\log(2V_{MAX}) = a + b * M_{V,K} \quad (4.4)$$

where we fit for intercept a and slope b . This is the so-called inverse TF, which is less sensitive to bias due to luminosity incompleteness (Willick 1994; Schechter 1980). For each TF relation, cluster and field, V and K_S bands, the intrinsic scatter is that portion of the measured scatter that cannot be explained by measurement error. We estimate the intrinsic scatter by considering the reduced χ^2 statistic. Following Bamford et al. (2006), we iteratively determine the scatter that we need to add to our measurement errors in order to achieve $\chi_r^2 = 1$. The best inverse fit parameters for all four subsamples are listed in Table 4.2. We note that the zero points and slopes are indistinguishable between cluster and field; as we will discuss below, only the scatter in the relation differs between cluster and field.

Field galaxies show a tight TF relation in both bands, with slope consistent with the local relation (Verheijen 2001). We find an intrinsic scatter of 0.35 mag in V and 0.5 mag in K_S , again restricting ourselves to $Q = 1$ rotation curves brighter than our magnitude cut. The seemingly higher intrinsic scatter in K_S is at odds with the expectation that lower dust extinction in the K_S -band should make the TF tighter

Table 4.2. Inverse fits to Tully-Fisher relation

Sample	a	b	RMS ($\Delta \log(2V_{MAX})$)	RMS ($\Delta M_{K,V}$)
Field K_S	-0.7 ± 0.3	-0.14 ± 0.01	0.07 ± 0.01	0.5 ± 0.05
Cluster K_S	-0.5 ± 0.2	-0.14 ± 0.01	0.17 ± 0.01	1.18 ± 0.05
Field V	-2.1 ± 0.4	-0.22 ± 0.02	0.08 ± 0.01	0.35 ± 0.05
Cluster V	-1.9 ± 0.2	-0.20 ± 0.01	0.19 ± 0.01	0.93 ± 0.05

than in bluer bands, and our result seems to indicate that we underestimate the measurement uncertainties. However, the shallower slope of the K_S -band TF causes its scatter, when expressed in magnitudes, to be more sensitive to small errors in the measured V_{MAX} . In fact, expressed in terms of $\Delta \log(V_{MAX})$, the field sample scatter in V and K_S are indistinguishable, yielding 0.08 ± 0.01 and 0.07 ± 0.01 , respectively. As measurement uncertainties are generally largest in the V_{MAX} direction, this simply indicates that absolute magnitude is more properly the independent variable in our TF relation. In the following we will preferentially express the TF scatter in terms of $\Delta \log(2V_{MAX})$, except when comparing to other authors.

The 0.35 mag scatter we find in V is comparable to the 0.38 mag R -band scatter reported by Verheijen (2001) for nearby galaxies. Our K_S -band scatter of 0.5 mag is about 50% larger than their reported 0.31 mag. However, Kannappan et al. (2002) have suggested that, because local studies tend to weed out kinematically irregular galaxies, the true scatter, if a more representative sample of spirals is selected, could actually be much higher. At intermediate redshift, small irregularities in rotation curves are harder to detect, due to limited spatial resolution, and so a higher measured scatter might reasonably be expected.

Even so, the scatter we measure for the field TF is significantly lower than has been found by other authors at intermediate redshift (e.g., Nakamura et al. 2006; Böhm et al. 2004; Bamford et al. 2006). In a recent large study of 89 field galaxies, Bamford et al. (2006) measure an intrinsic scatter in the B -band TF of 0.9 mag, significantly larger than our measured V -band scatter, though they include galaxies

across a larger redshift range. In the redder bands that we measure, we can see that a tight TF relation still exists in the field at lookback times of over 5 Gyr.

In stark contrast to the field TF, the relation that we measure for cluster spirals (lower panels of Figure 4.4) shows a remarkably high scatter, $\Delta \log(V_{MAX}) = 0.19 \pm 0.01$ (0.93 mag) and 0.17 ± 0.01 (1.18 mag) in V and K_S , respectively. These values are each more than twice as large as the scatter in our field sample. This cannot be understood in terms of higher measurement error in the cluster sample, as the two samples were selected in the same way from the same parent data set, and we have restricted the analysis to only the highest-quality rotation curves ($Q = 1$). When we include all 77 rotation curves ($Q = 1$ and $Q = 2$), we observe the same difference between cluster and field, but with overall higher measurements of scatter.

4.4.1 A Comparison to Independent Measurements

Recently, Metevier et al. (2006) have also published a Tully-Fisher relation for the cluster Cl 0024, examining rotation curves of 15 spirals. Four of the galaxies in their sample are in common with our own, allowing us for the first time to evaluate the agreement between repeat observations and independent analysis of intermediate redshift spiral rotation curves. In our sample, galaxies p0i27c3, p0i145c4, p0i163c4, and p19i2c4 correspond to their TFR05, TFR07, TFR10, and TFR12, respectively.

Visual comparison of their observed rotation curves to our own (Figure 4.2) indicates that they are of comparable quality, but with some differences in rotation curve extent. Comparing our estimates of V_{MAX} to their V_{ARC} , we find an RMS difference of $\Delta V/V = 34\% \pm 17\%$, with individual measurements differing by as much as 100 km s^{-1} . Three out of four measurements differ by more than 2σ .

In Metevier et al. (2006), V_{ARC} is conceptually identical to our V_{MAX} : both attempt to measure the broad flat part of each spiral's rotation curve. Furthermore, our procedure for modeling the rotation curve follows steps very similar to their GAUSS2D code. However, we each adopt slightly different rotation curve functions; they use an arctan function to approximate $V(R)$, while we use the function given in

Equation 4.2, adopted from Böhm et al. (2004).

To test the effect of adopting a different rotation curve function, we rerun our model fits for the four galaxies in common with Metevier et al. (2006), this time fitting the observed rotation curves to an arctan function, and adopting the best-fit scale lengths from their paper. We find that adopting their rotation curve function brings two of our four velocity measurements into agreement. For the two other objects, variations in the observed rotation curves may explain the discrepancy. In p0i163c4/TF10, Metevier et al. (2006) uncover a downturn in the rotation curve at high radius, which is not reached by our own data. Conversely, for object p0i145c4/TF12, our rotation curve extends to larger radius and reveals that the velocity continues to increase beyond the end of the curve measured by Metevier et al. (2006).

It is striking that such a small difference in the choice of rotation curve function can yield such a large difference in the resulting velocity value. When comparing their results to other Tully-Fisher studies, Metevier et al. (2006) take pains to comprehensively account for many of the systematic differences between studies, most having to do with the way velocities were measured or defined. They show that these small differences greatly affect estimates of the average luminosity evolution of spirals as a function of redshift. Because of the difficulty in comparing TF relations across samples, and the additional, previously underappreciated systematic arising from the choice of rotation curve function, we do not attempt in this study to make a rigorous estimate of the luminosity evolution implied by our TF zero point.

In fact, generally, and for our present goal of studying environmental influences on spiral galaxies, these variations between studies highlight the importance of matched samples of cluster and field spirals. Our current matched sample, which contains the largest number of cluster galaxies so far, allows us to move beyond the Tully-Fisher relation, to study directly the kinematics of spirals galaxies in the hope of uncovering the source of the large scatter seen in the cluster TF relation.

4.5 Trends in Spiral Masses, Densities, and M/L

Movement of a galaxy in the TF plane can be caused by various effects. Increased star formation or dustiness moves a galaxy along the luminosity axis, while increased total mass, changes to the radial mass profile, or other kinematic disturbances can alter a galaxy's measured V_{MAX} . In this section, we attempt to identify the source of the high scatter observed in the cluster TF, compared to the field in the same redshift range. Because our cluster sample spans a large range in cluster-centric radius, it makes sense to examine the residuals of the TF and other dynamical characteristics of the cluster spirals as a function of environment within the clusters.

4.5.1 Tully-Fisher Residuals and M/L

We first turn toward the simplest quantity to examine: the residuals from the TF, considered to represent a change in mass to light ratio (M/L). The higher scatter seen in the cluster TF, compared to the field, could plausibly be due to changes in star formation rate or dust obscuration as galaxies fall into the cluster. This could cause a radial gradient in M/L , which we would observe as an increased TF scatter.

However, because enhanced scatters are measured in both V - and K_S -band TF relations, we do not expect that the enhancement can be solely attributed to an increase or decrease in star formation or dust during cluster infall. If such a scenario were the main driver of the scatter, we would expect that the V -band scatter would be higher than the K_S -band, yet they are broadly equivalent. We would also expect to see a correlation between TF residuals and other indicators of star formation rate or dustiness. To test this, we plot, in Figure 4.5, the V -band TF residuals versus $V - K_S$ color for all galaxies in our cluster sample. Here, and for the rest of this chapter, residuals are plotted in the sense that a positive residual is overluminous for its measured velocity, or, alternatively, has an anomalously low V_{MAX} given its luminosity. No obvious correlation is observed in Figure 4.5. While several of our objects with lowest measured V_{MAX} are not plotted here because they do not have K_S detections, these were also excluded from the TF relation fitting, and so are not

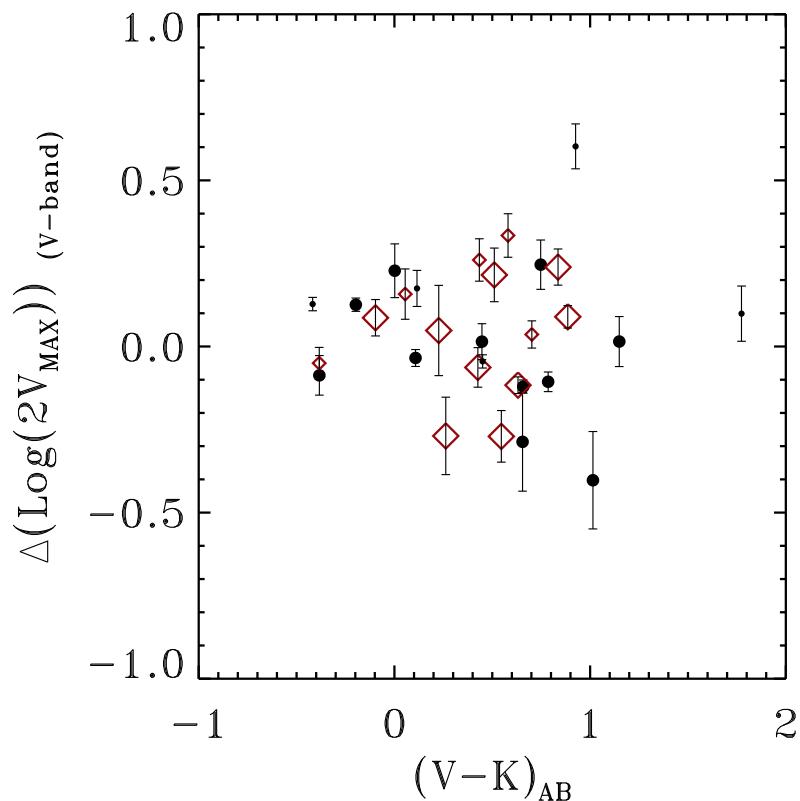


Figure 4.5 The residuals from the local V -band Tully-Fisher relation, in the $\log(2V_{MAX})$ direction, versus rest $(V - K_S)_{AB}$ color. Magnitudes are corrected for inclination-dependent internal extinction, as discussed in the text. Symbols are coded as in Figure 4.4.

the source of the enhanced scatter.

Even though star formation rate and dust content do not appear to correlate with TF residuals, the galaxies of our cluster sample span a wide range of environments, and so we also examine whether the increased TF scatter is related to a gradient in M/L across the cluster, as might be the case if spirals in the outskirts have formed more recently than those in the cluster cores. In Figure 4.6, we plot the TF residuals as a function of R/R_{VIR} , the projected cluster-centric radius scaled by each cluster's Virial radius: 1.7Mpc for Cl 0024 (T03) and 2.7 Mpc for MS 0451 (Chapter 6). As MS 0451 is much more massive than Cl 0024, a galaxy at 1 Mpc radius in Cl 0024 experiences a very different environment from a galaxy at the same radius in MS 0451. As we will see below, some key trends emerge when we choose to scale by Virial radius,

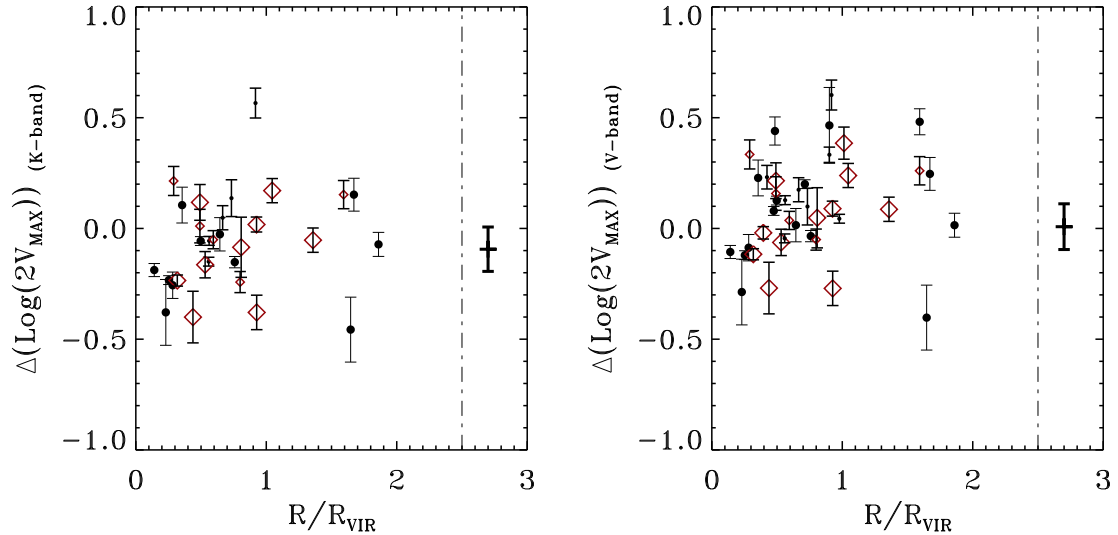


Figure 4.6 The residuals from the local Tully-Fisher relation as a function of normalized projected radius, R/R_{VIR} . Symbols are coded as in Figure 4.4. Black crosses to the right of the dash-dotted line indicate the median and RMS residuals of the field TF. Positive residuals indicate that a galaxy is overluminous for its measured velocity, or, alternatively, has an anomalously low V_{MAX} given its luminosity.

rather than plotting radius directly on the x -axis.

Examined by eye, the residuals from the V band TF in Figure 4.6 (right panel) hint at a radial gradient as a function of R/R_{VIR} , with galaxies at higher radius seeming to be overluminous. However, straight line fits to the V and K_S band residuals find a small gradient toward higher radius, but with slope no greater than the error bar on a typical point. A simple gradient in star formation rate or M/L across the cluster therefore cannot be the only mechanism responsible for the increased scatter in the cluster TF compared to the field. We note, however, that we cannot rule out the possibility that several different mechanisms are simultaneously contributing to the TF scatter by acting on spirals in different environments within the clusters.

4.5.2 Densities and Masses

Since variations in star formation rate and dust content alone cannot account for the observed scatter in the cluster TF, we are led to consider the idea that the cluster spirals are more kinematically disturbed than their field counterparts. One

way to test for disturbed dynamics in a spiral galaxy is to consider the photometric effective radius, r_s , of each galaxy. We can combine r_s with V_{MAX} to calculate two fundamental dynamical properties of spiral disks: dynamical mass, $M(< r) \propto V^2 r$ and central surface mass density, $\Sigma_m(< r) \propto V^2/r$. Unlike the Fundamental Plane of ellipticals, the Tully-Fisher relation in the local universe does not seem to have any dependence on galaxy size (r_s) (e.g., Verheijen 2001). Therefore, in an undisturbed population of spirals, we would not expect to uncover any independent environmental trends in quantities that only depend on r_s and V_{MAX} . Any trends that do exist must be the result of some cluster-related physical process.

In fact, surface densities allow us to directly probe for the action of a key physical mechanism, galaxy harassment (Moore et al. 1999). Harassment is predicted to have a stronger effect on the least dense galaxies falling into a cluster, to the point of completely disrupting the most tenuous spirals. Any observed gradient in the mean density of spirals could then implicate the action of this physical process.

We choose to study M and Σ_m within a radius of $1.25r_s$, a characteristic radius chosen because it is typically reached in all of our observed rotation curves, and it is a radius at which most of our rotation curves have already leveled off to V_{MAX} .

In Figure 4.7, we plot galaxy density as a function of projected radius R (bottom panel) as well as the normalized quantity R/R_{VIR} (top). In the top panel, one notices a striking break in the densities of spirals at approximately $1R_{VIR}$. Near and outside of this radius, spirals seem to exhibit nearly uniformly low central densities, which are puzzlingly even lower than those of field galaxies in the sample. Within the Virial radius, on the other hand, a large spread in densities is seen, and perhaps a radial gradient of decreasing density outward from the cluster center. In the lower panel, this trend appears scrambled, indicating that whatever physical process may cause this effect, its strength scales as the cluster Virial radius. This observation rules out several possible mechanisms, and will be discussed further in the next section.

It is natural to wonder if the observed break in density as a function of radius is due to simple luminosity segregation: if more massive spirals are found near the cluster center, perhaps these also have higher central densities. However, by consulting

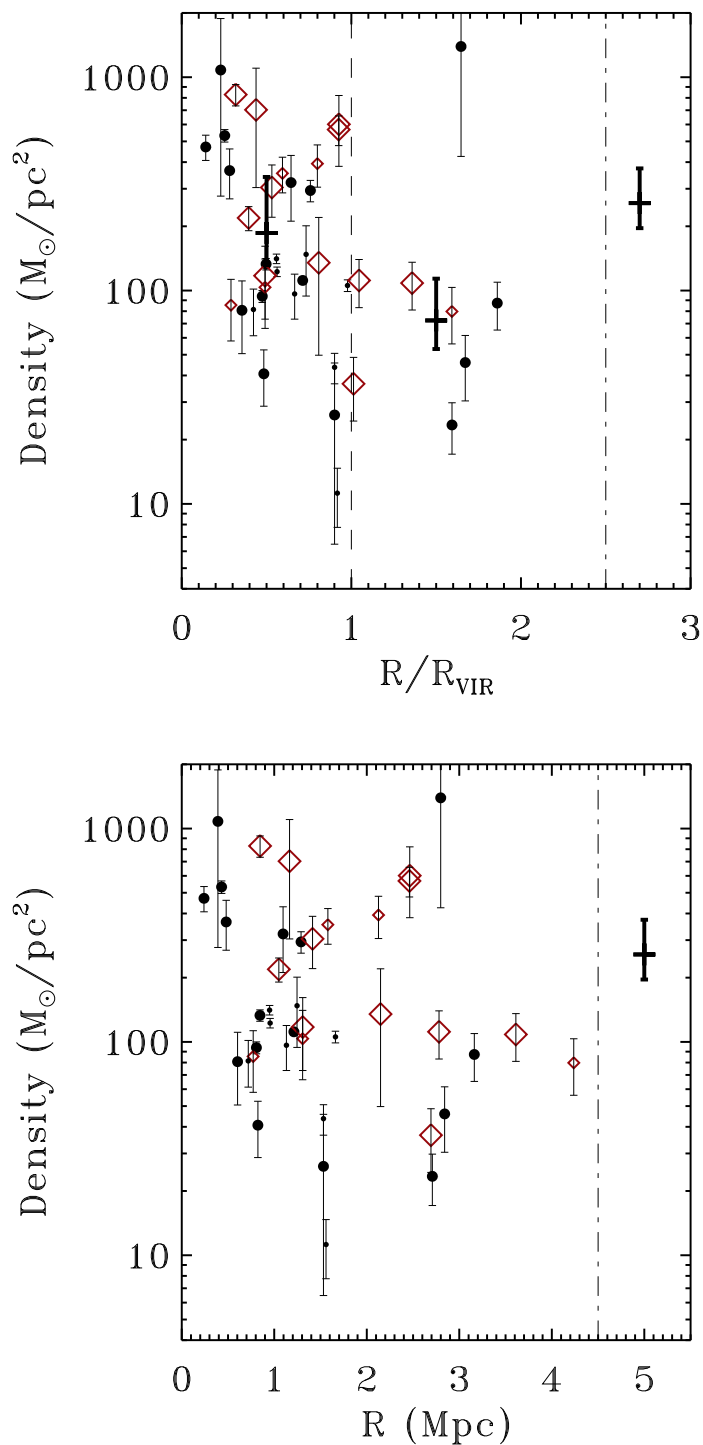


Figure 4.7 Top: Projected central density of cluster spirals, measured within $1.25r_s$, versus R/R_{VIR} , calculated according to $\Sigma_m(< r) = V^2/(Gr)$ Bottom: Central density versus R . In both panels, the thick cross to the right of the dash-dotted line indicates the median density for the field sample. At top, additional thick crosses indicate the median densities inside and outside $1 R_{\text{VIR}}$. Symbols are coded as in Figure 4.4.

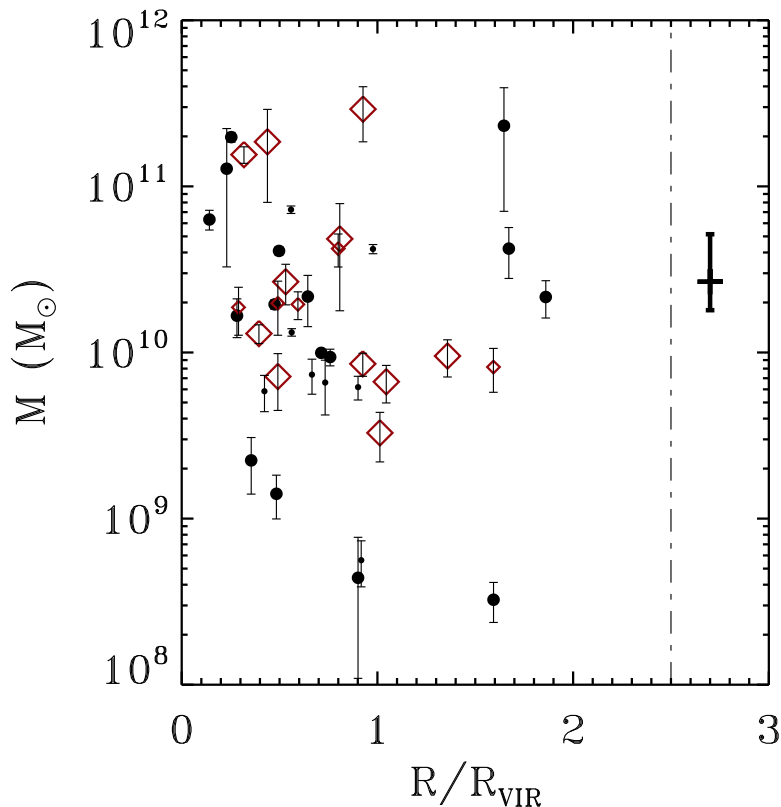


Figure 4.8 Dynamical mass (within $1.25r_s$) as a function of R/R_{VIR} , calculated according to $M(< r) = V^2 r / G$. We find galaxies with a range of dynamical masses, both within and outside of the Virial radius. Symbols are coded as in Figure 4.4. The median for the field sample is displayed to the right of the dash-dotted line.

Figure 4.8, where we plot dynamical mass as a function of R/R_{VIR} , it becomes apparent that this is not the case. The low density spirals found in the clusters' outskirts in fact exhibit a wide spread in total mass. Because the total number of observed spirals in the cluster outskirts is small, K-S tests comparing the distributions of mass and density for low-R vs. high-R spirals are inconclusive. However, the cluster sample as a whole does exhibit a larger overall spread in Σ_m than the field sample, and includes a larger fraction of both low and high-density spirals: a K-S test gives a 1.3% chance that the two samples are drawn from the same parent distribution. This indicates that the cluster environment may be affecting the internal mass distributions of spirals at all cluster radii.

4.6 Discussion

What physical mechanisms, then, could be acting on cluster spirals to reproduce both the overall higher scatter in the TF and the observed radial trend in density? The effects seem to persist as far as $2R_{VIR}$ from the cluster cores, so even though some of the observed galaxies at high radius may be part of a “backsplash population”, it is very unlikely that nearly all star forming spirals in our sample have already been through the cluster center. Therefore, we do not think it likely that tidal processes are responsible, as they are only strong near the cluster center. Instead, we can consider several proposed physical mechanisms that are strong enough at large radius to alter the dynamics of a spiral, either directly or indirectly.

In the cluster outskirts, recent mergers are an obvious candidate to drive both the large TF scatter and the abnormally low densities (see Chapter 1). Mergers are less common in the low density field, and this could explain why we do not see any low-density spirals in our field sample. Unknown selection biases, though, could prevent us from including similar field galaxies in our Tully-Fisher sample. If the effects of a recent merger last for at least 1 Gyr (Bekki 1998), then recent mergers can affect the TF scatter even in the cluster core. Therefore, we can not rule out the possibility that increased merging in the cluster outskirts serves to drive a high fraction of cluster spirals away from the TF relation.

In the inner regions of galaxy clusters, mergers are suppressed due to the high relative speeds of galaxies, which prevent the creation of a gravitationally bound pair during close encounters. Instead, an infalling cluster galaxy is likely to experience repeated close encounters at high speed due to the high density of galaxies in the cluster. This process, called galaxy–galaxy harassment, can lead to dramatic changes in a galaxy. Moore et al. (1999) have shown through simulations that the fate of a harassed galaxy depends on its original mass and central density. Strongly concentrated Sa/Sb type galaxies were seen to puff up their disks during infall, and so harassment may represent one way in which spirals transform into S0s in clusters. On the other hand, lower density Sc/Sd spirals are more strongly affected by harassment; Moore

et al. (1999) found that they were either completely disrupted, or else transformed into an object resembling a dwarf galaxy.

If harassment is acting to transform the lowest density spirals into dwarfs, then we would expect to observe a deficit of such low-density spirals near the cluster cores. High-density spirals, on the other hand, should be more resistant to harassment, and are likely to persist to smaller cluster radii. This prediction qualitatively matches the trend in densities seen in Figure 4.7, but the picture is unclear. The puzzling lack of high-density galaxies at large cluster radius, and the persistence of low-density galaxies to $\sim 0.5R_{VIR}$ raise questions about this interpretation. We have already seen in Figure 4.8 that galaxies of a wide range of masses are represented in the cluster outskirts, so harassment alone may not present a complete explanation for the observations. Frequent mergers in the cluster outskirts, however, could very well provide the missing ingredient for keeping spiral densities low there.

Finally, we consider processes that depend on the hot intracluster medium (ICM). Generally, even strong interactions with the ICM like ram-pressure stripping are thought to be too weak to explain the observed disruptions in the kinematics of spiral disks (Quilis et al. 2000). Rather, such ICM-related processes act largely to suppress star formation within infalling disks. Since changes in star formation rate do not appear to be responsible for the increased scatter in the cluster TF, it is unlikely that an ICM-related process is involved. However, it is possible that shock fronts within the ICM can enhance the ICM's ability to affect a spiral disk even at high cluster radius (Chapter 3). Cl 0024 may be undergoing a face-on merger with a large group (Czoske et al. 2002), and so shocks may be important in this cluster. Shocks in the ICM may induce centrally concentrated starbursts within infalling cluster galaxies, but it is not clear that such an interaction would generate emission lines with enough spatial extent to allow measurement of rotation curves. Further, since all ICM related processes suppress star formation over time, our sample of exclusively star-forming spirals can only provide an incomplete picture at best of the effects of ICM shocks.

One possible concern with our result on the cluster TF relation is that cluster to

cluster variation could be high (as seen for example by the MORPHS and EDISCS studies, (Poggianti et al. 1999; White et al. 2005)). In fact, previous studies of Cl 0024 have shown that its galaxy population may be overly active, possibly due to the ongoing merger with a foreground large group (Czoske et al. 2002). Indeed, we saw in Chapter 3 that the Fundamental Plane of elliptical and S0 galaxies in Cl 0024 exhibits a higher scatter than found in most other intermediate redshift clusters (e.g., Kelson et al. 2000b), though this effect is most significant in the inner 1 Mpc of the cluster. It is possible that the increased TF scatter we see is connected to the similarly enhanced Fundamental Plane scatter. However, while our cluster TF includes a majority of points from Cl 0024 (24 galaxies cf. 16 for MS 0451), it seems clear by inspection of Figure 4.4 that MS 0451 also contains spirals that deviate highly from the local TF. As MS 0451 is thought to be in a more advanced stage of cluster assembly than Cl 0024 (Chapter 6), the universality of our measured TF scatter remains uncertain until similarly large samples for several more intermediate redshift clusters become available.

4.7 Conclusions

In this work, we have studied the dynamics of cluster and field spirals at intermediate redshifts, via an analysis of their optical rotation curves.

We have presented one of the most complete Tully-Fisher relations available for both cluster and field spirals at these redshifts, and have demonstrated that the field relation is quite tight even at these high look back times. In contrast, the cluster TF exhibits a remarkably high scatter. By comparing the trends of Tully-Fisher residuals vs radius with those in colors and local mass density we found that the increased scatter cannot be explained solely in terms of environmental effects on the star formation rates of infalling galaxies. We therefore proposed that the increased scatter in the Tully-Fisher relation is due to kinematic disturbances, as expected for example for cluster harassment.

We also found a trend in galaxy mass density as a function of cluster centric radius

in the sense that spiral galaxies are denser in the central regions of clusters. This is expected if harassment plays a significant role, as the densest disks would be most likely to survive during the infall. However, we found a paucity of high-density spiral galaxies in the cluster outskirts, which cannot be explained by harassment alone. We suggest that a combination of enhanced merging in the cluster outskirts with galaxy harassment in the intermediate and inner cluster regions may be required to explain the observed trend in galaxy density.

Larger matched samples covering a larger number of galaxy clusters are needed to determine if the observed trends are universal across clusters at these redshifts.

Acknowledgements We thank Daisuke Nagai, Andrew Benson, and Kevin Bundy for valuable discussions.

Table 4.3: Information and rotation measurements of Cl 0024, MS 0451, and field spirals

Object	Sample	z	RA [deg]	DEC [deg]	r_s [kpc]	i [deg]	SI PA [deg]	M_V [mag]	M_K [mag]	V_{MAX} [km/s]	Q
(1)	(2)	(3)	(4)	(5)	(6)	(7)	(8)	(9)	(10)	(11)	
p0i27c3	Cl0024	0.392	6.639747	17.156639	5.23	54.2	11	-21.80±0.05	-22.58±0.06	219 ± 14	1
p38i14c3	Cl0024	0.400	6.631994	17.154470	4.91	50.5	60	-21.67±0.06	-22.32±0.06	322 ± 119	1
p0i163c4	Cl0024	0.394	6.674678	17.164650	8.70	62.0	3	-22.89±0.09	-23.55±0.05	300 ± 10	1
p0i145c4	Cl0024	0.399	6.676911	17.158810	3.05	28.2	13	-20.43±0.07	-20.05±0.30	147 ± 19	1
N36671	MS0451	0.527	73.521355	-2.994348	6.68	39.6	36	-22.89±0.07	-23.47±0.05	105 ± 16	2
N37826	MS0451	0.530	73.523247	-2.988543	6.18	57.4	10	-23.12±0.06	-23.75±0.05	316 ± 18	1
p38i122c2	Cl0024	0.390	6.618957	17.155710	2.38	36.1	41	-19.84±0.06	-19.84±0.32	61 ± 11	1
N35977	MS0451	0.531	73.506584	-2.993443	3.48	67.4	13	-20.30±0.07	—	122 ± 7	1
p37i110c3	Cl0024	0.377	6.671664	17.129601	3.82	80.4	22	-20.81±0.07	—	78 ± 9	2
P51837	MS0451	0.526	73.566147	-3.065880	7.33	62.3	55	-21.77±0.08	-22.04±0.05	317 ± 90	1
p37i18c3	Cl0024	0.392	6.676580	17.128189	6.50	69.8	0	-20.75±0.05	—	109 ± 3	1
p36i29c3	Cl0024	0.400	6.616654	17.189550	2.66	79.8	29	-20.62±0.07	—	45 ± 6	1
N25094	MS0451	0.535	73.499481	-3.053076	6.24	68.7	42	-21.56±0.07	-21.61±0.06	112 ± 20	2
P62230	MS0451	0.530	73.562500	-3.073720	3.53	55.2	44	-21.21±0.06	-21.72±0.05	89 ± 16	1
p36i77c4	Cl0024	0.396	6.640263	17.205460	7.91	77.6	0	-22.22±0.06	-22.02±0.10	143 ± 4	1
P63232	MS0451	0.538	73.494949	-2.982716	4.23	47.4	28	-20.92±0.06	-21.35±0.06	158 ± 21	1
p37i2c3	Cl0024	0.377	6.676347	17.117929	10.23	75.5	0	-21.31±0.13	-21.76±0.20	167 ± 4	2
p36i37c4	Cl0024	0.388	6.630331	17.208891	4.69	69.2	1	-21.07±0.06	-20.65±0.23	105 ± 2	2
P54663	MS0451	0.541	73.597534	-3.063867	3.35	56.1	21	-21.65±0.06	-22.35±0.05	152 ± 14	2
p19i2c4	Cl0024	0.396	6.591903	17.168131	3.71	31.0	29	-21.47±0.06	-22.62±0.05	152 ± 26	1
p19i1c4	Cl0024	0.397	6.595224	17.186880	3.94	32.8	8	-20.69±0.07	-20.80±0.20	86 ± 10	2
p13i19c4	Cl0024	0.381	6.617717	17.218800	4.26	78.8	0	-21.34±0.05	—	96 ± 1	1
p23i151c2	Cl0024	0.393	6.679020	17.103390	3.02	23.8	21	-20.32±0.05	-22.09±0.06	93 ± 16	2

Table 4.3 — Continued

Object	Sample	z	RA [deg]	DEC [deg]	r_s [kpc]	i [deg]	SI PA [deg]	M_V [mag]	M_K [mag]	V_{MAX} [km/s]	Q
(1)	(2)	(3)	(4)	(5)	(6)	(7)	(8)	(9)	(10)	(11)	
p18i234c4	Cl0024	0.396	6.721228	17.167561	2.55	62.9	16	-20.14±0.08	-20.25±0.29	121 ± 6	1
N27099	MS0451	0.550	73.635056	-3.040075	4.67	77.9	29	-21.73±0.06	-21.35±0.07	189 ± 21	2
N49410	MS0451	0.528	73.533180	-2.924410	8.54	35.4	53	-21.70±0.05	-21.93±0.05	150 ± 47	1
p24i55c2	Cl0024	0.388	6.639475	17.082970	1.85	71.6	27	-19.29±0.09	—	30 ± 11	1
p25i136c3	Cl0024	0.395	6.584536	17.114901	5.37	81.9	24	-21.16±0.08	—	67 ± 5	2
p24i1c2	Cl0024	0.392	6.646124	17.081320	3.19	60.4	13	-19.93±0.10	-20.85±0.24	26 ± 4	2
N46608	MS0451	0.540	73.473412	-2.938749	1.75*	61.1	21	-21.79±0.05	-22.67±0.05	139 ± 13	1
N48527	MS0451	0.544	73.488052	-2.927898	9.94	50.3	40	-22.05±0.05	-22.60±0.05	341 ± 62	1
p13i15c2	Cl0024	0.397	6.598421	17.232731	9.00	75.9	0	-21.29±0.05	—	136 ± 4	2
N34128	MS0451	0.534	73.427948	-3.003162	4.28	75.5	3	-20.84±0.06	—	55 ± 9	1
N48766	MS0451	0.551	73.469215	-2.925409	3.49	33.9	26	-21.30±0.05	-22.14±0.05	87 ± 11	1
N47732	MS0451	0.534	73.413109	-2.930732	4.23	46.3	24	-20.26±0.06	-20.17±0.15	94 ± 11	1
N64729	MS0451	0.540	73.520599	-2.835176	4.57	44.2	38	-21.37±0.06	-21.80±0.05	84 ± 12	2
p7i72c2	Cl0024	0.373	6.597922	17.299730	1.68	46.0	18	-19.04±0.07	—	27 ± 3	1
p30i4c3	Cl0024	0.393	6.552849	17.050751	5.82	35.8	54	-21.46±0.13	-22.48±0.10	398 ± 138	1
p10i41c4	Cl0024	0.396	6.801073	17.199739	13.68	41.4	30	-22.30±0.10	-23.04±0.05	110 ± 18	1
p33i308c4	Cl0024	0.382	6.603914	17.000919	7.10	46.8	26	-20.21±0.05	-20.65±0.25	110 ± 13	1
p5i171c4	field	0.313	6.742421	17.238001	3.43	74.8	0	-20.77±0.11	-21.38±0.07	99 ± 3	1
N33315	field	0.314	73.373642	-3.008564	4.16	55.8	47	-21.67±0.13	—	159 ± 29	1
N22367	field	0.325	73.610954	-3.070553	5.06	74.7	45	-21.95±0.05	-22.29±0.05	185 ± 34	1
N47194	field	0.326	73.525711	-2.939083	7.08	33.0	44	-21.81±0.06	-22.27±0.05	172 ± 43	1
N58982	field	0.326	73.631409	-2.867468	4.26	44.3	14	-20.04±0.06	-19.57±0.17	115 ± 10	1
N11649	field	0.329	73.513878	-3.123671	2.40	57.4	42	-20.53±0.07	-21.36±0.05	80 ± 14	1
N30997	field	0.333	73.444008	-3.020530	2.59	62.4	20	-20.55±0.06	-21.05±0.05	104 ± 8	1

Table 4.3 — Continued

Object	Sample	z	RA [deg]	DEC [deg]	r_s [kpc]	i [deg]	SI PA [deg]	M_V [mag]	M_K [mag]	V_{MAX} [km/s]	Q
(1)	(2)	(3)	(4)	(5)	(6)	(7)	(8)	(9)	(10)	(11)	
N11932	field	0.362	73.463303	-3.124372	3.95	41.0	67	-20.96±0.06	-21.27±0.05	235 ± 133	1
N48819	field	0.363	73.460930	-2.927250	1.93	28.1	26	-20.41±0.05	-21.16±0.05	83 ± 10	2
N55288	field	0.364	73.419220	-2.892889	5.20	62.6	50	-20.56±0.06	-20.23±0.08	113 ± 17	2
N37713	field	0.367	73.467995	-2.987958	4.95	27.2	0	-21.06±0.05	-21.91±0.05	204 ± 20	1
N21079	field	0.371	73.350967	-3.074297	2.86	42.9	33	-20.45±0.05	-21.42±0.05	118 ± 18	1
N31950	field	0.371	73.444237	-3.017617	3.69	55.2	41	-21.43±0.05	-22.03±0.05	182 ± 32	1
N35309	field	0.390	73.625328	-2.996757	3.32	66.3	21	-21.18±0.05	-21.51±0.05	131 ± 11	1
N57426	field	0.391	73.473892	-2.878548	3.73	60.3	38	-21.66±0.05	-22.98±0.05	274 ± 43	1
N18456	field	0.401	73.598076	-3.087556	4.13	61.0	14	-21.55±0.05	-22.13±0.05	182 ± 11	1
N35519	field	0.413	73.426918	-2.997052	3.83	40.8	43	-20.43±0.05	-20.76±0.06	135 ± 27	2
N19992	field	0.419	73.515671	-3.081446	6.52	51.5	4	-21.36±0.20	—	121 ± 11	1
N18483	field	0.425	73.465881	-3.088012	4.56	71.7	3	-22.18±0.05	-22.83±0.05	177 ± 6	1
p17i129c4	field	0.443	6.766013	17.151690	10.24	84.6	2	-22.69±0.07	-21.99±0.20	215 ± 3	2
N36846	field	0.447	73.670662	-2.991703	2.73	45.3	0	-21.60±0.05	-22.75±0.05	180 ± 11	1
N40959	field	0.447	73.624619	-2.969724	3.40	34.8	13	-22.12±0.05	-22.88±0.05	187 ± 19	1
N41465	field	0.447	73.629173	-2.963893	4.67	74.7	21	-21.33±0.05	-20.84±0.08	142 ± 11	1
N56286	field	0.463	73.505577	-2.884414	4.59	53.6	3	-21.53±0.05	-21.70±0.05	209 ± 10	1
p11i11c4	field	0.476	6.724503	17.193130	2.77	27.3	18	-20.51±0.09	-20.69±0.27	74 ± 13	1
N25636	field	0.491	73.394081	-3.050711	6.04	28.5	15	-21.67±0.06	-22.66±0.05	174 ± 22	2
p8i163c3	field	0.492	6.569071	17.296320	3.14	56.7	7	-20.97±0.10	-21.55±0.19	128 ± 5	1
N59564	field	0.494	73.547920	-2.870288	4.66	71.4	22	-22.00±0.05	-22.16±0.05	172 ± 15	1
p1i97c4	field	0.494	6.770693	17.324760	3.00*	38.8	16	-21.59±0.06	-22.20±0.12	59 ± 8	2
N11338	field	0.505	73.540504	-3.126556	5.12	36.2	33	-21.76±0.06	-22.80±0.05	258 ± 45	1
N25124	field	0.506	73.698349	-3.052146	7.84	39.4	44	-21.90±0.06	-22.83±0.05	194 ± 45	1

Table 4.3 — Continued

Object	Sample	z	RA [deg]	DEC [deg]	r_s [kpc]	i [deg]	SI PA [deg]	M_V [mag]	M_K [mag]	V_{MAX} [km/s]	Q
(1)	(2)	(3)	(4)	(5)	(6)	(7)	(8)	(9)	(10)	(11)	
p23i180c2	field	0.536	6.677425	17.101549	5.56	56.0	14	-21.26±0.07	-22.08±0.14	146 ± 10	1
p21i99c3	field	0.537	6.475233	17.202730	2.68	36.1	3	-20.93±0.05	-20.97±0.28	157 ± 14	1
N37427	field	0.579	73.516296	-2.988545	5.59	31.0	43	-22.45±0.06	-23.48±0.05	215 ± 53	1
p34i20c3	field	0.595	6.533985	16.984360	4.26	53.3	2	-21.15±0.05	-21.06±0.32	109 ± 7	1
N41286	field	0.600	73.466621	-2.966479	2.53	43.0	22	-21.33±0.05	-20.67±0.11	107 ± 12	1
p34i94c2	field	0.614	6.553948	16.984819	11.47	38.2	30	-21.23±0.07	-21.58±0.33	251 ± 37	2

Cluster galaxies are arranged in order of increasing R/R_{VIR} , where $R_{VIR} = 1.70$ Mpc for Cl 0024 and $R_{VIR} = 2.66$ for MS 0451. The cluster centers are (6.6500, 17.1433) and (73.5454, -3.0186) J2000, for Cl 0024 and MS 0451, respectively. Field galaxies are arranged in ascending redshift order. Col. (1): Object name. Col (2): Indicates which subsample that each galaxy belongs to: Cl 0024, MS 0451, or field. Col (3): Redshift of each galaxy. Cols (4) and (5): J2000 coordinates for each galaxy. Cols (6) and (7): Scale lengths r_s and inclinations i measured via GALFIT. $i = 90^\circ$ indicates edge on. * Denotes objects where R_S was set manually to improve the fit. Col (8): Indicates the misalignment between the PA of the spectroscopic slit and the major axis of the galaxy. Typical formal errors on r_s , i , and SI PA are 10%, 0.5°, and 1°, respectively; systematic uncertainties in i and SI PA are typically $\sim 10^\circ$. Cols (9) and (10): Absolute magnitudes in rest-frame V and K bands, corrected for inclination-dependent internal extinction. Col (11): Measured V_{MAX} . In cases where more than one emission line was measured, this is a weighted average. Col (12): Rotation curve quality. $Q = 1$ curves display turnovers on both ends; $Q=2$ curves display only one turnover, or an uncertain fit.

Chapter 5

GALEX Observations of “Passive Spirals” in Cl 0024: Clues to the Formation of S0 Galaxies ¹

We present results from deep *GALEX* UV imaging of cluster Cl 0024 at $z \sim 0.4$. Rest-frame far UV emission is detected from a large fraction of so-called “passive spiral galaxies”—a significant population which exhibits spiral morphology with little or no spectroscopic evidence for ongoing star formation. This population is thought to represent infalling galaxies whose star formation has been somehow truncated by environmental processes, possibly in morphological transition to S0 galaxies. Compared to normal cluster spirals, we find that passive spirals are redder in *FUV*–optical color, while exhibiting much stronger UV emission than cluster E/S0s—as expected for recently truncated star formation. By modeling the different temporal sensitivities of UV and spectroscopic data to recent activity, we show that star formation in passive spirals decayed on timescales of less than 1 Gyr, consistent with “gas starvation”—a process where the cluster environment prevents cold gas from accreting onto the spiral disk. Intriguingly, the fraction of spirals currently observed in the passive phase is consistent with the longer period expected for the morphological transformation and the subsequent build-up of cluster S0s observed since $z \simeq 0.4$.

¹Much of this chapter has been previously published as Moran et al. (2006).

5.1 Introduction

In normal spiral galaxies, the ultraviolet (UV) luminosity depends sensitively on the presence of two components: young, hot stars and dust. UV continuum observations are sensitive to star formation on timescales of less than a few 100 Myr and can thus place strong constraints on both current and recent activity, particularly if independent estimates of dust extinction are available. Due to its wide field of view, the *Galaxy Evolution Explorer (GALEX)* satellite allows an efficient census of the UV content of galaxies (Martin et al. 2005). Here we use *GALEX* imaging to address a key issue in galaxy evolution: the search for objects in morphological transition in intermediate redshift clusters.

It has been known for many years that galaxies in rich clusters are generally bluer and more active at intermediate redshift (Butcher & Oemler 1978). With the aid of *Hubble Space Telescope (HST)* imaging, recent quantitative studies of the evolving morphology–density relation (Dressler et al. 1997; Smith et al. 2005a; Postman et al. 2005) lend support to the suggestion that blue star-forming cluster spirals have been somehow transformed into red S0s (Couch & Sharples 1987). In order to understand how such transformations might occur, several spectroscopic and photometric surveys of intermediate redshift clusters have sought to pinpoint samples of galaxies which are in the (presumed short-lived) *transitional phase* (e.g., Couch et al. 1998; Poggianti et al. 1999; Balogh et al. 1999).

Several candidate object classes have been identified from spectroscopic data utilizing the combination of [O II] emission and Balmer absorption, which are respectively sensitive to ongoing star formation and recent star formation on timescales of $\simeq 1$ Gyr. These include the “E+A” or “k+a” galaxies that exhibit a deep Balmer H δ line (Dressler & Gunn 1983, 1992), and the “e(a)” galaxies that combine [O II] emission with strong Balmer absorption (Poggianti et al. 1999). Recent studies indicate that e(a) spectra are largely associated with dusty starburst galaxies (Poggianti & Wu 2000), and that (k+a)s are associated with the poststarburst remnants of a merger or close encounter (Goto 2005; Tran et al. 2003—but see also Poggianti et al. 2004).

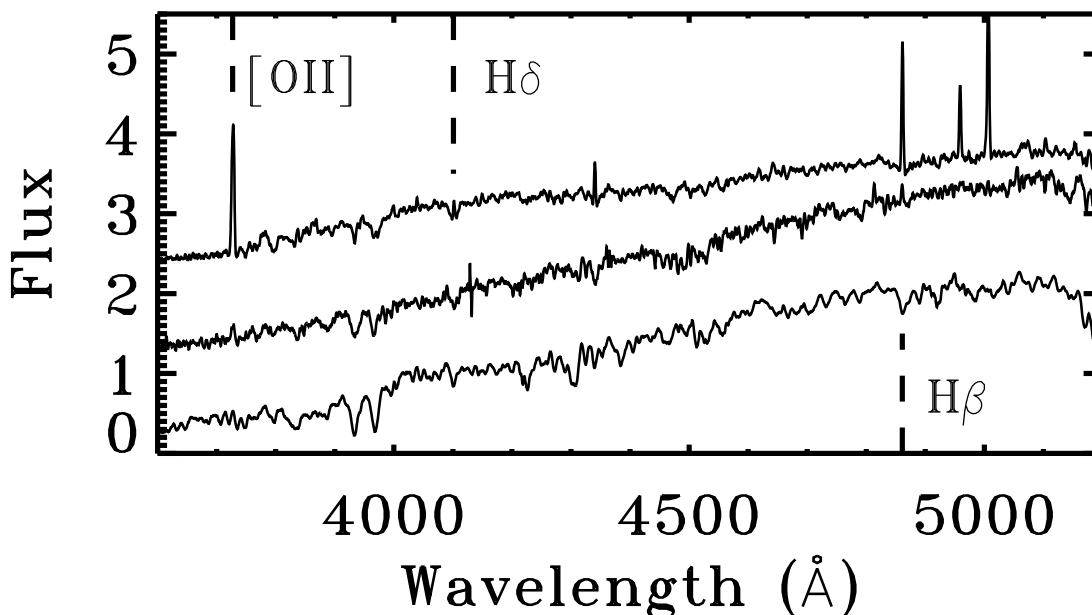


Figure 5.1 Normalized coadded spectra of E+S0 galaxies (lower spectrum), passive (middle) and active (upper) spiral galaxies, offset vertically, in arbitrary units, created as in Chapter 3. Key spectral lines are marked.

However, there are few intermediate redshift S0 galaxies with e(a) or poststarburst spectral signatures (Poggianti et al. 1999). Indeed, in Chapter 3, we found no difference between the stellar populations of Es and S0s in Cl 0024—an unexpected result if S0s were recently created from starbursting systems. Clearly, our understanding of the evolutionary link between e(a)/k+a galaxies and S0s remains incomplete.

Recently, a further interesting class has been identified—the so-called passive spirals (Couch et al. 1998; Dressler et al. 1999; Poggianti et al. 1999; Goto et al. 2003). These objects exhibit spiral morphology in *HST* images, but reveal weak or no [O II] emission. Some authors have suggested that these are spiral-to-S0 transition objects where cessation of star formation occurs on a faster timescale than the transformation of spiral morphology. Such a delay in the morphological transformation would naturally explain the older stellar populations inferred from optical spectra of S0s (Poggianti et al. 1999, Chapter 3). Theoretical models by Bekki et al. (2002) have shown that this scenario is consistent with gas “starvation”, an interaction with the intracluster medium that serves to inhibit star formation by halting the accretion of

cold halo gas onto the galaxy disk (see also Larson et al. 1980, T03). Without further gas accretion, Bekki et al. (2002) found that the spiral arms fade within $\simeq 3$ Gyr.

Goto et al. (2003) find that passive spirals in the SDSS reside preferentially in intermediate density environments, confirming this is a cluster-related phenomenon. Balmer H δ absorption is weaker in passive spirals than in the overall spiral population (Goto et al. 2003; Poggianti et al. 1999), suggesting their stellar populations already resemble the older populations found in E+S0 (“early-type”) galaxies. To date, however, little else is known about the detailed star formation histories of passive spirals.

In this work, we combine *GALEX* UV imaging of Cl 0024 at $z = 0.4$ with our *HST* imaging and Keck spectroscopy to constrain the recent and ongoing star formation rates (SFRs) of passive spirals. By comparing our measurements of UV–optical colors and key spectral lines with model star formation histories, we can for the first time distinguish between several explanations for the nature of the passive spirals.

5.2 Observations and Sample Selection

5.2.1 Data

We make use of *HST* imaging and Keck spectroscopy of Cl 0024+17 from the survey described in Chapter 2. To briefly recap, these data consist of a sparsely sampled mosaic of 39 WFPC2 images taken in the F814W filter ($\sim I$ band), providing coverage to a projected radius of >5 Mpc. Reliable morphological classifications are available to to $I = 21.1$ (T03, Chapter 2) and we combine these classifications with Keck spectroscopy in order to define three samples of cluster members: passive spiral, “active” or star-forming spiral, and E+S0.

Cl 0024+17 was observed for 13.3 ks with *GALEX* in 2004 October (GO-22; Cycle 1; PI Treu) in both near (NUV) and far ultraviolet (FUV) filters (Martin et al. 2005; Morrissey et al. 2005). The NUV band closely matches the rest-frame FUV at $z \simeq 0.4$ ($\lambda_c \sim 1620\text{\AA}$), so we focus on that band. Galaxy fluxes were measured within $6''$ circular apertures, centered on the optical position, and then aperture corrected for

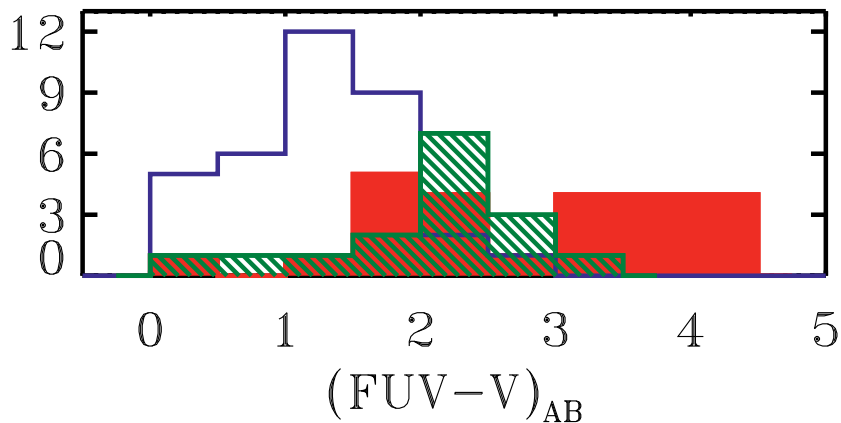


Figure 5.2 The distribution of rest-frame $(FUV - V)_{AB}$ colors for active spiral (blue), passive spiral (hatched green), and early-type (solid red) galaxies.

agreement with SExtractor-derived total magnitudes (`MAG_AUTO`). Using k -correction as described in Chapter 2, we convert observed NUV and F814W fluxes to rest-frame FUV and V luminosities.

In compiling a sample of spirals whose spectra indicate they are passive, we primarily draw from our DEIMOS spectroscopic sample (Chapter 2), but augment the sample with cluster members from the CFHT survey of Czoske et al. (2001), who reported the strengths of (or the absence of) several spectral lines including $[O II]$.

5.2.2 Sample Selection

As faint emission line objects are easier to robustly identify than those without emission, there is a potential bias against identifying “passive” objects. To minimize this effect, we adopt a bright magnitude limit $F814W \leq 21.1$ (equivalent to $M_V = -19.6$), where the sample is nearly unbiased. (See Chapter 2). Reliable visual morphologies are available to the same limit.

We define as “passive” any Sa–Sd spirals which have $EW([O II]) > -5\text{\AA}$ (Dressler et al. 1999; Poggianti et al. 1999), with “active” spirals having $EW([O II]) \leq -5\text{\AA}$; a more stringent limit is precluded by signal/noise considerations. While this definition does not exclude (k+a) or e(a) spirals as separate classes, our Cl 0024 sample contains

only two spirals with $\text{EW}(\text{H}\delta) \equiv \text{H}\delta_A > 5\text{\AA}$, both with $[\text{O II}]$ emission. To be consistent in comparing passive spirals with E+S0 galaxies, we likewise exclude all early types with $\text{EW}([\text{O II}]) < -5\text{\AA}$ ($\sim 25\%$). We manually examined all optical and UV galaxy images to ensure correct associations. We removed from the sample all galaxies where the UV flux is centered on a neighbor, or is otherwise contaminated; this reduced the total sample by 12%. The final sample consists of 68 cluster spirals, of which 24 are passive and 44 active. The comparison sample of passive E+S0s contains 75 objects. In Figure 5.1, we show coadded, normalized spectra for each type.

5.3 UV Emission in Passive Cluster Spirals

While the optical spectra of passive spirals are noteworthy for their resemblance to those of red early types (Figure 5.1, Dressler et al. 1999), their FUV properties reveal a very different picture. A large fraction of passive spirals in Cl 0024 emit vigorously in the FUV. The fraction of UV-detected passive spirals ($>3\sigma$) is $67 \pm 17\%$, not significantly different from that of active spirals ($80 \pm 13\%$). However, only $25 \pm 7\%$ of the early-type galaxies are similarly detected in the UV, clearly indicating that the stellar populations of passive spirals differ from those of the early-type galaxies.

Moreover, Figure 5.2 shows that the UV-detected passive spirals have $\text{FUV} - V$ colors intermediate between the bluer active spirals and the early types, which span a wide range extending the furthest to the red. A K-S test confirms that the $\text{FUV} - V$ colors of passive spirals differ from those of E+S0s with $>99\%$ confidence. These intermediate colors strongly suggest that passive spirals bridge the gap between the blue and red galaxy sequences. Below, we evaluate this suggestion by considering model star formation histories.

5.4 Model Star Formation Histories

The detection of strong FUV emission from passive spirals is perhaps surprising in a simple picture where the UV light and optical emission lines are generated simulta-

neously from the same star forming regions. Here, we explore possible explanations. The key to understanding the observation lies in the hierarchy of lifetimes of the stars responsible for the strong $H\delta$ absorption (10^9 yrs), FUV flux (10^7 – 10^8 yrs) and hard ionizing photons (10^7 yrs).

It is useful at this point to introduce the $FUV - V$ vs. $H\delta_A$ diagram, which we will use as our main diagnostic tool. Firstly, by comparing signatures of star formation over different timescales, this diagram allows us to explore the recent star formation history of active and passive spirals and to assess whether they can be connected in an evolutionary sequence. Secondly—since $FUV - V$ is sensitive to dust extinction while $H\delta$ is not (e.g., MacArthur 2005; Sato & Martin 2006)—this diagram allows us to explore whether the redder $FUV - V$ colors of passive spirals with respect to active spirals could be due to dust instead of differences in the recent star formation history.

Figure 5.3 shows the location of passive and active spirals in the $FUV - V$ vs $H\delta_A$ diagram. Active spirals (open blue triangles) are clustered at a blue $FUV - V$ color with moderately strong Balmer absorption ($H\delta \sim 4\text{\AA}$), whereas the passive spirals (solid green triangles) extend to redder $FUV - V$ colors with weaker $H\delta$. The mean location of each population is marked as an error-barred point; errors indicate uncertainty in the mean. The error-barred point with the weakest $H\delta$ is a composite of 13 passive spirals that cannot be plotted individually, either due to lack of reliable $H\delta$ or contamination of FUV flux. We coadded available spectra for these galaxies to measure $H\delta$, and we adopt the mean of available $FUV - V$. This composite lies near the locus of individually plotted passive spirals at low $H\delta$ and red $FUV - V$.

Evolutionary tracks from the population synthesis code of Bruzual & Charlot (2003) are overlaid in Figure 5.3. We consider only solar metallicity, and only plot model points reached in less than the time from formation at $z \sim 5$ to observation at $z = 0.4$ (~ 8 Gyrs). Tracks are in red for regimes where $EW([O\ II]) > -5\text{\AA}$; we use SFRs and L_B from the Bruzual & Charlot (2003) models to estimate $EW([O\ II])$ according to the relation in Barbaro & Poggianti (1997). We calculate $[O\ II]$ attenuation by dust following Calzetti et al. (1994), with nebular emission extinguished more

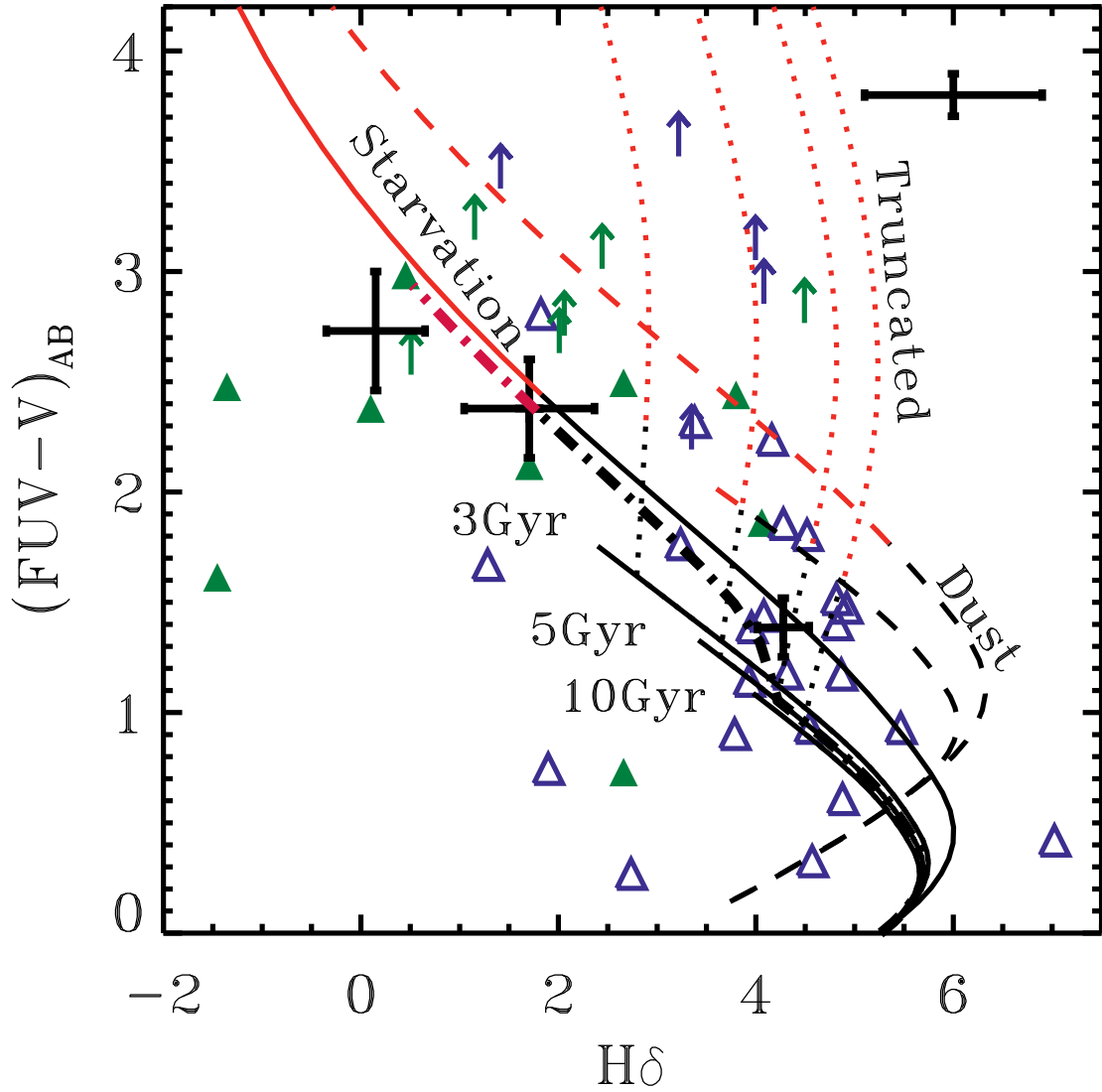


Figure 5.3 $(FUV - V)_{AB}$ color, rest frame, versus $H\delta_A$, for passive (filled green triangles) and active (open blue triangles) spirals, with typical error at upper right. Arrows indicate lower limits on $FUV - V$, color coded in the same manner. Black crosses indicate, from lower right to upper left, the mean location of the active spirals (with error on the mean), the same for passive spirals, and a composite of 13 passive spirals that cannot be plotted individually. Solid, dotted, dashed, and dash-dotted lines respectively mark several classes of model star formation histories, as labeled on the plot and discussed in the text. Tracks are colored red for regimes where $EW([O II]) > -5\text{\AA}$. Model ages increase generally from the lower right to the upper left.

strongly than the stellar continuum ($E_*/E_g \sim 0.5$), but caution that this is only a representative model. We subtract 0.9\AA from $H\delta$ for all model tracks to account for infilling by nebular emission (Barbaro & Poggianti 1997).

Solid lines represent exponentially declining SFRs. Those marked with characteristic timescales $\tau = 3, 5, 10$ Gyr have been found to reproduce the optical spectra of Sa, Sb, and Sc-type galaxies (“active” spirals), respectively (Poggianti & Barbaro 1996). Dashed lines include dust extinction of $A_V = 0.6$, corresponding to the mean difference in $FUV - V$ between the passive and active spirals, for a Cardelli et al. (1989) extinction law with $R_V=3.1$. The lower dashed line is a representative $\tau = 5$ Gyr model with dust. The uppermost dashed and solid lines represent a $\tau = 1$ Gyr SFR (with and without dust) and will be discussed below. Active spirals largely occupy the region in between tracks with zero and moderate extinction.

While adding extinction to the active spiral models can serve to reproduce the lack of emission lines and the redder $FUV - V$ colors of the passive spirals, as expected it has very little effect on the $H\delta$ values. Thus, while a model with extinguished star formation is sufficient to explain those passive spirals with higher $H\delta$, *it is unable to account for the bulk of the population observed with weaker $H\delta$* . Conceivably, more complex dust screens could account for this deficiency, but we will explore a more straightforward explanation where the SFR is suppressed as a result of environmental processes.

We first consider “truncated” star formation: in Figure 5.3, we plot (as dotted lines) several representative $\tau = 3 - 10$ Gyr models where SFR instantaneously falls to zero at an age between $t = 5 - 7$ Gyr, representing a range of initial formation ages. Such models eventually generate both lower $H\delta$ values and redder $FUV - V$ colors after star formation is turned off, but the UV emission decays too rapidly, falling below our *GALEX* detection limit well before low $H\delta$ values are reached.

Only models with a relatively fast exponential decline in SFR ($\tau \leq 1$ Gyr, upper solid and dashed lines in Figure 5.3) can match the $FUV - V$ and $H\delta$ of the bulk of passive spirals. Alternatively, any of the active spiral models with $\tau = 3 - 10$ Gyr can migrate toward the $\tau = 1$ Gyr track if its star formation begins to decline at a

much steeper exponential rate (thick dash-dotted line in Figure 5.3), entering into a spectroscopically passive phase. The two scenarios are essentially equivalent, differing only in the age of the galaxy when it enters the passive phase, and the amount of dust extinction applied.

5.5 Discussion

Remarkably, the star formation histories with a sharp decline in SFR resemble those expected for spirals affected by “starvation” (Bekki et al. 2002; Larson et al. 1980). As the accretion of gas is rapidly cut off, star formation decays on a short timescale as the remaining disk gas is used up ($0.8 \text{ Gyr} < \tau < 2 \text{ Gyr}$, according to Larson et al. 1980). More generally, we might expect that any “gentle” physical mechanism that inhibits star formation without immediately affecting the spiral morphology would behave similarly. A gentle mechanism is also easier to reconcile with the observed homogeneity of the stellar populations and dynamical properties of S0 galaxies (Chapter 3, but see also Chapter 6). Models with no explicit break in SFR, but with low values of τ ($\sim 1 \text{ Gyr}$), reproduce the passive spiral data as well as the starvation model, and seem not to require the action of any physical mechanism. Yet passive spirals seem to be most prevalent in clusters (Goto et al. 2003), suggesting that a cluster-related mechanism contributes to their formation.

Since few passive spirals are observed with an FUV upper limit (8/24), we might expect that any morphological transition occurs soon after a passive spiral fades below our FUV limiting magnitude. For the model starvation track plotted as a thick dash-dotted line in Figure 5.3, the total lifetime from the halt of gas accretion to the point where the FUV luminosity fades below our detection limit is $\sim 3 \text{ Gyrs}$, in good agreement with the morphological transformation timescale predicted by Bekki et al.

This particular evolutionary track spends $\sim 1.5 \text{ Gyr}$ in a phase with $\text{EW}([\text{O II}]) \geq -5.0 \text{ \AA}$ and detectable FUV (for the mean $M_V = -20$). The fraction of all bright spirals in this UV-detected, spectroscopically passive phase is $27 \pm 7\%$ in Cl 0024, though some contamination is likely from galaxies undergoing dust-obscured star

formation. These statistics enable us to consider whether the fraction of passive spirals observed is consistent with the buildup of the S0 fraction from $z = 0.4$ to $z = 0.0$.

Following Smith et al. (2005a), we define the ratio of S0 to ellipticals today, $N_{S0,z=0}/N_{E,z=0}$, in terms of the passive spiral fraction and S0 fraction at $z = 0.4$:

$$\frac{N_{S0,z=0}}{N_{E,z=0}} = \left(\frac{N_{S0,z=0.4}}{N_{E,z=0.4}} + \frac{\Delta t}{\tau} \frac{N_{psp,z=0.4}}{N_{E,z=0.4}} \right) \frac{N_{E,z=0.4}}{N_{E,z=0.4} + \Delta N_E} \quad (5.1)$$

where Δt is the look-back time to $z = 0.4$, 4 Gyr, and τ is the passive spiral lifetime of 1.5 Gyr. The last term accounts for the buildup of ellipticals through other means, which we set equal to 1 for this simple analysis. Taking $N_{S0,z=0.4}/N_{E,z=0.4} = 0.65$ (Dressler et al. 1997) and $N_{psp,z=0.4}/N_{E,z=0.4} = 0.25$,² we calculate $N_{S0,z=0}/N_{E,z=0} = 1.3$, in rough agreement with $N_{S0,z=0}/N_{E,z=0} \sim 1.7 \pm 0.6$ from Dressler et al. (1997). This shows that passive spirals undergoing starvation can evolve into present day S0s, consistently with the observed evolution of the morphology density relation.

While starved spirals cannot build up the *entire* population of local S0s due to differences in the stellar mass functions of local S0s and spirals (Kodama & Smail 2001), our result provides strong evidence that the abundant passive spiral population at intermediate redshift is an important transition population which contributes to the present-day cluster S0 population. By combining the different postburst timescales probed by *GALEX* UV imaging and optical spectroscopy, we have delineated a duty cycle of gradual decline in activity consistent with the recent growth in the S0 population.

Acknowledgements We thank L. MacArthur and I. Smail for valuable comments.

²According to Dressler et al. (1997), the ratio of ellipticals to spirals is nearly unity in Cl 0024, so $N_{psp,z=0.4}/N_{E,z=0.4} \simeq N_{psp}/N_{sp}$.

Chapter 6

Identifying the Physical Processes Responsible for the Observed Transformation of Spirals into S0s ¹

We present further results on our comprehensive comparative survey of Cl 0024 and MS0451. Combining *HST* and *GALEX* imaging with Keck spectroscopy, we identify and study several key classes of “transition objects” whose stellar populations or dynamical states indicate a recent or ongoing change in morphology and star formation rate. For the first time, we have been able to conclusively identify spiral galaxies in the process of transforming into S0 galaxies. This has been accomplished by locating both spirals whose star formation is being quenched as well as their eventual successors, the recently created S0s. Differences between the two clusters in both the timescales and spatial location of this conversion process allow us to evaluate the relative importance of several proposed physical mechanisms that could be responsible for the transformation. Combined with other diagnostics that are sensitive to either ICM-driven galaxy evolution or galaxy–galaxy interactions—including the residuals from the Fundamental Plane and the properties of “signpost” compact emission line galaxies—we describe a self-consistent picture of galaxy evolution in clusters. We find that spiral galaxies within infalling groups have already begun a slow process of conversion into S0s primarily via gentle galaxy–galaxy interactions that act to quench star formation. The fates of spirals upon reaching the core of the cluster depend heavily on the cluster ICM, with rapid conversion of all remaining spirals into S0s via

¹A version of this chapter has been accepted for publication in ApJ, as Moran et al. (2007b)

ram-pressure stripping in clusters where the ICM is dense. In the presence of a less-dense ICM, the conversion continues at a slower pace, with galaxy–galaxy interactions continuing to play a role along with “starvation” by the ICM. We conclude that the buildup of the local S0 population through the transformation of spiral galaxies is a heterogeneous process that nevertheless proceeds robustly across a variety of different environments from cluster outskirts to cores.

6.1 Introduction

It is well known that environmental processes play a significant role in shaping the evolution of galaxies as they assemble onto clusters. With the aid of Hubble Space Telescope (*HST*) imaging and deep optical spectroscopy, recent studies have quantified this evolution in galaxy properties, painting a picture where the fraction of early-type (elliptical and S0) galaxies and the fraction of passive non-star-forming galaxies both grow with time, and at a rate that seems to depend sensitively on the local density of galaxies (Smith et al. 2005a; Postman et al. 2005; Dressler et al. 1997; Poggianti et al. 1999).

Yet there are a wide variety of physical processes that may be responsible for these evolutionary trends—including galaxy mergers, galaxy–galaxy harassment, gas stripping by the ICM, or tidal processes (Moore et al. 1999; Fujita 1998; Bekki et al. 2002). Observationally, it has so far been impossible to fully separate the effects of the various physical processes, in large part due to the overlapping regimes of influence for each of the proposed mechanisms (see Chapter 1, T03). Further complicating the picture, the large scale assembly states of clusters show considerable variety (Smith et al. 2005b), such that the dominant forces acting on galaxies are likely to vary from cluster to cluster, or over the course of an individual cluster’s assembly history. But gaining an understanding of the complex interplay between a variable ICM, the properties of assembling galaxies, and the overall cluster dynamical state is crucial if we are to have a complete picture of the growth and evolution of galaxies in a hierarchical universe.

In this work, we combine *HST* optical and *GALEX* UV imaging of Cl 0024 and MS 0451 with ground-based (Keck) spectroscopy of member galaxies, in an attempt to trace directly the buildup of passive early-type galaxies via a detailed “case study” of the galaxy population across each cluster. In several previous chapters, whose key results are restated in §6.2, we have performed several targeted investigations of galaxy stellar populations and star formation rates as a function of cluster-centric radius, local density, and morphology. Our goal for this study is to bring our complete survey data set to bear on the question of how galaxies are affected by their environment, as a function of both the overall cluster properties and of local environment within each cluster. For maximum clarity and deductive power, we focus our investigation on several key populations of “transition galaxies” in the clusters—galaxies whose stellar populations or dynamical states indicate a recent or ongoing change in morphology or star formation rate.

In evaluating cluster galaxies for signs of evolution, we have adopted a strategy to make maximal use of our *HST*-based morphologies by characterizing signs of recent evolution in spirals and early types separately. This approach is similar to using the color–magnitude relation to divide our sample into “red sequence” and “blue cloud” galaxies, but it provides additional leverage to identify galaxies in transition. Early-type galaxies that have either been newly transformed or prodded back into an active phase, or spiral galaxies where star formation is being suppressed or enhanced will all stand out in our sample. At the same time, their morphologies reveal important information about their formation histories prior to their current transition state, information that colors alone do not provide. Our strategy also has the benefit of allowing us to directly investigate the hypothesis that many cluster spirals transform into S0s between $z \sim 0.5$ and today (Dressler et al. 1997)—an investigation that will form the basis of this chapter.

In the next section, we restate our rationale for selecting Cl 0024 and MS 0451, describe the large-scale properties of each cluster, and give a summary of what we have concluded so far in our study of galaxy evolution in both clusters. In §6.3, we briefly describe the survey data we will draw from. In §6.4, we will investigate the

properties of “passive spirals” across the two clusters, suggesting that they are in the process of transforming into S0 galaxies. We confirm in §6.5 that this is the case, via identification of newly created S0s that we believe reflect the distinct passive spiral populations found in each cluster. In §6.6, we consider the environments of these galaxies in transition, and begin to investigate the physical mechanisms that may be responsible for these transformations. In §6.7, we outline a model of how galaxy evolution proceeds in each cluster. We consider the Fundamental Plane as a way to further constrain the physical mechanisms at work, and derive similar constraints from the populations of compact emission line galaxies in both clusters. Finally, in §6.8, we summarize our conclusions about the transformation of spirals into S0s at $z \sim 0.5$. In this work, we adopt a standard Λ CDM cosmology with $H_0 = 70 \text{ km s}^{-1} \text{ Mpc}^{-1}$, $\Omega_m = 0.3$, and $\Omega_\Lambda = 0.7$.

6.2 A Comparative Survey of Two $z \sim 0.5$ Clusters

As discussed in Chapter 1, Cl 0024 and MS 0451 were chosen for study primarily because of their comparable total masses, similar galaxy richness, and strong lensing features, while exhibiting X-ray properties that are quite distinct (see Table 1.1). While MS 0451 is one of the most X-ray luminous clusters known (Donahue et al. 2003), Cl 0024 is somewhat underluminous in the X-ray, with a mass inferred from *XMM/Newton* observations that significantly underestimates the mass derived from other methods (Zhang et al. 2005). MS 0451 has X-ray luminosity seven times larger than Cl 0024, with a corresponding gas temperature nearly three times as high. This implies a large difference in the density and radial extent of the intracluster medium (ICM) between the two clusters. As a result, ICM-related physical processes are naively expected to be more important in the evolution of currently infalling MS 0451 galaxies than in Cl 0024.

In the schematic diagram presented as Figure 1.2, we have applied simple scaling relations to estimate the regimes of influence for several key physical processes which could be acting on infalling galaxies, following the procedure described in Chapter 1.

ICM-related processes, such as gas starvation (Larson et al. 1980; Bekki et al. 2002) and ram-pressure stripping (Gunn & Gott 1972) begin to affect galaxies at much larger radius in MS 0451. An important caveat, however, is that the role of difficult-to-observe shocks in the ICM are unknown, and are not accounted for in Figure 1.2 (but see §6.7). Similarly, the two clusters' differing masses set the radial regions where galaxy merging will be effective; because of the $\sim 50\%$ higher mass of MS 0451, typical galaxy relative velocities become too fast for mergers to occur at a higher radius than in Cl 0024.

The differing regimes of influence for the physical mechanisms illustrated in Figure 1.2 provide the key template for our attempt to disentangle the relative importance of the various processes. By surveying the galaxies of both clusters for signs of recent transformation or disturbance, across the entire radial range to ~ 5 Mpc, we hope to associate the sites and characteristics of galaxies in transition with the likely causes from Figure 1.2.

An additional factor not reflected in Figure 1.2, however, is the overall assembly state and level of substructure in each cluster. Therefore, Figure 1.2 can only be used as a guide, and we must carefully consider the effects that large-scale cluster assembly and irregularities may have on their galaxies as well. For example, the effects of tidal processes and galaxy–galaxy harassment, which according to Figure 1.2 should occur in much the same regions across both clusters, may very well differ greatly between clusters depending on how well each is virialized. As we will discuss below, there are marked differences in the levels of substructure between the two clusters, and these may drive important differences between the galaxy populations.

6.2.1 Kinematic Structure of the Two Clusters

While it is evident from their different X-ray luminosities that MS 0451 and Cl 0024 provide quite different environments for their constituent galaxies, our detailed study of environmental effects on cluster galaxies requires a comprehensive characterization of the two clusters and their respective environments. Here, we study the radial

velocities and spatial distributions of galaxies in each cluster, in order to evaluate the global kinematic structure of each cluster and identify significant substructures.

Our extensive *HST* imaging and Keck spectroscopy, described more fully in Chapter 2, readily reveal marked differences in the distributions of galaxies between the two clusters, suggesting that the clusters have quite dissimilar recent assembly histories. In Figure 2.8, we have displayed the distribution of redshifts for members of both Cl 0024 and MS 0451. The redshift distribution of MS 0451 members is broadly consistent with a Gaussian distribution. A somewhat better fit to the data is given by a two-component double Gaussian function, but the distribution splits into these two peaks only for galaxies at large radius ($R > 2$ Mpc), suggesting that we are observing two filaments feeding galaxies into the virialized center of MS 0451. Cl 0024 galaxies likewise exhibit a double-peaked structure in redshift space, with two components that are widely separated and asymmetric in height. This feature was discovered by Czoske et al. (2001), and is thought to be the remnant of a high-speed, face-on encounter between the main cluster and a smaller subcluster or large group (Czoske et al. 2002).

The effects of this collision, even an estimated several Gyrs after it occurred (Czoske et al. 2002), are still important in the core of Cl 0024—for example, as shown by intriguing recent claims of a “dark matter ring” in the core of Cl 0024 (Jee et al. 2007). The measured line of sight velocity dispersion in the core of 650 ± 50 km s⁻¹ implies a 30%–50% lower mass than has been directly measured through strong and weak lensing constraints (Kneib et al. 2003). The fact that the galaxy velocity distribution and X-ray emitting gas both underestimate the mass leads to the conclusion that the core of Cl 0024 is not in virial nor hydrostatic equilibrium, an assumption that was made for each of these mass estimates. The lower relative velocities of galaxies in the Cl 0024 core may importantly affect the action of physical processes whose strengths vary with galaxy velocity. For example, gas stripping by the ICM may be even less effective in Cl 0024 than naively predicted by Figure 1.2. The effects of galaxy–galaxy harassment may also be different, as close galaxy encounters may happen at both lower frequency and lower relative velocities than have previously

been modeled in detail (e.g., Moore et al. 1999).

The spatial distribution of galaxies in MS 0451 and Cl 0024 also show key differences. In Figure 6.1, we construct modified Dressler-Shectman (D-S) plots for the region within R_V of each cluster (Dressler & Shectman 1988). In such plots, each cluster member is indicated by a circle, with the size of the circle proportional to that galaxy’s “Dressler-Shectman statistic”:

$$\delta^2 = 11/\sigma^2[(\bar{v}_{local} - \bar{v})^2 + (\sigma_{local} - \sigma)^2] \quad (6.1)$$

where line-of-sight velocity \bar{v}_{local} and dispersion σ_{local} are measured with respect to each galaxy’s ten nearest neighbors, and \bar{v} and σ are the global cluster values. This statistic measures each galaxy’s local deviation from a smooth, virialized velocity and spatial distribution. In other words, groups of large circles on the plot tend to indicate the presence of an infalling group. In Figure 6.1, we further color code each galaxy according to its velocity with respect to the cluster center, with red (blue) indicating motion away from (toward) the observer. Galaxies marked with black points have low line-of-sight velocities, $<300 \text{ km s}^{-1}$ with respect to the cluster core.

The D-S plot for Cl 0024 reveals the presence of at least two significant groups near to the cluster core: an infalling group at high velocity nearly along the line of sight to the cluster center, and a previously noted large group to the northwest of the cluster core, presumably assembling onto the core in an orientation almost in the plane of the sky. The large structure to the NW is also detected in both the weak lensing map (Kneib et al. 2003) and *XMM-Newton* observations (Zhang et al. 2005), which additionally suggest the presence of a shock front at the interface between the group and the main cluster.

In contrast, the D-S plot for MS 0451 reveals an elongated but largely smooth distribution of galaxies. The cluster’s elliptical shape is clearly visible, but the segregation of red points to the southeast and blue points to the northwest suggests a uniform contraction of the cluster along its major axis. While it is possible that the observed velocity field is due to cluster-scale rotation, previous analyses of the X-ray

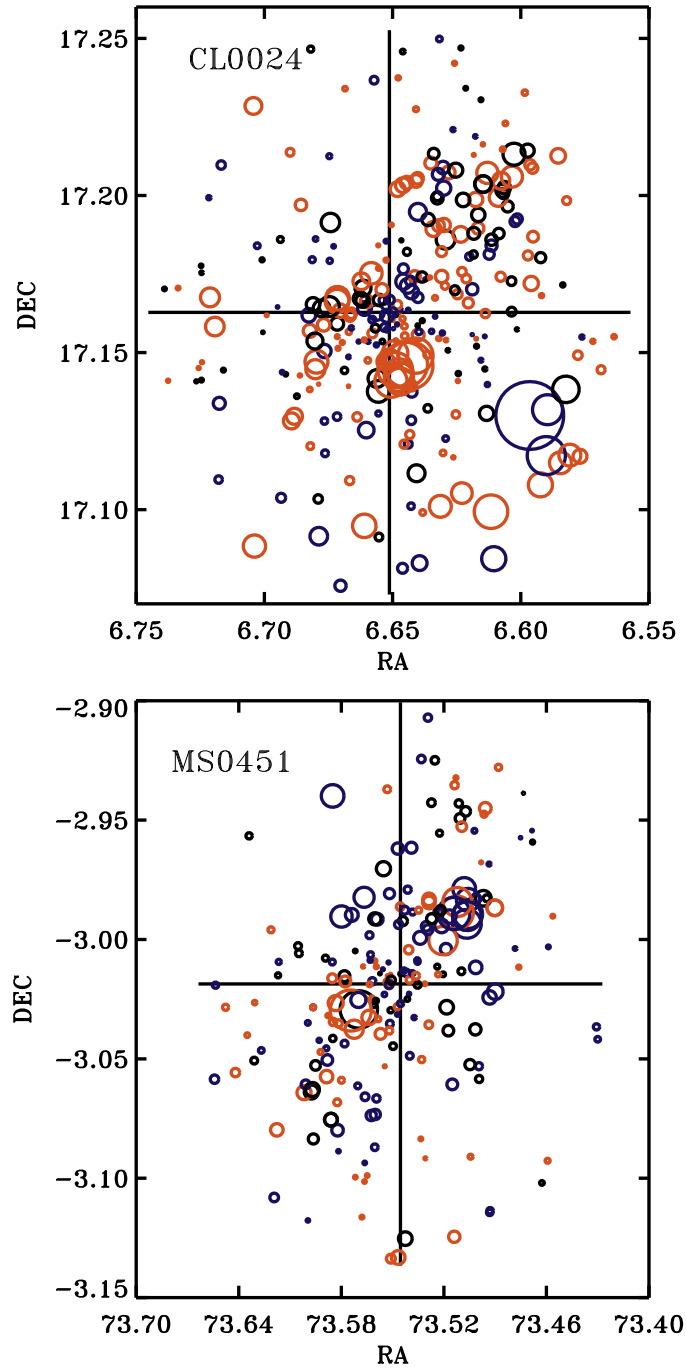


Figure 6.1 Dressler-Shectman plots for CL0024, top, and MS0451, bottom. Including only spectroscopically confirmed objects within $1 R_V$ of the cluster center, each circle indicates the spatial position of a cluster member, with the circle size proportional to its local deviation from a smooth velocity distribution (see text). Circles are coded blue for galaxies with cluster-centric velocity toward the observer with amplitude of $>300 \text{ km s}^{-1}$, red for galaxies with the same velocity amplitude away from the observer, and black for galaxies with low cluster-centric velocities, $<300 \text{ km s}^{-1}$.

and Sunyaev-Zeldovich observations prefer a prolate or triaxial shape for MS 0451 (Donahue et al. 2003; De Filippis et al. 2005), whereas the cluster would necessarily be oblate if the observed velocities are due to rotation. We may be seeing this spread in velocities reflected in the redshift distribution of MS 0451, which splits into two peaks at large radius, likely indicating infall from two directions. One might worry that the elongated distribution gives MS 0451 an artificially large velocity dispersion, σ , but cluster mass estimates derived from σ are consistent with those derived from the X-ray and weak lensing analysis (Donahue et al. 2003, and references therein). The origin of the elliptical shape is unclear, but may represent the remnant of a past major merger. Nevertheless, still-bound infalling groups appear to be absent or insignificant within the virial radius.

The overall increased level of substructure observed in Cl 0024 is likely to have implications for the galaxy population. In comparison to MS 0451, Cl 0024 galaxies are more likely to have been a member of an infalling group in the recent past, and so we may expect to see more signs of recent group “preprocessing” in Cl 0024. Furthermore, in the chaotic environment of Cl 0024 the ICM is more likely to be disturbed, and so shocks, cold fronts, or other features in the ICM may be present, and could play an important role in the star formation histories of cluster members (Roettiger et al. 1996).

6.2.2 Previous Work

Between the extremely dense ICM in MS 0451 and the active assembly state of Cl 0024, these two clusters provide very distinct environments for their member galaxies. In the course of this work, we will examine how the properties of transition galaxies in each cluster reflect these distinct environments. However, as our new results rely on and incorporate several of the key findings of previous chapters, we present here a brief summary of our investigations so far. We highlight in particular several results which, in the initial interpretation, hint at the action of one or more physical mechanisms from Figure 1.2.

- By constructing the Fundamental Plane (FP) of Cl 0024, we observed that elliptical and S0 galaxies (E+S0s) exhibit a high scatter in their FP residuals, equivalent to a spread of 40% in mass to light ratio (M/L_V) (Chapter 3). The high scatter occurs only among galaxies in the cluster core, suggesting a turbulent assembly history for cluster early types, perhaps related to the recent cluster–subcluster merger (Czoske et al. 2002).
- Around the virial radius of Cl 0024, we observed a number of compact, intermediate mass ellipticals undergoing a burst of star formation or weak AGN activity, indicated by strong [O II] emission (Chapter 3). The [O II] emitters reside in relatively low density and high speed regions, and so we deemed that they are not likely the remnants of mergers. Though we will revisit the merger hypothesis in §6.7, we tentatively concluded that the observed activity is caused by a rapidly acting physical process: two candidates are galaxy harassment and shocks in the ICM, perhaps generated by the subcluster merger in Cl 0024.
- We searched for disruptions in the internal structures and star formation rates of disk galaxies due to tidal effects or galaxy–galaxy interactions, by measuring emission line rotation curves and constructing the Tully-Fisher relation (Chapter 4). We find that the cluster TF relation exhibits significantly higher scatter than the field relation, echoing the high scatter seen in the Cl 0024 FP. We argue that the high scatter in both K - and V -band TF relations demonstrate that cluster spirals are kinematically disturbed by their environment. We proposed that such disturbances may be due to galaxy merging and/or harassment.
- We combined *GALEX* UV observations with key spectral line indices to place strict constraints on the recent star formation histories of “passive spiral” galaxies, an important class of transition object (Chapter 5). Passive spirals show spiral morphology in *HST* images, but reveal weak or no [O II] emission in their spectra, suggesting a lack of current star formation. Through *GALEX* UV imaging, we find that passive spirals in Cl 0024 exhibit UV emission nearly as strong as regular star-forming spirals, implying the presence of young stars.

Their unusual combination of UV emission with weak H δ strength supports a picture where passive spirals have experienced a rapid decline and eventual cessation of star formation over the last ~ 1 Gyr. The timescale of this decline implicates “starvation” by the ICM as the likely cause (Larson et al. 1980; Bekki et al. 2002)—a process where the intracluster medium (ICM) strips gas from a galaxy’s halo, causing star formation to decline due to the absence of new cold gas accretion onto the disk.

Each of these previous investigations has revealed a partial view of environmental evolution across the studied clusters. Through these investigations, we have identified several physical mechanisms that we could call “likely suspects” for driving galaxy evolution in clusters, and these seem to fall into two classes: galaxy–ICM interactions and galaxy–galaxy interactions. However, a unified picture is still lacking. Both of these flavors of interaction have been implicated before in the decline of star formation and the possible conversion of spirals into S0s (see Boselli & Gavazzi 2006, and references therein), yet a detailed evaluation of their importance remains elusive.

We aim in this work to complete our accounting of galaxy evolution across these two quite distinct clusters, building on and linking our earlier studies into what we hope will be a more comprehensive picture of how cluster galaxies are affected by their environment at intermediate redshift. To accomplish this, we will first document what we believe to be direct evidence for the transformation of spirals into S0s: through an analysis of their stellar populations and recent star formation rates, we link the passive spiral galaxies in both clusters to their eventual end states as newly generated cluster S0 galaxies. Only then, as we examine the physical mechanisms responsible for this transformation, will we draw on the above summarized results to place extra constraints on the physics driving the transformation. This discussion will include an extension of our analysis of the Fundamental Plane and the strongly emitting compact E+S0s in Cl 0024 to include MS 0451, in order to further strengthen the constraints we can place on galaxy–galaxy interactions and galaxy–ICM interactions, respectively.

6.3 Data and Analysis

While our imaging and spectroscopic data on Cl 0024 and MS 0451 have been fully described in Chapter 2, we give here a brief summary of the data we will make use of in this study.

We make use of *HST* imaging of Cl 0024 and MS 0451 both to calculate absolute V -band magnitudes (M_V , see Chapter 2), and to select a sample of cluster galaxies with reliable morphological classifications. For both clusters, such reliable classification is possible to rest frame absolute magnitude $M_V = -19.5$, corresponding to $I = 22.1$ in MS 0451 and $I = 21.2$ in Cl 0024. Broader classification as early or late type is possible to a fainter limit, $M_V = -18.0$. In the following, all galaxies assigned morphological types T=0,1,2 are together labeled as “early types” or E+S0s, and all galaxies with T=3,4,5 are labeled as spirals.

We further make use of *GALEX* UV imaging of Cl 0024 and MS 0451, which were respectively observed for 15ks and 80ks, reaching comparable depths in rest frame FUV (observed NUV). We also make use of supplemental ground-based imaging to aid in determining k -corrections to transform observed magnitudes to the nearest rest-frame bands (Chapter 2). Here, all absolute magnitudes will be expressed on the AB system. We note also that, in all cases where we quote rest-frame colors, we have applied a k -correction equal to the *median* k -correction for all galaxies of the same morphological type and in the same cluster, rather than the individually fit k -corrections. We do this to avoid introducing any additional scatter into the rest-frame colors (due to uncertainties in the k -corrections), above that present in the observed-frame colors. In general, the difference between the two methods is <0.1 mag, and we do not expect the method of k -correction to impact our analysis significantly.

In our Keck spectroscopic survey, we have obtained spectra of over 300 member galaxies per cluster, to $M_V = -18.0$. The spectroscopic sample is $>65\%$ complete for objects with $F814W < 21.1$ in Cl 0024 ($M_V = -19.6$ at the cluster redshift). In MS 0451, completeness to the same absolute magnitude limit is lower, $\sim 30\%$, because of the deeper observations required (to $F814W = 22.0$). In both clusters, the

spectroscopic sample remains representative of the cluster population as a whole to $M_V = -19.6$, roughly 1.5 magnitudes below M_* . However, in the range $-19.6 < M_V < -18.0$, we are biased toward detection of emission line cluster galaxies over absorption line galaxies, and completeness is lower in MS 0451 than Cl 0024. In the following, we will restrict our analysis to cluster members with $M_V < -19.6$, except where specified otherwise.

6.3.1 Spectral Line Measurement and Velocity Dispersion

We measure spectral line indices for several key emission and absorption lines following the Lick system (Worthey et al. 1994). We focus in this work on indicators of recent or ongoing star formation, including [O II]3727 and the Balmer lines $H\delta_A$ and $H\beta$. We also measure the $D_n(4000)$ index, which indicates the strength of the 4000Å break; we adopt the definition from Balogh et al. (1999).

In order to make maximal use of our spectra for investigation of the stellar populations and star formation rates of cluster transition galaxies, we took great care to measure the equivalent widths (EWs) of key spectral lines in an optimal way. We developed a code in IDL which measures EWs via an inverse-variance weighted integration of the flux across the line. The inverse variance ($1/\sigma^2$) for each pixel in a spectrum is automatically generated as output from the DEIMOS reduction pipeline. Weighting by inverse variance minimizes the effects of poorly subtracted sky lines or other low S/N regions of the spectrum in the calculation of EWs, and allows for accurate uncertainty estimates on the indices. The code also robustly measures *lower limits* on emission line EWs in spectra where emission lines are bright but the underlying stellar continuum is undetected. As in earlier chapters, we adopt the convention that emission lines have negative equivalent widths and absorption lines positive.

In total, we measure EWs for samples of 116 and 124 spiral galaxies in MS 0451 and Cl 0024, respectively, as well as samples of 130 and 109 E+S0s in MS 0451 and Cl 0024. Of these, 60 E+S0s in MS 0451 and 71 in Cl 0024 have high S/N spectra suitable for measurement of the velocity dispersion and construction of the

Table 6.1. Photometric and spectroscopic measurements for all cluster galaxies

RA ($^{\circ}$)	DEC ($^{\circ}$)	z	Morph	F814W mag	M_V mag	[OII] \AA	$D_n(4000)$	$H\delta_A$ \AA
6.443974	17.141319	0.3792	E/S0	21.9	-18.8	-25.6 ± 1.0	1.10 ± 0.02	1.6 ± 0.1
6.462808	17.145109	0.3978	S0	19.1	-21.7	2.2 ± 0.0	1.79 ± 0.01	—
6.477189	17.274000	0.3967	S0	20.0	-20.7	-1.8 ± 0.2	1.74 ± 0.02	1.2 ± 0.1
6.481423	17.247549	0.3969	Sc+d	20.7	-20.1	-30.8 ± 1.7	1.20 ± 0.02	5.6 ± 0.1
6.499555	17.336269	0.3951	S0	19.9	-20.8	9.9 ± 4.1	—	-3.8 ± 0.1
6.508250	17.056641	0.3992	Sa+b	20.5	-20.2	-2.4 ± 0.4	1.36 ± 0.02	1.8 ± 0.2
6.510695	17.325680	0.3931	S0	19.2	-21.5	-13.6 ± 0.5	1.77 ± 0.01	-1.8 ± 0.1
6.511346	17.324520	0.3913	S0	19.7	-21.0	-9.4 ± 0.8	1.34 ± 0.02	4.6 ± 0.1
6.514315	17.317190	0.3946	E	18.8	-21.9	1.2 ± 0.4	1.77 ± 0.02	—
6.517361	17.105089	0.4059	Sa+b	18.8	-21.9	1.8 ± 0.5	1.80 ± 0.02	-2.1 ± 0.1
...								

Note. — The complete version of this table is available electronically from <http://www.astro.caltech.edu/~simm/clusters/>. This version is only a sample.

Fundamental Plane (See Chapter 2). Photometric characteristics and key spectral line measurements for each of these galaxies are listed in Table 6.1.

6.4 Passive Spirals

The discovery of passive spirals in clusters at intermediate redshift (Couch et al. 1998; Dressler et al. 1999; Poggianti et al. 1999) has led to their recognition as promising candidates for the role of “transition object” during the theorized conversion of cluster spirals into S0s between $z \sim 0.5$ and today. Such a conversion, though controversial (e.g., Burstein et al. 2005), has been expected because of the striking contrast between the large number of spirals observed in clusters at $z \sim 0.5$ and the correspondingly large population of S0s found in clusters locally. In our initial analysis of these passive spirals in Cl 0024 (Chapter 5), we found evidence in their stellar populations for a slow decline in star formation, confirming that passive spirals—at least in Cl 0024—exhibit the prerequisite cessation of star formation needed for any transformation into S0s. Perhaps more importantly, we found that the *abundance* of passive spirals in Cl 0024 is quite high, over 25% of the total spiral population—enough, perhaps, to account for the *entire* buildup of S0s in clusters (but see Kodama & Smail 2001).

However, several questions remain about the nature of passive spirals and their purported S0 end states. Among them: Apart from their lack of emission lines, how do the passive spirals as a class differ from the star forming spirals, and are their properties uniform between clusters? If they are truly destined to transform into S0s, can we identify directly these new S0s, perhaps just after their new morphologies become firmly in place? Finally, in what environments do the passive spirals reside, and with what implications for the physical mechanisms driving their creation? In this section, we attempt to answer the first of these questions, specifying more fully the properties and recent star formation histories of the passive spirals. In §6.5 and §6.6, we will then consider the next two questions, in our attempt to piece together the full evolutionary history of Cl 0024 and MS 0451 galaxies.

We define as “passive” any spiral with an [O II] equivalent width $EW([O II]) >$

Table 6.2. Passive spirals and UV emission

	Fraction of UV-detected:			$N_{passive}/N_{spirals}$
	Active Spirals	Passive Spirals	E+S0s	
Cl 0024	$86\% \pm 6\%$	$65\% \pm 14\%$	$25\% \pm 7\%$	$28\% \pm 7\%$
MS 0451	$88\% \pm 5\%$	$37\% \pm 15\%$	$8\% \pm 3\%$	$26\% \pm 6\%$

-5\AA . Though this definition necessarily allows some contamination from star-forming galaxies that are either moderately dusty or forming stars at a low rate, we will demonstrate below via coadded spectra that all emission lines are weak or absent in the passive spirals. We note that we would classify as “passive” many of the spiral galaxies in local clusters that are observed to be H I-deficient but retain a low level of star formation (Gavazzi et al. 2006). By examining multi-color (NUV and F814W) imaging of the cluster by eye, we remove from the sample all galaxies where the UV flux is likely to be significantly contaminated by neighboring objects or image artifacts.

We also restrict our passive spiral sample to those objects with $H\delta_A < 5.0\text{\AA}$; we assign otherwise passive spirals with $H\delta_A$ stronger than this to the “poststarburst” category. We note that this $H\delta$ limit differs from the definition adopted by some other authors (e.g., Poggianti et al. 1999), who label all passive galaxies with $H\delta > 3\text{\AA}$ as poststarburst. However, the difference is primarily due to different measurement methods for $H\delta$: we find that a large number of star-forming and passive spirals exhibit $3\text{\AA} < H\delta_A < 5\text{\AA}$ in our sample, which is within the range where Kauffmann et al. (2003) report that star formation histories are consistent with continuous star formation. Therefore, spiral galaxies in our sample with $[O II] > -5\text{\AA}$ and $H\delta$ between 3\AA and 5\AA are perhaps more properly called “post-*starforming*”, as there is no need to invoke a starburst to explain their $H\delta$ values. We therefore group them with the remainder of the passive spirals.

After culling contaminated objects and dividing our sample according to their $[O II]$ and $H\delta$ strengths, we find that $87\% \pm 5\%$ of MS 0451 spirals with $[O II]$ emission

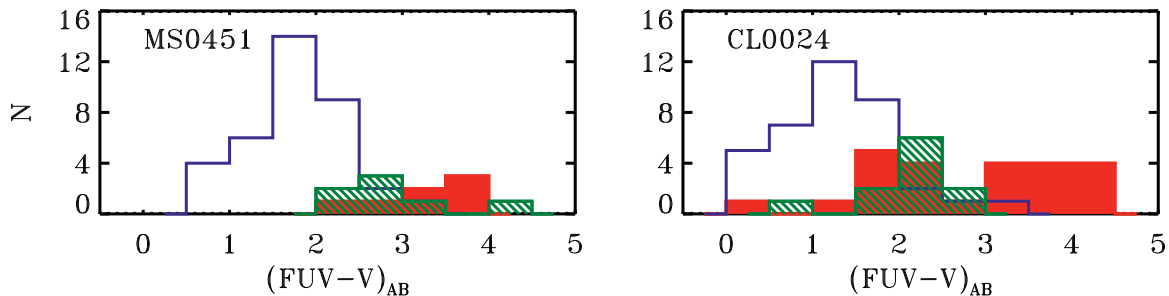


Figure 6.2 Distributions of $FUV - V$ colors in MS 0451 (left) and Cl 0024 (right). Open blue histograms indicate the colors of normal star-forming spirals. Green hatched histograms display the colors for those passive spirals that are detected in the UV, and solid red histograms likewise indicate the colors of E+S0s that have been detected in the UV.

(brighter than $M_V = -19.6$) are detected in our *GALEX* imaging, similar to the detection rate in Cl 0024. Conversely, only $37\% \pm 15\%$ of spectroscopically passive spirals are similarly detected (dropping to $32\% \pm 13\%$ if we were to include the poststarburst spirals), significantly less than the UV-detected fraction in Cl 0024 (see Table 6.2). As the rest-frame luminosity limits for detection of FUV are virtually the same between the two *GALEX* exposures ($M_{FUV} < -17.6$ in MS 0451 and $M_{FUV} < -17.9$ in Cl 0024), this represents an important difference in UV luminosity between the two clusters' passive spiral populations.

In Figure 6.2, we display the distributions of rest-frame $FUV - V$ colors for star-forming spirals, passive spirals, and early types in each cluster. It is clear that, despite the overall lower fraction of UV-detected passive spirals in MS 0451, those that are detected exhibit the same intermediate colors as in Cl 0024. To further investigate the colors of passive spirals, and to include those that were not UV detected, we also utilize our ground-based *R*- and *I*-band imaging to measure rest-frame $B - V$, for passive and normal spirals. We observe a trend similar to that seen in the UV-optical colors: the median passive spiral is ~ 0.1 magnitudes redder than the median star-forming spiral in Cl 0024, and 0.2 magnitudes redder in MS 0451. K-S tests indicate that passive spirals have a color distribution significantly different from that of normal spirals, in both clusters.



Figure 6.3 Montage of active and passive spirals from deep multi-color ACS imaging of the core of Cl 0024. The top row displays three typical spirals whose spectra exhibit emission lines. The next two rows are composed of passive spirals, which qualitatively exhibit two forms: those with blue disks, but with possibly lower surface brightness than star-forming spirals (middle row), and those with distinctly red disks (bottom row). All galaxy images were extracted from the same multi-color image with identical image scaling and color balance, with F850LP in red, F775W in green, and F555W in blue.

In fact, we can verify visually that passive spirals appear different from normal star forming spirals. In Figure 6.3, we display color postage-stamp images of nine spirals in Cl 0024, derived from deep multicolor ACS imaging of the center of Cl 0024 which we retrieved from the *HST* archive (GTO Proposal 10325, PI: Ford). In the top row, we display three normal star-forming cluster spirals. The next two rows show cluster passive spirals, which appear to fall into two basic types. Shown in the middle row, some passive spirals appear to retain blue disks, but at surface brightnesses lower than that of star-forming spirals. While some star formation may be occurring, we note that our spectroscopic slits are large enough that we do not believe we are simply “missing” regions of star formation in our observations. In the bottom row, we see three examples of passive spirals with distinctly red disks, yet with spiral arms and dust lanes still present. These appear similar to the $z = 0$ “anemic spirals” first identified by van den Bergh (1976); indeed, inspection of the integrated spectrum of a prototypical ‘anemic spiral’, NGC 4569 (Gavazzi et al. 2004), indicates that it would likely satisfy our definition of “passive spiral”. It seems, then, that passive spirals could genuinely be disk-dominated systems where star formation is on the decline or has halted.

In counterpoint to their lower incidence of UV emission, the overall frequency of passive spirals in MS 0451 is quite similar to that found in Cl 0024 (Table 6.2). In both clusters, more than a quarter of all spirals are passive—important confirmation that passive spirals are a significant component of both clusters despite the large difference between the clusters’ global properties.

Yet their presence in two quite distinct clusters leads us to question whether the passive spirals are a cluster-related phenomenon at all, or if they could instead represent some fraction of all spirals that have internally exhausted their star formation. If they are indeed generated in the cluster environment, then we would not expect to find passive spirals in the field at these same intermediate redshifts. We have therefore examined a sample of 105 field spirals in the redshift range $0.3 < z < 0.65$, identified in the course of our spectroscopic campaign. Out of 62 galaxies where [O II] falls within our wavelength coverage, we measure a passive spiral fraction of only

$6\% \pm 3\%$. This low incidence in the field confirms that the generation of passive spirals is a cluster-related phenomenon at these redshifts (Poggianti et al. 1999). The $6\% \pm 3\%$ of passive spirals found in the field may indicate that some passive spirals can be formed in groups.

Despite their overall similar abundance in both clusters, the weaker UV emission in MS 0451 passive spirals presents a puzzle that leads us to again consider the different assembly states and ICM properties of the two clusters. To more precisely quantify the nature of the passive spirals in each cluster, we introduce as a key diagnostic plot the $FUV - V$ vs. $D_n(4000)$ diagram. $D_n(4000)$ is sensitive to stellar populations with ages of ~ 2 Gyr, with a dependence on metallicity that only becomes apparent for old stellar populations (Poggianti & Barbaro 1997), while the $FUV - V$ color is sensitive to star formation on a much shorter timescale (10^7 – 10^8 yr). As we will see, comparing $D_n(4000)$ to $FUV - V$ color provides a valuable tool to discriminate between different star formation histories for passive and star-forming spirals.

In Figure 6.4, we plot $D_n(4000)$ versus rest-frame $FUV - V$ color for MS 0451 (top) and Cl 0024 (bottom). Star-forming spirals are indicated by open blue triangles, and passive spirals are indicated with solid green triangles. Arrows denote 3σ lower limits for $FUV - V$ colors for those galaxies not detected in the UV, colored blue for star-forming spirals and green for passive spirals. We also include on the diagram, plotted as small triangles or lower limit arrows, the population of starburst and poststarburst spirals with $H\delta_A > 5\text{\AA}$, similarly color coded to indicate the presence (blue) or lack (green) of [O II] emission. For clarity, we plot only a subset of cluster galaxies with especially small uncertainties in $D_n(4000)$, < 0.07 .

It is clear from the diagram that most star-forming spirals in both clusters exhibit blue $FUV - V$ color (median of 1.6 ± 0.1) combined with weak $D_n(4000)$ strength (median 1.22 ± 0.02). Such values indicate young stellar populations, and are expected for galaxies with ongoing star formation.

Turning to examine the locations of passive spirals, we note that passive spirals in MS 0451 largely occupy a different region of the plot than Cl 0024 passive spirals. Cl 0024 passive spirals with UV detections—the majority—cluster quite tightly on the

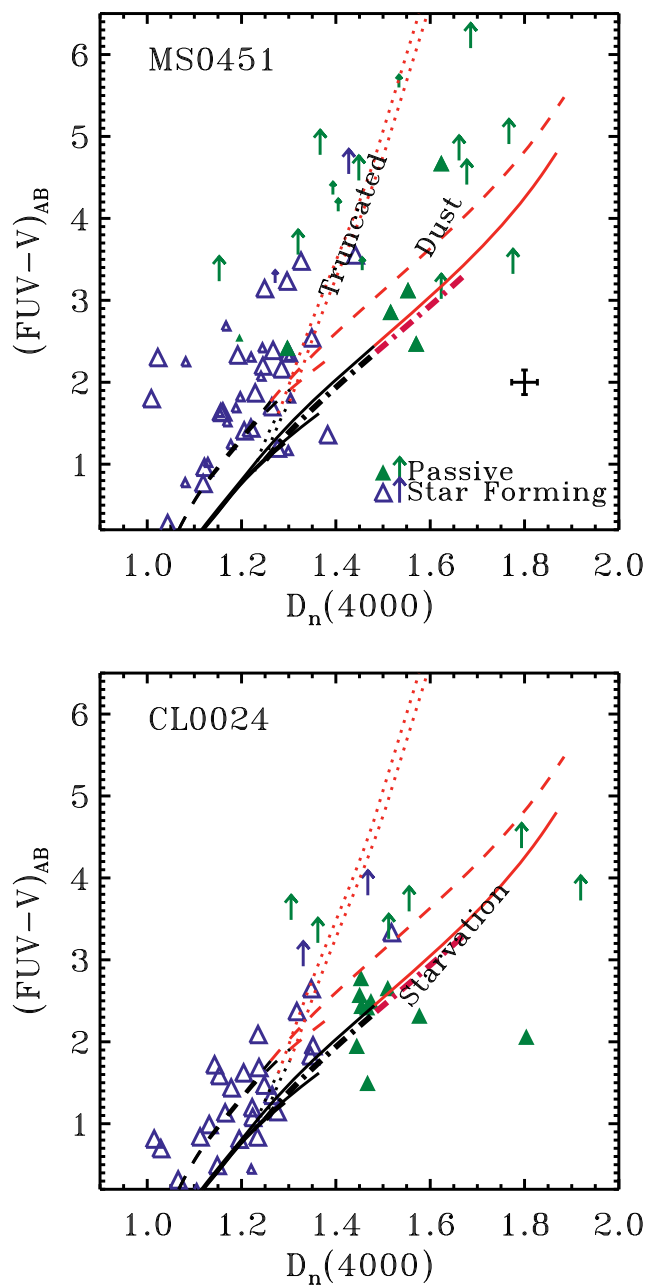


Figure 6.4 FUV $-$ V colors vs. $D_n(4000)$ strength for spirals in MS 0451 (top) and Cl 0024 (bottom). Star-forming and passive spirals are indicated by open blue triangles and solid green triangles, respectively. Arrows denote 3σ lower limits for FUV $-$ V colors for those galaxies not detected in the UV, colored blue for star-forming spirals and green for passive spirals. Small symbols indicate spirals with $H\delta_A > 5\text{\AA}$, similarly color coded. We plot only galaxies with $D_n(4000) < 0.07$. Solid, dotted, dashed, and dash-dotted lines respectively indicate model tracks for exponentially declining, dust-enriched, truncated, or “starved” star formation, as described in the text. Tracks are colored red for regimes where $[O II] > -5\text{\AA}$.

plot at moderate $FUV - V$ colors (median 2.5 ± 0.1) and moderately strong $D_n(4000)$ (median 1.47 ± 0.02). In contrast, as we have already noted, many of the MS 0451 passive spirals have only upper limits on their FUV emission, some at quite red $FUV - V$ colors. Across both clusters, these UV-undetected objects seem also to exhibit a wider spread in $D_n(4000)$ than the UV-detected passive spirals (rms of 0.23 ± 0.06 cf. 0.08 ± 0.02). The dominance of UV-detected passive spirals in Cl 0024, compared to the UV-undetected type that are predominant in MS 0451, begs the question of whether passive spirals are created in different ways in each of the two clusters. As we will show, the two types of passive spirals—UV detected and undetected—may have fundamentally different star formation histories.

To help decipher the star formation histories of passive spirals in Cl 0024 and MS 0451, we overlay in Figure 6.4 evolutionary tracks from the population synthesis code of Bruzual & Charlot (2003). Using these, we can test several classes of models that could explain the origin of passive spirals. Specifically, can passive spirals be created by simply adding dust to a star-forming spiral? Can they be created by suddenly switching off star formation in a galaxy, which we will call “truncation” models? Or, finally, can we create the passive spirals by switching a star-forming spiral into a phase where its star formation rate declines more rapidly over a timescale of 0.5–2 Gyr (a “starvation” model)?

In Figure 6.4, solid lines indicate the track followed in $FUV - V$ vs. $D_n(4000)$ space by several model stellar populations with exponentially-declining SFRs, with characteristic timescales $\tau \sim 3\text{--}7$ Gyr. Such models have been found to reproduce the optical spectra of Sa–Sc-type star forming galaxies (Poggianti & Barbaro 1996). Dashed lines add dust extinction of $A_V = 0.6$ to these same models, corresponding to the mean difference in $FUV - V$ between the (UV-detected) passive and active spirals. Active spirals largely occupy the region in between tracks with zero and moderate extinction. Tracks are in red for regimes where $[O II] > -5\text{\AA}$, estimated from the models in the same way as in Chapter 5.

Only models with a relatively fast exponential decline in SFR ($\tau \leq 1$ Gyr, upper solid and dashed lines in Figure 6.4) can match the peculiar combination of interme-

diate $FUV - V$ and strong $D_n(4000)$ exhibited by the bulk of the UV-detected passive spirals. Any star forming spirals that transition into this sort of rapid decay of star formation, eventually entering a spectroscopically passive phase, will reproduce the positions of the UV-detected passive spirals in the diagram (thick dash-dotted “starvation” line in Figure 6.4).

Conversely, passive spirals with lower limits on their color, which dominate the population in MS 0451, seem to be most consistent with models where star formation is rapidly truncated at an age of <7 Gyr, indicated by the dotted lines in Figure 6.4. Stacking together the UV images for undetected passive spirals, we still detect no significant UV emission. Though confusion noise becomes significant in the stacked image, the nondetection implies that the median $FUV - V$ is at least ~ 1 magnitude fainter than the upper limits indicated in Figure 6.4.

The positions of these UV-undetected spirals on the plot could also be explained by strong levels of dust obscuration. However, $24 \mu\text{m}$ imaging of both clusters with MIPS on the *Spitzer Space Telescope* indicates that there is a deficit of obscured dusty starbursts in MS 0451, in comparison to Cl 0024 (Geach et al. 2006). If the UV-undetected passive spirals were simply dusty, we would expect to see the *opposite* trend in the MIPS observations, since there are so many of these objects in MS 0451. We therefore believe that the rapid truncation of star formation is the most likely explanation for the UV-undetected passive spirals.

The population of spirals in MS 0451 includes a number of poststarburst galaxies that also seem to be consistent with rapidly truncated star formation; in fact, rapid truncation of a starburst is thought to be the primary way that these galaxies achieve such high $H\delta$ values (Poggianti et al. 1999). Indeed, the poststarburst spirals may be closely related to the UV-undetected passive spirals in MS 0451. Several apparently star-forming galaxies also reside along the “truncated” track. Together, these could represent a continuum of galaxies in various stages of having their star formation halted. However, the supposedly rapid timescale for the cessation of star formation begs the question of why we would see any star-forming spirals in the region of the plot where models indicate that they should already be passive. Some mix of models,

with increased dust obscuration combined with the truncation of star formation, could provide an explanation.

While we have found passive spirals to be abundant in both Cl 0024 and MS 0451, it appears that they are largely formed through different mechanisms in each cluster. The more rapid cessation of star formation required to explain the MS 0451 passive spirals is likely due to some physical mechanism that exerts a stronger force on galaxies in MS 0451 than in Cl 0024. This once again brings to mind the hot, dense ICM of MS 0451, which at least has the potential to apply a much stronger force (ram-pressure stripping) on infalling galaxies than in Cl 0024. In the next section, we will examine the stellar populations of early-type galaxies across the two clusters, in an attempt to identify the expected end products of these rapidly and slowly quenched passive spirals: S0s with signatures of recent star formation on varying timescales.

6.5 Star Formation Histories of E+S0 Galaxies

While careful analysis of local S0 galaxies has revealed some signs that their stellar populations are younger than those of ellipticals (e.g., Poggianti et al. 2001), such signatures have so far been elusive at intermediate redshift, despite expectations that S0s with newly halted star formation would be abundant. Now, however, under the hypothesis that passive spirals in MS 0451 and Cl 0024 must be disappearing from our spiral sample as they fade in UV and increase in $D_n(4000)$, we turn again to a study of the stellar populations of early-type galaxies.

The different characteristics of passive spirals in Cl 0024 and MS 0451 help to provide a key for uniquely linking the passive spirals to their potential S0 descendants. Because the properties of passive spirals largely differ between the two clusters, so too will any S0s that have just recently changed their morphology.

With this in mind, we wish to examine recent star formation as well as any ongoing star formation in the cluster E+S0s. In Figure 6.5, we plot $D_n(4000)$ strength versus [O II] EW for all early types in Cl 0024 (left) and MS 0451 (right), with symbols coded to indicate their morphologies (as shown in the legend).

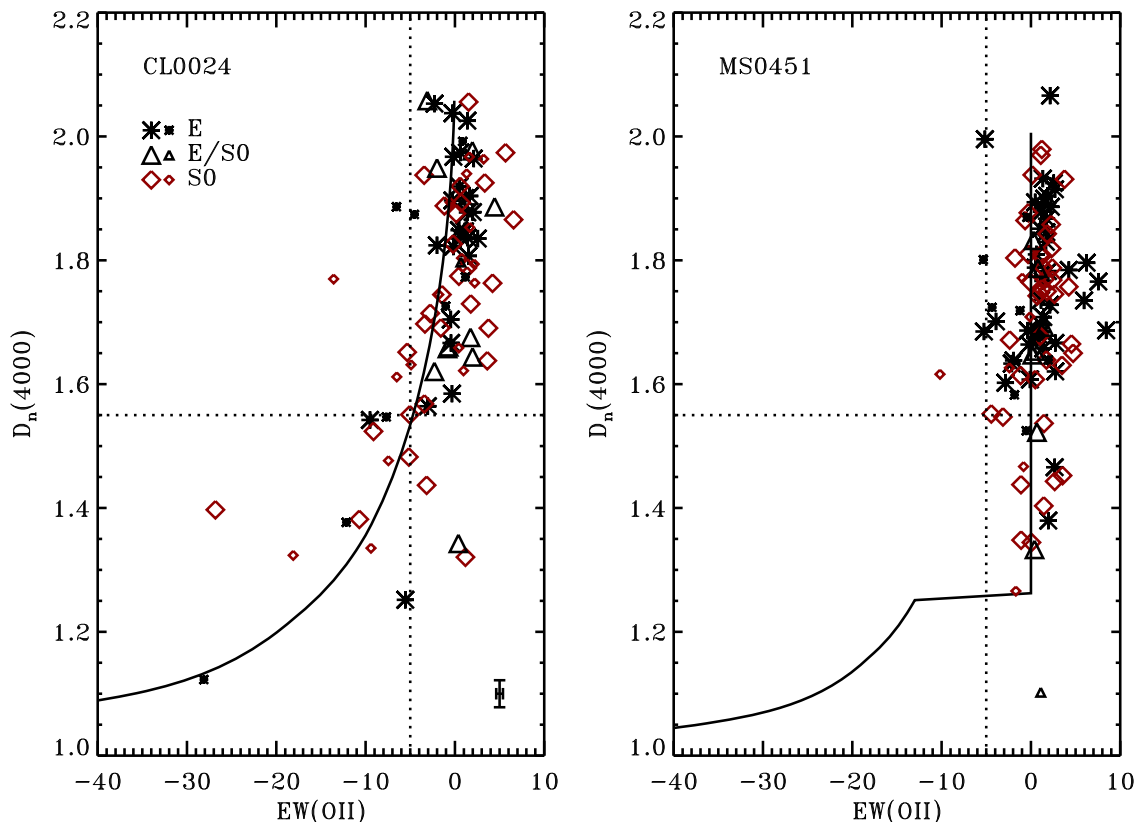


Figure 6.5 $D_n(4000)$ Balmer break strengths vs. $[O II]$ equivalent widths for cluster early types in Cl 0024 (left) and MS 0451 (right). Symbol shapes and colors denote galaxy morphologies as indicated on the figure. Small symbols indicate galaxies that are located outside the cluster virial radius, and large symbols mark galaxies within R_V . Solid line in the left panel is the best-fitting model track, a starvation ($\tau = 1$ Gyr) model with dust, while in the right-hand panel the best fit is to a truncation model (at age 5 Gyr). The best-fit model tracks for each cluster are similar to those seen in Figure 6.4.

Most bright E+S0s in both clusters exhibit the signatures of old stellar populations: weak or absent $[O II]$ and a strong Balmer break ($D_n(4000) \gtrsim 1.6$). In Cl 0024, however, we observe a striking tail of galaxies extending from the locus of old E+S0s toward weaker $D_n(4000)$, coupled with significant $[O II]$ emission. MS 0451 exhibits a similar tail of early-type galaxies toward weak $D_n(4000)$ strength, but *without* any associated $[O II]$ emission.

If we apply a cut at $D_n(4000) = 1.55$, indicated by the horizontal dotted lines in the figure, we find that 10%–15% of the total E+S0 population in each cluster has $D_n(4000)$ below 1.55. While somewhat arbitrary, the chosen $D_n(4000)$ dividing line

lies well below the expected value for an early-type galaxy that has been passively evolving since formation at $z \geq 1$. In fact, in the case of a prototypical elliptical whose stars were created in a short burst, $D_n(4000)$ should fade from 1.25 to 1.7 in less than ~ 2 Gyr, according to Bruzual & Charlot (2003) models—less than the time from $z = 1$ to $z \sim 0.5$.

There are essentially two possible explanations for finding E+S0 galaxies with such low $D_n(4000)$: either they have undergone recent star formation, or they harbor an AGN that contributes to the spectrum. If they have formed stars recently or are continuing to form stars, then they must have either formed a significant population of stars at $z < 1$ while already displaying early-type morphology, or else transformed morphology from a star-forming spiral to an early type (either singularly or through a merger). Under each of these scenarios, there must be some way to account for the presence of emission lines in the Cl 0024 objects but a lack thereof in MS 0451.

A third possibility—that we have simply misclassified some spiral galaxies as S0s—is easy to discount based on this last requirement. If the low $D_n(4000)$ S0s are truly just spirals, then we would not expect in MS 0451 to *exclusively* miscast as S0 just those spirals with no [O II] emission, while at the same time misclassifying spirals with a range of [O II] in Cl 0024. On the other hand, if we are biased towards mixing up the morphological classifications of passive spirals and S0s, this only strengthens the notion that one type may be transforming into the other.

To better assess the star formation histories of these peculiar objects, we overplot in Figure 6.5 two characteristic model tracks equivalent to those plotted for the passive spirals in Figure 6.4. In Cl 0024, we plot a starvation-like track ($\tau = 1$ Gyr with internal $A_V = 0.6$), while in MS 0451, we plot the track of a galaxy with star formation truncated rapidly at an age of 5 Gyr. In each case, the model track reproduces the positions of the galaxies very well. We note that most physically plausible truncated-spiral tracks are inconsistent with the distribution of points in Cl 0024, as no such models reach $D_n(4000) \gtrsim 1.4$ before truncation, yet we still see galaxies with [O II] emission in this range. Remarkably, then, a single starvation track reproduces the positions of both the low- $D_n(4000)$ early types and most passive spirals (Figure 6.4) in

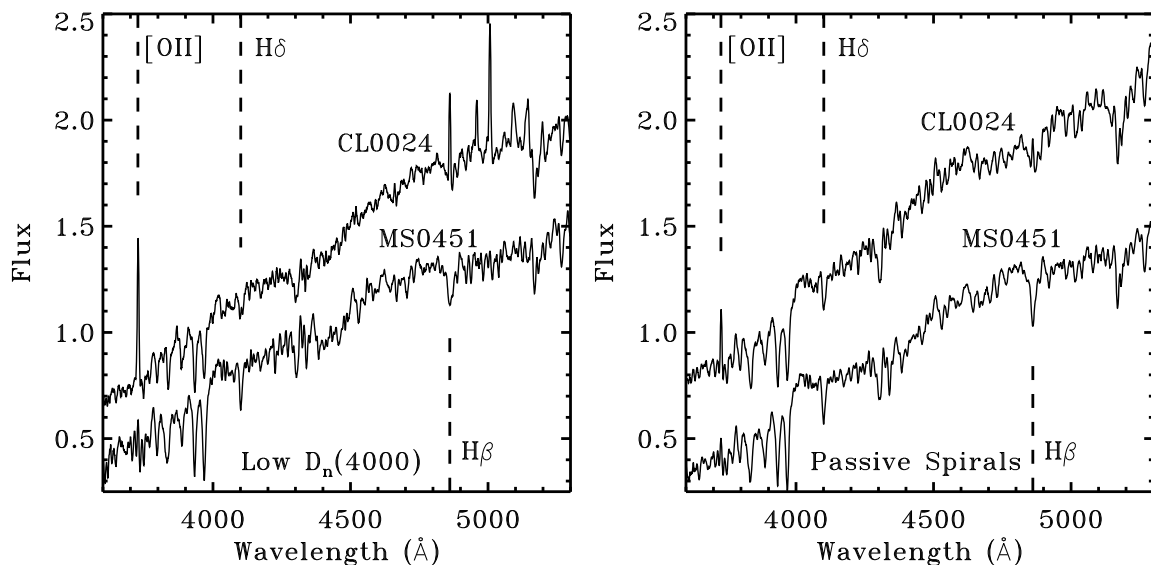


Figure 6.6 Left: Normalized, coadded spectra of E+S0s in Cl 0024 and MS 0451 with $D_n(4000) < 1.55$, including only spectra with $S/N > 5$ (\AA^{-1}). Cl 0024 spectrum is shifted upward in flux (arbitrary units) for display purposes. The locations of several key spectral lines are marked. Right: Normalized, coadded spectra of passive spirals in Cl 0024 and MS 0451, also restricted to spectra with $S/N > 5.0$. In each cluster, the $[\text{O II}]$, $\text{H}\delta_A$, and $\text{H}\beta$ strengths of passive spirals closely resemble those of the low- $D_n(4000)$ early types in the same cluster.

Cl 0024, while a truncated star formation track similarly matches the star formation histories of both classes in MS 0451. These similarities in star formation history suggest an evolutionary link between the passive spirals and the low- $D_n(4000)$ early types in each cluster.

We can further evaluate the likelihood of a connection between the passive spirals and the low- $D_n(4000)$ early types through a consideration, for each cluster, of the coadded spectra of both classes. In Figure 6.6, we plot in the left-hand panel the coadded spectra of all E+S0s in the clusters with $D_n(4000) < 1.55$, and in the right-hand panel, the coadded spectra of passive spirals in each cluster. In each case, we only include galaxies with overall spectral $S/N > 5.0$ (\AA^{-1}) in the summation. The locations of several key spectral lines are marked.

Considering the coadded early types first, we can immediately cast doubt on the idea that AGN are responsible for the low $D_n(4000)$. While a substantial contribution

from a flat AGN continuum can serve to weaken the Balmer break in a galaxy, the same effect should also dilute the observed depth of stellar absorption lines, such as $H\delta$. Yet it is clear from the coadded spectra that the low- $D_n(4000)$ early types in both clusters exhibit moderately strong $H\delta_A$: $2.2 \pm 0.2\text{\AA}$ and $1.2 \pm 0.2\text{\AA}$ for MS 0451 and Cl 0024, respectively. As both values are much higher than the median $H\delta_A = -1.0 \pm 0.2$ of cluster ellipticals, their Balmer strengths are consistent with the interpretation that they contain young stars, and *inconsistent* with a significant AGN (dust obscured or otherwise) contributing to the galaxy’s spectrum.

Though the spectra make clear that these “young S0s” (as we will call them) truly contain a population of young stars, is it possible that these galaxies have recently undergone a “rejuvenation” of star formation through some interaction (as we hypothesized in Chapter 3)? Serious doubt is cast on this hypothesis by the lack of MS 0451 E+S0s currently containing emission lines in their spectra. After a moderate starburst on top of an established stellar population, Bruzual & Charlot (2003) models predict a return to a passive spectrum with strong $D_n(4000)$ in as little as 100 Myr after the burst. To have so many S0s experience a rejuvenation episode so recently, yet observe none of them currently in a starburst phase, is implausible.

We are left, then, with the possibility that these young S0s truly represent the end states of the passive spirals. The contrast between young S0s in Cl 0024, whose [O II] strengths are consistent with a gradual decline in star formation, and those in MS 0451, where the lack of [O II] indicates recent truncation, evokes the similar dichotomy between passive spirals with a slow truncation of star formation (mostly in Cl 0024) and those exhibiting a more rapid truncation (mostly in MS 0451). Comparing the coadded spectra of the two classes in more detail, we find further evidence to support an evolutionary link between passive spirals and young S0s.

First, the passive spiral spectrum for Cl 0024 exhibits a weak [O II] emission line of $-3.1 \pm 0.5\text{\AA}$, despite the population having been selected for their low [O II]. The presence of some [O II] emission in both the passive spirals and the young S0s ([O II] = $-10.1 \pm 0.5\text{\AA}$) is consistent with the slow decay in star formation thought to be acting. It may be that, in some cases, the transformation to S0 morphology

occurs *before* the final cessation of star formation. MS 0451 passive spirals, in contrast, have an [O II] EW consistent with zero, as do their S0 counterparts. Again, this is consistent with the rapid truncation of star formation in MS 0451 passive spirals, followed by an almost simultaneous transformation into S0 morphology. The morphological transformation cannot be significantly delayed after the halt in star formation, because the S0s' low $D_n(4000)$ and strong H δ strictly limit the time since last star formation to <100 Myr, according to the model tracks of Figure 6.4 and 6.5.

Second, the H δ values of passive spirals in each cluster are similar to those of their counterpart young S0s. In Cl 0024, passive spirals exhibit weaker H δ than normal star forming spirals— $H\delta_A = 1.8 \pm 0.2\text{\AA}$ in the coadded spectrum compared to a median $H\delta_A = 3.9 \pm 0.2\text{\AA}$ for star-forming spirals (See also Chapter 5). The coadded spectrum of young S0s exhibits a similarly moderate $H\delta = 1.2 \pm 0.2\text{\AA}$, between the typical values for spirals and for ellipticals. In MS 0451, passive spirals ($H\delta = 3.0 \pm 0.2\text{\AA}$) and young S0s ($H\delta = 2.2 \pm 0.2\text{\AA}$) exhibit H δ strengths that also mirror each other closely. Yet they exhibit overall higher strengths than in Cl 0024, another indication that the halt in star formation was quite recent for galaxies in MS 0451.

The close similarities between passive spirals and young S0s *within* each cluster, coupled with the clear differences in populations *between* the two clusters strongly argues in favor of a model where passive spirals and young S0s represent an evolutionary sequence. At the same time, we have not yet fully explored possible explanations for why this evolutionary sequence behaves differently in the two clusters. In the next section, we begin consideration of this issue by examining the local environments in which passive spirals and young S0s are found.

6.6 The Local Environments of Passive Spirals and Young S0s

So far, we have treated the populations of passive spirals and young S0s largely as a uniform population within each cluster. The reality, however, is more complex. While

the passive spirals in MS 0451 were largely found to have different star formation histories than Cl 0024 passive spirals, the segregation is imprecise: MS 0451 contains a proportion of UV-detected spirals ($\sim 1/3$) consistent with a slow decline in star formation, while Cl 0024 conversely contains a similar fraction of passive spirals whose star formation may have been truncated more rapidly. To help disentangle this puzzle, we focus now more closely upon the local environments in which the passive spirals and their remnant S0s are found.

We start by examining the spatial distribution of transition galaxies across both clusters. In Figure 6.7, we plot the positions of all passive spirals (green squares) and young S0s (red triangles). We also plot the populations of compact narrow emission line galaxies (CNELGs) found in each cluster (blue pentagons), which will be discussed further in §6.7. Thick black dots indicate cluster E+S0s, small black dots are cluster spiral and irregulars, and small grey dots indicate spectroscopically confirmed non-members, to illustrate the spatial coverage of our spectroscopic campaign.

The first striking feature to note in Figure 6.7 is that passive spirals and young S0s occur both in the cluster core and at higher radius, even beyond R_V , with no obvious segregation between the passive spirals and S0s. Secondly, in MS 0451 both passive spirals and young S0s appear to be more spread out across the cluster than in Cl 0024, where more than half are located within 1 Mpc of the cluster center. Both features reveal important clues to the physical processes at work.

Careful inspection of those passive spirals found beyond the cluster cores gives the impression that many have other cluster members nearby. Could passive spirals be preferentially found in infalling groups? Some evidence for passive spirals in groups at these redshifts has already been noted (Jeltema et al. 2007). To evaluate quantitatively this possibility, we calculate the projected local densities of these passive spirals, using the 10 nearest neighbors method, following T03 and Dressler et al. (1997). Considering only galaxies outside of the cluster cores ($R > 1$ Mpc in Cl 0024 and $R > 1.5$ Mpc in MS 0451, $\sim 50\%$ of R_V), we find that passive spirals are found at a median local density of $\Sigma = 36 \pm 5 \text{ Mpc}^{-2}$ in MS 0451 and $\Sigma = 51 \pm 15 \text{ Mpc}^{-2}$ in Cl 0024, both somewhat higher than the density of a typical infalling spiral of

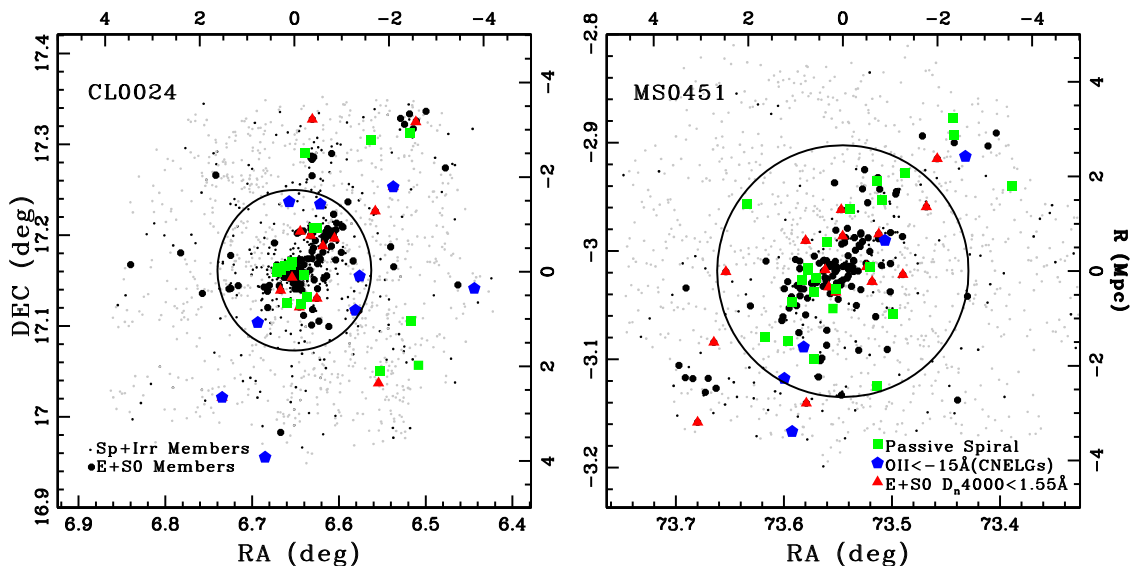


Figure 6.7 Distribution of galaxies in the field of Cl 0024 (left), and MS 0451 (right). Galaxies showing spectroscopic signs of recent evolution are marked. Spectroscopically confirmed cluster members are marked with large (E+S0s) and small (spirals) black dots. Objects with spectroscopically determined redshifts outside the cluster are marked as grey dots. Blue pentagons are compact narrow emission line galaxies ($[\text{O II}] < -15\text{\AA}$, and to $M_V < -18.0$). Solid green squares are passive spirals. Filled red triangles mark early types with $D_n(4000) < 1.55$. Top and right axes show projected radius from the cluster center, in Mpc. Large circle indicates the virial radius in each cluster. Passive spirals and young S0s are found even in the outskirts of both clusters, perhaps residing in groups.

$\Sigma = 28 \pm 3 \text{ Mpc}^{-2}$ across both clusters.

Passive spirals, therefore, seem to be forming both within infalling groups and closer to the cluster core—two distinct regions where the dominant physical forces acting on galaxies are likely to be quite different. Remarkably, we find that four out of the five UV-detected passive spirals in MS 0451 reside in groups outside the cluster core. Recalling from Figure 6.4 that these UV-detected passive spirals closely follow a “starvation-like” gradual cessation of star formation, we conclude that *nearly all* passive spirals within infalling groups are experiencing a cessation of star formation spread over a ~ 1 Gyr timescale.

In contrast, virtually all MS 0451 passive spirals within 1.5 Mpc of the cluster center have undergone a rapid truncation in star formation. In Cl 0024 it appears that rapid truncation of star formation can also occur, but only extremely close to

the cluster core: 4/6 passive spirals without UV detection are located within 300 kpc of the Cl 0024 center.

While passive spirals are abundant in the region around the MS 0451 center, there is a hole of ~ 600 kpc radius, within which we observe almost no spirals of any type. Unlike in Cl 0024, where spirals are observed even within ~ 100 kpc of the central galaxies, no spirals survive to reach the center of MS 0451. Even accounting for the larger virial radius of MS 0451, this spiral-free zone is significantly larger than that seen in Cl 0024: within $0.2R_V$ (~ 530 kpc in MS 0451 and ~ 340 kpc in Cl 0024), only $4\% \pm 3\%$ of MS 0451 members in our sample are spirals ($< 2\%$ passive), compared to $42\% \pm 7\%$ ($9\% \pm 3\%$ passive) in Cl 0024. As the time required for a galaxy to travel ~ 600 kpc across the core of MS 0451 is only 0.4 Gyrs, it appears that spirals in this environment must indeed be converted to early morphology quite rapidly.

Both the central hole in MS 0451 and the central concentration of UV-undetected passive spirals in Cl 0024 can be better understood by considering the local ICM densities of the transition galaxies in each cluster. In Figure 6.8, we make use of *Chandra* X-ray data for each cluster to plot the expected strength of ram pressure as a function of radius for Cl 0024 and MS 0451. Each track is generated by calculating the gas density $\rho(R)$ from the best-fit isothermal β -model from Donahue et al. (2003) and Ota et al. (2004), for MS 0451 and Cl 0024, respectively. We then estimate ram pressure $P = \rho v^2$ by adopting each cluster's line of sight velocity dispersion, σ , as the characteristic velocity of a galaxy in that cluster.

Figure 6.8 reveals that virtually all UV-undetected passive spirals are found in regimes where the ram pressure is significant ($> 20\%$ of that required to strip a Milky Way analogue), while UV-detected passive spirals are largely confined to regions of lower gas density. While the corresponding radial ranges differ between Cl 0024 and MS 0451, the UV-undetected passive spirals span a nearly identical range of ram-pressure strengths in each cluster. This argues strongly in favor of ram-pressure stripping as the mechanism responsible for the UV-undetected passive spirals. We note that no spirals survive in environments where the ram pressure is more than a few times that required to strip the Milky Way, and a natural consequence of this limit is

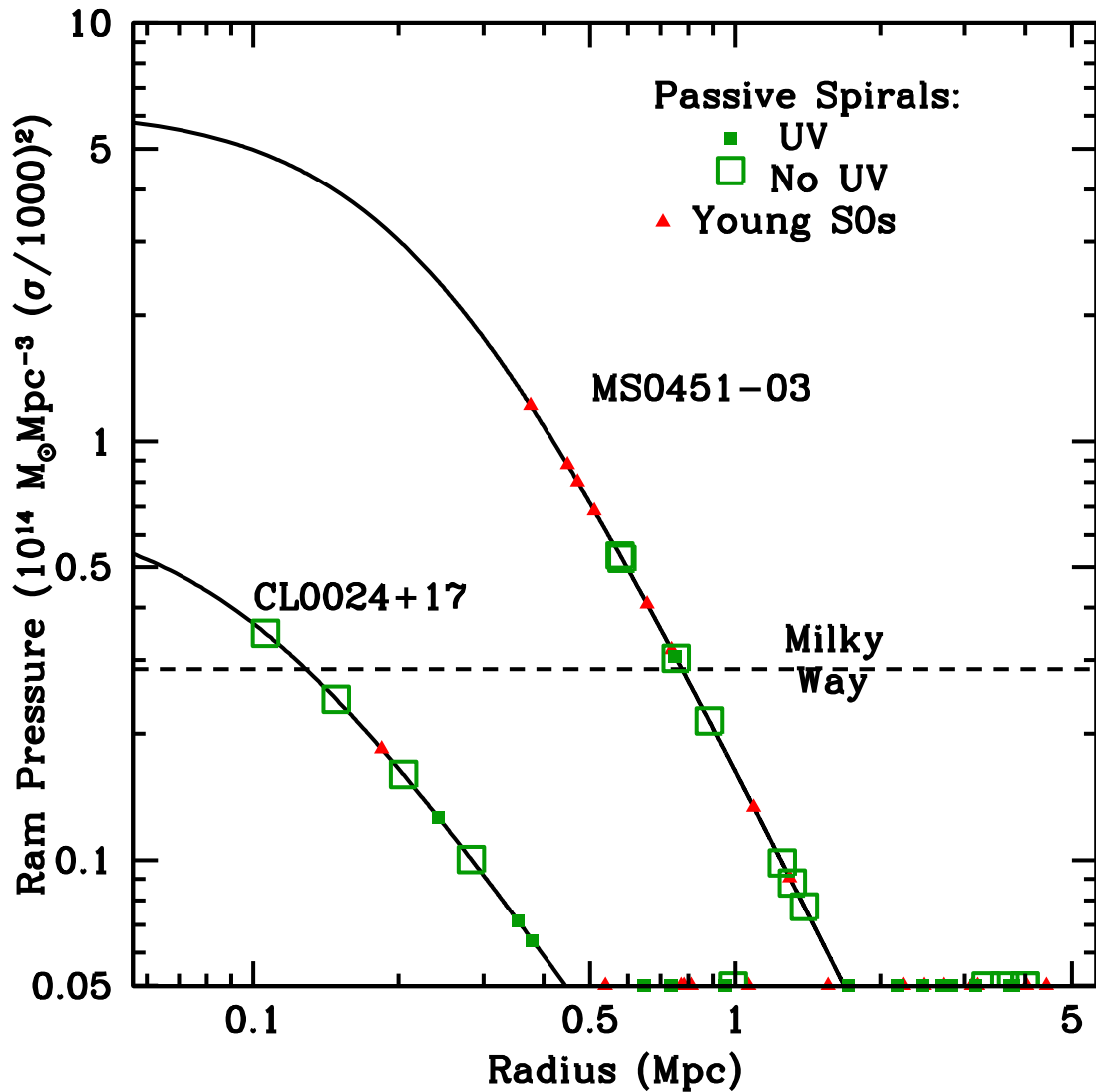


Figure 6.8 Strength of ram pressure as a function of radius, for both Cl 0024 and MS 0451. Solid lines indicate ram pressure $P(R)$ as described in the text. Dotted line indicates the pressure required to strip a spiral with characteristics of the Milky Way (T03; Gunn & Gott 1972). Overplotted on each track are the radial positions of passive spirals (UV detected and undetected) and young S0s in that cluster. Where the ram pressure falls below the lower bound of the plot, we mark the positions of galaxies along the lower edge of the plot. Most UV-undetected passive spirals are found in regimes of high ram pressure, while no passive spirals survive in regimes where ram pressure is more than a few times that required to strip a Milky Way-like spiral.

that no spirals in MS 0451 survive to reach $R < 600$ kpc (though, as expected, several young S0s appear at slightly lower radii). In §6.7.2, we will discuss in more detail the relation between this presumed ram-pressure stripping and other mechanisms that may be acting to transform morphology.

6.7 Physical Processes Driving the Transformation

So far, we have shown in §6.4 and §6.5 that the large population of passive spiral galaxies in both Cl 0024 and MS 0451 are transforming into S0s on a variety of timescales. Building on this, in §6.6, we have successfully matched the timescales of transformation with specific environments within each cluster. Consequently, we are now able to construct a road map describing the sites and timescales of transformations across both clusters.

To summarize, we find that some passive spirals are generated within infalling groups, experiencing a gradual decline in star formation rate and eventual transformation to S0 morphology. In the central regions of both clusters, a high proportion of spirals are seen to be passive. In Cl 0024, star formation within these spirals continues to decay at a relaxed pace, with few signs of rapid interaction with the cluster environment except near the very center where the effects of ram pressure begin to be important. In contrast, passive spirals all across the core of MS 0451 have had their star formation truncated rapidly, with a subsequent rapid transformation into S0 morphology.

In this section, we use this road map to consider the constraints that we can place on the physical processes operating in each of these three regimes: groups in the cluster outskirts, the Cl 0024 core, and the MS 0451 core.

6.7.1 The Cluster Outskirts

In the hierarchical assembly of clusters, groups infalling from the cluster outskirts can be thought of as the building blocks. T03 argued that the existence of the morphology–density relation implies that a galaxy’s evolutionary history is tightly

linked to its group’s history, until the group is absorbed into the cluster. Furthermore, the observation that mass and light trace each other tightly on large to small scales (Kneib et al. 2003) suggests that groups of roughly constant mass to light ratio—rather than individual galaxies—coalesce to build up the cluster.

The “preprocessing” of galaxies within these infalling groups is a crucial feature of evolution within both clusters, as here we are probing galaxies in a key density range at a key point in time: at $z > 0.5$, observations indicate that the early-type fraction is growing only in the cores of clusters, while below $z \sim 0.5$ evolution begins to accelerate in lower density regions (Smith et al. 2005a; Postman et al. 2005). As such, gaining an understanding of the physical processes driving galaxy transformation within the infall regions of clusters at $z \sim 0.5$ can shed light on the observed evolution in the morphology–density relation.

By virtue of the fact that passive spirals in the cluster outskirts are preferentially found in groups, we do not expect that the clusters’ ICM plays a direct role in suppressing star formation. Even in MS 0451, the force of the ICM should not be significant beyond the virial radius (Figure 1.2). And while we had previously argued in favor of starvation by the ICM (Chapter 5), which can be effective at large cluster radius, there is little reason to expect it to act on galaxies in groups more effectively than isolated spirals.

However, we cannot rule out the presence of gaseous interactions *within* groups. Indeed, X-ray observations of groups in the local universe reveal that they often harbor an intragroup medium (Mulchaey 2000), and simulations by Bekki et al. (2002) suggest that the starvation mechanism can operate similarly within large groups as it would in the overall cluster (see also Hester 2006; Fujita & Goto 2004). Intriguingly, X-ray bright groups seem to contain a higher early-type fraction than X-ray undetected groups (Zabludoff & Mulchaey 1998), consistent with the notion that the gas plays a role in shaping galaxy morphology.

The predicted timescale for cessation of star formation under starvation is consistent with our observed decline over 0.5 – 2 Gyr (Fujita 2004); in simulations by Okamoto & Nagashima (2003), a timescale of 1–2 Gyr for the halt in star formation

after gas removal provided a good fit to observations. We emphasize, however, that the ~ 1 Gyr decline in star formation represents only one observable phase of the predicted total timescale for conversion of a spiral to an S0 via starvation (≥ 3 Gyr, Bekki et al. 2002; Boselli et al. 2006). The slow action of starvation would preserve recognizable spiral structure for over 1 Gyr after star formation stops, and we have shown in Chapter 5 that these lifetimes for each phase are consistent with the hypothesis that all such passive spirals will become S0s by $z = 0$.

Yet direct observations of the intragroup gas are challenging at these redshifts, especially for small groups (but see Jeltema et al. 2007), and other mechanisms may also be able to reproduce the observed timescale for the cessations of star formation. In addition, some models suggest that modification of star-formation rates due to starvation only begin to be visible many Gyr after the halo is stripped (Boselli et al. 2006), and so the effectiveness of starvation in groups would depend in some sense on the dynamical age of each group, which is difficult to quantify. Gentle gas stripping or starvation by a diffuse intragroup medium therefore remains an attractive, but difficult to test, possibility.

Alternatively, the increased frequency of galaxy–galaxy interactions among members of a group, compared to the interaction rate between isolated galaxies, could be driving the creation of passive spirals in the cluster outskirts. We note that, at the group scale, the effects of impulsive galaxy–galaxy interactions are difficult to separate from galaxy–galaxy tidal interactions that act over a longer timescale, and so we consider them together here. While galaxy–galaxy harassment at the typical velocity dispersions of bound groups has not been widely studied, there are some advantages to this explanation. First, on a larger cluster scale, simulations indicate that harassment of massive cluster spirals results in gas being funneled to the central bulge (Moore et al. 1999), providing a natural mechanism to accelerate star formation and deplete a spiral’s gas supply; a similar gas funneling effect due to tidal effects during group preprocessing has also been proposed (e.g., Mihos 2004).

While simulations would be necessary to test the hypothesis, one could imagine a “gentle harassment” mechanism that induces a transport of gas to the galaxy cen-

ter without immediately destroying the spiral arms. A slow group-scale harassment could possibly reproduce the timescales for quenching of star formation indicated by the “starvation” model tracks in Figure 6.4. We note that the timescale for final conversion to S0 morphology may be different from the timescale under starvation, and could provide an important discriminator between the two possibilities in the future.

Depending on the rate of gas transport, it is possible that a brief increase in star-formation rate could be detected before the final quenching (Fujita 1998; Kodama & Smail 2001), and this could provide another way to distinguish between this mechanism and starvation. However, within the uncertainties, we cannot confirm any small starbursts among galaxies within infalling groups in our sample. Dividing our total sample of star-forming galaxies by radius into three equally-sized bins, we do not see evidence for an enhancement of either the mean or median [O II] of a star-forming galaxy in any of the three radial zones. Nor do we see any change in the fraction of star-forming galaxies with strong ($< -20\text{\AA}$) [O II]. However, as the expected lifetime for a burst is short (Fujita 2004), we cannot rule out the presence of small bursts that change the median specific star-formation rate by less than 20%.

A definitive distinction between gas-related processes and galaxy interactions therefore remains elusive. Importantly, however, we have already established that galaxy–galaxy harassment is affecting spirals across both clusters, and at a level that does not destroy their spiral structure: in Chapter 4, we found that the high scatter in the cluster Tully-Fisher relation compared to the field was most readily understood if galaxy harassment is acting to perturb the kinematics of spirals. We also observed a strange deficit in the cluster outskirts of spirals with high central mass concentrations; one possible explanation is that these galaxies have dropped out of our emission-line sample as they become passive due to the aforementioned funneling of gas to their centers.

While hardly a settled issue, we expect that the action of harassment is more likely to be at the root of the galaxy evolution in infalling groups, as the mechanism is already known to be acting in Cl 0024 and MS 0451. Yet some contribution from

the intra-group gas is also possible, and the two effects could act in combination. Future study of the bulges of spirals and S0s could help distinguish between the mechanisms by establishing whether significant mass has been funneled to centers of galaxies during their evolution, as predicted in the case of harassment.

6.7.2 The Cluster Cores

We turn now to the cores of both clusters, where spirals in MS 0451 appear to have their star formation quenched at a more rapid pace than in Cl 0024. The most obvious explanation for the accelerated truncation of star formation within the central region of MS 0451 is, of course, its much denser ICM. As we saw in Figure 6.8, rapid truncation of star formation appears to occur in both clusters only in regimes where the ram pressure is high. Due to the dense ICM in MS 0451, such an environment is much more widespread in this cluster, and so, unlike in Cl 0024, most of the passive spirals in its core are experiencing a rapid truncation of star formation.

Ram-pressure stripping, in regimes where it is effective, can strip an entire spiral disk in less than 100 Myr (Quilis et al. 2000; Fujita & Nagashima 1999). Detailed analysis of local analogs of passive spirals thought to be undergoing ram-pressure stripping suggest a timescale of ~ 300 Myr for the process to produce a galaxy similar to the UV-undetected passive spirals we observe (Boselli et al. 2006; Cortese et al. 2007). Both of these are consistent with the maximum timescale of 400 Myr implied by the 600 kpc hole devoid of spirals at the center of MS 0451. Further, there is some evidence that poststarburst/poststarforming galaxies in the Coma cluster—similar to, but fainter than those in MS 0451—are generated via ram-pressure stripping (Poggianti et al. 2004).

The fact that we observe passive spirals at all implies that the transformation to S0 is not precisely simultaneous with the halt in star formation (Poggianti et al. 1999). However, the “truncated” star formation history models presented in Figures 6.4 and 6.5 suggest that $D_n(4000)$ strength will increase at a fast rate after truncation, such that we must be seeing young S0s within 100 Myrs of the halt in star formation. The

similar fraction of galaxies observed in both the passive spiral phase and the young S0 phase support the idea that the lifetimes for each phase are comparable, at about 100 Myr.

Yet there are several remaining uncertainties in this simple picture. Ram-pressure stripping alone does not alter disk kinematics and spiral structure on such a short timescale, so there must be an additional mechanism to speed the conversion. In the cluster cores, harassment and/or tidal interactions could provide this additional impetus (e.g., Cortese et al. 2007; Mihos 2004). In Cl 0024, in the absence of rapid truncation by the ICM, a similar harassment or tidal process must be at work. However, the complex substructure of Cl 0024, and particularly the effects of the recent cluster collision, may generate importance differences between the two clusters.

In order to better constrain the mechanisms affecting passive spirals in the cores of Cl 0024 and MS 0451, we are aided by two supplementary observations, one of which illuminates the action of harassment, with the other providing further constraints on ICM interactions—particularly the hypothesis that shocks in the ICM could be important.

6.7.2.1 Compact Emission-Line Ellipticals

As discussed in Chapter 3, we found in Cl 0024 a population of relatively faint elliptical galaxies with strong emission, concentrated in a narrow range in radius close to the virial radius. We cast doubt on the idea that major mergers were the cause of these apparent starbursts, and we speculated that another rapidly acting physical interaction must be triggering these bursts of activity. Strong shocks in the ICM of Cl 0024 could easily have been generated (Roettiger et al. 1996) during the cluster–subcluster merger (Czoske et al. 2002), and these shocks could be responsible for the triggered starbursts/AGN we observe.

If this were the case, we hypothesized that we would not see such bursts in MS 0451, as its smoother large-scale structure makes it less likely that such shocks would be generated. Referring back to Figure 6.7, however, we see that objects of this type are indeed found in the outskirts of both clusters. While only half as many

are identified in MS 0451 as in Cl 0024, this detection rate is consistent with the lower spectroscopic completeness of our MS 0451 campaign for galaxies at these low luminosities: in MS 0451, 10% of detected cluster members are at $M_V \geq 19.6$, while in Cl 0024, the fraction is 20%.

The properties of these objects—compact size, $\text{EW}([\text{O II}]) < -15\text{\AA}$, and typical luminosities $M_V = -19.2$, associate them with a class of objects dubbed Compact Narrow Emission Line Galaxies (CNELGs) (Koo et al. 1995), or their more luminous cousins the Luminous Blue Compact Galaxies (LBCGs) (e.g., Noeske et al. 2006). Analysis by Rawat et al. (2007) of deep ACS imaging of LBCGs reveals that more than 1/3 show signs of a recent merger. Their positions outside of dense regions in both MS 0451 and Cl 0024 support the notion that these galaxies may simply represent the remnants of a merger between small, gas-rich galaxies.

In this interpretation, two important constraints can be put on the physical processes acting on passive spirals. First, we have eliminated the possibility that strong shocks in the Cl 0024 ICM have a significant effect, even on low-mass galaxies. Secondly, the minimum cluster radii at which these CNELGs/LBCGs are found identifies empirically the point at which merging becomes impossible and harassment must begin to dominate any galaxy–galaxy interaction.

In Cl 0024, this occurs nearly at the Virial radius, while in MS 0451 it occurs at a similar projected radius of 1.5 Mpc. We expect, then, that harassment within 1.5 Mpc should scale in strength similarly between the two clusters. If harassment is responsible for the slow conversion of spirals to S0 in the Cl 0024 core, it should also be acting on MS 0451 spirals with similar strength.

6.7.2.2 Fundamental Plane

An analysis of the Fundamental Plane can provide sensitive constraints on the star formation and kinematic histories of E+S0s (Chapter 3). In Cl 0024, we observed that elliptical and S0 galaxies form a clear FP (Figure 6.9), yet they exhibit a high scatter,

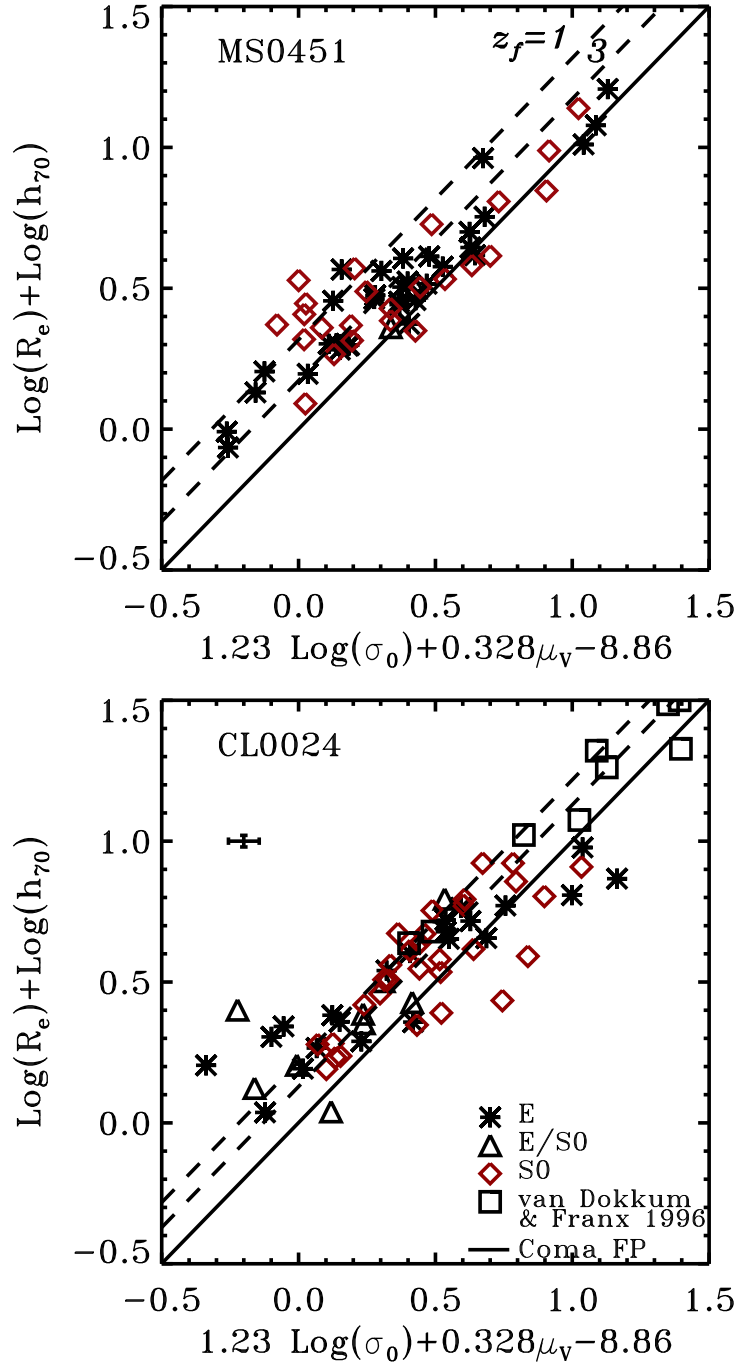


Figure 6.9 The Fundamental Plane of E+S0s in MS 0451, top, and Cl 0024, bottom. Symbols represent different morphologies, as indicated in the legend. Solid line is the local FP for the Coma cluster, adapted from Lucey et al. (1991). Dotted lines indicate the expected positions for early types that formed in a single burst at $z = 1$ or $z = 3$, calculated according to the models of Bruzual & Charlot (2003). A typical errorbar is shown in the upper left of the Cl 0024 panel.

equivalent to a spread of 40% in mass to light ratio (M/L_V).² Upon closer inspection, this high scatter appeared to occur only among galaxies within 1 Mpc of the cluster core. We suggested in Chapter 3 that the enhanced scatter in the cluster core may somehow be related to the recent cluster–subcluster merger in Cl 0024 (Czoske et al. 2002). By examining the FP and its residuals for MS 0451 as well, we can test the hypothesis that galaxy interactions in the core of Cl 0024 are enhanced over that expected for a relaxed cluster.

In constructing the FP for both clusters, surface brightness (μ_V) and effective radius (R_e) are determined via the *GALFIT* software (Peng et al. 2002), which fits a 2D model to the *HST* imaging. We fit models following the deVaucouleur’s function to each galaxy, and apply a k -correction from observed F814W magnitudes to rest-frame V -band surface brightness, μ_V , as discussed in Chapter 3.

The resulting FP for our sample of 60 E+S0 galaxies in MS 0451 is shown in Figure 6.9, alongside the previously published FP for Cl 0024. For both Cl 0024 and MS 0451, we overplot the local FP from the Coma cluster (Lucey et al. 1991) as a solid line, adapted to our chosen cosmology. In addition, we plot two parallel dotted lines indicating the galaxies’ expected FP intercept if they had formed in a single burst at $z_f = 1$ or $z_f = 3$, calculated using the Bruzual & Charlot (2003) models. It is clear that the E+S0 populations in both clusters have largely formed their stars at $z > 1$. Nevertheless, the high scatter in the Cl 0024 FP also seems to be present in MS 0451. Limiting our sample to the 67 galaxies with $\sigma > 100 \text{ km s}^{-1}$ as in Chapter 3, the overall scatter is 0.18 ± 0.02 , expressed in terms of a spread in $\log(M/L_V)$, compared to 0.16 ± 0.02 for Cl 0024.

A small portion of this large scatter in M/L_V can be attributed to the higher redshift of MS 0451, where an equivalent spread in galaxy formation ages translates into a larger FP scatter at $z = 0.54$ than at $z = 0.4$. In Figure 6.9, this effect is most easily seen by noting the larger separation between the $z_f = 1$ and $z_f = 3$ model lines in the MS 0451 panel, compared to the Cl 0024 panel. If MS 0451 early types were

²As discussed in Chapter 3, a galaxy’s deviation from the FP can be thought of as a change in mass to light ratio, via the relation $\Delta \log(M/L_V) = \Delta\gamma/(2.5\beta)$, where β is the slope of the FP and $\Delta\gamma$ is each galaxy’s deviation from the cluster’s overall FP intercept γ .

to passively evolve between $z = 0.54$ and $z = 0.4$, the single stellar population (SSP) models of Bruzual & Charlot (2003) predict a decrease in the FP scatter of only up to ~ 0.04 . With a typical uncertainty in $\Delta \log(M/L_V)$ of ~ 0.05 for each point, a small additional amount of scatter can be attributed to measurement error. However, if we assume that the measurement uncertainties and intrinsic scatter add in quadrature, we can only attribute an additional ~ 0.01 of the scatter to measurement uncertainties.

This still leaves an unexpectedly high spread in mass to light ratios for MS 0451 early types. In Figure 6.10, we plot each galaxy’s residual from the FP as a function of its dynamical mass, calculated according to $M = 5\sigma^2 R_e/G$. In both clusters, we observe a clear “downsizing” trend that has been described by several authors (e.g., Cowie et al. 1996; Treu et al. 2005b), the tendency for less massive E+S0s to exhibit lower mass to light ratios, implying younger stellar populations.

To judge the effects of “downsizing”, we fit a straight line to the FP residuals as a function of mass, limiting the fit to masses above $5 \times 10^{10} M_\odot$, where selection effects are minimal. In MS 0451, subtracting off this extra “tilt” to the FP greatly tightens the observed scatter, to $\Delta \log(M/L_V) = 0.12$, a level of scatter consistent with that of other well-virialized clusters at lower redshift (e.g., Kelson et al. 2000b).

Performing the same exercise on Cl 0024, however, results in no improvement in the FP scatter. Close inspection of the morphologies of galaxies in Figure 6.10 uncovers the reason. While ellipticals in Cl 0024 display a tight sequence in mass, S0s, especially at intermediate masses of $\sim 10^{11} M_\odot$, exhibit a remarkable scatter in their FP residuals. These residuals do not appear to correlate with any typical measures of star formation rate or mass to light ratio, including $D_n(4000)$, $H\delta$, or even broadband optical colors. It seems, then, that the previously described FP scatter in the core of Cl 0024 can be ascribed almost entirely to S0s whose properties do not obey any simple trends with mass or star formation.

Furthermore, a significant number of Cl 0024 galaxies exhibit FP residuals with $\Delta \log(M/L_V) > 0$, an unphysical quantity that either indicates stellar populations older than those of Coma cluster early types (impossible due to the much younger age of the universe at $z = 0.4$ and the extreme mass to light ratios implied), or else

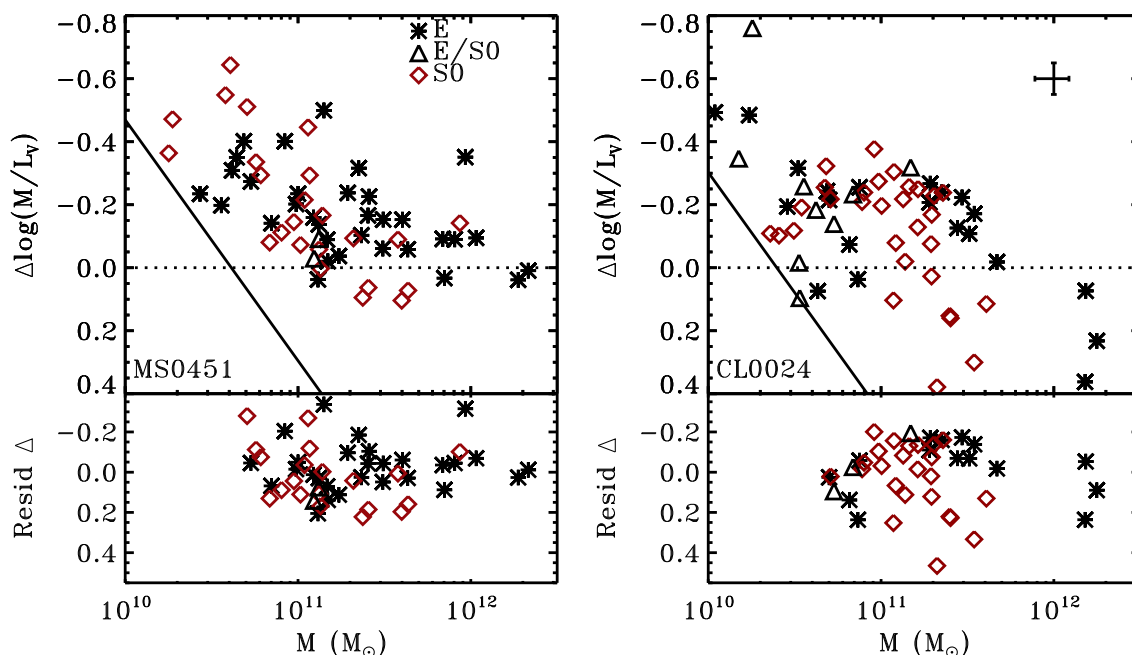


Figure 6.10 $\Delta \log(M/L_V)$ versus dynamical mass, M , for MS 0451 (left) and Cl 0024 (right). Symbols denote different morphologies as indicated on the legend. We are insensitive to galaxies in the area to the lower left of each solid black line, due to the luminosity limit of our sample. Above, $\sim 5 \times 10^{10} M_\odot$, we are nearly unbiased. Lower split panels show the residuals from fitting and subtracting a straight line to galaxies at $M > 5 \times 10^{10} M_\odot$. $\Delta \log(M/L_V)$ for S0s in Cl 0024 do not form a tight sequence in mass, while their counterparts in MS 0451 and the Es in both clusters do form a tight sequence. Many Cl 0024 galaxies also occupy unphysical locations at $\Delta \log(M/L_V) > 0$.

indicates the breakdown of the Fundamental Plane for these objects. In contrast, all of the scatter in MS 0451 early types is in the expected direction, in the sense that some galaxies have younger stellar populations with $\Delta \log(M/L_V) < 0$, while the most massive ellipticals and S0s lie neatly on the local FP.

What could be generating such abnormal galaxies in Cl 0024 but not in MS 0451? Enhanced levels of galaxy–galaxy interaction due to the complex substructure in Cl 0024 is the most likely explanation. The difference between a slow conversion of spirals to S0s (in Cl 0024) and a rapid truncation of star formation (in MS 0451) could also affect the positions of S0s on the FP. Future simulations to test this possibility would be welcome. We note that the actual “young S0s” are only sparsely represented

in Figure 6.10, due to the smaller sample of galaxies that can be plotted on the FP, and are not driving the observed difference by themselves.

What, then, are the implications for the physical processes driving galaxy evolution in the cores of both clusters? In short, we can conclude that the complex recent assembly history of Cl 0024 *does not* enhance the ability of the ICM to transform galaxies via shocks, but it *does* appear to enhance the observed kinematic disturbance of galaxies within the cluster core. Some mix of galaxy–galaxy interaction and tidal interaction therefore must dominate in the core of Cl 0024, driving the steady decline in star formation rate within its spiral population. Only for galaxies that reach the inner ~ 300 kpc will ram-pressure stripping become important.

In contrast, the quenching of star formation in MS 0451 is almost certainly driven by ram pressure from the ICM, probably coupled with galaxy and tidal interactions that serve to erase spiral structure and complete the morphological conversion. In MS 0451, the effects of harassment/tidal interaction must complete the morphological conversion more rapidly than in Cl 0024, where the stellar populations of passive spirals indicate that they are long-lived ($\sim 1\text{--}2$ Gyr). At the same time, the effects of this conversion must somehow decay rapidly enough in MS 0451 S0s to be unobserved in the residuals from the FP. Future investigations into the effects of harassment on the S0 Fundamental Plane could help shed light on this issue.

6.8 Discussion and Conclusions

In this work, we have presented new results from our comprehensive comparative survey of two massive, intermediate redshift galaxy clusters, Cl 0024 + 17 ($z = 0.39$) and MS 0451 – 03 ($z = 0.54$). We have identified and studied several key classes of transition objects in the clusters: the passive spirals and the young S0s. Through UV imaging and measurements of spectral line indices, we have concluded that some passive spirals have experienced a decline in star formation over a ~ 1 Gyr timescale, mostly in Cl 0024, while others, mostly in MS 0451, have experienced a more rapid

truncation in star formation. For the first time, we have been able to conclusively identify spiral galaxies in the process of transforming into S0 galaxies, by directly linking the passive spirals in each cluster with their descendant S0s.

Having established that the transformation from spiral to S0 galaxies is taking place in each cluster, we have leveraged the differences between clusters in the timescales and spatial location of the conversion process, in order to evaluate the relative importance of several proposed physical mechanisms that could be responsible for the transformation. Combined with other diagnostics that are sensitive to either ICM-driven galaxy evolution or galaxy–galaxy interactions—including the residuals from the Fundamental Plane and the properties of signpost compact emission line galaxies—we paint a tentative but remarkably self-consistent picture of galaxy evolution in clusters.

We find that spiral galaxies within infalling groups have already begun a slow process of conversion into S0s primarily via gentle galaxy–galaxy interactions that act to quench star formation, perhaps aided by interaction with the intragroup gas. The fates of spirals upon reaching the core of the cluster depend heavily on the cluster ICM, with rapid conversion of all remaining spirals into S0s via ram-pressure stripping in clusters where the pressure of the ICM is $\gtrsim 20\%$ of that needed to strip a canonical Milky Way–like spiral. In the presence of a less-dense ICM, the conversion continues at a slower pace, with galaxy–galaxy interactions continuing to play a role, perhaps along with “starvation” or gentle stripping by the ICM.

Several authors have raised objections to a scenario where S0s are created via simple fading of spiral disks. First, S0s are observed to have higher bulge-to-disk ratios than their supposed spiral progenitors (e.g., Burstein et al. 2005), suggesting that if the spiral to S0 conversion takes place, significant redistribution of mass or significant new star formation is required (Christlein & Zabludoff 2004; Kodama & Smail 2001). Second, other authors have noted that the local abundance of S0s is only weakly correlated with environment, such that processes like ram-pressure stripping that act only in cluster cores cannot be responsible for the entire buildup of S0s (Dressler 2004, 1980).

We have here demonstrated, however, that simple stripping of gas does *not* build up the entire population of cluster S0s. Rather, a combination of gas effects and galaxy interactions are responsible, in ratios that vary widely and depend on both the cluster dynamical state and the location within the cluster or its outskirts. The buildup of bulges through new star formation (Christlein & Zabludoff 2004) that is expected from harassment-like encounters could potentially balance out the expected fading of disks after ram-pressure stripping has run its course. It may still be necessary to invoke significant obscured star formation to bridge the observed gap between the bulges of spirals and S0s (Kodama & Smail 2001); the higher detection rate of such systems in Cl 0024 compared to MS 0451 (Geach et al. 2006) may indicate that such obscured starbursts are part of the preprocessing that occurs before galaxies encounter a dense ICM.

Furthermore, the wide distribution of passive spirals across both clusters, and their association with groups in the cluster outskirts, indicates that the resulting S0s will likely be spread across a wide range of environments. The typical densities of infalling groups at $z \sim 0.5$ are likely realized even in isolated groups by $z = 0$ (Fujita & Goto 2004), and so it seems that, though a variety of mechanisms are responsible, passive spirals could be the progenitors of most local S0s.

In Chapter 5, a rough assessment of the frequency of passive spirals and their expected lifetimes in Cl 0024 suggested that passive spirals could account for the entire buildup of S0s between $z = 0.4$ and $z = 0$. In MS 0451, we observe a similar number of spirals currently in the passive phase, but we have shown that the timescale for conversion is much shorter than in Cl 0024. This suggests that all existing spirals should be converted to S0 in MS 0451 even *before* $z = 0$, and the rate of any future buildup should be limited by the infall rate of new galaxies. As MS 0451 is a remarkably well-evolved system at $z = 0.54$, comparable in mass to Coma or Virgo ($6.9 \times 10^{14} M_{\odot}$ and $1.1 \times 10^{15} M_{\odot}$, respectively, Biviano et al. 1993; Fouqué et al. 2001; Geller et al. 1999), this is perhaps not surprising.

It suggests, however, that there may exist a generic tipping point in the evolution of a massive cluster: beyond the threshold in ram-pressure strength that we have

identified here (which is reached through some combination of cluster mass and ICM density), spirals are transformed so rapidly upon infall that they will be essentially absent. By $z = 0$, many clusters have likely reached this threshold, as evidenced by their low spiral fractions (Dressler et al. 1997; Dressler 1980). This sort of dichotomy between well-evolved and still-assembling clusters could, for example, explain why some clusters, like Coma, reveal few signs of evolution in their massive galaxies (Poggianti et al. 2004), while others, like Virgo, have a rich population of passive spirals and galaxies with other signs of recent evolution (e.g., Chung et al. 2007).

Regardless, the results presented here indicate that the abundant cluster spirals found at intermediate redshift, *do*, in fact, transform into the equally abundant S0 population seen today. The transformation process at $z = 0.5$, as we have seen, is beginning to operate even in groups at the cluster outskirts. As a result, the conversion of passive spirals to S0s can account for the evolution of the morphology–density relation at both the cluster and group scale from intermediate redshift to today.

Acknowledgements We would like to thank T. Heckman, G. Kauffmann, S. Yi, and other members of the *GALEX* science team for valuable discussions on passive spirals. We also thank A. Boselli for insightful comments, especially on the various physical processes and their timescales.

Chapter 7

Conclusions and Future Work

7.1 Summary

In this thesis, we have combined extensive spectroscopy with wide-field *HST* imaging to perform a detailed case study of two intermediate redshift galaxy clusters, Cl 0024+1654 ($z = 0.395$) and MS 0451-03 ($z = 0.540$). Leveraging a comprehensive multiwavelength data set that spans the X-ray to infrared, and with spectral line measurements serving as the key to revealing both the recent star-formation histories and kinematics of infalling galaxies, we have, through several investigations, shed light on the environmental processes that are acting to transform galaxies in clusters. Some of our key findings are as follows:

- By constructing the Fundamental Plane (FP) of Cl 0024, we observed that elliptical and S0 galaxies (E+S0s) exhibit a high scatter in their FP residuals, equivalent to a spread of 40% in mass to light ratio (M/L_V) (Chapter 3). The high scatter occurs only among galaxies in the cluster core, suggesting a turbulent assembly history for cluster early types, which we believe to be related to the recent cluster–subcluster merger (Czoske et al. 2002).
- We noted in Chapter 3 a substantial population of early-type galaxies in the core of Cl 0024 that seem to contain small populations of young stars. We proposed a scenario where remnant star formation persists in Cl 0024 early types, decaying as they fall into the cluster core, but with an apparent “rejuvenation”

event occurring within the virial radius. We now know from Chapter 6 that this apparent rejuvenation more likely represents the appearance of young S0s, recently transformed from passive spirals, into the early-type sample.

- Around the virial radius of Cl 0024, we observed a number of compact, intermediate mass ellipticals undergoing a burst of star formation or weak AGN activity, indicated by strong [O II] emission (Chapter 3). While we speculated that these objects could be due to interactions with shocks in the ICM, our later observation of similar objects in MS 0451 led us to conclude that they are likely merger remnants, with locations that mark the minimum radius at which merging is effective in each cluster.
- We searched for disruptions in the internal structures and star-formation rates of disk galaxies due to tidal effects or galaxy–galaxy interactions, by measuring emission line rotation curves and constructing the Tully-Fisher relation (Chapter 4). We find that the cluster TF relation exhibits significantly higher scatter than the field relation, echoing the high scatter seen in the Cl 0024 FP. We argue that the high scatter in both K - and V -band TF relations demonstrate that cluster spirals are kinematically disturbed by their environment. We proposed that such disturbances may be due to galaxy merging and/or harassment.
- We combined *GALEX* UV observations with key spectral line indices to place strict constraints on the recent star-formation histories of “passive spiral” galaxies, an important class of transition object (Chapter 5). Through *GALEX* UV imaging, we find that passive spirals in Cl 0024 exhibit UV emission nearly as strong as regular star forming spirals, implying the presence of young stars. Their unusual combination of UV emission with weak $H\delta$ strength supports a picture where passive spirals have experienced a rapid decline and eventual cessation of star formation over the last ~ 1 Gyr. The timescale of this decline implicates “starvation” by the ICM as the likely cause (Larson et al. 1980; Bekki et al. 2002).

- In Chapter 6, we document what we believe to be the first direct evidence for the transformation of spirals into S0s: through an analysis of their stellar populations and recent star-formation rates, we link the passive spiral galaxies in both clusters to their eventual end states as newly generated cluster S0 galaxies. Differences between the two clusters in both the timescales and spatial location of this conversion process allow us to evaluate the relative importance of several proposed physical mechanisms that could be responsible for the transformation.

Considering each of these pieces of evidence for interactions with the environment, we outlined in Chapter 6 a self-consistent picture of galaxy evolution in clusters. Under our model, spiral galaxies within infalling groups have already begun a slow process of conversion into S0s primarily via gentle galaxy–galaxy interactions that act to quench star formation, though a starvation-like interaction with an intragroup medium may also be at work.

The fates of spirals upon reaching the core of the cluster depend heavily on the cluster ICM, with rapid conversion of all remaining spirals into S0s via ram-pressure stripping in regimes where the strength of ram pressure exceeds 20% of that required to strip a canonical Milky Way–like spiral. In the presence of a less-dense ICM, the conversion continues at a slower pace, with galaxy–galaxy interactions continuing to play a role along with “starvation” by the ICM.

We conclude that the buildup of the local S0 population through the transformation of spiral galaxies is a heterogeneous process that nevertheless proceeds robustly across a variety of different environments from cluster outskirts to cores.

7.2 Reconciling Nature and Nurture

We return now to the essential question of nature vs. nurture posed in Chapter 1, and attempt to specify a bit more precisely the role of environment and of intrinsic processes in the buildup of galaxies in the universe.

While this thesis has focused on identifying the processes contributing to the “nurtured” evolution of cluster galaxies, we have nevertheless identified several effects

that could perhaps best be attributed to “nature”. In Chapter 3, the residuals from the Fundamental Plane revealed a gradient in stellar population ages for E+S0s as a function of radius. Likewise, we observed a tight “downsizing” trend (Cowie et al. 1996) in the stellar population ages of MS 0451 E+S0s, in the sense that lower-mass early types have younger ages. Both effects are perhaps best explained as arising from the different hierarchical formation histories experienced by galaxies spanning a range of masses and initial overdensities at formation. Each trend has been reproduced generally by hierarchical formation simulations that include intrinsic processes such as feedback (Croton et al. 2006; de Lucia et al. 2006).

However, evaluating the relative contributions of “nature” and “nurture” to the buildup of the galaxy populations we see today remains a controversial question. In the field at $z \sim 0.5$, Tanaka et al. (2007) find evidence that the median luminous red-sequence galaxy has recently truncated star formation on a fast timescale; based on this, they claim that galaxy–galaxy interaction plays a larger role in the buildup of the red sequence than “starvation”, which is inconsistent with the timescales for truncation they observe. This result may seem to conflict with our observation in Chapter 6 that star formation is being slowly quenched in group passive spirals. However, selection effects may play a role, in that they are most sensitive to detecting rapidly halted star formation in massive red galaxies that may include merging systems, while we specifically exclude such mergers due to their often irregular morphologies.

As a result, comparison of the two studies gives some insight into the question of nature vs. nurture. Being sensitive to merging systems, Tanaka et al. may well be observing the buildup of field ellipticals at $z \sim 0.5$, occurring via a combination of merging and AGN feedback. In contrast, our work has focused on the subsequent creation of S0s that is beginning in groups and finishing in clusters at the same redshift. This interpretation is supported by further work reported in Tanaka et al. (2007) claiming to observe a similar truncation of star formation in groups at $z \sim 0.8$. If S0s are rare in the universe at $z \sim 0.8$ (Smith et al. 2005a), then the evolution they observe likely involves the continuing buildup of ellipticals.

Considering the implication of these studies together, we note that they are

broadly consistent with the simple scenario posed in Chapter 1 for the evolution of galaxies within the hierarchical framework. That is, ellipticals form through mergers and cease forming stars first (perhaps via feedback), while S0s only form later as the strength and importance of environmental interactions increase in step with the buildup of large scale structure and clusters. Illustrated by the work in this thesis, it seems then that both of these processes—nature *and* nurture—are essential parts of the overall evolutionary history of the universe that led to the mix of morphologies and spread in star formation that we observe today.

7.3 Future Work

One of the key accomplishments of this thesis has been to directly trace the evolution of the passive spiral galaxies into cluster S0s. Yet analysis of galaxies in the SDSS shows that passive spirals are exceedingly rare in the universe today (Goto et al. 2003), at only $\sim 0.28\%$ of the total population. Their spectral properties (weak $H\delta$) and environments (in the outskirts of clusters) seem to indicate that they are more akin to the UV-detected passive spirals that predominate in the outskirts of our two $z \sim 0.5$ clusters.

Given that 25% of cluster spirals are passive at $z \sim 0.5$, it will be interesting to trace the decline in passive spirals over the next 5 Gyrs of cosmic history, and there are several key questions to be asked. Does the typical environment of a passive spiral move outward from the cluster core as group preprocessing has more time to act on spirals before they assemble onto clusters? How does the importance of ram-pressure stripping change as clusters evolve? Goto (2005) claims that the velocity dispersions of the various accreted populations indicate that harassment has been more important in the recent past than ram pressure, but it remains unknown whether the overall decline in spirals near cluster cores (Butcher & Oemler 1978; Dressler et al. 1997) is due to increased ram pressure or whether spirals disappear via harassment/group starvation even before encountering the ICM.

One way to begin answering these questions is to repeat the exercise of this thesis

on galaxy clusters at lookback times approximately halfway between $z \sim 0.5$ and today, at around $z = 0.2$. The LoCuSS survey aims to study ~ 100 clusters in the range $0.15 < z < 0.3$, and we have recently submitted a proposal to obtain *GALEX* imaging of 30 of these clusters, critical data to allow us to probe the stellar populations of passive spirals across these fields. By securing observations of a statistically significant sample of galaxy clusters at lower redshift where follow-up spectroscopy along with X-ray observations are more efficient, we can also hope to resolve the current uncertainty in whether starvation or harassment is driving the creation of passive spirals found in groups (Chapter 6).

Just as with $z \sim 0.2$ observations, probing the galaxy populations of higher redshift clusters will help to establish how the dominant physical processes acting to transform galaxies have evolved over time. The immaturity of large scale structure at $z \sim 0.8 - 1$ could well diminish the importance of group preprocessing, yet a number of clusters with dense ICMs and high fractions of red galaxies have been observed (Tanaka et al. 2007; Tran et al. 2007). Detailed observations of clusters at these higher redshifts may prove to be essential in understanding any role that environment plays in the original formation of the giant ellipticals.

An important outstanding issue, however, is the unknown abundance of S0s at $z \geq 0.8$. Visual determination of morphologies becomes uncertain at these high redshifts, due to effects like surface brightness dimming, band shifting, and loss of resolution. Even with ACS imaging, separating ellipticals from S0s is challenging. Postman et al. (2005), who attempted such a separation in their analysis of the morphology–density relation, find an S0 fraction that could be anywhere from 0%–30%, consistent with a wide range of evolutionary scenarios.

A promising alternative method involves separating Es from S0s via their kinematics. With deep resolved spectroscopy, it is in principle possible to distinguish between rotationally supported S0s and pressure-supported ellipticals, in much the same way that Binney (1982) originally considered the ratio of rotational velocity, v , to velocity dispersion, σ , to prove that ellipticals are not flattened by rotation but rather consist of stars on randomly oriented orbits.

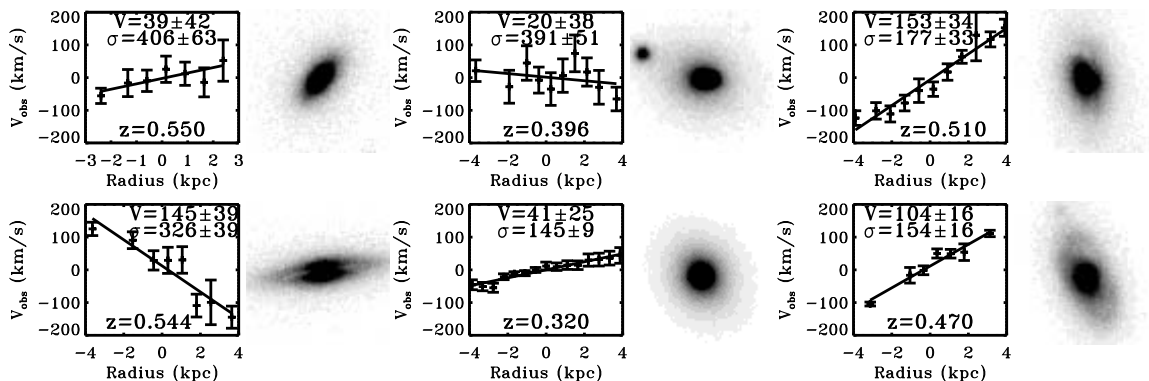


Figure 7.1 Selection of *HST* F814W images and rotation curves for field and cluster early types from our surveys of Cl 0024 and MS 0451. From top left to bottom right: two cluster Es, two cluster S0s, one field E and one field S0. In each case, the redshift, z , rotational velocity, v , and stellar velocity dispersion, σ , are listed with their errors.

As a pilot study for applying Binney’s technique to higher redshift, in Moran et al. (2007c) we have used the deep Keck spectroscopy of our E and S0 galaxies in Cl 0024 and MS 0451 to measure resolved rotation curves from absorption lines (Figure 7.1). Comparing our v and σ measurements to the visually determined morphologies, we empirically devise several discriminators that successfully separate Es from S0s at $z \sim 0.5$, as well as in a test sample at $z = 0$. Having verified the technique, future observations at $z \sim 0.8$ should be able to ascertain the S0 fraction to better precision than has been possible to date.

Finally, an essential component of star formation—one which is often neglected in intermediate to high z studies—is the HI and H₂ gas that indirectly and directly provide the source material for new stars. Studies of HI in spiral galaxies in and around local clusters find that they are largely depleted of HI, even when star formation appears to be ongoing (Boselli & Gavazzi 2006, and references therein). This is often interpreted as due to ram pressure in the ICM, particularly in the case of the Virgo cluster where the ICM is somewhat weak and many spirals continue to survive (Biviano et al. 1993).

Yet the connection between gas-poor galaxies in the local universe and the overall decline in star formation that reaches its peak at $z \sim 0.5$ has not yet been established. The first HI observations of clusters beyond the local universe have only recently been

reported (Verheijen et al. 2007, at $z = 0.2$), yielding tantalizing evidence that blue “Butcher-Oemler” spirals near the centers of clusters are gas depleted. Likewise, it is just now becoming possible to explore the H_2 content of galaxies at intermediate redshift. At the redshift of Cl 0024 ($z = 0.395$), the CO (3–2) line is redshifted into the 1mm wavelength band. Direct detection of this line in a typical, gas-rich spiral galaxy should be possible with recently commissioned millimeter facilities such as CARMA and the Submillimeter Array (SMA), as evidenced by initial exposure time estimates we have performed.

Due to the sensitivity limits of previous generations of instruments, molecular gas observations of galaxies spanning the redshift range from 0.1 to at least 1.0—corresponding to more than half the age of the universe—have largely been lacking, being limited to a handful of QSOs (e.g., Scoville et al. 1993). As a result, a small survey of the gas content in a sample of cluster galaxies in, e.g., Cl 0024, could be very powerful. Such a survey would add greatly to our understanding of the evolution in gas content within both typical galaxies and “transition” objects, and paint a more complete picture of how the decline in cosmic star-formation rate progresses across time. Crucially, we could establish whether passive spiral galaxies are truly gas poor, or if they have simply entered a temporary quiescent state, as has been suggested by, e.g., Burstein et al. (2005). This is an especially important question for the passive spirals found within infalling groups, where our UV observations indicate that young stars are still present.

Together, these future observations of transition galaxies at both higher and lower redshift than those presented in this thesis, combined with direct observations of molecular gas content, have the potential to fill in large blank areas in our map of how galaxies evolve and cease to form stars during their assembly into clusters.

Bibliography

Abell, G. O., Corwin, H. G., Jr., & Olowin, R. P. 1989, ApJS, 70, 1

Abraham, R. G., et al. 1996a, ApJS, 107, 1

Abraham, R. G., et al. 1996b, ApJ, 471, 694

Balogh, M. L. & Morris, S. L. 2000, MNRAS, 318, 703

Balogh, M. L., Morris, S. L., Yee, H. K. C., Carlberg, R.G., & Ellingson, E. 1999, ApJ, 527, 54

Bamford, S. P., Aragón-Salamanca, A., & Milvang-Jensen, B. 2006, MNRAS, 366, 308

Bamford, S. P., Aragón-Salamanca, A., Milvang-Jensen, B., & Simard, L. 2005, MNRAS, 361, 109

Barbaro, G. & Poggianti, B. M. 1997, A&A, 324, 490

Barr, J., Davies, R., Jørgensen, I., Bergmann, M., & Crampton, D. 2005, AJ, 130, 445

Bekki, K. 1998, ApJ, 502, L133

Bekki, K., Couch, W. J., & Shioya, Y. 2002, ApJ, 577, 651

Bender, R., Burstein, D., & Faber, S.M. 1992, ApJ, 399, 462

Bender, R., Burstein, D., & Faber, S.M. 1993, ApJ, 411, 153

- Bender, R., Saglia, R. P., Ziegler, B., Belloni, P., Greggio, L., Hopp, U., & Bruzual, G. 1998, *ApJ*, 493, 529
- Bertin, E. & Arnouts, S. 1996, *A&AS*, 117, 393
- Bettoni, D., Galletta, G., & Garcia-Burillo, S. 2003, *A&A*, 405, 5
- Binney, J. 1982, *ARA&A*, 20, 399
- Biviano, A. Girardi, M., Giuricin, G., Mardirossian, F., & Mezzetti, M. 1993, *ApJ*, 376, 458
- Blanton, M. R., et al. 2003, *AJ*, 125, 2348
- Böhm, A., et al. 2004, *A&A*, 420, 97
- Boselli, A., Boissier, S., Cortese, S., Gil de Paz, A., Seibert, M., Madore, B. F., Buat, V. & Martin, D. C. 2006, *ApJ*, 651, 811
- Boselli, A. & Gavazzi, G. 2006, *PASP*, 118, 517
- Bower, R., Kodama, T., & Terlevich, A. 1998, *MNRAS*, 299, 1193
- Bower, R., Lucey, J. R., & Ellis, R. S. 1992, *MNRAS*, 254, 601
- Bressan, A., Chiosi, C., & Tantalo, R. 1996, *A&A*, 311, 425
- Bruzual, G. & Charlot, S. 2003, *MNRAS*, 344, 1000
- Burstein, D., Faber, S. M., Gaskell, C. M., & Krumm, N. 1984, *ApJ*, 287, 586
- Burstein, D., Ho, L. C., Huchra, J. P., & Macri, L. M. 2005, *ApJ*, 621, 246.
- Butcher, H. & Oemler, J., Jr. 1978, *ApJ*, 226, 559
- Calzetti, D., Kinney, A. L., & Storchi-Bergmann, T. 1994, *ApJ*, 429, 582
- Cardelli, J. A., Clayton, G. C., & Mathis, J. S. 1989, *ApJ*, 345, 245

- Cattaneo, A., Dekel, A., Devriendt, J., Guiderdoni, B., & Blaizot, J. 2006, MNRAS, 370, 1651
- Christlein, D. & Zabludoff, A. I. 2004, ApJ, 616, 192
- Chung, A., van Gorkom, J. H., Kenney, J. D. P., & Vollmer, B. 2007, ApJ, 659, L115
- Cooper, M. C., et al. 2007, MNRAS, 376, 1445
- Cortese, L., et al. 2007, MNRAS, 376, 157
- Couch, W. J., Barger, A. J., Smail, I., Ellis, R. S., & Sharples, R. M. 1998, ApJ, 497, 188
- Couch, W. J. & Sharples, R. M. 1987, MNRAS, 229, 423
- Cowie, L. L. & Songaila, A. 1977, Nature, 266, 501
- Cowie, L. L., Songaila, A., Hu, E. M., & Cohen, J. G. 1996, AJ, 112, 839
- Croton, D., et al. 2006, MNRAS, 365, 11
- Cuillandre J.-C., Luppino, G., Starr, B., & Isani, S. 2000, Proc. SPIE, 4008, 1010
- Czoske, O., Kneib, J.-P., Soucail, G., Bridges, T. J., Mellier, Y., & Cuillandre, J.-C. 2001, A&A, 372, 391
- Czoske, O., Moore, B., Kneib, J.-P., & Soucail, G. 2002, A&A, 386, 31
- Davis, M., et al. 2003, Proc. SPIE, 4834, 161
- De Filippis, E., Sereno, M., Bautz, M., & Longo, G. 2005, ApJ, 625, 108
- de Lucia, G., Springel, V., White, S. D., Croton, D., & Kauffmann, G. 2006, MNRAS, 366, 499
- Desai, V., et al. 2007, ApJ, 660, 1151
- Djorgovski, S. & Davis, M. 1987, ApJ, 313, 59

- Donahue, M., Gaskin, J. A., Patel, S. K., Joy, M., Clowe, D., & Hughes, J. P. 2003, *ApJ*, 598, 190
- Dressler, A. 1980, *ApJ*, 236, 351
- Dressler, A. 2004, in *Carnegie Observatories Centennial Symposia*, Eds: J.S. Mulchaey, A. Dressler, & A. Oemler, (Cambridge University Press: Cambridge, UK), 206
- Dressler, A. & Gunn, J. E. 1983, *ApJ*, 270, 7
- Dressler, A. & Gunn, J. E. 1992, *ApJS*, 78, 1
- Dressler, A., Lynden-Bell, D., Burstein, D., Davies, R. L., Faber, S. M., Terlevich, R., & Wegner, G. 1987, *ApJ*, 313, 42
- Dressler, A. & Shectman, S. A. 1988, *AJ*, 95, 985
- Dressler, A., Smail, I., Poggianti, B., Butcher, H., Couch, W. J., Ellis, R. S., & Oemler, A., Jr. 1999, *ApJS*, 122, 51
- Dressler, A., et al. 1997, *ApJ*, 490, 577
- Ellingson, E. 2004, in *IAU Colloq. 195, Outskirts of Galaxy Clusters: Intense Life in the Suburbs*, ed. A. Diaferio, (Cambridge, UK: Cambridge University Press), 327
- Ellingson, E., Yee, H. K. C., Abraham, R. G., Morris, S. L., & Carlberg, R. G. 1998, *ApJS*, 116, 247
- Ellis, R. S., Smail, I., Dressler, A., Couch, W. J., Oemler, A., Jr., Butcher, H. & Sharples, R. M. 1997, *ApJ*, 483, 582
- Evrard, A. E. 1991, *MNRAS*, 248, 8
- Faber, S. M., et al. 2003, *Proc. SPIE*, 4841, 1657
- Fabricant, D., Franx, M., & van Dokkum, P. 2000, *ApJ*, 539, 577

- Fasano, G., Poggianti, B. M., Couch, W. J., Bettoni, D., Kjrgaard, P. & Moles, M. 2000, *ApJ*, 542, 673
- Fisher, D., Fabricant, D., Franx, M., & van Dokkum, P. 1998, *ApJ*, 498, 195
- Fouqué, P. Solanes, J. M., Sanchis, T. & Balkowski, C. 2001, *A&A*, 375, 770
- Fritz, A., Ziegler, B., Bower, R. G., Smail, I., & Davies, R. L. 2005, *MNRAS*, 358, 233
- Fujita, Y. 1998, *ApJ*, 509, 587
- Fujita, Y. 2001, *ApJ*, 550, 612
- Fujita, Y. 2004, *PASJ*, 56, 29
- Fujita, Y. & Goto, T. 2004, *PASJ*, 56, 29
- Fujita, Y. & Nagashima, M. 1999, *ApJ*, 516, 619
- Furlanetto, S. R. & Loeb, A. 2004, *ApJ*, 611, 642
- Gavazzi, G., Boselli, A., Cortese, L., Arosio, I., Gallazzi, A., Pedotti, P., & Carrasco, L. 2006, *A&A*, 446, 839
- Gavazzi, G., Zaccardo, A., Sanvito, G., Boselli, A., & Bonfanti, C. 2004, *A&A*, 417, 499
- Geach, J. E., et al. 2006, *ApJ*, 649, 661
- Geller, M. J., Diaferio, A., & Kurtz, M. J. 1999, *ApJ*, 517, L23
- Gerhard, O., Kronawitter, A., Saglia, R. P. & Bender, R. 2001, *AJ*, 121, 1936
- Gerken, B., Ziegler, B., Balogh, M., Gilbank, D., Fritz, A., & Jäger, K. 2004, *A&A*, 421, 59
- Gill, S. P., Knebe, A., & Gibson, B. 2005, *MNRAS*, 356, 1327

- Gómez, P.L., et al. 2003, *ApJ*, 584, 210
- Goto, T. 2005, *MNRAS*, 357, 937
- Goto, T., et al. 2003, *PASJ*, 55, 771
- Granato, G. L., De Zotti, G., Silva, L., Bressan, A. & Danese, L. 2004, *ApJ*, 600, 580
- Gunn, J. E. & Gott, J. R. 1972, *ApJ*, 176, 1
- Hester, J. A. 2006, *ApJ*, 647, 910
- Homeier, N.L., et al. 2005, *ApJ*, 621, 651
- Holden, B.P., et al. 2005, *ApJ*, 620, L83
- Horne, K. 1986, *PASP*, 98, 609
- Jee, M. J., et al. 2007, *ApJ*, 661, 728
- Jeltema, T. E., Mulchaey, J. S., Lubin, L. M., & Fassnacht, C. D. 2007, *ApJ*, 658, 865
- Jørgensen, I., Franx, M., & Kjaergaard, P. 1995a, *MNRAS*, 276, 1341
- Jørgensen, I., Franx, M., & Kjaergaard, P. 1995b, *MNRAS*, 273, 1097
- Jørgensen, I., Franx, M., & Kjaergaard, P. 1996, *MNRAS*, 280, 167
- Kannappan, S. J., Fabricant, D. G., & Franx, M. 2002, *AJ*, 123, 2358
- Kauffmann, G., White, S. D. M., Heckman, T. M., Ménard, B., Brinchmann, J. Charlot, S. Tremonti, C., & Brinkmann, J. 2004, *MNRAS*, 353, 713
- Kauffmann, G., et al. 2003, *MNRAS*, 341, 33
- Kelson, D. D., Illingworth, G. D., Franx, M., & van Dokkum, P. G. 2001, *ApJ*, 552, L17

- Kelson, D. D., Illingworth, G. D., van Dokkum, P. G., & Franx, M. 2000a, ApJ, 531, 137
- Kelson, D. D., Illingworth, G. D., van Dokkum, P. G., & Franx, M. 2000b, ApJ, 531, 184
- Kennicutt, R. C., Jr. 1992, ApJ, 388, 310
- Kneib, J-P., et al. 2003, ApJ, 598, 804
- Kodama, T., Balogh, M., Smail, I., Bower, R. G. & Nakata, F. 2004, MNRAS, 354, 1103
- Kodama, T. & Smail, I. 2001, MNRAS, 326, 637
- Kodama, T., Smail, I., Nakata, F., Okamura, S., & Bower, R. G. 2001, ApJ, 562, 9
- Kodama, T., et al. 2005, PASJ, 57, 309
- Koo, D., Guzmán, R., Faber, S. M., Illingworth, G. D., Bershady, M. A., Kron, R. G. & Takamiya, M. 1995, ApJ, 440, 49
- Kuntschner, H. 2000, MNRAS, 315, 184
- Kuntschner, H., Lucey, J.R. Smith, R. J., Hudson, M. J. & Davies, R. L. 2001, MNRAS, 323, 615
- Larson, R. B., Tinsley, B. M., & Caldwell, C. N. 1980, ApJ, 237, 692
- Lewis, I., et al. 2002, MNRAS, 334, 673
- Lubin, L. M., Oke, J. B., & Postman, M. 2002, AJ, 124, 1905
- Lucey, J.R., Guzmán, R., Carter, D. & Terlevich, R. J. 1991, MNRAS, 253, 584
- MacArthur, L. A. 2005, ApJ, 623, 795
- Margoniner, V. E., de Carvalho, R. R., Gal, R. R. & Djorgovski, S. G. 2001, ApJ, 548, 143

- Martin, D. C., et al. 2005, ApJ, 619, L1
- Mastropietro, C., Moore, B., Mayer, L., Debattista, V. P., Piffaretti, R., & Stadel, J. 2005, MNRAS, 364, 607
- Menanteau, F., et al. 2004, ApJ, 612, 202
- Metevier, A. J. & Koo, D. C., 2004, IAUS, 220, 415
- Metevier, A. J., Koo, D. C., Simard, L. & Phillips, A. 2006, ApJ, 643, 764
- Mihos, C. 2004, in IAU Symposium no. 217, Recycling Interstellar and Intergalactic Matter, ed. P-A. Duc, J Braine, E Brinks, (San Francisco:ASP), 390
- Milvang-Jensen, B., Aragón-Salamanca, A. Hau, G., Jørgensen, I. & Hjorth, J. 2003, MNRAS, 339, 1
- Moore, B., Katz, N. et al. 1996, Nature, 379, 613
- Moore, B., Lake, G., & Katz, N. 1998, ApJ, 495, 139
- Moore, B., Lake, G., Quinn, T. & Stadel, J. 1999, MNRAS, 304, 465
- Moran, S. M., Ellis, R. S., Treu, T., Salim, S., Rich, R. M., Smith, G. P. & Kneib, J-P. 2006, ApJ, 641, L97
- Moran, S. M., Ellis, R. S., Treu, T., Smith, G. P., Rich, R. M., & Smail, I. 2007b, ApJ, in press
- Moran, S. M., Ellis, R. S., Treu, T., Smith, G. P., Smail, I., Dressler, A., & Coil, A. L. 2005, ApJ, 634, 977
- Moran, S. M., Loh, B. L., Ellis, R. S., Treu, T., Bundy, K. & MacArthur, L. A. 2007c, ApJ, 665, 1067
- Moran, S. M., Miller, N., Treu, T., Ellis, R. S. & Smith, G. P. 2007a, ApJ, 659, 1138
- Morrissey, P., et al. 2005, ApJ, 619, L7

- Mulchaey, J. 2000, *ARA&A*, 38, 289
- Naab, T. & Burkert, A. 2003, *ApJ*, 597, 893
- Nakamura, O., Aragón-Salamanca, A., Milvang-Jensen, B., Arimoto, N., Ikuta, C. & Bamford, S. P. 2006, *MNRAS*, 366, 144
- Natarajan, P., Kneib, J-P., Smail, I. & Ellis, R. S. 1998, *ApJ*, 499, 600
- Noeske, K. G., Koo, D. C., Phillips, A. C., Willmer, C. N. A., Melbourne, J., de Paz, A. G., & Papaderos, P. 2006, *ApJ* 640, L143
- Nulsen, P. E. J. 1982, *MNRAS*, 198, 1007
- Okamoto, T. & Nagashima, M. 2003, *ApJ*, 587, 500
- Oosterloo, T., Fraternali, F., & Sancisi, R. 2007, *AJ*, 134, 1019
- Ota, N., Pointecouteau, E., Hattori, M., & Mitsuda, K. 2004, *ApJ*, 601, 120
- Peng, C. Y., Ho, L. C., Impey, C. D., & Rix, H. 2002, *AJ*, 124, 266
- Poggianti, B. M. & Barbaro, G., 1996, *A&A*, 314, 379
- Poggianti, B. M. & Barbaro, G., 1997, *A&A*, 325, 1025
- Poggianti, B. M., Bridges, T. J., Komiyama, Y., Yagi, M., Carter, D., Mobasher, B., Okamura, S., & Kashikawa, N. 2004, *ApJ*, 601, 197
- Poggianti, B. M., Smail, I., Dressler, A., Couch W. J., Barger, A. J., Butcher, H., Ellis, R. S., & Oemler, A., Jr. 1999, *ApJ*, 518, 576
- Poggianti, B. M. & Wu, H., 2000, *ApJ*, 529, 157
- Poggianti, B. M., et al. 2001, *ApJ*, 563, 118
- Poggianti, B. M., et al. 2006, *ApJ*, 642, 188
- Postman, M., Lauer, T. R., Szapudi, I. & Oegerle, W. 1998, *ApJ*, 506, 33

- Postman, M., et al. 2005, *ApJ*, 623, 721
- Quilis, V., Moore, B., & Bower, R. 2000, *Science*, 288, 1617
- Rawat, A., Kembhavi, A. K., Hammer, F., Flores, H. & Barway, S. 2007, *A&A*, 469, 483
- Roettiger, K., Burns, J., & Loken, C. 1996, *ApJ*, 473, 651
- Ruderman, J.T. & Ebeling, H. 2005, *ApJ*, 623, 81
- Rusin, D., et al. 2003, *ApJ*, 587, 143
- Ryu, D., Kang, H., Hallman, E. & Jones, T. W. 2003, *ApJ*, 593, 599
- Saglia, R. P., Bender, R., & Dressler, A. 1993, *A&A*, 279, 75
- Sato, T. & Martin, C.L. 2006, *ApJ*, 647, 946
- Schechter, P. L. 1980, *AJ*, 85, 801
- Schlegel, D. J., Finkbeiner, D. P., & Davis, M. 1998, *ApJ*, 500, 525
- Scoville, N. Z., Padin, S., Sanders, D. B., Soifer, B. T., & Yun, M. S. 1993, *ApJ*, 415, L75
- Smail, I., Dressler, A., Couch, W. J., Ellis, R. S., Oemler, A., Jr., Butcher, H. & Sharples, R. M. 1997, *ApJS*, 110, 213
- Smith, G. P., Treu, T., Ellis, R. S., Moran, S. M., & Dressler, A. 2005a, *ApJ*, 620, 78
- Smith, G. P., et al. 2005b, *MNRAS*, 359, 417
- Tanaka, M., Hoshi, T., Kodama, T. & Kashikawa, N. 2007, *MNRAS*, 379, 1546
- Tantalo, R. & Chiosi, C. 2004, *MNRAS*, 353, 917
- Thomas, D., Maraston, C., & Bender, R. 2003, *MNRAS*, 339, 897
- Toniazzo, T. & Schindler, S. 2001, *MNRAS*, 325, 509

- Trager, S. C., Worthey, G., Faber, S. M., Burstein, D. & Gonzalez, J. J. 1998, ApJS 116, 1
- Tran, K.-V., Franx, M., Illingworth, G., Kelson, D. D., & van Dokkum, P. 2003, ApJ, 599, 865
- Tran, K.-V. H., Franx, M., Illingworth, G. D., van Dokkum, P. Kelson, D. D., Blakeslee, J. P., & Postman, M. 2007, ApJ, 661, 750
- Tran, K.-V. H., van Dokkum, P., Illingworth, G. D., Kelson, D., Gonzalez, A., & Franx, Marijn 2005, ApJ, 619, 134
- Treu, T., Ellis, R. S., Kneib, J-P., Dressler, A., Smail, I., Czoske, O., Oemler, A., & Natarajan, P. 2003, ApJ, 591, 53 (T03)
- Treu, T, Ellis, R. S., Liao, T. X. & van Dokkum, P. G. 2005a, ApJ, 622, L5
- Treu, T., Stiavelli, M., Bertin, G., Casertano, S., & Møller, P. 2001a, MNRAS, 326, 237
- Treu, T., Stiavelli, M., Casertano, S., Møller, P., & Bertin, G. 2002, ApJ, 564, L13
- Treu, T., Stiavelli, M., Casertano, S., Møller, P., & Bertin, G., 1999, MNRAS, 308, 1037
- Treu, T., Stiavelli, M., Møller, P., Casertano, S., & Bertin, G. 2001b, MNRAS, 326, 221
- Treu, T., et al. 2005b, ApJ, 633, 174
- Tully, R. B. & Fisher, J. R. 1977, A&A, 54, 661.
- Tully, R. B. & Fouque, P. 1985, ApJS, 58, 67
- Tully, R. B., & Pierce, M. 2000, ApJ, 533, 744
- Tully, R. B., Pierce, M., Huang, J., Saunders, W., Verheijen, M., & Witchalls, P. 1998, AJ, 115, 2264

- van den Bergh, S. 1976, *ApJ*, 206, 883
- van der Marel, R. 1994, *MNRAS*, 270, 271
- van der Wel, A., Franx, M., van Dokkum, P. G., Rix, H.-W., Illingworth, G. D. & Rosati, P. 2005, *ApJ*, 631, 145
- van Dokkum, P. & Franx, M. 1996, *MNRAS*, 281, 985
- van Dokkum, P. & Franx, M. 2001, *ApJ*, 533, 90
- Verheijen, M. 2001, *ApJ*, 563, 694
- Verheijen, M., van Gorkom, J., Szomoru, A., Dwarakanath, K. S., Poggianti, B., & Schiminovich, D. 2007, *NewAR*, 51, 70
- Vogt, N., Forbes, D. Phillips, A., Gronwall, C., Faber, S. M., Illingworth, G., & Koo, D. 1996, *ApJ*, 465, L15
- White, S. D. M., et al. 2005, *A&A*, 444, 365
- White, S. D. M., Navarro, J. F., Evrard, A. E. & Frenk, C. S. 1993, *Nature*, 366, 429
- Whitmore, B. C., Gilmore, D. M., & Jones, C. 1993, *ApJ*, 407, 489
- Willick, J. 1994, *ApJS*, 92, 1
- Wilson, J. C., et al. 2003, *Proc. SPIE*, 4841, 451
- Worthey, G., Faber, S. M., Gonzalez, J. J., & Burstein, D. 1994, *ApJS*, 94, 687
- Worthey, G. & Ottaviani, D. 1997, *ApJS*, 111, 377
- Wuyts, S., van Dokkum, P. G., Kelson, D. D., Franx, M. & Illingworth, G. D. 2004, *ApJ*, 605, 677
- Zabludoff, A. & Mulchaey, J. 1998, *ApJ*, 496, 39
- Zhang, Y. -Y., Böhringer, H., Mellier, Y., Soucail, G., & Forman, W. 2005, *A&A*, 429, 85

Ziegler, B.L., Böhm, A., Jäger, K., Heidt, J., & Mllenhoff, C. 2003, ApJ, 598, L87

Ziegler, B. L., Bower, R. G., Smail, I., Davies, R. L. & Lee, D. 2001, MNRAS, 325,
1571

Ziegler, B. L., Thomas, D., Böhm, A., Bender, R., Fritz, A., & Maraston, C. 2005,
A&A, 433, 519